

2019 년 8 월

박사학위 논문

**Investigation of Development of  
Thermo-Mechanical Analysis Method for a Wire  
Feeding Type Directed Energy Deposition Process**

조선대학교 대학원

기계공학과

**BIH LII CHUA**

# **Investigation of Development of Thermo-Mechanical Analysis Method for a Wire Feeding Type Directed Energy Deposition Process**

와이어 공급형 직접식 에너지 적층 공정의 열-구조 연계 해석  
기법 개발에 관한 연구

2019 년 8 월 23 일

**Graduate School of Chosun University**

**Department of Mechanical Engineering**

**BIH LII CHUA**

# **Investigation of Development of Thermo-Mechanical Analysis Method for a Wire Feeding Type Directed Energy Deposition Process**

지도교수 안 동 규

이 논문을 공학 박사학위신청 논문으로 제출함

2019 년 4 월

조선대학교 대학원

기 계 공 학 과

**BIH LII CHUA**

## BIH LII CHUA 의 박사학위논문을 인준함

위원장	조선대학교	교수	한길영 (인)
위원	조선대학교	교수	박종락 (인)
위원	조선대학교	교수	오동욱 (인)
위원	한국생산기술연구원	박사	손용 (인)
위원	조선대학교	교수	안동규 (인)

2019 년 6 월

조선대학교 대학원

## TABLE OF CONTENTS

<b>NOMENCLATURES .....</b>	<b>v</b>
<b>LIST OF FIGURES.....</b>	<b>x</b>
<b>LIST OF TABLES .....</b>	<b>xvii</b>
<b>ABSTRACT .....</b>	<b>xix</b>
<b>I. INTRODUCTION .....</b>	<b>1</b>
<b>A. Research Backgrounds.....</b>	<b>1</b>
1. Additive Manufacturing.....	1
2. Directed Energy Deposition .....	3
3. Wire Feeding Type Directed Energy Deposition System in Republic of Korea .....	6
<b>B. Research Motivation .....</b>	<b>8</b>
<b>C. Previous Research Works .....</b>	<b>10</b>
1. Thermo-Mechanical Analysis for DED Process .....	10
2. Applications of Titanium Alloy Ti-6Al-4V .....	17
<b>D. Objective and Scope of the Thesis.....</b>	<b>18</b>
<b>II. BEAD PROFILE FOR WIRE FEEDING TYPE DIRECTED ENERGY DEPOSITION PROCESS.....</b>	<b>21</b>
<b>A. Wire Feeding Type Directed Energy Deposition Apparatus .....</b>	<b>21</b>
<b>B. Derivation of Bead Profile for Single Bead Deposition .....</b>	<b>23</b>
1. Description of Experiments.....	23
2. Methodology .....	23
3. Results and Discussion.....	27
<b>C. Derivation of Bead Profile for Multi-Layer Deposition .....</b>	<b>35</b>

1.	Description of Multi-Layer Deposition and Related Works .....	35
2.	Polygonal-Shaped Cross Section Profile and Constant Width Model	37
3.	Results and Discussion.....	40
D.	Derivation of Bead Profile for Planar Deposition.....	43
1.	Description of Planar Deposition and Related Works .....	43
2.	Methodology .....	45
3.	Results and Discussion.....	46
<b>III.</b>	<b>CALIBRATION OF HEAT SOURCE MODEL.....</b>	<b>49</b>
A.	Introductory Remarks .....	49
1.	Description of Heat Source Model.....	49
2.	Related Works .....	50
B.	Numerical Analysis of Single Bead Deposition .....	52
1.	Physical Description.....	52
2.	Formulation of Heat Flux Model and Heat Losses .....	52
3.	Material Properties and Boundary Conditions.....	56
C.	Calibration of Penetration Depth and Efficiency of Heat Flux.....	58
1.	Calibration Methodology .....	58
2.	Finite Element Analysis .....	59
3.	Results and Discussion.....	60
<b>IV.</b>	<b>SELECTION OF DESIGN PARAMETERS AND DEPOSITION STRATEGIES FOR A WIRE FEEDING TYPE DIRECTED ENERGY DEPOSITION PROCESS.....</b>	<b>69</b>
A.	Derivation of Proper Gap Between Deposition Beads .....	69
1.	Description of the Analysis.....	69
2.	Analysis Conditions .....	70
3.	Results and Discussion.....	71
B.	Influence of Corner Deposition on Formation of Heat Affected Zone,	

	<b>Stress Influenced Region and Thermal Stress .....</b>	<b>83</b>
1.	<b>Description of the Analysis .....</b>	<b>83</b>
2.	<b>Analysis Conditions .....</b>	<b>83</b>
3.	<b>Results and Discussion.....</b>	<b>85</b>
<b>C.</b>	<b>Influence of Deposition Strategy on Thermo-Mechanical Characteristics of a Multi-Layer Deposition .....</b>	<b>92</b>
1.	<b>Description of the Analysis .....</b>	<b>92</b>
2.	<b>Analysis Parameters and Boundary Conditions .....</b>	<b>93</b>
3.	<b>Results and Discussion.....</b>	<b>99</b>
<b>D.</b>	<b>Verification of Thermo-Mechanical Analysis for a Multi-Layer Deposition.....</b>	<b>108</b>
1.	<b>Description of the Experiments .....</b>	<b>108</b>
2.	<b>Results and Discussion.....</b>	<b>109</b>
<b>E.</b>	<b>Investigation of Optimum Interpass Time for a Multi-Layer Deposition .....</b>	<b>112</b>
1.	<b>Description of the Analysis and Methodology .....</b>	<b>112</b>
2.	<b>Analysis Parameters .....</b>	<b>114</b>
3.	<b>Results and Discussion.....</b>	<b>115</b>
<b>F.</b>	<b>Investigation of Influence of Power of Laser on Interpass Temperature for a Multi-Layer Deposition.....</b>	<b>120</b>
1.	<b>Description of the Analysis and Methodology .....</b>	<b>120</b>
2.	<b>Analysis Parameters .....</b>	<b>120</b>
3.	<b>Results and Discussion.....</b>	<b>121</b>
<b>G.</b>	<b>Influence of Interpass Time and Deposition Pattern on Thermo-Mechanical Characteristics of a Planar Deposition .....</b>	<b>124</b>
1.	<b>Description of the Analysis .....</b>	<b>124</b>
2.	<b>Analysis Parameters and Boundary Conditions .....</b>	<b>124</b>
3.	<b>Results and Discussion.....</b>	<b>125</b>

**V. ACTIVATION ALGORITHM OF FINITE ELEMENTS ..... 135**

- A. Introductory Remarks ..... 135**
  - 1. Description of Activation Algorithm ..... 135
  - 2. Related Works ..... 136
- B. Proposed Element Activation Algorithm..... 138**
  - 1. Description of Proposed Element Activation Algorithm ..... 138
- C. Selection of Front Element Cross Section for Proposed Element Activation Algorithm..... 143**
  - 1. Description of Heat Transfer Analysis and Boundary Conditions ... 143
  - 2. Heat Flux Model..... 144
  - 3. Results and Discussion..... 145
- D. Heat Transfer Characteristics Using Proposed Element Activation Algorithm ..... 151**
  - 1. Description of Analysis and Analysis Conditions ..... 151
  - 2. Results and Discussion..... 151
- E. Thermo-Mechanical Analysis Using Proposed Proposed Element Activation Algorithm..... 158**
  - 1. Description of Analysis and Analysis Conditions ..... 158
  - 2. Results and Discussion..... 159

**VI. CONCLUSIONS AND FUTURE WORKS..... 163**

**REFERENCES ..... 166**

**ACKNOWLEDGEMENTS..... 181**

**CURRICULUM VITAE ..... 183**



## NOMENCLATURES

$\theta$	Angle of corner deposition
$\theta_{\text{sys}}$	Azimuthal angle of a cylindrical coordinate system
$\rho$	Density
$\varepsilon$	Emissivity
$\alpha$	Thermal diffusivity
$\beta$	Volumetric thermal expansion coefficient of fluid
$\delta_d$	Depth error of heat affected zone
$\phi_{\text{OL}}$	Overlap ratio
$\alpha_r$	Wetting angle of deposited bead
$\sigma_s$	Stefan-Boltzmann constant
$\alpha_s$	Volumetric thermal expansion of solid
$\sigma_u$	Ultimate strength
$\sigma_{u,c}$	Critical ultimate strength
$\delta_w$	Width error of heat affected zone
$\sigma_y$	Yield strength
$\sigma_{y,c}$	Critical yield strength
$\eta$	Efficiency of laser
$\lambda$	Wavelength of laser
$\lambda_f$	Safety factor to estimate critical fatigue limit
$\lambda_y$	Safety factor to estimate critical yield strength
$\mu_p$	Increment of depth of HAZ per unit increment of power of laser
$\mu_v$	Increment of depth of HAZ per unit increment of travel speed of table
$\nu$	Poisson's ratio

$v_k$	Kinematic viscosity
$\omega_p$	Increment of width of HAZ per unit increment of power of laser
$\omega_v$	Increment of width of HAZ per unit increment of travel speed of table
$\mu_a$	Absorption coefficient
$\Delta d$	Difference between the estimated results from FEAs and those of experiments
$A_b$	Area of cross section of a deposited bead
$A_{el}$	Estimated area of cross section of a deposited bead using semi-ellipse
$A_{exp}$	Cross section area of measured bead
$A_{gen}$	Cross section area of generated bead
$A_{L1}$	Area of half polygonal-shaped cross section profile of a single bead
$A_{LP}$	Area of half polygonal-shaped cross section profile of an overlapping bead
$A_{LS}$	Area of half polygonal-shaped cross section profile of a stacked layer bead
$A_p$	Cross section area of polygonal-shaped profile bead
$A_r$	Relative nozzle area
$A_s$	Surface area
$b$	Contant of front element cross section ahead of center of beam
$C_p$	Specific heat of capacity
$C_r$	Cooling rate
$D$	Diameter of nozzle
$d_{exp}$	Vertical displacement measured in experiment
$d_{FEA}$	Vertical displacement estimated by FEA
$d_{HAZ,a}$	Actual depth of heat affected zone
$d_{HAZ,e}$	Estimated depth of heat affected zone
$d_p$	Penetration depth of laser
$D_r$	Deposition rate
$E$	Young's modulus
$E_{HAZ}$	Eccentricity of HAZ

$E_s$	Specific heat energy
$g$	Gravitational acceleration constant
$g_b$	Optimum distance between beads in a planar deposition
$Gr_L$	Grashof number
$g_w$	Optimum distance between beads in a planar deposition
$H$	Distance between nozzle to plate surface
$h_b$	Height of deposited bead
$h_{conv}$	Coefficient of convection
$h_{rad}$	Coefficient of radiation
$h_s$	Height of stacked bead
$K$	Gaussian beam propagation factor
$k$	Thermal conductivity
$L_B$	Length of bead
$L_c$	Characteristics length
$L_{i,HAZ}$	Inner distance of HAZ
$L_{i,SIR}$	Inner distance of SIR
$L_{o,HAZ}$	Outer distance of HAZ
$L_{o,SIR}$	Outer distance of SIR
$m$	Number of sets of measured coordinates
$n$	Number of points
$Nu_L$	Nusselt number
$P$	Power of laser
$Pr$	Prandtl number
$Q$	Heat flux
$\dot{Q}$	Heat generation
$q''_{conv}$	Heat flux due to convection
$q''_{rad}$	Heat flux due to radiation

$Q_0$	Maximum heat flux at the center of beam
$r$	Radial distance from the center of beam
$r_0$	Effective radius of beam
$r_b$	Radius of beam
$r_e$	Effective radius of beam at $z_e$
$r_i$	Effective radius of beam at $z_i$
$R$	Effective distance from stagnation point
$R_{h/w}$	Height-to-width ratio
$R^2$	Coefficient of determination
$Ra_L$	Rayleigh number
$Re_L$	Reynolds number
$R_{FRV}$	Ratio of wire feedrate and welding speed
$R_m$	Reflectance of a material
$SIR_f$	Stress influenced region for fatigue limit
$SIR_y$	Stress influenced region for yield strength
$t$	Time
$t_{ip}$	Interpass time
$t_{layer}$	Process time of the corresponding layer
$t_{step}$	Step time
$T$	Temperature
$T_\infty$	Ambient temperature
$T_\beta$	Beta transus temperature
$T_f$	Gas temperature
$T_{ip}$	Interpass temperature
$T_m$	Melting temperature
$T_{max}$	Maximum temperature

$T_{\text{ref}}$	Reference temperature
$T_s$	Surface temperature
$T_t$	Temperature at time t
$T_{(t-1)}$	Temperature at time (t-Δt)
$V$	Relative travel speed between laser and specimen
$V_f$	Velocity of fluid
$V_x$	Relative travel speed between laser and specimen along x-axis
$V_y$	Relative travel speed between laser and specimen along y-axis
$w_b$	Width of deposited bead
$w_{\text{HAZ},a}$	Actual width of heat affected zone
$w_{\text{HAZ},e}$	Estimated width of heat affected zone
$x$	X-coordinate relative to the fixed coordinate system of the model
$X$	X-coordinate relative to the frame of beam
$x_e$	Mesh size of finite element
$y$	Y-coordinate relative to the fixed coordinate system of the model
$Y$	Y-coordinate relative to the frame of beam
$\hat{y}_i$	Normalized y-coordinate of a bead profile at measurement point i
$y_i$	y-coordinate of a bead profile at measurement point i
$y_{\text{max}}$	Maximum y-coordinate of a bead profile
$z$	Z-coordinate relative to the fixed coordinate system of the model
$Z$	Z-coordinate relative to the frame of beam
$z_e$	z-coordinate at surface of bead
$z_i$	z-coordinate at penetration of beam
$z_i$	z-coordinate of a bead profile at measurement point i
$\bar{z}_i$	Averaged z-coordinate of a bead profile at measurement point i
$\bar{z}_i(\mathbf{P})$	Coordinate $\bar{z}_i$ for different power of laser at $\hat{y}_i$

## LIST OF FIGURES

Fig. 1	Additive manufacturing processes and their suitability for metallic material <sup>7,23</sup> .....	3
Fig. 2	Schematics of DED systems according to type of feedstock <sup>18,38</sup> .....	4
Fig. 3	Prototype of a wire feeding type DED process (Courtesy of KIMM) .....	21
Fig. 4	Schematic diagram of a front feeding DED process <sup>99</sup> .....	22
Fig. 5	Procedure to estimate the cross section profile of a deposited bead.....	24
Fig. 6	Cross sectional view of a deposited bead .....	24
Fig. 7	Quadratic regression line of coordinate $z_i$ for different power of laser at 4 mm/s .....	25
Fig. 8	Cross section views of deposited beads according to power of laser and travel speed of table <sup>99</sup> .....	27
Fig. 9	Dimensions of deposited beads according to power of laser.....	28
Fig. 10	Specific heat energy according to power of laser and travel speed of table .....	29
Fig. 11	Estimated deposition rate according to power of laser and travel speed of table .....	30
Fig. 12	Averaged coordinates for cross section profile of half deposited beads for various power of laser and travel speed of table .....	31
Fig. 13	Cross section profile of half deposited beads with normalized y-coordinate for various power of laser and travel speed of table .....	31
Fig. 14	Regenerated cross section profile for a deposited bead for various power of laser and travel speed of table.....	33
Fig. 15	Schematic diagram of a multi-layer deposition of a wire feeding type DED process .....	35
Fig. 16	Procedure to model a polygonal-shaped cross section profile of a multi-layer deposited bead .....	37
Fig. 17	Polygonal-shaped cross section profile of bead and effect of curved profile on heat input .....	38
Fig. 18	Polygonal-shaped cross section profile of multi-layer deposited bead.....	40

Fig. 19	Comparison between polygonal-shaped cross section profile, semi-ellipse cross section profile, and actual single bead profile.....	41
Fig. 20	Cross section profiles for multi-layer DED depositions for selected process parameters	42
Fig. 21	Schematic diagram of a planar deposition of a wire feeding type DED process.....	43
Fig. 22	Procedure to model a polygonal-shaped cross section profile of a planar deposited bead .....	45
Fig. 23	Flat top overlapping cross section profile of planar deposited bead.....	46
Fig. 24	Cross section profiles for planar DED depositions for selected process parameters (P = 1.5 kW and V = 8 mm/s) .....	48
Fig. 25	Measurement results of beam profile at 1 kW and 5 kW (Courtesy of KIMM).....	49
Fig. 26	Top-hat heat flux with conical penetration .....	53
Fig. 27	Thermal properties of Ti-6Al-4V .....	57
Fig. 28	Procedure to calibrate penetration depth and efficiency of heat flux <sup>99</sup> .....	58
Fig. 29	FE model to estimate the dimension of HAZ according to different penetration depth and efficiency of heat flux <sup>99</sup> .....	60
Fig. 30	Sectional view of deposited bead and heat affected zone <sup>99</sup> .....	61
Fig. 31	Estimated heat affect zone using different penetration depth and efficiency of heat flux <sup>99</sup> .....	64
Fig. 32	Estimated efficiency at limit of acceptable ranges of width errors and depth errors of HAZ for different efficiency of heat flux <sup>99</sup> .....	65
Fig. 33	Comparison of dimensions of HAZ between experiments and FEAs.....	67
Fig. 34	FE model to estimate the dimension of HAZ according to different penetration depth and efficiency of heat flux <sup>29</sup> .....	70
Fig. 35	Mechanical properties of Ti-6Al-4V <sup>133,134</sup> .....	71
Fig. 36	Estimated HAZ according to different process parameters <sup>29</sup> .....	73
Fig. 37	Influence of process parameters and length of bead on the width and depth of HAZ <sup>29</sup> ...	74

Fig. 38 Influence of power of laser and travel speed of table on the increment of width and depth of HAZ<sup>29</sup> .....76

Fig. 39 Comparison of thermal stress distributions at the end of deposition of bead and at the end of cooling process ( $L_B = 100 \text{ mm}$ )<sup>29</sup> .....78

Fig. 40 Maximum temperature of the bead after cooling process<sup>29</sup> .....79

Fig. 41 Temperature dependent yield strength and ultimate strength<sup>134</sup> .....79

Fig. 42 Formation of  $SIR_y$  and  $SIR_f$  according to power of laser and travel speed of table for  $L_B = 100 \text{ mm}$ <sup>29</sup> .....80

Fig. 43 Width of  $SIR_y$  and  $SIR_f$  according to power of laser, travel speed of table and length of bead<sup>29</sup> .....81

Fig. 44 FE model to investigate the influence of angle of corner deposition on formation of HAZ and  $SIR$ <sup>88</sup> .....84

Fig. 45 Temperature distribution of the specimen at the end of deposition of bead and at the end of cooling process<sup>88</sup> .....86

Fig. 46 Temperature histories at measured locations for different angles of corner deposition ( $P = 1.5 \text{ kW}$ ).....86

Fig. 47 Estimated HAZ at the middle of corner deposition for different power of laser and travel speed of table<sup>88</sup> .....87

Fig. 48 Estimated dimensions of HAZ at the middle of corner deposition for different power of laser and travel speed of table<sup>88</sup> .....88

Fig. 49 Residual stress distribution of the deposited bead after cooling process<sup>88</sup> .....89

Fig. 50 Influence of angle of corner deposition and power of laser on residual stress at the deposited corner<sup>88</sup> .....90

Fig. 51 Formation of  $SIR$  according to power of laser and angle of corner deposition<sup>88</sup> .....91

Fig. 52 Inner and outer distances of  $SIR$  at the deposited corner<sup>88</sup> .....91

Fig. 53 FE model to investigate the influence of deposition strategy on thermo-mechanical characteristics of multi-layer deposition.....93



Fig. 54	Time frame of multi-layer deposition for different interpass times .....	94
Fig. 55	Gas properties of air and argon <sup>138</sup> .....	95
Fig. 56	Temperature dependent coefficient of natural convection for different surfaces of substrate.....	96
Fig. 57	Schematic diagram of impinging jet from a single round nozzle <sup>126</sup> .....	98
Fig. 58	Temperature dependent emissivity <sup>127</sup> .....	99
Fig. 59	Influence of different deposition strategies on temperature distributions of part at the end of deposition .....	101
Fig. 60	Influence of interpass time on temperature of the mid-length of layer-3 bead at the end of deposition (upward deposition direction).....	101
Fig. 61	Comparison of temperature histories for different deposition patterns (interpass time of 2 s and upward deposition direction).....	102
Fig. 62	Comparison of cooling rates for different deposition patterns (interpass time of 2 s and upward deposition direction).....	103
Fig. 63	Influence of different deposition strategies on vertical displacement distributions of part after cooling process.....	105
Fig. 64	Influence of different deposition directions on vertical displacement of mid-length of layer-3 bead after cooling process .....	105
Fig. 65	Influence of different deposition strategies on residual stress distributions of part after cooling process .....	106
Fig. 66	Influence of different deposition patterns on residual stress of mid-length of layer-3 bead after cooling process.....	107
Fig. 67	Influence of different deposition directions on residual stress of mid-length of layer-3 bead after cooling process .....	107
Fig. 68	Procedure to verify the results of thermo-mechanical FEAs .....	108
Fig. 69	Experimental specimen of multi-layer deposition beads for sideward and upward deposition directions.....	109

Fig. 70	Comparison of vertical displacement between estimated results from FEAs and those of experiments .....	111
Fig. 71	Differences of vertical displacement at measurement points for different cooling times .....	111
Fig. 72	Procedure to estimate optimum interpass time for multi-layer deposition .....	113
Fig. 73	Location of interpass temperature control node .....	113
Fig. 74	Finite element model of 20 layers deposition to investigate optimum interpass time ....	114
Fig. 75	Interpass temperatures of multi-layer depositions using different interpass times .....	115
Fig. 76	Estimation of interpass temperatures at each layer for different interpass times.....	116
Fig. 77	Estimated and selected optimum interpass times for different layers.....	117
Fig. 78	Comparison of interpass temperatures between optimum interpass time and fixed interpass time of 20 seconds.....	118
Fig. 79	Dimensions of melt pool at different layers during deposition process using optimum interpass time.....	119
Fig. 80	Comparison of total deposition time for 20 layers of beads using using different interpass times .....	119
Fig. 81	Finite element model of 20 layers deposition to investigate influence of power of laser on interpass temperature.....	121
Fig. 82	Estimated melt pool at layer 5, 10 and 20 using different powers of laser.....	122
Fig. 83	Interpass temperatures of multi-layer depositions using different powers of laser .....	123
Fig. 84	Estimation of interpass temperatures at each layer for different powers of laser .....	123
Fig. 85	FE model to investigate the influence of deposition strategy on thermo-mechanical characteristics of planar deposition .....	125
Fig. 86	Comparison of temperature histories on bead 1, 2 and 3 for different deposition patterns (interpass time of 1 s) .....	126
Fig. 87	Estimated dimensions of melt pool during formation of bead 1, 2 and 3 using different interpass times .....	127

Fig. 88 Influence of different deposition strategies on vertical displacement distributions of planar deposited part after cooling process ..... 129

Fig. 89 Influence of different interpass times on vertical displacement after cooling process ... 130

Fig. 90 Influence of different deposition strategies on residual stress distributions of planar deposited part after cooling process ..... 131

Fig. 91 Influence of different interpass times on maximum residual stress within bead 6 after cooling process ..... 131

Fig. 92 Interpass temperatures of planar depositions using different interpass times..... 132

Fig. 93 Estimation of interpass temperatures at each bead for different interpass times ..... 133

Fig. 94 Estimated and selected proper interpass times for different beads during planar deposition ..... 133

Fig. 95 Interpass temperatures of planar depositions using selected proper interpass time..... 134

Fig. 96 Depth of melt pool for different beads during deposition process using different interpass times ..... 134

Fig. 97 Schematics of the inactive element activation..... 138

Fig. 98 Heat flux on top of elements..... 139

Fig. 99 Setting of front element cross section activated ahead of center of beam..... 140

Fig. 100 Activation algorithm of inactive finite elements for heat transfer FEA using Matlab and ABAQUS..... 141

Fig. 101 Activation algorithm of inactive finite elements for mechanical FEA using Matlab and ABAQUS..... 142

Fig. 102 FEA model to investigate the influence of number of element cross section ..... 143

Fig. 103 Temperature histories at measured nodes for various constants of front element cross section..... 146

Fig. 104 Temperature distributions and length of melt pool on part during first layer and third layer deposition for various constants of front element cross section ..... 149

Fig. 105 Computational time required to complete a three-layer deposition..... 150

Fig. 106 FEA model to investigate the heat transfer characteristics using proposed element activation algorithm<sup>148</sup> .....151  
 Fig. 107 Temperature distribution at middle of bead section during element activation<sup>148</sup> .....153  
 Fig. 108 Temperature distribution during a multi-layer DED deposition .....154  
 Fig. 109 Temperature distribution during a planar DED deposition<sup>148</sup> .....154  
 Fig. 110 Nodal temperature along the bead of layer 3 when the center of laser beam is at x = 20 mm<sup>148</sup> .....155  
 Fig. 111 Comparison of dimension of melt pool for a multi-layer deposition<sup>148</sup> .....157  
 Fig. 112 FE model to verify thermo-mechanical characteristics of multi-layer deposition.....158  
 Fig. 113 Comparison of dimensions of HAZ between estimated result from FEAs and those of experiment .....159  
 Fig. 114 Distributions of vertical displacements estimated using proposed algorithm and SYSWELD .....160  
 Fig. 115 Comparison of vertical displacement between estimated results from FEAs using the proposed algorithm and those of experiments .....161  
 Fig. 116 Differences of vertical displacement at measurement points for different cooling times .....161  
 Fig. 117 Distributions of residual stresses estimated using proposed algorithm and SYSWELD 162

## LIST OF TABLES

Table 1	Classification of additive manufacturing based on principle <sup>5,7,17,30</sup> .....	2
Table 2	Features of heat sources in DED process <sup>37,39-46</sup> .....	4
Table 3	Deposition capability of different DED processes <sup>15,26,51-55</sup> .....	5
Table 4	Publications of thermo-mechanical FEA models for DED process.....	16
Table 5	Specification of the laser system.....	22
Table 6	Process parameters for experiment.....	23
Table 7	Cross section area of measured profile and estimated deposition rate for different process parameters.....	29
Table 8	Regression relationship of half bead profile for various power of laser and travel speed of table.....	32
Table 9	Comparison of cross section area of measured profile, semi-ellipse profile and generated profile for different process parameters.....	34
Table 10	Comparison of cross section area of generated profile, semi-ellipse profile and polygonal shaped profile for different process parameters.....	41
Table 11	Height of stacked bead for different process parameters.....	42
Table 12	Optimum distance between beads and overlap ratio for different process parameters.....	47
Table 13	Parameters of heat flux to estimate penetration depth and efficiency of laser.....	60
Table 14	Calibrated penetration depth and efficiency of laser <sup>99</sup> .....	66
Table 15	Analysis conditions for investigation of proper gap between deposition beads.....	70
Table 16	Estimated critical stresses at reference temperatures <sup>29</sup> .....	79
Table 17	Appropriate gap between adjacent beads <sup>29</sup> .....	81
Table 18	Analysis conditions to investigate the influence of angle of corner deposition on formation of HAZ and SIR.....	84

Table 19	Analysis conditions to investigate the influence of deposition strategy on thermo-mechanical characteristics of multi-layer deposition.....	94
Table 20	Parameters to estimate the coefficient of convection due to supply of argon.....	99
Table 21	Conditions of experiments to verify the thermo-mechanical FE models .....	109
Table 22	Comparison of dimensions of multi-layer deposition beads between the estimated from constant width model and those from experiments .....	110
Table 23	Experimental results of vertical displacement at measurement points according to cooling time (courtesy of KIMM).....	111
Table 24	Conditions of analyses to investigate the optimum interpass time for multi-layer deposition .....	115
Table 25	Regression relationship between interpass temperature and interpass time for different layers .....	117
Table 26	Conditions of analyses to investigate the influence of power of laser on interpass temperature for multi-layer deposition .....	121
Table 27	Analysis conditions to investigate the influence of deposition strategy on thermo-mechanical characteristics of planar deposition .....	125
Table 28	Analysis parameters and boundary conditions to investigate the influence of number of element cross section.....	144
Table 29	Conditions of heat source model and mesh size of finite element.....	145
Table 30	Conditions of analyses to verify the thermo-mechanical FE models .....	159

## ABSTRACT

### **Investigation of Development of Thermo-Mechanical Analysis Method for a Wire Feeding Type Directed Energy Deposition Process**

Chua Bih Lii

Advisor: Prof. Ahn Dong-Gyu, Ph.D.

Department of Mechanical Engineering

Graduate School of Chosun University

Directed energy deposition (DED) process is one of the important additive manufacturing (AM) processes to fabricate a near net shape metallic part. The DED process can be categorized into powder feeding type and wire feeding type. The wire feeding type DED process is highly suitable for building large volume metallic part because it is capable to produce part at high deposition rate with minimal wastage. Due to rapid change of temperature during the material deposition process, undesired distortion and residual stresses are induced in parts fabricated using wire feeding type DED process. In order to control these distortion and residual stress without performing experiment, modeling of the process using finite element analyses is preferred. However, thermo-mechanical analyses for a wire feeding type DED process have yet to be developed properly. Hence, a systematic development of thermo-mechanical analysis for a wire feeding type DED process is required.

The aim of this thesis is to develop a new comprehensive method in developing a thermo-mechanical analysis model for a wire feeding type DED process. A bead deposited using a wire

feeding type DED process has a curved cross section profile with a few millimeters high. The thick layer of deposited bead influences the thermo-mechanical characteristic of a DED-fabricated part. The cross section profile of bead depends on the process parameter such as power of laser and travel speed of table. In order to properly represent a deposited bead according to process parameter, a novel methodology to estimate the cross section of deposited bead for different power of laser and travel speed of table has been proposed. The cross section profiles of deposited beads for different power of laser and travel speed are derived via regression analysis of the cross section profile of bead extracted from experiments. The cross section area of the estimated profile and measured profile have been compared and discussed. Subsequently, methodologies to create bead profile for multi-layer and planar depositions are proposed. A unique polygonal-shaped bead profile and constant width model are proposed to estimate the cross section profile for a multi-layer deposition. A flat top model is introduced and discussed in order to obtain the cross section profile for a planar deposition. These proposed methodologies to estimate proper deposition bead profile for multi-layer and planar deposition of a wire feeding type DED process according to process parameter have been implemented for creation of FE models.

In order to produce an acceptable FEA results, a heat flux model must be properly selected and calibrated to represent the heat source used for a DED process. A Gaussian distribution double ellipsoidal heat flux model is typically assumed for a DED process by previous researchers. However, it is noticed that the heat flux model is not proper for a wire feeding type DED process in this thesis, which applies a top-hat distribution beam with small radius. Hence, a top-hat distribution heat flux model with consideration of efficiency and penetration depth is introduced to properly emulate the measured intensity distribution of laser beam used in the wire feeding type DED process. The moving heat flux model is implemented in welding-based commercial FEA software SYSWELD. Various heat transfer FEAs have been carried out using different efficiency and penetration depth of heat flux model on different shape of deposited beads of FE models, created according to process parameters. From the results of thermal FEAs, the predicted geometries of heat affected zone (HAZ) have been compared to those measured depth and width of HAZ from experimental study. A novel methodology to select a proper penetration depth and



efficiency of heat flux model for each combination of power of laser and travel speed of table has been introduced. From the selection of penetration depth and efficiency of heat flux model, the heat flux model is properly calibrated for each combination of power of laser and travel speed of table of a wire feeding type DED process.

The thermo-mechanical FEAs have been carried out using the calibrated heat flux model to investigate influence of process parameters such as power of laser and travel speed of table on the formation of heat affected zone (HAZ), stress influenced region (SIR) and induced thermal stress. A proper gap between deposition beads is proposed by comparing the width of HAZ and stress influenced region (SIR). The gap between adjacent deposition beads is required to avoid the effect of heat and residual stress between two adjacent parts deposited on a single substrate. In addition, the influence of angle of corner deposition on the formation of HAZ, SIR and thermal stress has been investigated and discussed. In order to minimize the thermal stress on the deposited part, the thermo-mechanical characteristics during planar and multi-layer deposition of a wire feeding type DED process have been studied according to deposition pattern and interpass time. From the results of thermo-mechanical FEAs, a proper deposition strategy has been suggested. The vertical displacements of measured points on a cantilevered specimen have been compared to the predicted vertical displacement from FEAs, in order to validate the thermo-mechanical FEA model. The influences of interpass time and deposition pattern on the formation of thermal stress of a cantilevered specimen have investigated and discussed using the validated thermo-mechanical FEA model.

In order to extend the applicability of the thermo-mechanical FEA model for a wire feeding type DED process for high intensity heat source using a general FEA software, an activation algorithm of finite element has been proposed. A selection criterion of mesh size of finite element and number of front element cross section of bead have been introduced and discussed in order to properly model the heat transfer during a DED process using a high intensity heat source with small beam radius. The selection algorithm of finite elements to be activated has been implemented using MATLAB. Subsequently, heat transfer and mechanical FEAs have been performed using ABAQUS to progressively simulate the addition of material during a DED process. Finally, the

proposed activation algorithm of finite element has been implemented in ABAQUS in order to obtain the thermo-mechanical characteristics of a multi-layer deposition on a cantilevered specimen. The results of the FEAs have been examined and verified by comparing them to measured displacements of experimental results.

# I. INTRODUCTION

## A. Research Backgrounds

### 1. Additive Manufacturing

Manufacturing is the major thrust for the industrialization of countries around the world that creates job opportunities, wealth and improvement in quality of life. The advancement in information digitization and demand for sustainable development in the twenty-first century has transformed the manufacturing from large scale production into sustainable mass customization via industrial revolution 4.0.<sup>1-3</sup> Additive manufacturing (AM) is one of the seven key elements that have been identified to achieve the paradigm shift of the fourth industrial revolution.<sup>4</sup>

Additive manufacturing produces objects from three-dimensional (3D) model data by joining materials, usually layer upon layer, as opposed to the traditional subtractive and formative manufacturing techniques.<sup>2,5-8</sup> The term AM encompasses many popular terminologies such as 3-D printing, rapid prototyping (RP), directed digital manufacturing (DDM), layered manufacturing, and additive fabrication.<sup>9,10</sup> AM is closely integrated with computer and does not require part-specific tooling for the fabrication of functional parts.<sup>11,12</sup> These important features of AM enable the fabrication of complex geometries, consolidated parts, functionally graded parts and customized parts that cannot be made by other means.<sup>12-16</sup> In addition, AM can reduce material and energy usage.<sup>17,18</sup>

Hence, AM has developed rapidly into scalable production stage for functional parts such as fuel nozzles for jet engine, valves, safety buckle and cooler vents in the past decade.<sup>17,19</sup> Besides, it demonstrated significant potential in reducing the cost of complex and critical parts such as jet engine brackets due to the improved design freedom for optimization, reduced material waste, and reduced post-processing steps.<sup>20,21</sup>

The AM technologies can be categorized into seven distinguished processes according to the ISO/ASTM 52900:2015 as shown in Table 1.<sup>7</sup> They are binder jetting (BJ), directed energy deposition (DED), material extrusion (ME), material jetting (MJ), powder bed fusion (PBF), sheet lamination (SL) and vat photopolymerization (VP).<sup>6,7</sup> Depending on the AM principle of material joining, different types of materials such as polymer, metal, ceramic and composite can be fabricated by the AM processes.<sup>7,22</sup>

Two main AM technologies that are suitable for fabrication of metallic parts are powder bed fusion and directed energy deposition, as shown in Fig. 1.<sup>8,23-25</sup> Both AM processes involve high localized heat input to fuse metallic parts together. It is costly and difficult to examine heat transfer characteristics and residual stress distribution during the deposition of material.<sup>26-29</sup> Thermo-mechanical analysis method is required to provide cheaper and efficient alternative to quantitatively investigate the heat transfer and residual stress generation.

**Table 1 Classification of additive manufacturing based on principle** <sup>5,7,17,30</sup>

AM Process	Basic principle	State of fusion and bond	Type of material	Related technologies
<b>Binder jetting</b>	Reactive curing	Chemical reaction bonding/ Solvent reactive curing	Polymer/ Metallic/ Ceramic	3D Printing (3DP) Powder bead and inkjet head (PBIH)
<b>Directed energy deposition</b>	Selective deposition of material to a substrate	Melted state	Metallic	Laser Metal Deposition (LMD), Laser Engineered Net Shaping (LENS), Direct Metal Deposition (DMD), Wire and Arc Additive Manufacturing (WAAM), Electron Beam Freeform Fabrication (EBF <sup>3</sup> )
<b>Material extrusion</b>	Extrusion of melted material	Thermal reaction bonding	Polymer	Fused Deposition Modelling (FDM), Fused Filament Fabrication (FFF)
<b>Material jetting</b>	Multi-jet material printing/ Light reactive photopolymer curing	Thermal reaction bonding/ Chemical reaction bonding	Polymer	Polyjet, Multi-Jet Modeling (MJM), Projet
<b>Powder bed fusion</b>	Selective fusion of material in a powder bed	Solid & melted state / Thermal reaction bonding	Polymer/ Metallic/ Ceramic	Selective Laser Sintering (SLS), Selective laser melting (SLM), Electron Beam Melting (EBM)
<b>Sheet lamination</b>	Fusion of stacked sheets	Chemical reaction bonding/ Thermal reaction bonding	Polymer/ Metallic/ Composite	Laminated Object Manufacture (LOM), Selective Deposition Lamination (SDL), Ultrasonic Consolidation (UC)
<b>Vat photopolymerization</b>	Light reactive photopolymer curing	Chemical reaction bonding	Polymer	Stereolithography apparatus (SLA), Digital Light Processing (DLP)

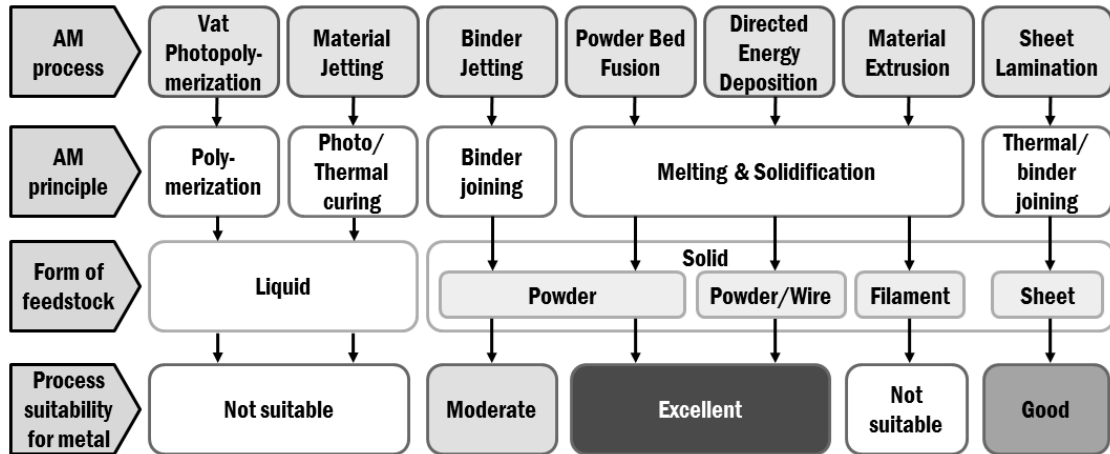


Fig. 1 Additive manufacturing processes and their suitability for metallic material<sup>7,23</sup>

## 2. Directed Energy Deposition

Nowadays, directed energy deposition (DED) process is a widely used AM technology for producing metallic parts. The DED process was first developed by Sandia National Laboratory using the technology known as laser engineered net shaping (LENS) in 1996.<sup>31</sup> It applies high intensity energy source to fuse the fed metallic material on the substrate in a layer-by-layer manner.<sup>5,20,25,32-36</sup> Due to the significant of DED in metal additive manufacturing, a standard guide for DED of metals has been designated by American Society for Testing Materials (ASTM) in 2016 to provide the specification and use of the DED technology.<sup>37</sup>

A DED system consists of four main components such as heat source, positioner, feedstock feed mechanism and a computer control system.<sup>37</sup> The DED process are commonly categorized into powder feeding type and wire feeding type, as shown in Fig. 2.<sup>26,32</sup> During the deposition of material, the metallic feedstock in the form of powder or wire is delivered directly to the heat source and combined with the melt pool to form the deposition.<sup>26,36,37</sup> Typical heat sources for DED process include a laser, electron beam and arc plasma.<sup>25,32-37</sup> The characteristics of the heat sources are summarized in Table 2.

Depending on the type of heat source, inert gas or vacuum condition may be needed to

shield the workpiece from oxidation during the DED process.<sup>36,37</sup> The motion of deposition is achieved by relative motion between the heat source and the workpiece on a positioner. Although DED systems can be used for surface cladding, a DED system must deposit the material in layer-by-layer manner based on the computer aided design (CAD) data to form a part, add a feature, or make a repair, to be qualified as AM according to the ASTM standard.<sup>37</sup>

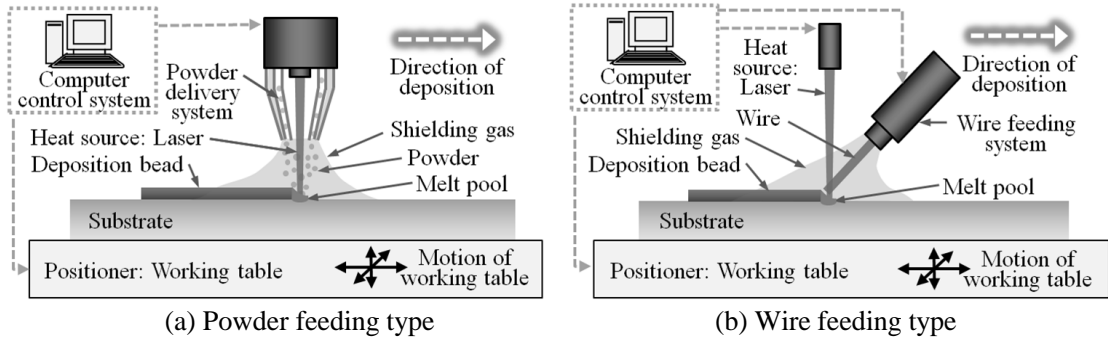


**Fig. 2 Schematics of DED systems according to type of feedstock<sup>18,38</sup>**

**Table 2 Features of heat sources in DED process<sup>37,39-46</sup>**

Feature	Laser	Electron beam	Arc plasma
Control of beam size	Beam delivery and focusing optics	Focusing coils	Pulse with a variety of waveforms and frequency
Coupling efficiency	5-40% <sup>37</sup> 15% <sup>40</sup> 28% <sup>41</sup> 38-55% <sup>45</sup>	60-70% <sup>42</sup> 80-98% <sup>43</sup>	90% <sup>44</sup>
Size of heat source	50 μm (spot diameter) <sup>37</sup> 25 mm (width of line) <sup>37</sup>	Fraction of a millimeter to several millimeters <sup>37</sup>	14 mm <sup>46</sup>
Working distance	150-200 mm <sup>37</sup>	Can be over 300 mm <sup>37</sup>	Less than 25 mm <sup>37</sup>
Atmosphere control	Localized shielding or inert gas glovebox <sup>37,39</sup>	Vacuum level 10 <sup>-2</sup> Pa or lower <sup>37,43</sup>	Localized shielding or inert gas glovebox <sup>37,44</sup>
Related technologies	LMD, LENS, DMD (Powder type)	EBF <sup>3</sup> (Wire type)	WAAM (Wire type)

Powder feeding type DED process produces part with better geometrical accuracy and surface roughness, as shown in Table 3.<sup>26</sup> However, the wire feeding type DED process has several advantages over the powder feeding type DED process. The wire feeding type DED process is suitable for building part with large volumes because it is capable to produce part at a higher deposition rate and density.<sup>20,47-50</sup> Unlike powder feeding type DED process that has powder capture efficiency of 40-80%, most of the wire feedstock is consumed during the DED process.<sup>26,37</sup> Besides, wire type feeding DED process is preferred for fabricating aerospace components with high purity because it is not susceptible to contamination during handling.<sup>49</sup> The wire, which is similar to welding wire feedstock, is cheaper and readily available.<sup>26,37</sup>

**Table 3 Deposition capability of different DED processes**<sup>15,26,51-55</sup>

Feeding type	Process	Layer thickness (μm)	Deposition rate (g/min)	Dimensional accuracy (mm)
Powder	Directed light fabrication (DLF)	200 <sup>26</sup>	10 <sup>26</sup>	±0.13 <sup>26</sup>
	Laser engineered net shaping (LENS)	380 <sup>15</sup>	6.5 <sup>15</sup>	0.02 - 0.4 <sup>55</sup>
Wire	Wire and arc additive manufacturing (WAAM)	1,500 <sup>26</sup> 2,500 <sup>52</sup>	12 <sup>26</sup> 83 <sup>51</sup> 50 - 130 <sup>54</sup>	±0.2 <sup>26</sup> 0.5 <sup>52</sup> (roughness)
	Electron beam freeform fabrication (EBF <sup>3</sup> )	500 - 1,270 <sup>53</sup>	Up to 330 <sup>26</sup>	±2.54 <sup>53</sup>

Due to the highly localized heat input and short interaction time, additive manufactured parts are subjected to rapid heating and cooling during repeated material deposition.<sup>18</sup> Due to shrinkage of material during cooling, undesired distortion and residual stresses are induced in the parts fabricated using wire feeding type DED process.<sup>27,52,56,57</sup> The residual stress is manifested in distortion when the part is unclamped and lead to loss of dimensional accuracy.<sup>58,59</sup> Besides, residual stresses, particularly tensile residual stress, may cause cracks in the heat affected zone

(HAZ) and affect the fracture toughness and fatigue strength of the fabricated part deleteriously.<sup>56,60-63</sup>

In order to control distortion and residual stress induced in the part, methods include physical clamping, symmetrical building, back-to-back building, preheating of base plate, intermittent stress-relief, optimization of part orientation and control of process parameters (using lower heat input) have been applied.<sup>37,52,64</sup> Overbuild of part is also applied to compensate distortion such that there will be sufficient material that can be machined away to obtain the desired final part geometry.<sup>37</sup>

### **3. Wire Feeding Type Directed Energy Deposition System in Republic of Korea**

The development of wire feeding type DED system in Republic of Korea was reported in the early 2000's with a novel process using hybrid approach of 3D welding and milling for freeform fabrication of metallic parts. The system was developed by Korea Institute of Science and Technology, Korea Institute of Machinery and Materials and Hongik University.<sup>65</sup> Core and cavity inserts were fabricated using the 3D welding and milling system.<sup>66</sup>

In the recent years, several wire feeding type DED systems have been developed. In 2017, a Korean startup company 5000°C developed a wire and arc additive manufacturing (WAAM) system to fabricate three dimensional structures using aluminum and steel.<sup>67</sup> In 2017, Pukyong National University and Hyundai Rotem fabricated a thin Ti-6Al-4V wall structure using an AM system based on gas tungsten arc welding (GTAW).<sup>68</sup> Besides, a Korean welding company Best F.A. Co. Ltd. showcased fabrication of metallic structure using WAAM system.<sup>69</sup> In addition, a laser assisted additive manufacturing system with rotating metal wire feeder was developed by Korea Institute of Machinery and Materials in 2017.<sup>70</sup>

Due to its potential, the wire feeding type DED system has gained importance to fabricate large metallic part. In 2018, Hyundai Heavy Industry embarked on development and class



certification of propeller for shipbuilding industry using WAAM process.<sup>67,71</sup> Research and development on a wire feeding type DED process in Republic of Korea must be intensified to close the gap with other developed countries to produce industrial parts, in term of technical implementation of technology and standard.

## B. Research Motivation

Additive manufacturing has shown promising result in producing parts with mechanical properties comparable to wrought materials.<sup>72,73</sup> Selection of processing conditions is important in producing the desired properties. In order to select a proper process condition, researchers usually apply experimental methodology to characterize the experimental results as a function of process parameters. However, this methodology is time consuming and costly, which involves setup and calibration of experimental devices and instrumentations, preparation and post-processing of specimens, microscopy and testing of the experimental result to quantify them. In order to predict and control residual stresses and distortions of the part fabricated by DED process, a better alternative using process modeling is required.<sup>17,29</sup>

Process modelling for DED process using finite element analysis (FEA) has been applied by several researchers.<sup>27,74-78</sup> Three dimensional thermo-mechanical models have been developed with moving heat flux and boundary conditions to mimic actual deposition of material during a DED process. Due to limited resources and various unknown during the process, assumption and simplification of FEA model are usually made. Most researchers have applied an assumed efficiency for their heat source model from literature. The calibration of heat source are usually conducted without considering the heat loss.<sup>79</sup> The shape of the solidified bead is assumed to be rectangular. Forced convection due to the shielding gas is usually neglected. These assumptions lead to inaccuracy in the FEA when the deposition rate is high, particularly in wire feeding type DED process. Hence, a systematic development of FEA model for a wire feeding type DED process is required.

In addition, finite elements are added programmatically in a finite element (FE) software by either activation of quiet elements or inactive elements during simulation. Inactive element activation technique can produce more accurate results. However, the knowledge about the

development of activation algorithm of finite element is difficult and limited to a few research groups. This limitation has hindered the wide usage of FEA simulation to investigate and to optimize the temperature field and induced thermal stress within the fabricated parts by a DED process. Besides, a suitable scheme of activation is required for a high intensity heat source model with small beam radius. Therefore, an activation algorithm of finite elements is needed.

## C. Previous Research Works

Physics-based modelling can be divided into micro-scale, meso-scale and macro-scale models, based on the length and timescale.<sup>80</sup> Micro-scale modelling is applied by solving the thermofluid dynamics within the melt pool to estimate the size and shape of melt pool, and quality of material consolidation such as porosity and surface roughness, in order to obtain the most suitable process window.<sup>80</sup> Meso-scale modelling involves the estimation of change in grains and microstructures based on the temperature field.<sup>80</sup> In order to predict the residual stresses and distortion of the fabricated metallic part during and after the build process, macro-scale models of finite element method (FEM) are used.<sup>80</sup> The macro-scale simulation for metal AM process involves numerical analysis known as thermo-mechanical analysis.

### 1. Thermo-Mechanical Analysis for DED Process

Thermo-mechanical analysis consists of two analyses; heat transfer analysis and mechanical analysis. Heat transfer analysis is the fundamental of the thermo-mechanical analysis to simulate the change in temperature field during a DED process through the application of moving heat source. Boundary conditions, clamp condition and deposition strategy are included in the thermo-mechanical analysis. The transient temperature field obtained from the heat transfer analysis is then applied as a thermal load in the quasi-static mechanical analysis. DED process has similar process characteristic with welding technology.

In 1999, Nickel et al. estimated stresses and distortion induced during a powder feeding type shape deposition manufacturing (SDM), which was jointly developed at Carnegie Mellon University and Stanford University.<sup>81,82</sup> However, for simplification, the analyses were simulated with a constant heat source being scanned over the surface of substrate without any material deposition.<sup>81</sup>

In 2000, Vasinonta et al. applied a two-dimensional thermo-mechanical model to predict the

temperature gradient and residual stress for a laser engineered net shaping (LENS) process.<sup>83</sup> Rosenthal's point heat source model was applied to simulate the laser beam. Convective heat transfer to the surrounding was not considered. From their investigation, it was revealed that the power and velocity of laser have minimal influence on maximum residual stress when preheating of base plate has been applied.

In 2003, Tsirkas et al. simulated the laser welding process using thermo-mechanical FEA with metallurgical transformation in SYSWELD.<sup>84</sup> A simplified FEA model with no specific mesh of bead was developed. They applied Gaussian distribution of heat source to predict the distortion of a butt-joint specimen. The predicted distortion was found to be within the range of standard deviation of 308  $\mu\text{m}$  from their measured mean value.

In 2006, Mughal et al. implemented a three-dimensional finite element (FE) model with consideration of material addition and temperature-dependent material properties using a FE software, ANSYS to simulate a gas metal arc welding (GMAW) based deposition process.<sup>85</sup> The thermo-mechanical analyses were used to investigate the deformation and stress distribution of the substrate according to different raster patterns of a single layer planar deposition. Seven rows of beads were deposited in the simulation with a 60 s interpass time of cooling being applied between rows.

In 2006, a three-dimensional FEA model for a single track laser cladding (LC) process was proposed by Deus and Mazumder using FE software ABAQUS.<sup>86</sup> In their study, a dilution model was introduced to determine the composition of the material being applied in a bi-material model. They investigated the influence of a curved melt front and a planar melt front on thermal stress. It was revealed that tensile stresses were formed near the end of the straight bead deposited by LC process. The magnitude of stress is similar regardless of the shape of melt front because the additional material at the melt front contributes a little constraint in the melt pool region.

In 2007, Bate et al. performed an uncoupled thermal and mechanical analyses using SYSWELD to estimate the thermal stress on a single bead deposited using a tungsten inert gas (TIG) welding process.<sup>87</sup> A Goldak double ellipsoid heat source model was calibrated based on the

dimension of fusion zone of the specimen and mean temperature measurement of thermocouples mounted on the specimen.

Although DED process shares similar characteristics with welding mechanics, the investigation into distortion and residual stress using thermo-mechanical analysis did not progress until the 2010s due to the limitation of computational power and memory. A single bead deposition is the basic unit of a multi-layer deposition in DED process.<sup>50,88</sup> As compare to welding, multiple beads can be deposited in various directions in order to create a three-dimensional parts in a DED process.

In 2010, Chiumenti et al. developed their own finite element software to perform a uncoupled thermo-mechanical FEA with consideration of solid-liquid phase change transformation on a ten-layer straight bead deposition using shaped metal deposition (SMD) process.<sup>60</sup> A simplified uniform heat source model was applied based on volume of wire feed. They implemented different mechanical properties for solid state, mushy state and liquid state. The computed vertical deformation was lower than the experiment by up to 400  $\mu\text{m}$ . The average of errors between measured and estimated residual stresses was 10 % in their study.

In 2011, Anca et al. studied the temperature and thermal stress distribution of a four-layer straight wall structure deposited by SMD process.<sup>89</sup> A double ellipsoidal heat source model was calibrated based on temperature data of thermocouples. The boundary of melt pool was interpreted based on solidus temperature of a material. Elements with any nodal temperature higher than the solidus temperature were assigned with zero strength in their thermo-mechanical FEA model. A difference of 0.2 mm in vertical displacement was observed between the experiment and simulation of a single bead deposition.

In 2011, Lundbäck et al. applied thermo-mechanical analysis to obtain the distortion of a wall structure deposited by a metal deposition (MD) process at Volvo Aero Corporation.<sup>90</sup> In this MD process, tungsten inert gas (TIG) process was applied to melt the metal wire feedstock. A multi-physics software MSC.Marc was used to implement their subroutine on metal deposition. It was noted that the calibrations of heat input models and flow stress are crucial to obtain accurate

results. The heat input was calibrated by comparing temperature measured using thermocouples and pyrometer with the temperature field estimated by heat transfer analysis. The flow stress model was calibrated by comparing the stress-strain curve for mechanical simulation with the isothermal compression test results at different strain rates ranging from  $0.001 \text{ s}^{-1}$  to  $1 \text{ s}^{-1}$ .

In 2011, Ding et al. demonstrated the application of a steady-state Eulerian thermal analysis of wire arc additive manufacturing (WAAM) for multi-layer straight deposition on a large workpiece.<sup>44,91</sup> A whole layer of elements was activated in their simplified model, which produced a lower distortion as compare with a progressive element activation model.<sup>91</sup> Their approach was 80 % faster than the conventional Lagrangian thermal analysis. However, this approach is not suitable for complex and non-symmetrical geometries.

In 2011, Zhang et al. performed thermal and mechanical analysis for a three-dimensional multi-bead pulsed laser powder deposition (PLPD) process using FE software ANSYS.<sup>92</sup> The cross sectional geometry of a bead was characterized by bead width, bead height, bead area, and wetting angle. In modeling the melting due to pulsed laser, a laminate layer with initial temperature of melting temperature was created for each laser pulse irradiation on a bead. The developed model was used to predict the formation of stray grain and thermal stress concentration.

In 2013, Liu et al. simulated the temperature field, distortion and residual stress of a three layers deposition by a powder feeding type direct metal deposition (DMD) process using FE software ABAQUS.<sup>93</sup> A uniformly distributed surface heat flux was defined as the moving heat source. The difference and error in vertical displacement between the simulation and experiment were approximately  $170 \mu\text{m}$  and 28.5 %, respectively.

In 2014, Farahmand and Kovacevic developed a three-dimensional transient thermo-elastic-plastic model using FE software ANSYS to investigate the temperature and stress field of a multi-track laser cladding.<sup>94</sup> A wide top-hat power distribution for a laser spot of 12 mm width and 3 mm length was applied as the heat source in the simulation. The FE model considered the latent heat and convective heat transfer in melt pool by modification of specific heat and thermal conductivity of the material when the simulated temperature has exceeded the melting temperature. From their

investigation, it was revealed that slower scanning speed produces higher tensile stress after cooling due to higher heat input.

In 2016, Yang et al. estimated the distortion and residual stress of a five layers rectangular wall structure fabricated by LENS process using three-dimensional thermo-mechanical analysis.<sup>27</sup> A moving volumetric heat source of double ellipsoidal model was employed in their simulation. An average coefficient of forced convection was applied to save computational cost. Their model was validated using the measured distortion distribution of the bottom surface of substrate. A discrepancy of the displacement between the simulation and experiment was up to 0.1118 mm.

The development of three-dimensional thermo-mechanical FEA model enables the investigation of process parameters on the formation of mechanical properties of the additive manufactured part.

In 2010, Crespo and Vilar investigated the effects of scanning speed and idle time between layer deposition using heat transfer analysis with consideration of metallurgical phase transformation.<sup>95</sup> The temperature distribution of a part fabricated by a laser powder deposition (LPD) process was estimated. They revealed that proper selection of idle time between deposition is needed to avoid heat accumulation on the bead, which causes phase change and non-uniform distribution of microstructures.

In 2016, Denlinger et al. employed thermal and mechanical analyses code CUBES to investigate the influence of dwell time between layer depositions on distortions and residual stresses of wall structure deposited using a powder feeding type DED process.<sup>96</sup> A Goldak double ellipsoidal model was applied to model the moving laser heat source. Their FEA model included the fixture clamp in order to capture the conductive heat loss at the fixture. They noted that residual stress has to be reset to zero when the temperature has risen above a stress relaxation temperature in order to obtain satisfactory agreement with experimental results by Denlinger et al.<sup>97</sup>

In 2017, Mukherjee et al. incorporated fluid flow model into the heat transfer analysis in order to model the thermo-mechanical characteristics of a straight bead wall in a FE software ABAQUS.<sup>61</sup> They investigated the influence of heat input and layer thickness on the stresses and



strains on the wall structure fabricated by a powder feeding type DED process. They concluded that the residual stresses can be reduced by increasing the heat input and reducing the layer thickness. However, the increment of heat input resulted to a higher distortion.

In 2018, Chua et al. examined the influence of process parameters such as power of laser and travel speed of table on temperature field and thermal stress distribution on the deposited bead and the substrate for a single layer deposition using a wire feeding type DED process.<sup>29</sup> The thermo-mechanical analyses were conducted using SYSWELD. The formation of heat affected zone (HAZ) and stress influenced region (SIR) were estimated. In order to minimize the undesired effect of HAZ and residual stress, an appropriate gap between deposited beads was proposed. Besides, Chua et al. studied the influence of angle of corner deposition on the temperature and residual stress of a deposited bead by a wire feeding type DED process.<sup>88</sup> They estimated that the residual stress increases when the angle of corner deposition increases.

In 2018, Lee et al. investigated the influence of interlayer cooling time on plate distortion using FEM for a laser metal deposition with wire (LMD-w) process.<sup>98</sup> A point-concentrated heat source model was applied in the model. In addition, initial temperature of filler material was set due to heating of wire. The 10-layer wall FEA model was implemented in FE software ABAQUS. The interlayer cooling time was set in the range of 91 s to 200 s in order to maintain a constant temperature of layer. The error of the predicted displacement was up to 37 %.

The summary of the aforementioned thermo-mechanical FEA models for DED process developed in the past two decades is listed in Table 4. Most of these FEA models assumed a rectangular bead shape because it is easier to create and to maintain the mesh integrity between layers. Heat source models such as Goldak double ellipsoidal heat flux and uniform surface heat flux are typically applied. The actual profile of the heat source may not be investigated during the application of heat source model. Algorithm for progressive element activation is applied to simulate the deposition of material on the substrate during a DED process in a FEA model. The know-how technology for developing thermo-mechanical FEA models for DED process using multi-physics FE softwares is dominated by researchers in the United States of America (USA).

**Table 4 Publications of thermo-mechanical FEA models for DED process**

Year	DED process	FEA model	FE software	Heat source	Material	Country	References
1999	SDM (powder)	3D model of substrate with no bead creation	ABAQUS	Constant surface heat flux	Aluminum	USA	[81]
2000	LENS (powder)	2D model of thin wall	ABAQUS	Point heat flux	AISI304	USA	[83]
2006	GMAW deposition (wire)	3D model of 7-bead planar deposition with rectangular bead	ANSYS	Goldak heat flux	Mild steel	Pakistan	[85]
2006	LC (powder)	3D model of single track deposition with curved bead	ABAQUS	Gaussian heat flux	AA333 & C95600 alloys	Portugal & USA	[86]
2010	SMD (wire)	3D model of 10-layer straight wall with rectangular bead	-	Uniform heat flux	AISI304 & Inconel718	Spain, Italy & Japan	[60]
2011	SMD (wire)	3D model of 4-layer straight wall with curved bead	-	Goldak heat flux	Ti-6Al-4V	Argentina & UK	[89]
2011	MD (wire)	3D model of 10-layer structure with rectangular bead	MSC.Marc	Goldak heat flux	-	Sweden	[90]
2011	WAAM (wire)	3D model of 4-layer straight wall with rectangular bead	ABAQUS	Goldak heat flux	Mild steel	UK	[44,91]
2011	PLPD (powder)	3D model of multi-bead multi layer deposition with curved bead	ANSYS	Constant surface heat flux	Inconel 625 & Inconel 738	USA	[92]
2013	DMD (powder)	3D model of 3-layer straight wall with rectangular bead	ABAQUS	Uniform surface heat flux	AISI304	USA	[93]
2014	LC (powder)	3D model of multi-track planar deposition with rectangular bead	ANSYS	Wide top-hat heat flux	AISI H13	USA	[94]
2016	LENS (powder)	3D model of 5-layer rectangular wall with rectangular bead	-	Goldak heat flux	Ti-6Al-4V	USA	[27]
2016	DED (powder)	3D model of 42-layer straight wall with rectangular bead	CUBES	Goldak heat flux	Ti-6Al-4V & Inconel 625	USA	[96]
2017	DED (powder)	3D model of 10-layer straight wall with rectangular bead	ABAQUS	Gaussian heat flux	Ti-6Al-4V & Inconel 718	USA	[61]
2018	DED (wire)	3D model of single-layer deposition with curved bead	SYSWELD	Top-hat heat flux	Ti-6Al-4V	Korea	[99]
2018	LMD-w (wire)	3D model of 10-layer wall with rectangular bead	ABAQUS	Point heat flux	Ti-6Al-4V	USA	[98]

## 2. Applications of Titanium Alloy Ti-6Al-4V

Titanium alloys were first developed for the aerospace industry. Titanium alloys were used for about 15% of total weight of an aircraft Boeing 787.<sup>100</sup> Titanium alloy Ti-6Al-4V is the most widely used grade, which account for about 45% of titanium alloys usage in the world.<sup>101,102</sup> Ti-6Al-4V is widely used high-value material for commercial fabrication because it has favourable mechanical properties such as high specific strength at extreme temperature, excellent corrosion resistance against sea water, good bio-compatibility, and electrochemical compatibility with carbon fiber composites.<sup>8,18,100,102</sup> Besides, Ti-6Al-4V has been used as main titanium alloy in biomedical field for a long period.<sup>103</sup>

Due to its high material cost, titanium alloy Ti-6Al-4V is one of the most researched materials in metal additive manufacturing process to improve the buy-to-fly ratio for various design of parts.<sup>104</sup> It has been applied in various high value industries such as aviation and aerospace, military, power generation, oil and gas, racing automotive, biomedical and high performance sport. Additive manufacturing processes are used to fabricate low quantity and complex-shaped Ti-6Al-4V parts. Existing Ti-6Al-4V industrial parts fabricated or repaired using DED process include safety buckle for Airbus A380, titanium pressure vessel for aerospace exploration, fuel nozzle for engine, structural components and propellant tank for fighter jet F-35, gearbox for race car, titanium brackets for miscellaneous purposes, blisk of gas turbine, gateway manifold for pipelines in oil and gas industry, and single frame of high performance bicycle.<sup>17,18,101,105-107</sup> Hence, continuous research and development using titanium alloy Ti-6Al-4V in DED process is viable for the future.

## D. Objective and Scope of the Thesis

The development of thermo-mechanical analysis method is still under intense research worldwide. The existing finite element models have several flaws, particularly for wire feeding type DED process. The deposited bead is usually simplified as a rectangular cross sectional shape. Besides, the thickness of deposited bead is high for a wire feeding type DED process. Therefore, a volumetric heat source is required to properly melt through the bead. Goldak double ellipsoidal heat flux and volumetric Gaussian heat flux with large beam size are usually applied. The applied heat source model must be calibrated to properly represent the process.<sup>79</sup> However, researchers have to assume efficiency and heat flux distribution for their heat source model before the calibration is performed because the heat source model has too many variables that needs to be adjusted. No quantification of acceptable error during calibration has been proposed. The influence of process parameter such as travel speed of moving table on the applied heat flux has not been studied. In addition, the calibration of heat source are usually conducted without considering the heat loss.<sup>79</sup> The coefficients of free convection and forced convection are assumed or neglected. These assumptions lead to inaccuracy in the FEA for a wire feeding type DED process. Hence, a systematic method for development of FEA model for a wire feeding type DED process is required to overcome these shortcomings. In addition, an activation algorithm of finite element that is suitable for a heat source model with small beam radius in a wire feeding type DED process is required in this study.

The main objective of this thesis is to propose a new method for developing a thermo-mechanical analysis model for a wire feeding type directed energy deposition process. The method includes a methodology to obtain the cross sectional of deposited bead, a methodology to estimate bead profile for planar deposition and multi-layer deposition using wire feeding type DED process, a methodology to calibrate heat source model using efficiency and penetration depth of laser beam, and a methodology to estimate temperature dependent coefficient of convection. In addition, an

activation algorithm of finite elements is proposed for a heat source model with small beam radius. The thermal and mechanical characteristics of a part deposited by a wire feeding type DED process is investigated using FEA in order to improve the quality of the part.

In Chapter II, the methodology to extract the bead profile for single bead deposition is described. From the measurement of bead profiles, estimated cross section profiles of deposited beads using different power of laser and travel speed are derived via regression analysis. The cross section area of the estimated profile and measured profile are compared and discussed. Subsequently, a methodology to create multi-layer bead profile is proposed. A unique polygonal-shaped bead profile and constant width model is suggested to estimate the cross section profile for a multi-layer deposition. In addition, a methodology to estimate bead profile for planar deposition is proposed. A flat top model is suggested and discussed in order to obtain the cross section profile for a planar deposition. Finite element meshes of the multi-layer deposition bead profile and the planar deposition bead profile are created to demonstrate the implementation of the proposed methodology.

Chapter III is concerned with the calibration of heat flux model for thermal finite element analyses (FEAs) in this thesis. The top-hat distribution heat flux model with consideration of efficiency and penetration depth is introduced to properly emulate the measured intensity distribution of laser beam used in a wire feeding type DED process. The moving heat flux model is implemented in commercial FEA software SYSWELD. Using thermal FEAs, the heat flux model is calibrated by comparing the estimated geometry of heat affected zone (HAZ) to the measured depth and width of HAZ from experimental study. A methodology to select a proper penetration depth and efficiency of heat flux model for each combination of power of laser and travel speed of table is suggested. When the penetration depth and efficiency of heat flux model is selected using the proposed methodology, the heat flux model is properly calibrated for each combination of power of laser and travel speed of table in a wire feeding type DED process.

In Chapter IV, the thermo-mechanical characteristics of the fabricated part are investigated

and discussed using the calibrated heat flux model in SYSWELD. The results of thermo-mechanical FEAs are used to estimate the formation of HAZ and stress influenced region (SIR) for different power of laser, travel speed of table and length of bead. A proper gap between deposition beads is selected by comparing the width of HAZ and SIR. The influence of angle of corner deposition on the formation of HAZ, SIR and thermal stress is investigated and discussed. The thermo-mechanical characteristics during planar and multi-layer deposition of a wire feeding type DED process studied according to deposition pattern and interpass time. In addition, a proper deposition strategy is suggested. Coefficient of natural convection according to temperature of surface and facing direction of surface, and coefficient of forced convection are determined to improve the accuracy of the thermo-mechanical analysis. The vertical displacements of measured points on a cantilevered specimen are compared to the predicted vertical displacement from FEAs, in order to validate the thermo-mechanical FEA model. Finally, the influence of interpass time and deposition pattern on the formation of thermal stress of a cantilevered specimen is investigated and discussed using the validated thermo-mechanical FEA model.

In Chapter V, an activation algorithm of finite elements is proposed and discussed. Due to the small beam radius of a heat flux model, selection of mesh size of finite element is proposed for the implementation of the activation algorithm of finite elements. The selection algorithm of finite elements to be activated is implemented using MATLAB. Subsequently, the lists of finite elements are inputted to ABAQUS to progressively simulate the addition of material during a DED process. The proper front element cross section is investigated and selected via heat transfer FEAs. Lastly, the proposed activation algorithm of finite element is implemented in ABAQUS in order to obtain the thermo-mechanical characteristics of a multi-layer deposition on a cantilevered specimen. The results of the FEAs are examined and verified by comparing them to the measured displacements from experimental results.

## II. BEAD PROFILE FOR WIRE FEEDING TYPE DIRECTED ENERGY DEPOSITION PROCESS

### A. Wire Feeding Type Directed Energy Deposition Apparatus

Fig. 3 illustrates the prototype of a wire feeding type DED process located in Korea Institute of Machinery and Materials (KIMM), Daejeon, Republic of Korea. The prototype has an overall dimension of 1000 mm (width) × 900 mm (depth) × 2330 mm (height).

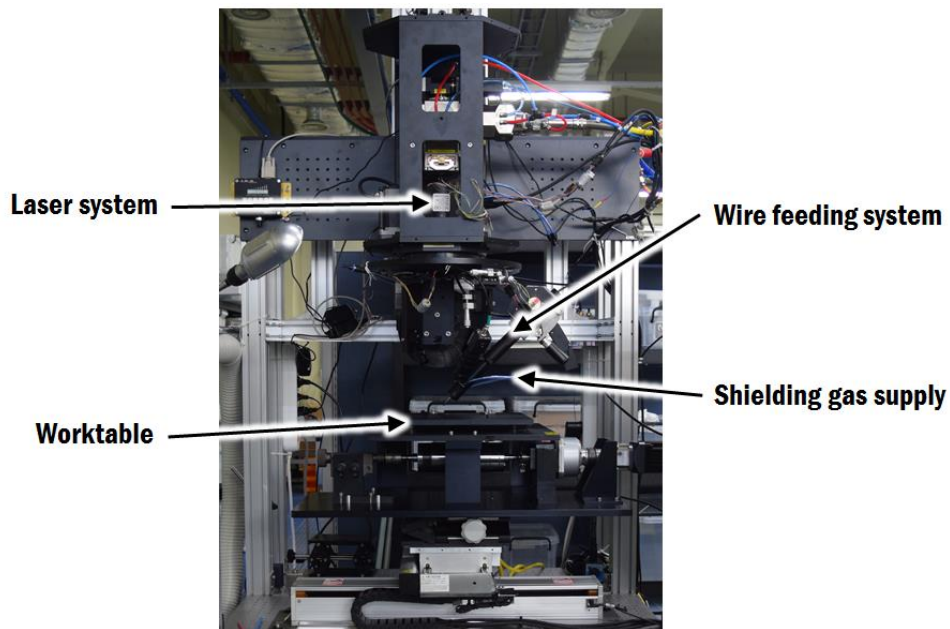


**Fig. 3 Prototype of a wire feeding type DED process (Courtesy of KIMM)**

The prototype consists of a laser system as the heat source, a numerically controlled worktable, a wire feeding system, shielding gas supply system and a computer control system. The laser system is a continuous wave fiber laser with 1070 nm wavelength and 5 kW of peak power, as listed in Table 5.

**Table 5 Specification of the laser system**

Parameters	Model	Laser type	Operating mode	Wavelength ( $\lambda$ , nm)	Peak power (kW)
Range	IPG Photonics, YLS-5000	Ytterbium fiber	Continuous wave	1,070	5.0

Titanium alloy Ti-6Al-4V is chosen as the material for this project because it has been investigated in AM processes and widely used for commercial fabrication.<sup>8,18</sup> The diameter of Ti-6Al-4V wire is 0.9 mm. In order to melt the wire and substrate simultaneously, the laser system is configured to have a beam size of 1.5 mm diameter on the substrate.

The allowable workspace of the system has the dimension of 400 mm (width)  $\times$  300 mm (depth)  $\times$  200 mm (height). The travel speed of the worktable in X-, Y-, and Z-direction are 30 mm/s, 75 mm/s and 20 mm/s, respectively. A front feeding of wire is applied in this system, as illustrated in Fig. 4. Argon gas is used as the shielding gas to prevent oxidation of deposited bead and substrate at the vicinity of the melt pool.

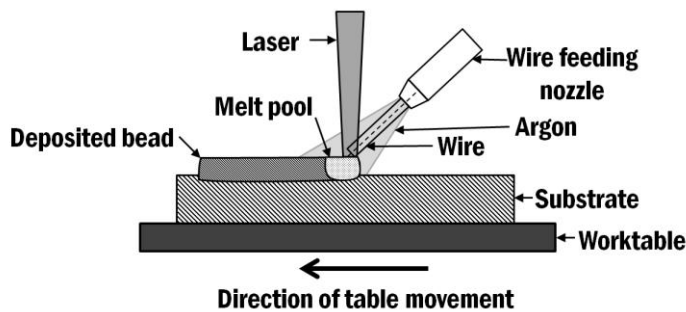


**Fig. 4 Schematic diagram of a front feeding DED process<sup>99</sup>**



## B. Derivation of Bead Profile for Single Bead Deposition

### 1. Description of Experiments

The shape of a deposited bead varies depending on process parameters and process conditions such as type of heat source, power of heat source, temperature of room and etc. Two major influencing parameters are the power of laser and the travel speed of table.<sup>47</sup>

In order to investigate the influence of process parameters on the shape of a deposited bead, six single beads are deposited on a Ti-6Al-4V substrate using a wire feeding type DED process according to different power of laser and travel speed of table, as tabulated in Table 6. In this experiment, the wire feeding type DED apparatus at KIMM is employed. During deposition, all corners of the substrate are clamped to a worktable.

**Table 6 Process parameters for experiment**

Parameters	Power of laser (P, kW)	Travel speed of table (V, mm/s)
Range	1.5, 2.0, 2.5	4, 8

### 2. Methodology

Fig. 5 shows the procedure to estimate the cross section profile of a deposited bead.<sup>29,99</sup> The deposited beads are cut into three sections in order to obtain the bead profile. A video microscope system (ICS, Sometech Inc.) are used to capture the cross sectional views of the deposited beads. The coordinates of the cross section profile of a deposited bead are extracted by measuring the height at fixed interval across the deposited beads, as shown in Fig. 6.

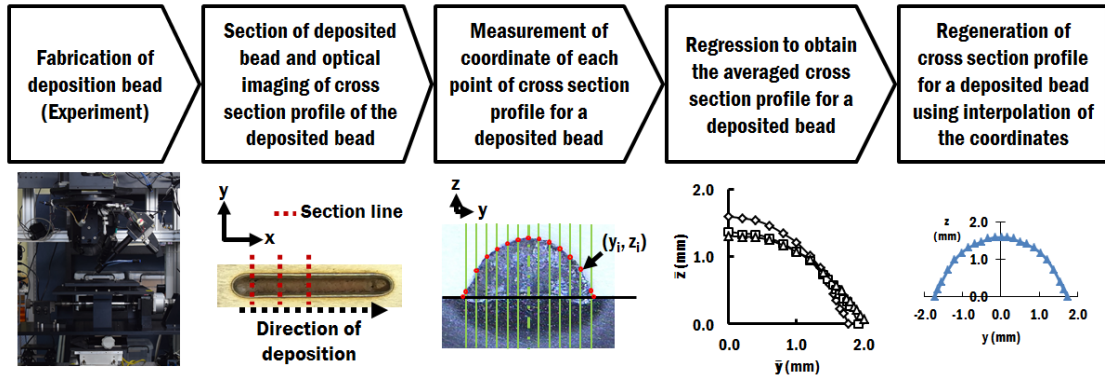


Fig. 5 Procedure to estimate the cross section profile of a deposited bead

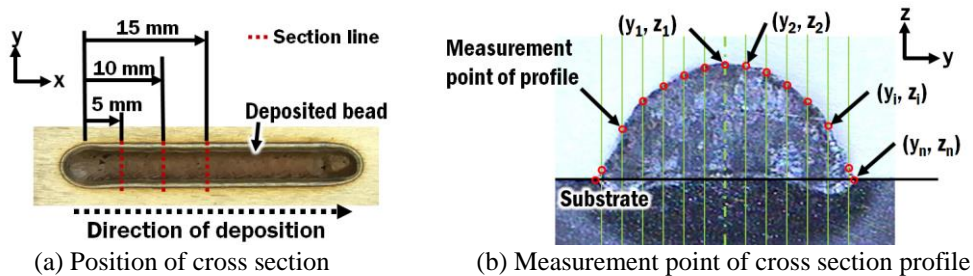


Fig. 6 Cross sectional view of a deposited bead

Three sets of measured coordinates are obtained from three section cuts for a deposited bead. In order to obtain an averaged cross section profile for a deposited bead, an averaged coordinates for point  $i$  ( $\bar{y}_i, \bar{z}_i$ ) is obtained from a number of sets of measured coordinates using Eqs. (1)-(2)

$$\bar{y}_i = \frac{\sum y_i}{m} \quad (1)$$

$$\bar{z}_i = \frac{\sum z_i}{m} \quad (2)$$

where  $y_i$ ,  $z_i$ , and  $m$  are the  $y$ -coordinate of a bead profile at measurement point  $i$ , the  $z$ -coordinate of a bead profile at measurement point  $i$ , and the number of sets of measured coordinates,

respectively. In this case of study, the number of sets ( $m$ ) is three because three section cuts are made.

Using the averaged coordinates  $(\bar{y}_i, \bar{z}_i)$ , a higher order polynomial regression line can be obtained to estimate the profile of a deposited bead. In order to reduce the complexity of the regression, a symmetrical bead profile is assumed. Therefore, only half side of the bead is considered. A bead can be regenerated from the obtained regression relationship.

In order to correlate the cross section profile of a deposited bead according to different power of laser ( $P$ ), a normalized y-coordinate ( $\hat{y}_i$ ) is introduced, as given in Eq. (3)

$$\hat{y}_i = \frac{\bar{y}_i}{y_{\max}} \quad (3)$$

where  $y_{\max}$  is the maximum y-coordinate of a bead profile.

Fig. 7 illustrates the concept of estimation of coordinate  $\bar{z}_i$  for different power of laser at a same travel speed of table (4.0 mm/s) by using regression lines for each normalized y-coordinate ( $\hat{y}_i$ ).

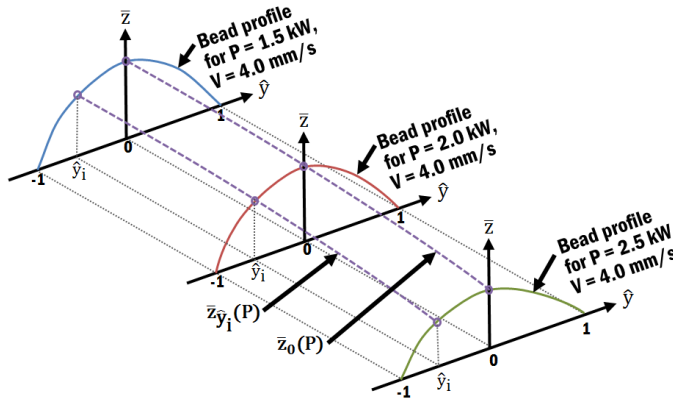


**Fig. 7 Quadratic regression line of coordinate  $\bar{z}_i$  for different power of laser at 4 mm/s**

For a same  $\hat{y}_i$ , the coordinate  $\bar{z}_i$  for different power of laser ( $\bar{z}_{\hat{y}}(P)$ ) is correlated using a

quadratic regression, as shown in Eq. (4)

$$\bar{z}_{\hat{y}_i}(P) = AP^2 + BP + C \quad (4)$$

where A, B, and C are the coefficients of a quadratic equation.

By solving partial derivatives of the least square method in Eqs. (5)-(8), the coefficients A, B, and C are determined using Eq. (9)<sup>108</sup>

$$R^2 \equiv \sum_{k=1}^n [\bar{z}_{\hat{y},k} - (AP_k^2 + BP_k + C)]^2 \quad (5)$$

$$\frac{\partial(R^2)}{\partial C} = -2 \sum_{k=1}^n [\bar{z}_{\hat{y},k} - (AP_k^2 + BP_k + C)] = 0 \quad (6)$$

$$\frac{\partial(R^2)}{\partial B} = -2 \sum_{k=1}^n [\bar{z}_{\hat{y},k} - (AP_k^2 + BP_k + C)] P_k = 0 \quad (7)$$

$$\frac{\partial(R^2)}{\partial A} = -2 \sum_{k=1}^n [\bar{z}_{\hat{y},k} - (AP_k^2 + BP_k + C)] P_k^2 = 0 \quad (8)$$

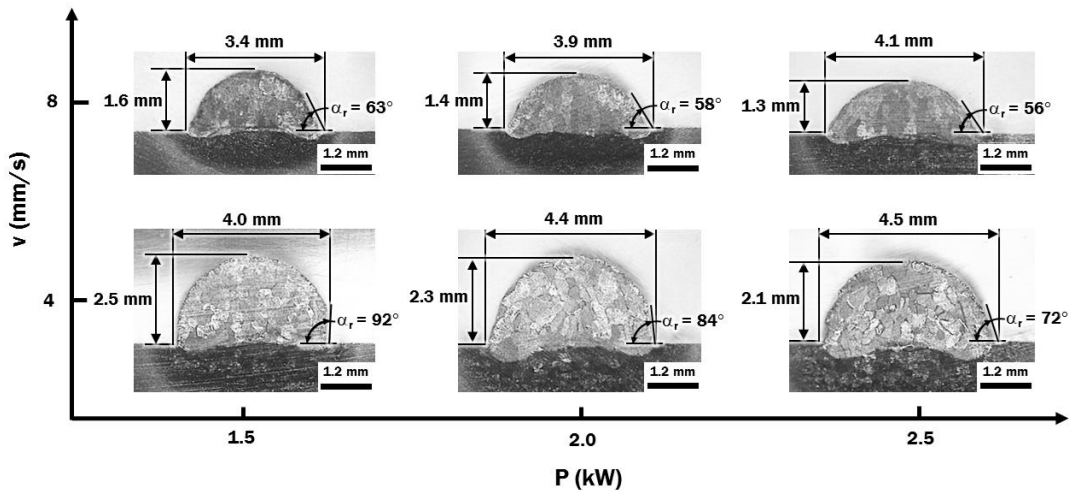
$$\begin{bmatrix} C \\ B \\ A \end{bmatrix} = \begin{bmatrix} \sum_{k=1}^n 1 & \sum_{k=1}^n P_k & \sum_{k=1}^n P_k^2 \\ \sum_{k=1}^n P_k & \sum_{k=1}^n P_k^2 & \sum_{k=1}^n P_k^3 \\ \sum_{k=1}^n P_k^2 & \sum_{k=1}^n P_k^3 & \sum_{k=1}^n P_k^4 \end{bmatrix}^{-1} \begin{bmatrix} \sum_{k=1}^n \bar{z}_{\hat{y},k} \\ \sum_{k=1}^n P_k \bar{z}_{\hat{y},k} \\ \sum_{k=1}^n P_k^2 \bar{z}_{\hat{y},k} \end{bmatrix} \quad (9)$$

where n is the number of points.

Through these regressions of  $\bar{z}_{\hat{y}_i}(P)$ , any intermediate bead profile for different power of laser at same travel speed of table can be estimated. Similarly, the maximum y-coordinate of a bead profile ( $y_{\max}$ ) for different power of laser at the same travel speed of table can be approximated using a quadratic regression analysis.

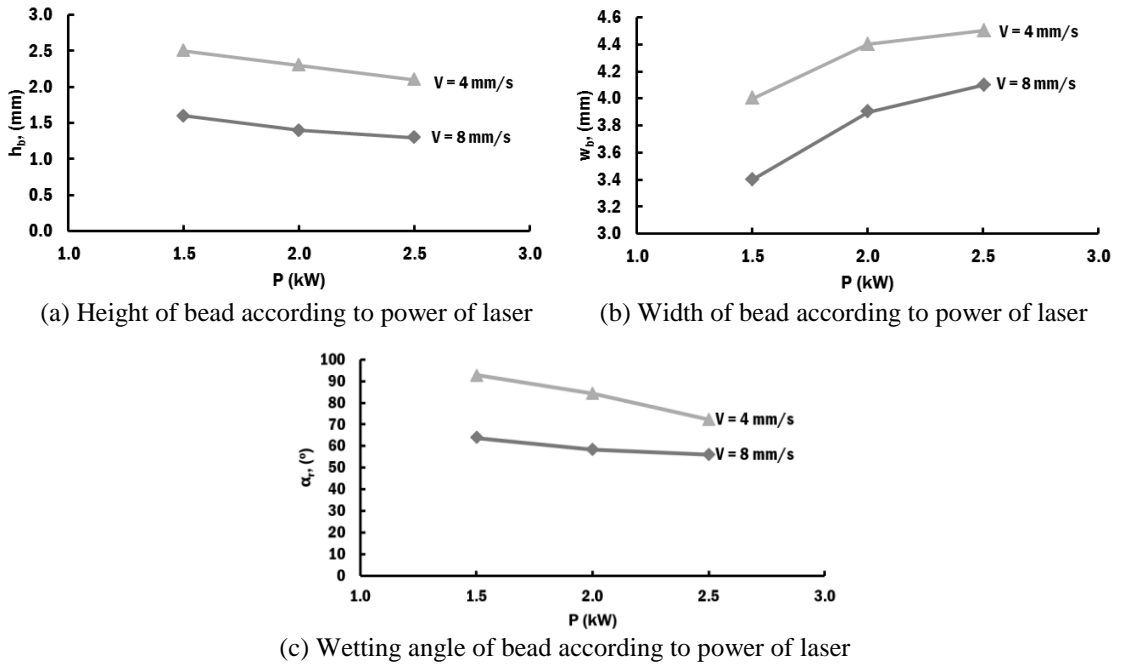
### 3. Results and Discussion

Fig. 8 shows the cross section views of deposited beads according to power of laser and travel speed of table obtained from experiment results. The dimensions shown were calculated from the averaged height, width and wetting angle of the beads. From the cross section views, it is observed that the wetting angle ( $\alpha_r$ ) is approximately  $90^\circ$  for the bead deposited using power of laser of 1.5 kW and travel speed of table of 4 mm/s, and the bead deposited using power of laser of 2.0 kW and travel speed of table of 4 mm/s. The high wetting angle is not suitable for planar deposition due to the fact that the melt wire has difficulty to flow at the corner of root and causes undesired porosity.



**Fig. 8 Cross section views of deposited beads according to power of laser and travel speed of table<sup>99</sup>**

From Fig. 9, it is revealed that the height of the bead ( $h_b$ ) and wetting angle of the bead ( $\alpha_r$ ) decreases when the power of laser increases for the same travel speed of table. However, the width of the bead ( $w_b$ ) increases when the power of laser increases for the same travel speed of table. The higher power of laser contributes higher heat input and temperature onto the bead and substrate. Hence, the melted wire with higher power of laser has sufficient time to wet a wider surface of substrate before solidification takes place.



**Fig. 9 Dimensions of deposited beads according to power of laser**

Besides, the dimensions of a deposited bead reduce as the travel speed increases. This is attributed to the reduction of specific heat energy ( $E_s$ ) transferred to the bead and substrate as the travel speed of table increases. The specific heat energy is described by Eq. (10).<sup>109</sup>

$$E_s = \frac{P}{V} \quad (10)$$

Fig. 10 shows the specific heat energy is lower for higher travel speed of table, as a result of shortened laser-substrate interaction time.

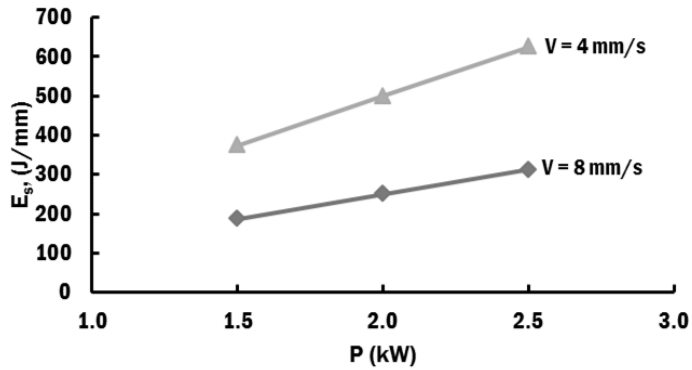


Fig. 10 Specific heat energy according to power of laser and travel speed of table

The deposition rate ( $D_r$ ) is approximated by multiplying the area of cross section of deposited bead ( $A_b$ ) and travel speed of table, as described in Eq. (11).

$$D_r = A_b \cdot V \quad (11)$$

The areas of cross section of deposited beads ( $A_{exp}$ ) from the experiment are estimated by using computer aided design (CAD) software CATIA, as listed in Table 7.

Table 7 Cross section area of measured profile and estimated deposition rate for different process parameters

Power of laser (P, kW)	Travel speed of table (V, mm/s)	Cross section area of measured bead profile ( $A_{exp}$ , mm <sup>2</sup> )	Deposition rate ( $D_r$ , mm <sup>3</sup> /s)
1.5	4	7.892	31.57
2.0	4	7.810	31.24
2.5	4	7.438	29.75
1.5	8	3.926	31.41
2.0	8	3.775	30.20
2.5	8	3.818	30.55

Fig. 11 shows the approximated deposition rates for different power of laser and travel speed of table. Deposition rates lie in the range of 29.75-31.57 mm<sup>3</sup>/s. In the case of same travel speed of table, the highest deposition rate occurs when the power of laser is 1.5 kW. This is associated with the fact that lower specific heat input has lesser amount of material loss via evaporation. The deposition rate dropped slightly when the power of laser is increased due to higher amount of material loss via evaporation.

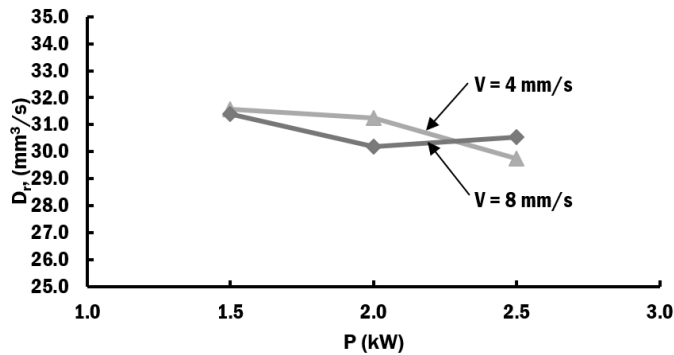


**Fig. 11 Estimated deposition rate according to power of laser and travel speed of table**

Based on the aforementioned results, it is concluded that DED process parameters using power of laser 1.5 kW at travel speed of table 8 mm/s is the most suitable for the wire feeding type DED process apparatus. Using this process parameter, Ti-6Al-4V deposition rate of 31.41 mm<sup>3</sup>/s has been achieved with acceptable wetting angle of 63°.

By employing the methodology in Fig. 5, cross section profiles for deposited beads from the experiment results is converted to averaged coordinates ( $\bar{y}_i, \bar{z}_i$ ), as shown in Fig. 12. Fig. 13 shows the cross section profiles for deposited bead with the application of normalized y-coordinate.



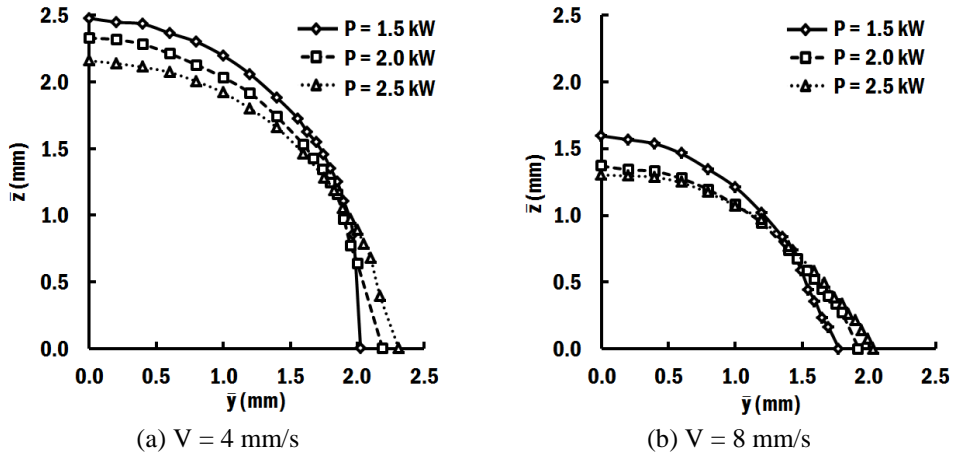


Fig. 12 Averaged coordinates for cross section profile of half deposited beads for various power of laser and travel speed of table

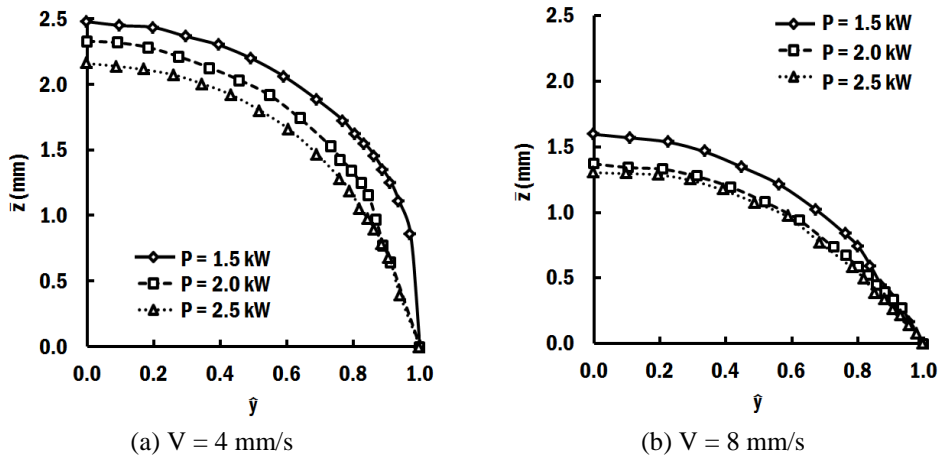


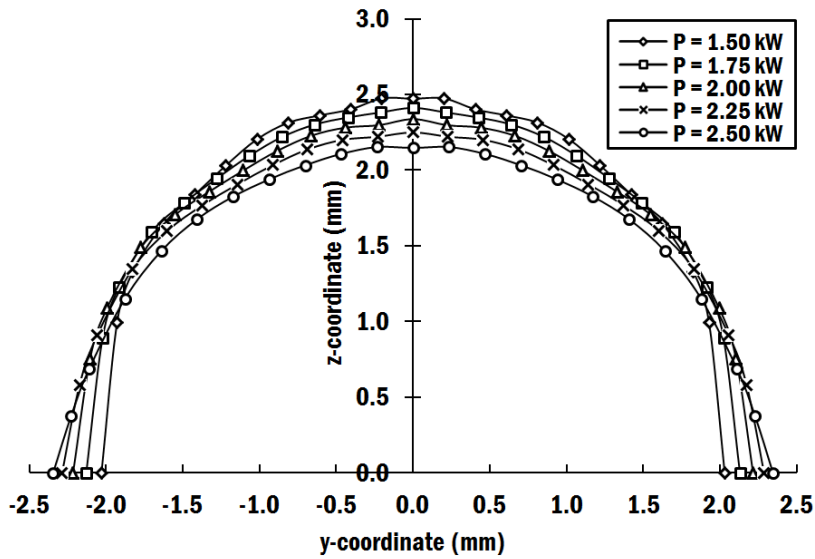
Fig. 13 Cross section profile of half deposited beads with normalized y-coordinate for various power of laser and travel speed of table

By employing Microsoft Excel to perform least square curve fitting to the cross section profiles in Fig. 13, a suitable high order polynomial regression relationships has been obtained, as listed in Table 8.

**Table 8 Regression relationship of half bead profile for various power of laser and travel speed of table**

Power of laser (P, kW)	Travel speed of table (V, mm/s)	Regression relationship between $\hat{y}$ and $\bar{z}$	Coefficient of determination ( $R^2$ )
1.5	4	$\bar{z} = -168.75\hat{y}^6 + 460.78\hat{y}^5 - 470.12\hat{y}^4 + 218.73\hat{y}^3 - 46.089\hat{y}^2 + 3.1208\hat{y} + 2.4668$	0.9886
2.0	4	$\bar{z} = 0.459\hat{y}^5 - 8.1459\hat{y}^4 + 10.439\hat{y}^3 - 5.5775\hat{y}^2 + 0.4801\hat{y} + 2.3246$	0.9980
2.5	4	$\bar{z} = -5.1525\hat{y}^4 + 6.8579\hat{y}^3 - 4.2696\hat{y}^2 + 0.4207\hat{y} + 2.1471$	0.9990
1.5	8	$\bar{z} = 8.2057\hat{y}^5 - 20.872\hat{y}^4 + 17.082\hat{y}^3 - 6.5499\hat{y}^2 + 0.5297\hat{y} + 1.5903$	0.9988
2.0	8	$\bar{z} = -0.6829\hat{y}^4 + 0.652\hat{y}^3 - 1.4079\hat{y}^2 + 0.0992\hat{y} + 1.3633$	0.9991
2.5	8	$\bar{z} = 0.8835\hat{y}^4 - 2.0845\hat{y}^3 - 0.0616\hat{y}^2 - 0.0289\hat{y} + 1.3041$	0.9995

The regression relationships in Table 8 provide the ability to determine the averaged z-coordinate at any arbitrary normalized y-coordinate. Based on the concept shown in Fig. 7 and quadratic regression analysis between three datasets of coordinates for a travel speed of table, the bead profiles for single bead deposition for different power of laser at travel speed of table of 4 mm/s and 8 mm/s have been derived as shown in Fig. 14.



(a)  $V = 4 \text{ mm/s}$

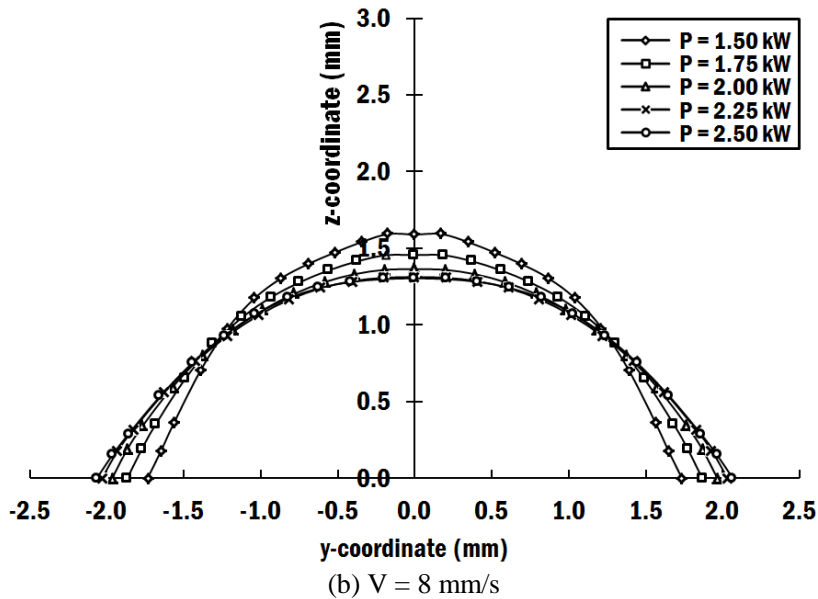


**Fig. 14 Regenerated cross section profile for a deposited bead for various power of laser and travel speed of table**

The cross section areas of the measured profile ( $A_{exp}$ ), the semi-ellipse profile ( $A_{ei}$ ), and the proposed regenerated profile ( $A_{gen}$ ) for each combination of power of laser and travel speed of table are compared, as shown in Table 9. The semi-ellipse profile is used as a benchmark to evaluate the performance of the generated profile. The area of cross section of deposited bead ( $A_{ei}$ ) is estimated based on the area of a semi-ellipse, as expressed in Eq. (12).

$$A_b = \frac{\pi \cdot w_b \cdot h_b}{4} \quad (12)$$

It is revealed that the cross section areas of generated bead profile for all cases are laid in the range of cross section area of measure bead profile. The error difference of cross section areas between the generated and measured bead profiles are in the range of -0.2% to 4.1%. As a comparison, the cross section area estimated using a semi-ellipse profile produces higher error

difference in the range of -0.5% to +13.6%. Hence, the generated bead profile is properly derived. The generated bead profile is used to represent the bead profile for different combinations of power of laser and travel speed of table in this thesis.

**Table 9 Comparison of cross section area of measured profile, semi-ellipse profile and generated profile for different process parameters**

Power of laser (P, kW)	Travel speed of table (V, mm/s)	Cross section area of measured bead profile ( $A_{exp}$ , mm <sup>2</sup> )	Cross section area of semi-ellipse profile ( $A_{el}$ , mm <sup>2</sup> )	Error difference between $A_{el}$ and $A_{exp}$ (%)	Cross section area of generated bead profile ( $A_{gen}$ , mm <sup>2</sup> )	Error difference between $A_{gen}$ and $A_{exp}$ (%)
1.5	4	7.892 ± 0.273	7.854	-0.5	8.121	+2.9
2.0	4	7.810 ± 0.212	7.948	+1.8	8.127	+4.1
2.5	4	7.438 ± 0.434	7.422	-0.2	7.563	+1.7
1.5	8	3.926 ± 0.177	4.273	+8.8	3.929	+0.1
2.0	8	3.775 ± 0.104	4.288	+13.6	3.800	+0.7
2.5	8	3.818 ± 0.101	4.186	+9.6	3.809	-0.2

## C. Derivation of Bead Profile for Multi-Layer Deposition

### 1. Description of Multi-Layer Deposition and Related Works

A single bead deposition is the fundamental unit of a multi-layer deposition in a wire feeding type DED process. Upon the deposition of a single bead, a new bead is deposited on top of the previous bead to form a multi-layer deposition in a DED process, as shown in Fig. 15. In contrast to a multi-pass welding process that involve deposition of weld material within a constrained space such as in a V-groove, a DED process may involve stacking of multiple layers of beads to form a three dimensional thin wall structure.

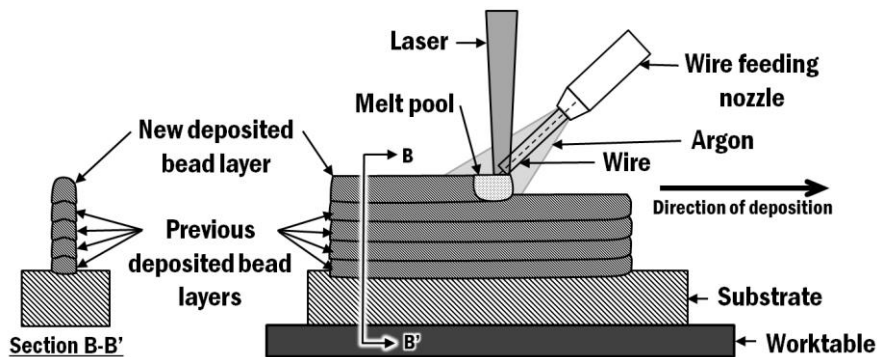


Fig. 15 Schematic diagram of a multi-layer deposition of a wire feeding type DED process

In order to simulate a multi-layer deposition of a wire feeding type DED process, researchers have developed finite element analysis models for multi-layer deposition with an assumed bead profile, as shown in Table 4.

Chiumenti et al. (2010), Lundbäck et al. (2011), Ding et al. (2011), and Lee et al. (2018), applied a rectangular bead profile for multi-layer deposition using the wire feeding type DED process.<sup>44,60,90,98</sup> The rectangular bead profile has the same width and height for each layer of deposition. The rectangular bead profile is preferred due to the ease of mesh creation. However,

this assumption is not suitable for a wire feeding type DED process, which has a deposited bead with height in a few millimeters.

Zhang et al. (2011) obtained curved bead profile for their multi-bead FE model by measuring the width of bead, the height of bead, the wetting angle and the bead area from experimental study.<sup>92</sup> This approach is direct and does not require the solution of fluid dynamics of melt pool in order to estimate the bead profile. However, experiment must be performed in order to obtain the bead profile, which is impractical.

Anca et al. (2011) employed an arc shaped bead profile in their study of wire feeding type DED process.<sup>89</sup> The deposition of first layer was created with an arc shaped bead profile, which was estimated from a single layer deposition experiment. The arc shaped bead profile was maintained for subsequent layers. The thickness for each subsequent deposited bead was represented by one finite element. However, the thickness of the deposited beads is not reported.

Kumar et al. (2014) applied mass addition approach based on enthalpy balance in a two-dimensional FE model to estimate the height of bead for a multi-layer powder type feeding DED deposition.<sup>110</sup> The mass addition is represented by fine square finite elements. Their simulation results revealed that the width of bead is constant when the power of laser is equal or higher than 1.0 kW. The additional height of bead varies slightly between deposition layers. Although this approach allows prediction of bead profile via finite element analysis, it is difficult and computational expensive to implement for a three-dimensional FE model.

From the empirical-statistical models of geometry of bead deposited using laser DMD processes, Pinkerton (2015) described that three process parameters such as power of laser, travel speed and mass flow rate of powder are the primary influencing variables to the height and width of bead.<sup>111</sup>

## 2. Polygonal-Shaped Cross Section Profile and Constant Width Model

A bead profile for multi-layer deposition is required to properly simulate a multi-layer deposition using a wire feeding type DED process. In order to model the cross section profile of the multi-layer bead, a polygonal-shaped cross section profile and a constant width model is proposed in the procedure shown in Fig. 16.

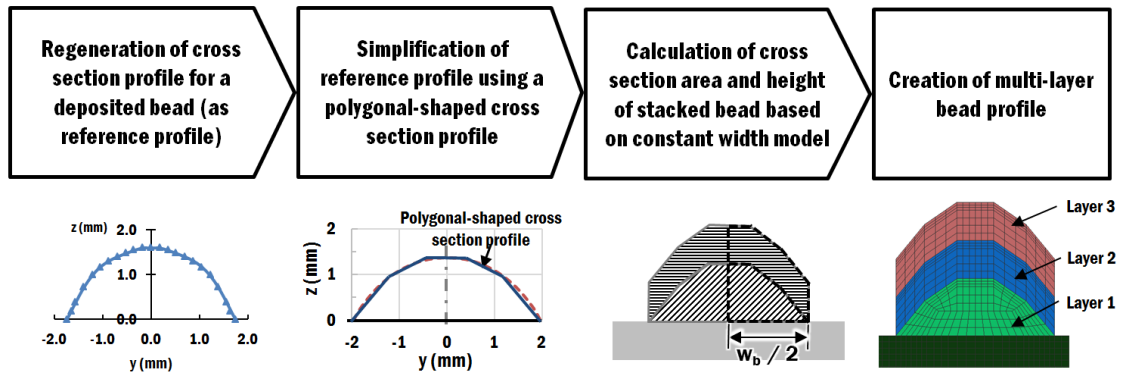
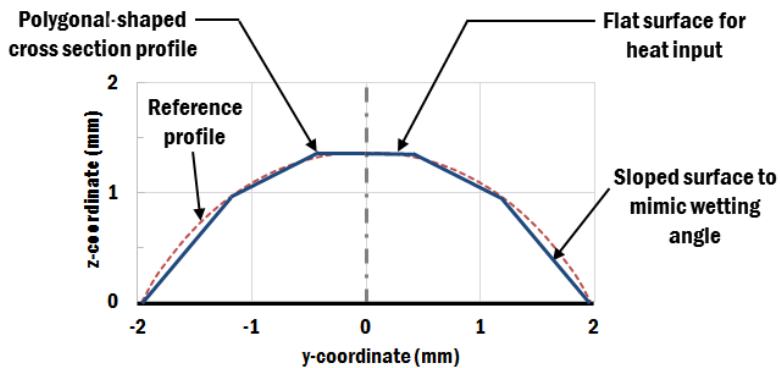


**Fig. 16 Procedure to model a polygonal-shaped cross section profile of a multi-layer deposited bead**

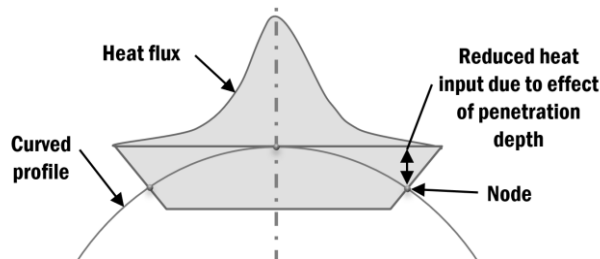
The regenerated curved-shaped cross section profile of a single bead in Fig. 14 can be simplified using a polygonal-shaped cross section profile. The polygonal-shaped cross section profile is proposed such that it has a flat surface at the top of the bead for heat flux input and sloped surfaces elsewhere to mimic the wetting angle of the bead, as illustrated in Fig. 17. The advantages of a polygonal-shaped cross section profile are:

- (1) A volumetric heat flux with small heat application region or a surface heat flux can be properly applied on the flattened surface on the top of bead. This is because deviation in location of node from the heat application region results in different heat input numerically, as illustrated in Fig. 17.

- (2) While the polygonal-shaped cross section profile inherits the simplicity of a rectangular bead, it is able to preserve the characteristics of a curve-shaped bead by having an approximated wetting angle and height of a bead.
- (3) The polygonal-shaped cross section profile is easier to create and to mesh than a curve-shaped cross section profile in a FE software.
- (4) The meshing of finite elements within a polygonal shape can be easily extended for multi-layer deposition, as well as for a planar deposition of a DED process.



(a) Simplification of reference profile using a polygonal-shaped cross section profile



(b) Reduced heat input for curved profile of a bead due to location of node

**Fig. 17 Polygonal-shaped cross section profile of bead and effect of curved profile on heat input**



In order to create the polygonal-shaped cross section for the creation of finite element model, the following steps are taken:

- (1) The flat surface of the top of bead is created at the height of the reference profile.
- (2) The width of the polygon is created according to the width of the reference profile.
- (3) A point in between the flat surface of the top of bead and substrate is selected such that it touches the reference profile and gives a satisfactory sloped surface that mimic the wetting angle.
- (4) These coordinates of points are rounded to the nearest 0.05 mm.

In order to estimate the bead profile for a multi-layer deposition, a constant width model is proposed, as illustrated in Fig. 18. The width of bead for a multi-layer is assumed to be a constant due to the fact that it depends on the power of laser and travel speed of table.<sup>111</sup> The following assumptions are made for the constant width model:

- (1) The volume of deposited material for each layer ( $A_{LS}$ ) is assumed to be constant and equal to the volume of deposited material for the first layer ( $A_{L1}$ ).
- (2) The cross section profile of deposited bead is symmetrical.
- (3) The cross section profile of deposited bead remains unchanged during multi-layer deposition of bead.
- (4) The primary process parameters such power of laser and travel speed of table remain constant for all deposited layers.

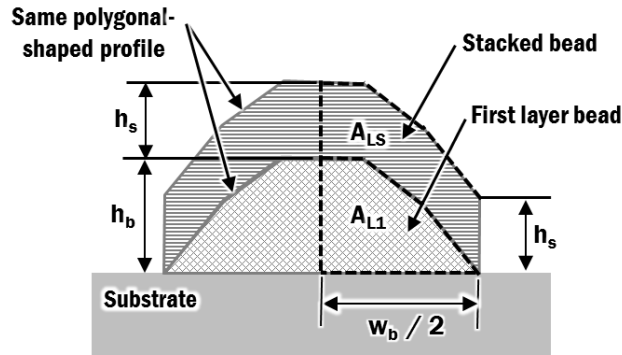


**Fig. 18 Polygonal-shaped cross section profile of multi-layer deposited bead**

Based on the assumptions, the constant width model is used to determine the height of stacked bead ( $h_s$ ) in a multi-layer deposition, as described in Eq. (13)

$$h_s = \frac{2A_{L1}}{w_b} = \frac{2A_{LS}}{w_b} \quad (13)$$

where  $A_{L1}$ , and  $A_{LS}$  are the area of half polygonal-shaped cross section profile of a single bead, and area of half polygonal-shaped cross section profile of a stacked layer, respectively.

### 3. Results and Discussion

Fig. 19 shows the estimated polygonal-shaped cross section profile by employing the methodology in Fig. 16. It shows that the polygonal-shaped cross section profile provides a better approximation to the actual bead profile compared to the semi-ellipse cross section profile. By comparing the area of cross section for various bead profiles in Table 10, it is revealed that polygonal-shaped profile provides consistent results with areas that are 3.4 % to 6.0 % smaller than intended reference profiles. In contrast, the error difference in cross section area due to semi-ellipse profiles is in the range of -1.9 % to +12.8 %.

**Table 10 Comparison of cross section area of generated profile, semi-ellipse profile and polygonal shaped profile for different process parameters**

Power of laser (P, kW)	Travel speed of table (V, mm/s)	Cross section area of generated bead profile ( $A_{gen}$ , mm <sup>2</sup> )	Cross section area of semi-ellipse profile ( $A_{el}$ , mm <sup>2</sup> )	Error difference between $A_{el}$ and $A_{gen}$ (%)	Cross section area of polygonal-shaped profile ( $A_p$ , mm <sup>2</sup> )	Error difference between $A_p$ and $A_{gen}$ (%)
1.5	4	8.121	7.854	-3.3	7.640	-5.9
2.0	4	8.127	7.948	-2.2	7.800	-4.0
2.5	4	7.563	7.422	-1.9	7.110	-6.0
1.5	8	3.929	4.273	+8.7	3.720	-5.3
2.0	8	3.800	4.288	+12.8	3.655	-3.8
2.5	8	3.809	4.186	+9.9	3.713	-2.5

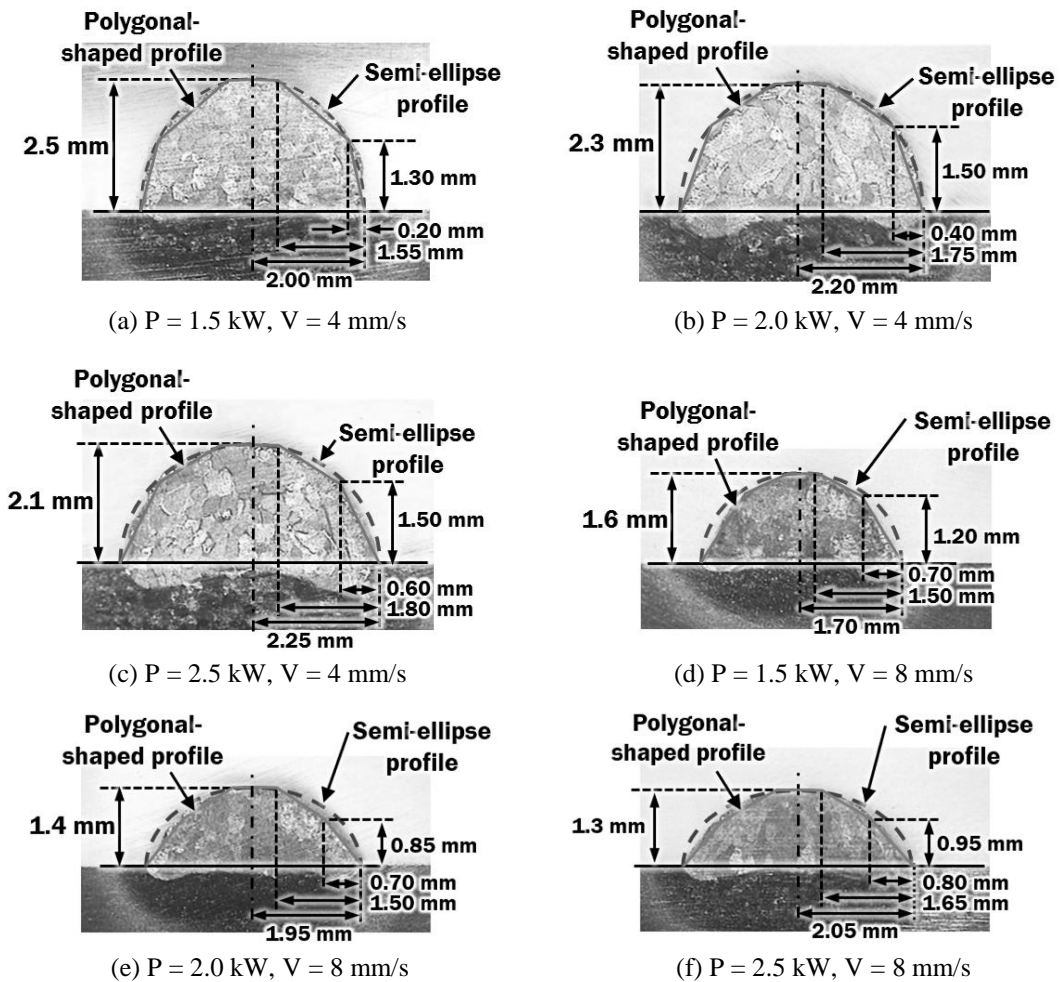


**Fig. 19 Comparison between polygonal-shaped cross section profile, semi-ellipse cross section profile, and actual single bead profile**

From the result of cross section area of polygonal shaped profile in Table 10, the Eq. (13) has been re-expressed in term of  $A_p$ , as in Eq. (14).

$$h_s = \frac{A_p}{w_b} \quad (14)$$

The height of stacked bead ( $h_s$ ) for different process parameters had been determined, as shown in Table 11.

**Table 11 Height of stacked bead for different process parameters**

Power of laser (P, kW)	Travel speed of table (V, mm/s)	Cross section area of polygonal-shaped profile ( $A_p$ , mm <sup>2</sup> )	Width of bead ( $w_b$ , mm)	Height of stacked bead ( $h_s$ , mm)
1.5	4	7.640	4.00	1.910
2.0	4	7.800	4.40	1.773
2.5	4	7.110	4.50	1.580
1.5	8	3.720	3.40	1.094
2.0	8	3.655	3.90	0.937
2.5	8	3.680	4.10	0.897

Using the polygonal-shaped cross section profile, cross section profiles for multi-layer DED deposition for selected process parameters has been created as shown in Fig. 20.

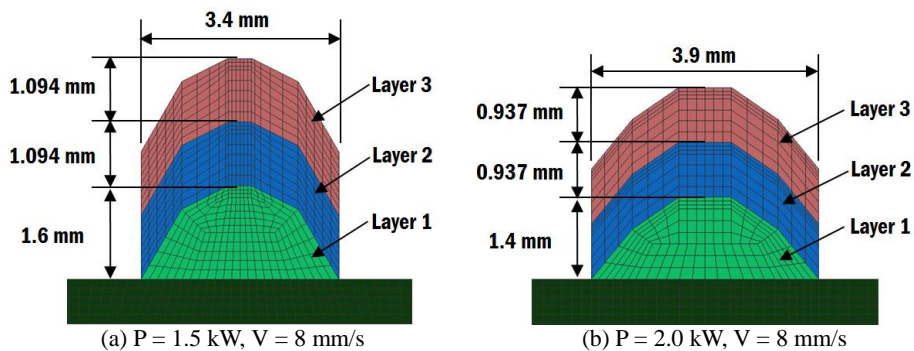


**Fig. 20 Cross section profiles for multi-layer DED depositions for selected process parameters**

## D. Derivation of Bead Profile for Planar Deposition

### 1. Description of Planar Deposition and Related Works

A planar deposition in a DED process involves deposition of multiple beads next to each other to form a layer of three dimensional flat structure, as depicted in Fig. 21. In contrast to a multi-pass cladding process that involves deposition of weld material to cover surface of a substrate, the primary purpose of planar deposition for a DED process is to form the sliced layer of a larger three dimensional AM structure.

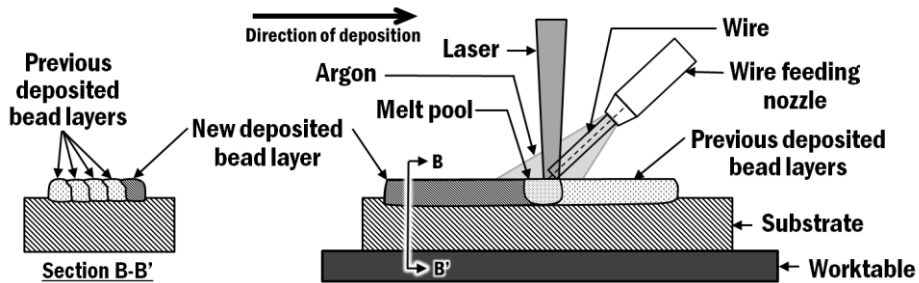


Fig. 21 Schematic diagram of a planar deposition of a wire feeding type DED process

The main intent of planar deposition of a DED process is to obtain a layer with uniform thickness to build upon. Hence, a flat layer is desired. In order to predict the optimum distance between beads that produce a flat top profile for planar deposition of a wire feeding type DED process, several overlapping models have been proposed by researchers.<sup>112-116</sup> In constructing these models, the bead section profile is required. The fundamental assumption made in these models is that the overlapped volume between beads is equal to the volume of materials that fill in the valley in between beads in order to form a flat top profile.<sup>112-114</sup>

In 2011, Suryakumar et al. built an flat top overlapping model based on bead section profile estimated using parabola curve for a hybrid layered manufacturing using gas metal arc welding

(GMAW).<sup>112</sup> The parabola curve was expressed as a function of width and height of bead. Comparing with the measured section area of bead, the errors of estimated bead section area using parabola curve were in the range of -12% to 10.7%. By using the fundamental assumption, the distance between beads was derived as two-third of the width of a bead.

In 2011, Cao et al. built a flat top overlapping model based on sine curve of single bead section profile to determine the optimum overlapping coefficient for a fixed process parameter.<sup>113</sup> The optimum distance between beads was estimated at 0.6366 of the width of a bead. The effects of interfacial force of liquid metal and arc pressure were neglected.

In 2013, Xiong et al. correlates beads section profile with ratio of wire feedrate and travel speed of welding torch ( $R_{FRV}$ ).<sup>114</sup> From their experiments using robotic GMAW-based additive manufacturing, they divided the bead section profile into parabola curve and arc curve according to  $R_{FRV}$ . The maximum errors of estimated bead section area using parabola curve and arc curve were reported as 12.6% and 20.7%, respectively. The optimum distances were derived according to the the bead section profile using the fundamental assumption for flat top overlapping models.

In 2015, Ding et al. proposed a tangent overlapping model (TOM) for a WAAM process.<sup>115</sup> Based on their experimental study, parabola curve was selected to estimate the bead section profile for different welding speed, and ratio of wire feedrate and travel speed of welding torch. A geometry of critical valley was introduced instead of a flat top geometry in their TOM. They concluded that the best distance between two beads was 0.738 of the width of a bead.

In 2018, a study was conducted by Li et al. using artificial neural network (ANN) to correlate their experimental results in order to obtain an optimum distance between the center of fed wire.<sup>116</sup> Using ANN, the computed optimum distance for their experimental study was 4.534 mm based on the width of bead of 6.144 mm.

## 2. Methodology

An overlapping bead profile is required to properly simulate a planar deposition using a wire feeding type DED process. In order to model the cross section profile of the planar bead, a polygonal-shaped cross section profile and a flat top overlapping model is proposed, and the procedure is as shown in Fig. 22.

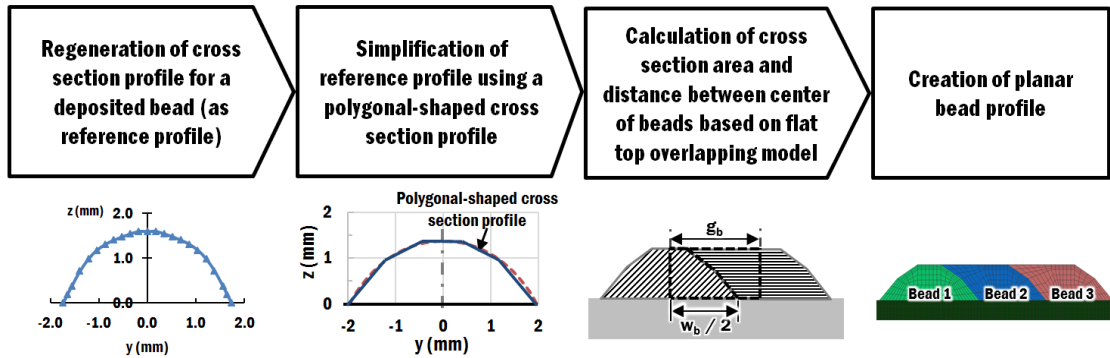


**Fig. 22 Procedure to model a polygonal-shaped cross section profile of a planar deposited bead**

The generation and simplification of bead profile into a polygonal-shaped cross section profile has been discussed previously in Chapter II Section C-2. The polygonal-shaped cross section profile is applied for the derivation of the optimum distance between beads ( $g_b$ ), as shown in Fig. 23. The derivation is based on the following assumptions made for a flat top overlapping model:

- (1) The primary process parameters such power of laser and travel speed of table remain unchanged for all deposited beads.
- (2) The cross section profile of deposited bead is symmetrical.
- (3) The half of cross section profile of deposited bead remains unchanged during planar deposition of bead.

- (4) The volume of deposited material for overlapping bead ( $A_{LP}$ ) is assumed to be equal to the volume of deposited material for the first layer ( $A_{L1}$ ) in order to form a flat top profile.

Based on these assumptions, the flat top overlapping model is used to determine the optimum distance between beads ( $g_b$ ) in a planar deposition, as in Eq. (15)

$$g_b = \frac{2A_{L1}}{h_b} = \frac{2A_{LP}}{h_b} \quad (15)$$

where  $A_{LP}$  is the area of half polygonal-shaped cross section profile of an overlapping bead, as shown in Fig. 23.

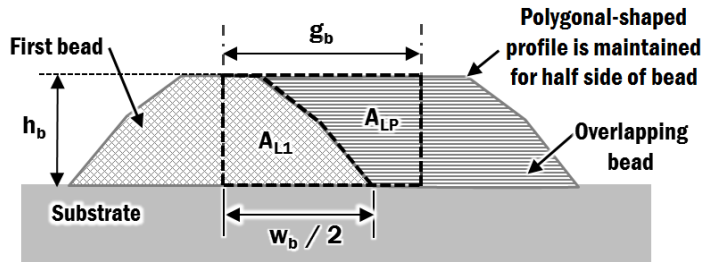


**Fig. 23 Flat top overlapping cross section profile of planar deposited bead**

### 3. Results and Discussion

From the result of cross section area of polygonal shaped profile in Table 10, the Eq. (15) has been rewritten in term of  $A_p$ , as in Eq. (16).

$$g_b = \frac{A_p}{h_b} \quad (16)$$

The optimum distances between beads ( $g_b$ ) in a planar deposition for different process



parameters have been determined, as shown in Table 12. From the results of optimum distances between beads, a distance to width ratio ( $g_w$ ) and an overlap ratio ( $\phi_{OL}$ )<sup>117</sup> are calculated by Eqs. (17) and (18).

$$g_w = \frac{g_b}{w_b} \quad (17)$$

$$\phi_{OL} = \left(1 - \frac{g_b}{w_b}\right) \times 100\% = (1 - g_w) \times 100\% \quad (18)$$

**Table 12 Optimum distance between beads and overlap ratio for different process parameters**

Power of laser (P, kW)	Travel speed of table (V, mm/s)	Cross section area of polygonal-shaped profile ( $A_p$ , mm <sup>2</sup> )	Height of bead ( $h_b$ , mm)	Optimum distance between beads ( $g_b$ , mm)	Distance-to-width ratio ( $g_w$ )	Overlap ratio ( $\phi_{OL}$ , %)
1.5	4	7.640	2.5	3.056	0.764	23.6
2.0	4	7.800	2.3	3.391	0.771	22.9
2.5	4	7.110	2.1	3.386	0.752	24.8
1.5	8	3.720	1.6	2.325	0.684	31.6
2.0	8	3.655	1.4	2.611	0.669	33.1
2.5	8	3.680	1.3	2.830	0.690	31.0

The results show that distance-to-width ratio vary in the range of 0.752 to 0.771 and 0.669 to 0.690 for travel speed of 4 mm/s and travel speed of 8 mm/s, respectively. This variation is due to the change in cross section area of polygonal-shaped profile according to power of laser and travel speed of table, as oppose to estimated area using a generalized curve profile for all process parameters in previous researches. Hence, the proposed optimum distance between beads is more proper than the past researches.

Besides, the increase in travel speed of table requires a higher overlap ratio. This is due to a higher travel speed produces a wider but shorter bead. Hence, more material is required to fill the area of the valley between two adjacent beads.

A cross section profile for planar DED deposition for a selected process parameter has been created as shown in Fig. 24. The finite element mesh between adjacent beads has been created successfully.

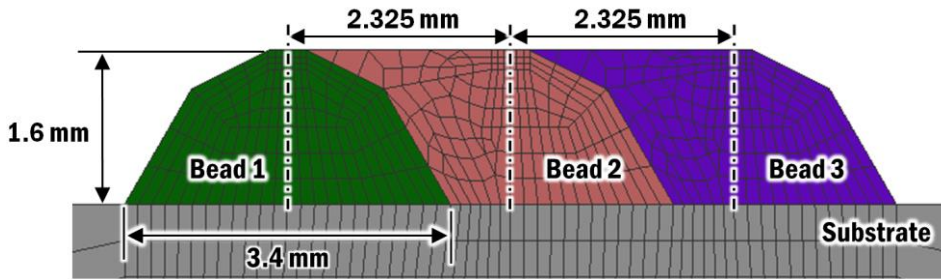


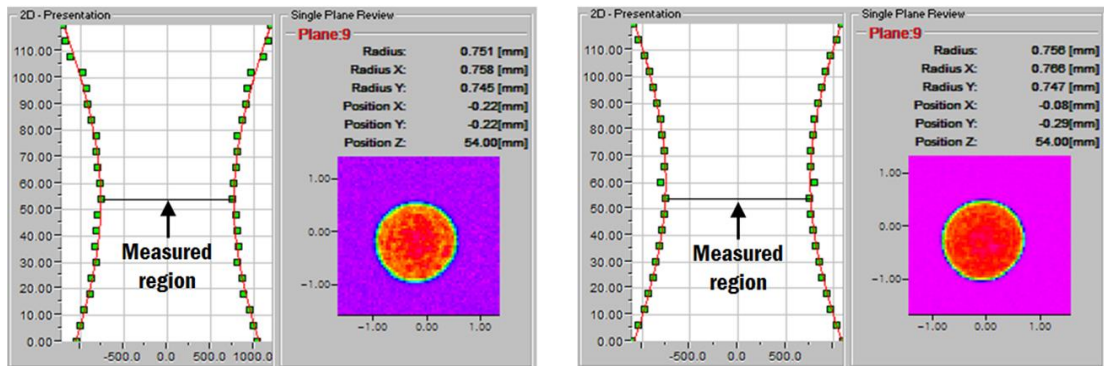
**Fig. 24 Cross section profiles for planar DED depositions for selected process parameters (P = 1.5 kW and V = 8 mm/s)**

### III. CALIBRATION OF HEAT SOURCE MODEL

#### A. Introductory Remarks

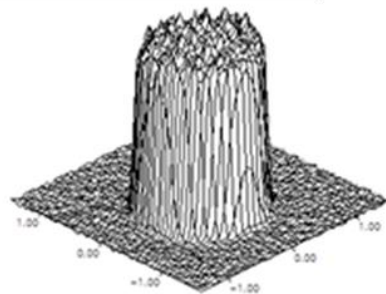
##### 1. Description of Heat Source Model

In this study, the laser system installed in the wire feeding type DED apparatus in KIMM is configured to have a beam size of 1.5 mm diameter on the substrate. Fig. 25 shows the measured beam profile has a top-hat distribution profile.



(a) Power of laser = 1 kW

(b) Power of laser = 5 kW



(c) 3D representation of a top-hat beam profile

Fig. 25 Measurement results of beam profile at 1 kW and 5 kW (Courtesy of KIMM)

In order to estimate the dimensions of weld pool and heat affected zone (HAZ) using heat transfer FEAs, proper heat input parameters such as beam distribution profile, efficiency of heat source and penetration depth of heat source are critical and must be calibrated.<sup>84,118</sup>

## 2. Related Works

The heat source is categorized into two types depending on heating mode, namely conduction mode and keyhole mode. In conduction mode, weld penetration is achieved by the heat conducting from the surface down to the core of metal bead to form a wide and shallow weld. Keyhole mode creates a deep and narrow weld due to expanding gas from vaporizing metal pushing outward from the depth of weld. In AM applications, keyhole is not observed due to a more defocused beam, such as laser or electron beam, is used.<sup>79</sup>

Typically, a volumetric heat flux ( $Q$ ) for a Gaussian distribution laser beam can be expressed as in Eq. (19)<sup>119</sup>

$$Q(r,Z) = \frac{2P(1-R_m)}{\pi r_b^2 d_p} \exp\left(-\frac{Z}{d_p}\right) \cdot \exp\left(-\frac{2r^2}{r_b^2}\right) \quad (19)$$

where  $r$  is the radial distance from center of beam,  $Z$  is the  $Z$ -coordinate relative to the center of beam,  $R_m$  is the reflectance of a material,  $r_b$  is the radius of laser beam, and  $d_p$  is the penetration depth. Radius of beam is defined as the radial distance from the beam axis to the location where power intensity is reduced to  $e^{-2}$ .<sup>120</sup> Penetration depth ( $d_p$ ) refers to the depth where the intensity of the wave decreases to  $e^{-1}$  of its surface value.<sup>121</sup> It is estimated by the reciprocal of absorption coefficient of a material ( $\mu_a$ ). Based on the absorption coefficient of titanium at wavelength of 1,070 nm, the penetration depth of laser light in a pure titanium is approximately 21 nm.<sup>122</sup>

Typically, different heat flux models are applied for AM processes due to the dynamic interaction between laser, material and substrate during material deposition. Gaussian heat flux and Goldak's double ellipsoidal heat flux are commonly used in FEAs of AM processes, as listed in

aforementioned Table 4.

In 2003, Tsirkas et al. applied a Gaussian distribution of heat flux with conical keyhole for a butt-joint laser welding.<sup>84</sup> They assumed an energy efficiency of 70 %. Instead of energy efficiency, Robert et al. modeled a transverse electromagnetic (TEM) laser energy with TEM<sub>00</sub> mode as a surface heat flux in an additive layer manufacturing process by considering the laser absorptivity of material.<sup>123</sup> They applied absorptivity of laser in a pure titanium block as 0.77. However, Frenk et al. experimentally found that the cladding process with slower scanning speed of laser has a higher absorptivity at the same powder feedrate.<sup>124</sup> Hence, calibration of heat source model is required.

In 2007, Bate et al. calibrated their Goldak double ellipsoidal heat source model based on the dimension of fusion zone of the specimen and temperature measurements.<sup>87</sup> In 2011, Anca et al and Lundbäck et al. calibrated their Goldak double ellipsoidal heat input model by comparing temperature measured at selected locations.<sup>89,90</sup>

The previous calibration methods applied an assumed efficiency during their calibration of heat flux model. The calibration was limited to a single case of process parameter. Therefore, new calibration method is required to properly estimate penetration depth and efficiency of applied heat source model in this study. The work presented in this Chapter was published by the author in 2018.<sup>99</sup> Chua et al. estimated the proper penetration depth and efficiency of applied heat source for different process parameters using the dimension of heat affected zone (HAZ) of a bead.

## B. Numerical Analysis of Single Bead Deposition

### 1. Physical Description

The experiment of single bead deposition has been described in Chapter II Section B-1. In the finite element modeling, the following assumptions are made:

- (1) The room temperature is at 20 °C.
- (2) The initial temperature of workpiece is at room temperature.
- (3) The translation and rotation for four corners of the substrate are constrained in all directions.

### 2. Formulation of Heat Flux Model and Heat Losses

In order to model the volumetric heat flux, the total power input should be received by the specimen as the integral of heat flux applied over volume of a specimen, as described in Eq. (20)

$$P = \int_V Q \, dV \quad (20)$$

where P is the power of heat source (unit: W), Q is the heat flux (unit: W/mm<sup>3</sup>), and V is the volume of specimen (unit: mm<sup>3</sup>).

For a top-hat distribution profile, the heat flux is defined as a constant within a range of effective radius ( $r_0$ ), as given in Eq. (21)

$$Q(r) = \begin{cases} Q_0, & r \leq r_0 \\ 0, & r > r_0 \end{cases} \quad (21)$$

where  $Q_0$  is the maximum heat flux at the center of beam.

The effective heat application region is approximated to be a conical shape, as shown in Fig. 26, which is commonly used for penetrating heat source. The effective radius of beam ( $r_0$ ) is assumed to decrease linearly with respect to depth, as expressed in Eq. (22)<sup>125</sup>

$$r_0(Z) = r_e + \left( \frac{r_i - r_e}{z_i - z_e} \right) (Z - z_e) \quad (22)$$

where  $Z$  is the  $z$ -coordinate relative to the frame of beam,  $z_e$  is the  $z$ -coordinate at surface of bead,  $z_i$  is the  $z$ -coordinate at penetration depth of beam,  $r_e$  is the effective radius of beam at  $z_e$ , and  $r_i$  is the effective radius of beam at  $z_i$ .

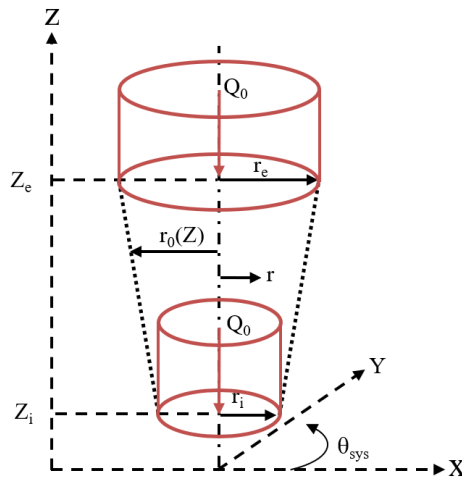


**Fig. 26 Top-hat heat flux with conical penetration**

Hence, the Eq. (20) is rewritten as in Eq. (23)

$$P = \int_{z_i}^{z_e} \int_0^{r_0(Z)} \int_0^{2\pi} Q(r) d\theta_{\text{sys}} \cdot r dr \cdot dZ \quad (23)$$

where  $\theta_{\text{sys}}$  is the azimuthal angle of a cylindrical coordinate system.

The solution for Eq. (23) is obtained, as given in Eq. (24).

$$P = \frac{\pi Q_0(z_e - z_i)}{3} (r_i^2 + r_e r_i + r_e^2) \quad (24)$$

The penetration depth of beam is defined in Eq. (25).

$$d_p = z_e - z_i \quad (25)$$

By substituting Eqs. (24) and (25) into Eq. (21), the top-hat heat flux model is described by Eq. (26).<sup>79</sup>

$$Q(r, Z) = \frac{3P}{\pi d_p (r_i^2 + r_e r_i + r_e^2)} \quad (26)$$

The radial distance from the center of beam ( $r$ ) can be associated with Cartesian coordinates, as in Eq. (27)

$$r = (X^2 + Y^2)^{0.5} \quad (27)$$

where  $X$ , and  $Y$ , are the  $x$ -coordinate relative to the frame of beam and the  $y$ -coordinate relative to the frame of beam, respectively.

The actual heat being absorbed by the material is less than the actual power of heat source due to reflection of wavelength and evaporation of material. These unpredictable losses are taken into consideration by the efficiency of heat source ( $\eta$ ) in Eq. (28).

$$Q(r, Z) = \frac{3\eta P}{\pi d_p (r_i^2 + r_e r_i + r_e^2)} \quad (28)$$



Hence, top-hat heat flux model in Cartesian coordinate system, with consideration of the boundary of heat application region, is given in Eq. (29).

$$Q(X,Y,Z)=\begin{cases} \frac{3\eta P}{\pi d_p(r_i^2+r_e r_i+r_e^2)} & , \quad r \leq r_0 \text{ or } z_i \leq Z \leq z_e \\ 0 & , \quad r > r_0 \text{ or } z_i > Z \text{ or } Z > z_e \end{cases} \quad (29)$$

Unlike Gaussian heat flux model in Eq. (19), the definition of boundary of heat application region is critical for top-hat heat flux because the top-hat heat flux model does not contain the  $r$  and  $Z$  terms.

The integral of volumetric heat flux with respect to volume is inputted as the heat generation term in a three-dimensional governing equation, given in Eq. (30), to solve for transient heat conduction analysis in a solid body

$$\dot{Q}(X,Y,Z,t)=\rho(T) \cdot C_p(T) \left( \frac{\partial T}{\partial t} \right) - \left\{ \frac{\partial}{\partial X} \left( k(T) \frac{\partial T}{\partial X} \right) + \frac{\partial}{\partial Y} \left( k(T) \frac{\partial T}{\partial Y} \right) + \frac{\partial}{\partial Z} \left( k(T) \frac{\partial T}{\partial Z} \right) \right\} \quad (30)$$

where  $\dot{Q}(X,Y,Z,t)$  is the heat generation,  $T$  is the temperature,  $\rho(T)$  is the temperature dependent density,  $C_p(T)$  is the temperature dependent specific heat,  $k(T)$  is the temperature dependent thermal conductivity, and  $t$  is time.

Heat transfer boundary conditions such as convection and radiation contribute to heat loss from surface. These heat losses are accounted as the integral of surface heat flux with respect to surface area and deducted from the heat generation term in Eq. (30).

The heat loss due to convection ( $q''_{\text{conv}}$ ) is described as a surface heat flux in Eq. (31) based on Newton's law of cooling<sup>126</sup>

$$q''_{\text{conv}} = h_{\text{conv}}(T_s - T_\infty) \quad (31)$$

where  $h_{\text{conv}}$  is the coefficient of convection,  $T_s$  is the surface temperature, and  $T_\infty$  is the ambient temperature.

The heat loss due to radiation ( $q''_{\text{rad}}$ ) is estimated as surface heat flux based on Stefan-Boltzmann law, as given in Eq. (32)<sup>126</sup>

$$q''_{\text{rad}} = \varepsilon\sigma_s(T_s^4 - T_\infty^4) \quad (32)$$

where  $\varepsilon$ , and  $\sigma_s$ , are the emissivity of a material and the Stefan-Boltzmann constant, respectively. The Stefan-Boltzmann constant is  $5.670 \times 10^{-8} \text{ W/m}^2 \cdot \text{K}^4$ .<sup>126</sup>

Eq. (32) can be rewritten in the form of Newton's law of cooling, as given in Eq. (33)

$$q''_{\text{rad}} = h_{\text{rad}}(T_s - T_\infty) \quad (33)$$

where  $h_{\text{rad}}$ , is the coefficient of radiation, as given in Eq. (34)

$$h_{\text{rad}} = \varepsilon\sigma_s(T_s^2 + T_\infty^2)(T_s + T_\infty) \quad (34)$$

The heat losses due to convection and radiation ( $q''_{\text{loss}}$ ) can be grouped into a single first order equation, as described in Eq. (35), which can be solved more efficiently in FEA.

$$q''_{\text{loss}} = (h_{\text{conv}} + h_{\text{rad}})(T_s - T_\infty) \quad (35)$$

### 3. Material Properties and Boundary Conditions

In order to simulate a DED process that involves high temperature, temperature dependent material properties are required in the numerical analysis for better accuracy. In this thesis, the selected material for the substrate and deposited bead is an alpha-beta titanium alloy Ti-6Al-4V.

Fig. 27 shows the thermal conductivity ( $k$ ), specific heat ( $C_p$ ) and density ( $\rho$ ) of solid Ti-6Al-4V for thermal analysis.<sup>127</sup> The melting temperature ( $T_m$ ) of Ti-6Al-4V is in the range of 1,600 °C to 1,650 °C.<sup>128</sup> The beta transus temperature ( $T_\beta$ ) of Ti-6Al-4V is estimated at 995 °C.<sup>50,102</sup>

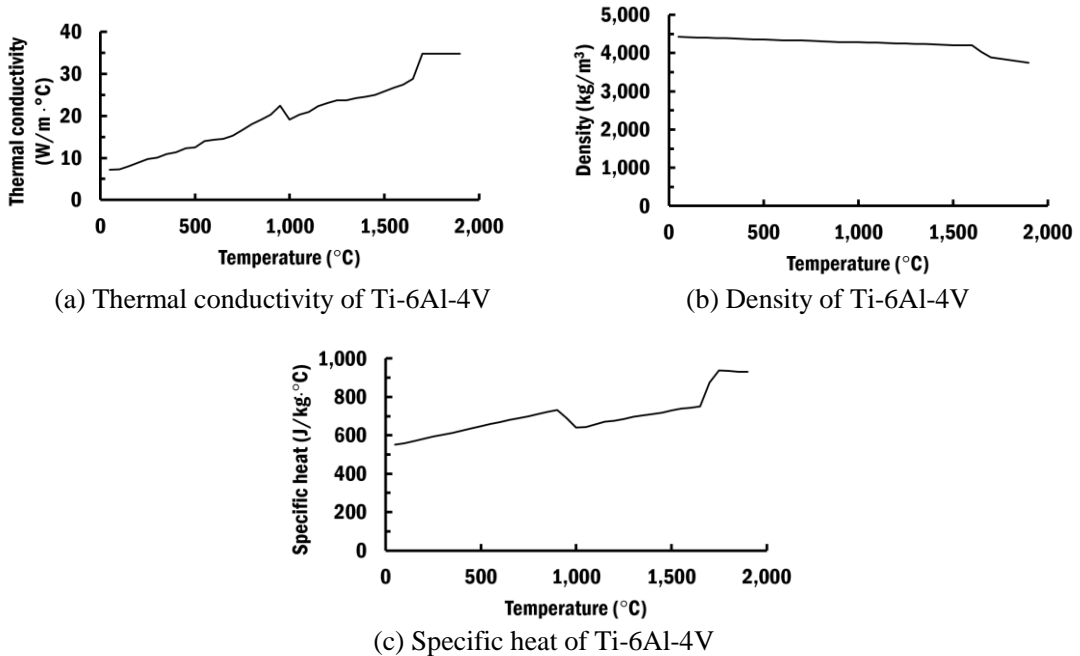


**Fig. 27 Thermal properties of Ti-6Al-4V**

In this study, the convective cooling by all exposed surfaces of the deposited bead and substrate to the surrounding is considered with a coefficient of convection ( $h_{conv}$ ) of 25 W/m<sup>2</sup>·K.<sup>125</sup> Emissivity ( $\epsilon$ ) for solid Ti-6Al-4V is assumed at 0.8.<sup>129</sup> A Poisson's ratio ( $\nu$ ) is assigned for Ti-6Al-4V as 0.342.<sup>130</sup> These boundary conditions are applied in the FEAs of single bead deposition to calibrate the penetration depth and efficiency of heat source.

## C. Calibration of Penetration Depth and Efficiency of Heat Flux

### 1. Calibration Methodology

Fig. 28 shows the calibration methodology of penetration depth and methodology according to process parameters such as power of laser and travel speed of table. The experiments of single bead deposition are conducted for different power of laser and travel speed of table in order to determine the bead section profile, as described earlier in Chapter II Section B.

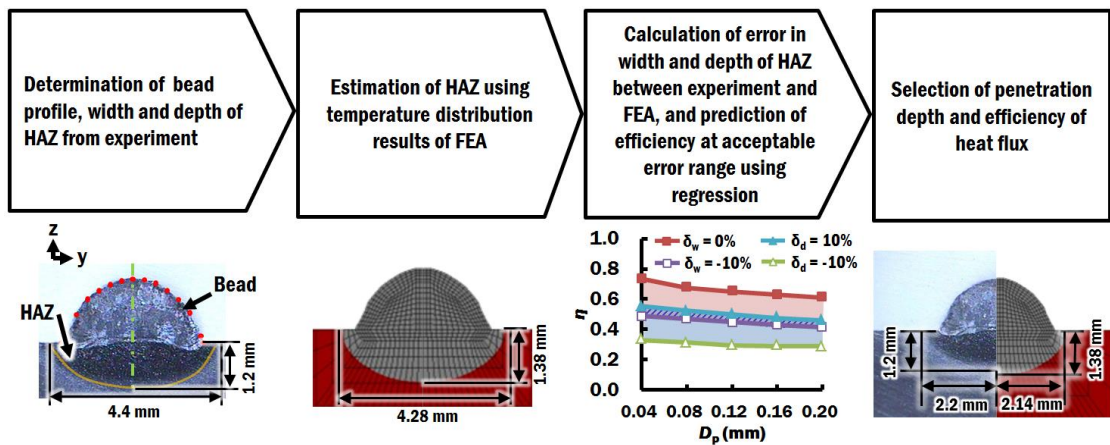


Fig. 28 Procedure to calibrate penetration depth and efficiency of heat flux<sup>99</sup>

From the experimental results, the width and depth of heat affected zone (HAZ) according to power of laser and travel speed of table is obtained. Finite element models according to the process parameters are created based on the actual bead section profile. Thermal FEAs are performed using various penetration depth and efficiency of heat flux. From the temperature distributions of the FEAs, the width and depth of HAZ is estimated from the section of bead where it is undergoing a quasi steady-state heat transfer during the DED deposition.<sup>29</sup>

The width and depth of the estimated HAZ and measured HAZ are compared. The width

error ( $\delta_w$ ) and the depth error ( $\delta_d$ ) of HAZ are determined by Eqs. (36) and (37), respectively.

$$\delta_w = \frac{(w_{HAZ,e} - w_{HAZ,a})}{w_{HAZ,a}} \times 100\% \quad (36)$$

$$\delta_d = \frac{(d_{HAZ,e} - d_{HAZ,a})}{d_{HAZ,a}} \times 100\% \quad (37)$$

where  $w_{HAZ,e}$  is the estimated width of HAZ,  $w_{HAZ,a}$  is the actual width of HAZ,  $d_{HAZ,e}$  is the estimated depth of HAZ, and  $d_{HAZ,a}$  is the actual depth of HAZ.

The acceptable range of width errors of HAZ is set at -10% to 0% such that the estimated width of HAZ is smaller than the actual width of HAZ, because the estimated dimension is an ideal case. The depth of HAZ is smaller than width of HAZ, thus may result in higher error in depth of HAZ. The acceptable range of depth errors of HAZ is set at -10% to 10% to avoid over-constraint conditions. Using linear regression analysis, the efficiencies for different penetration depths of heat flux are predicted at errors  $\delta_w = -10\%$ ,  $\delta_w = 0\%$ ,  $\delta_d = -10\%$ , and  $\delta_d = 10\%$ . A penetration depth of heat flux that has low errors within the acceptable ranges for all process parameters is selected. Using the selected penetration depth of heat flux, the efficiency of each process parameters is selected. Hence, this methodology indirectly calibrates the penetration depth and efficiency of heat flux model for different process parameters.

## 2. Finite Element Analysis

A symmetrical three-dimensional FE model is created to estimate the dimension of HAZ according to different penetration depth and efficiency of heat flux. The FE model contains a 25 mm straight bead on a 180 mm × 100 mm × 5 mm substrate, as shown in Fig. 29. Temperature dependent thermal properties of Ti-6Al-4V are assigned to the bead and substrate. The thermal

FEAs are carried out using commercial FE software SYSWELD 12.0.

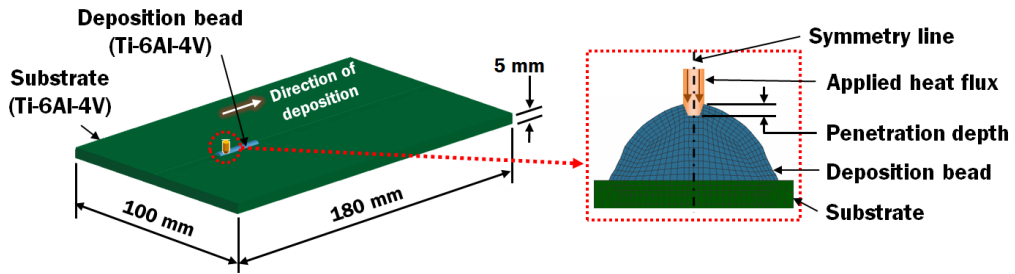


Fig. 29 FE model to estimate the dimension of HAZ according to different penetration depth and efficiency of heat flux<sup>99</sup>

The top-hat heat flux model is applied at the top of the bead. The applied parameter for the heat source model is listed in Table 13. The effective radius of heat flux at surface of bead ( $r_c$ ) is assumed to be equal to the radius of beam ( $r_b$ ). The effective radius of heat flux at penetration depth ( $r_i$ ) is assumed to be half of the effective radius of heat flux at surface due to decrease in heat input at penetration depth.<sup>125,131</sup>

Table 13 Parameters of heat flux to estimate penetration depth and efficiency of laser

Parameters	Effective radius of beam at surface $z_c$ ( $r_c$ , mm)	Effective radius of beam at surface $z_i$ ( $r_i$ , mm)	Penetration depth ( $d_p$ , mm)	Efficiency of laser ( $\eta$ )
Range	0.75	0.375	0.04, 0.08, 0.12, 0.16, 0.20	0.40 – 0.70

### 3. Results and Discussion

Fig. 30 shows the measured dimensions of HAZ according to different power of laser and travel speed of table. The HAZ of Ti-6Al-4V is associated with the change in microstructure from an alpha-beta phase to a body-centered cubic structured beta phase due to peak temperature.<sup>50</sup> Therefore, the HAZ is estimated by the region that is heated above the beta transus temperature ( $T_\beta$ )

of 995 °C during the simulation of a deposition process.<sup>50,102</sup>

From Fig. 30, it is revealed that the DED process produces a shallow peripheral penetration type of fusion zone (FZ). This can be attributed to the usage of cold wire, which is not preheated when being fed to the heat source. Due to the waviness of the fusion zone, the heat transfer to the side of substrate is more accurate and consistent than to the depth of substrate.

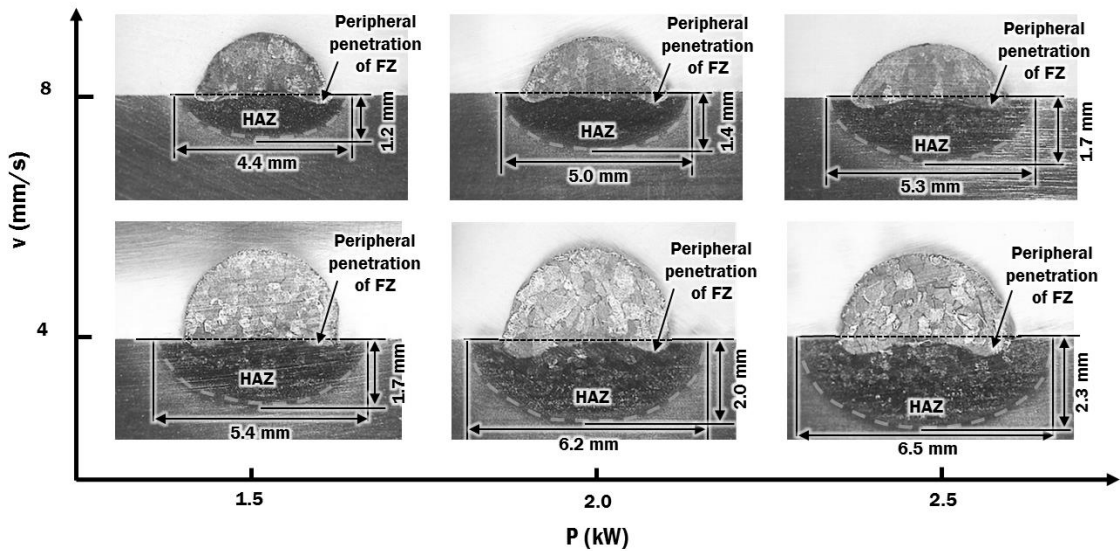
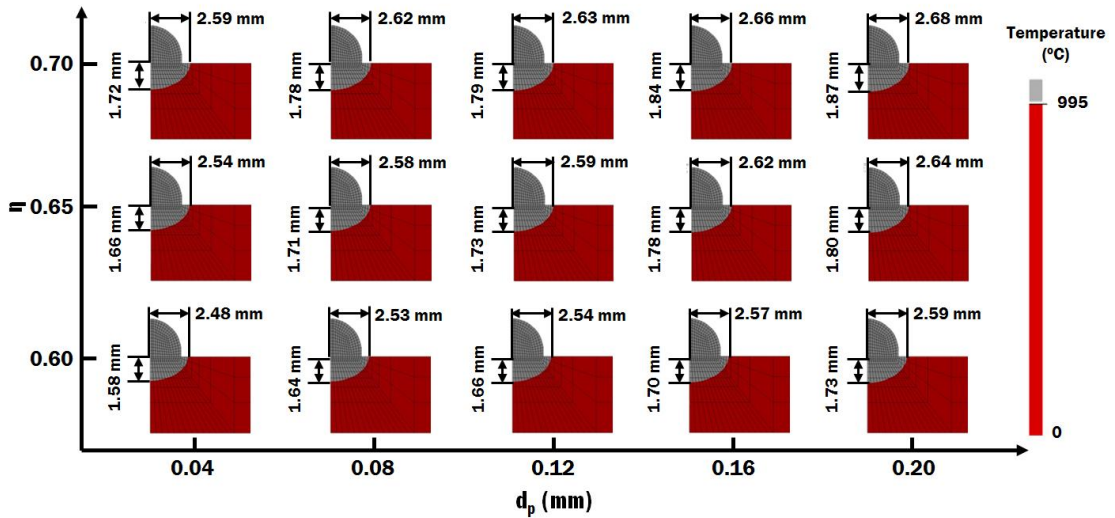
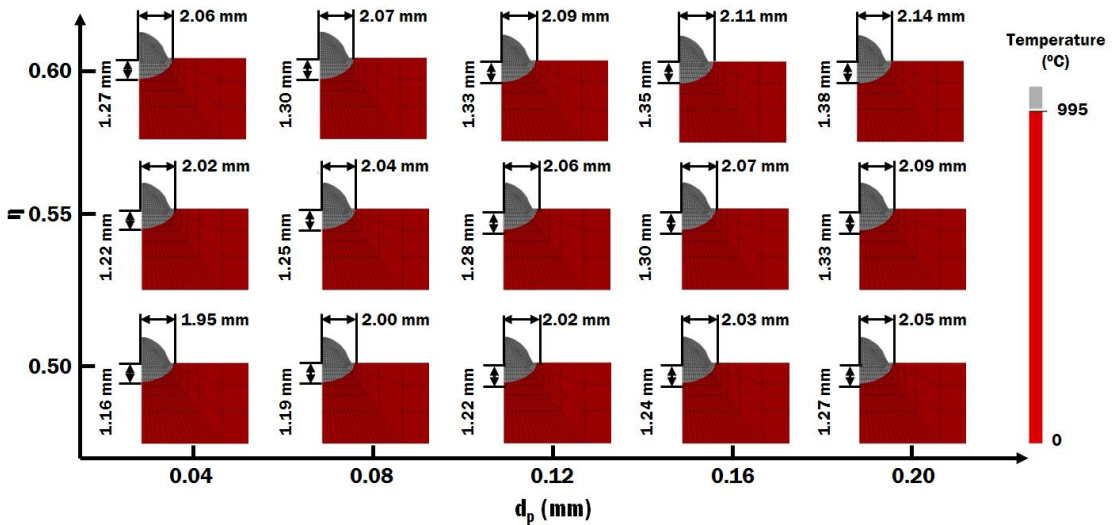


**Fig. 30** Sectional view of deposited bead and heat affected zone<sup>99</sup>

From the thermal FEAs, the width and depth of HAZ for different penetration depth and efficiency of heat flux has been estimated, as shown in Fig. 31. It is revealed that the width and depth of HAZ grow with the increase of penetration depth for the same process condition due to higher heat input near the substrate. The increase of efficiency also produces a larger HAZ due to increase of overall heat input. Thus, proper calibration of penetration depth and efficiency of heat flux is critical for the estimation of HAZ using FEAs.

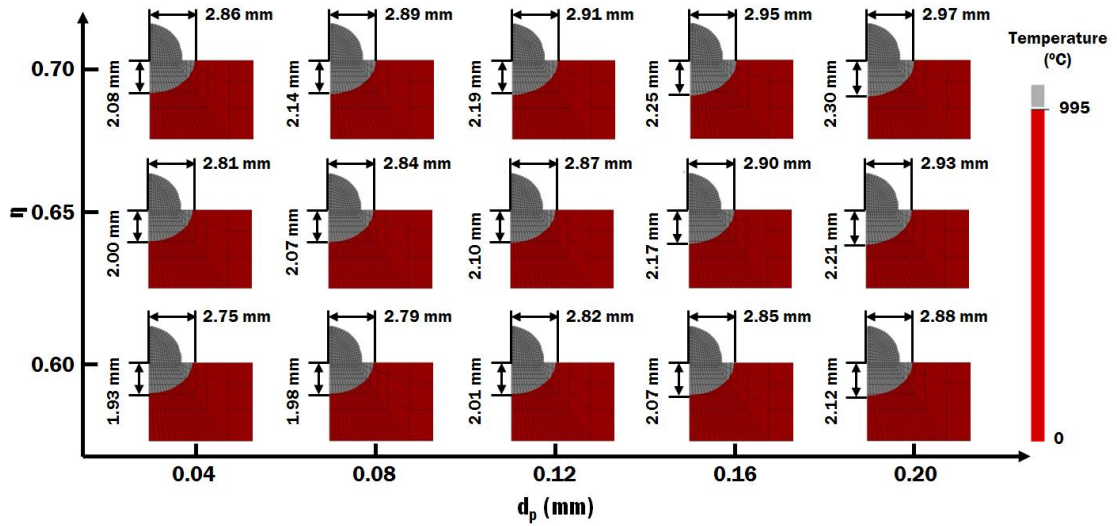


(a)  $P = 1.5 \text{ kW}$ ,  $V = 4.0 \text{ mm/s}$

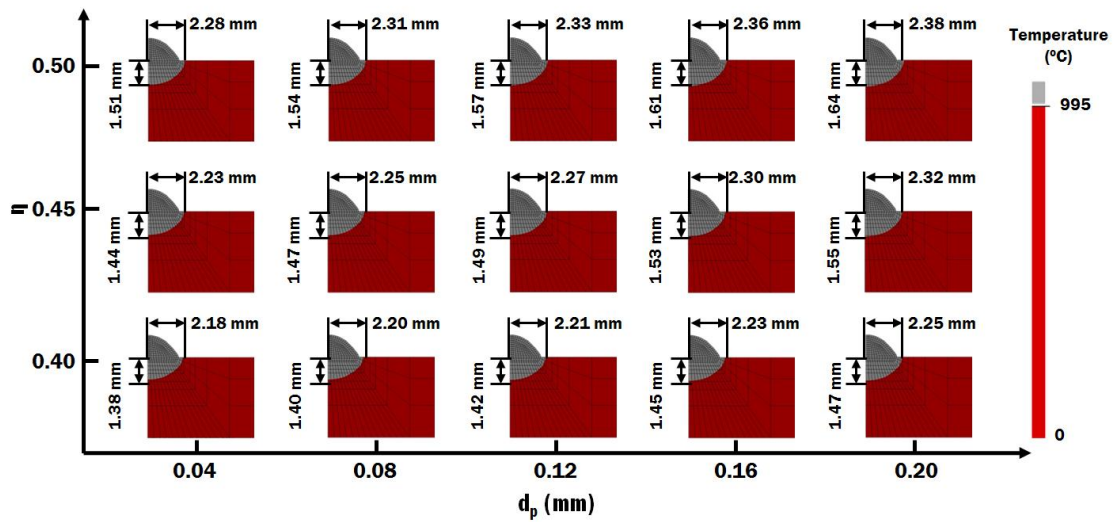


(b)  $P = 1.5 \text{ kW}$ ,  $V = 8.0 \text{ mm/s}$

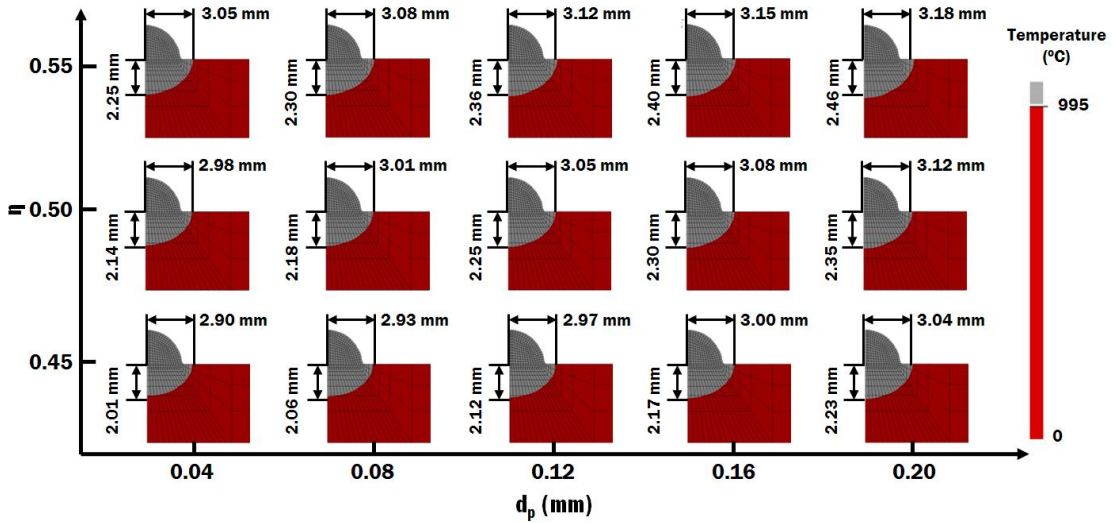




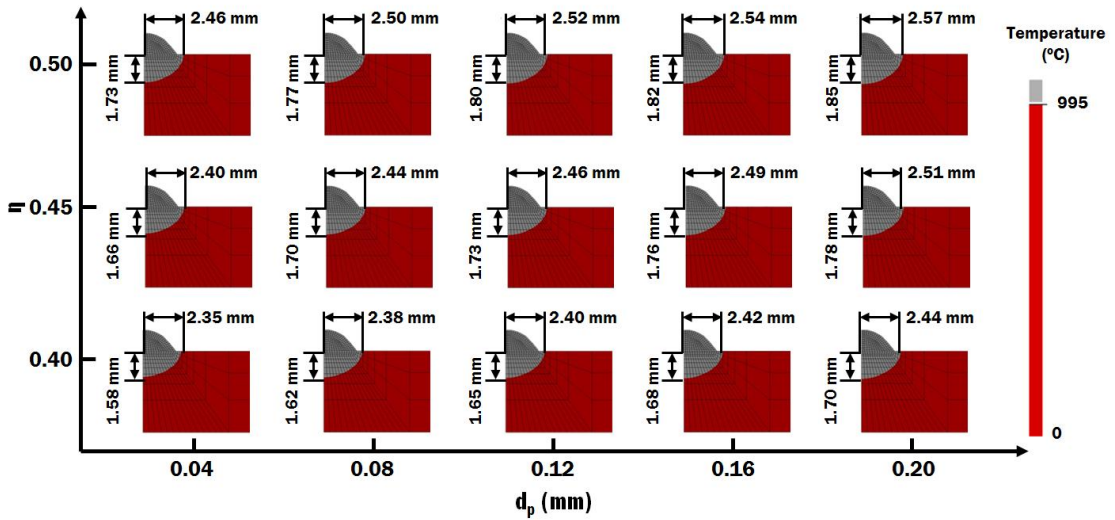
(c)  $P = 2.0$  kW,  $V = 4.0$  mm/s



(d)  $P = 2.0$  kW,  $V = 8.0$  mm/s



(e)  $P = 2.5$  kW,  $V = 4.0$  mm/s

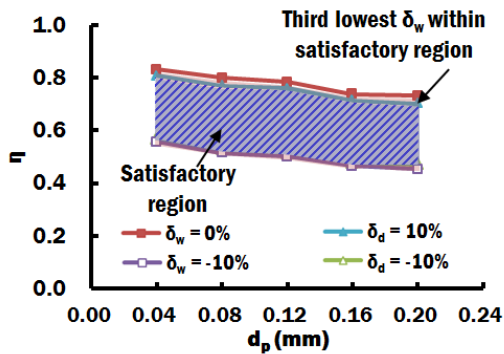


(f)  $P = 2.5$  kW,  $V = 8.0$  mm/s

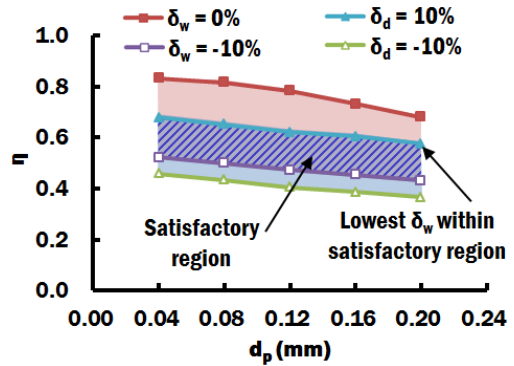
**Fig. 31 Estimated heat affect zone using different penetration depth and efficiency of heat flux<sup>99</sup>**

The width errors and depth errors of HAZ are calculated. The calculated results are used to estimate the efficiency of heat flux at errors  $\delta_w = -10\%$ ,  $\delta_w = 0\%$ ,  $\delta_d = -10\%$ , and  $\delta_d = 10\%$  for a

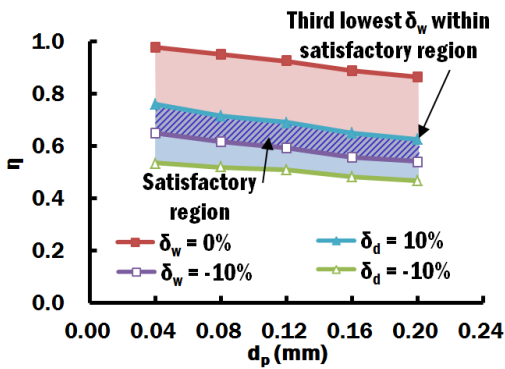
penetration depth of heat flux via linear regression, as shown in Fig. 32. The hatched region represents the region that fall within the targeted acceptable ranges of width error and depth error of HAZ.



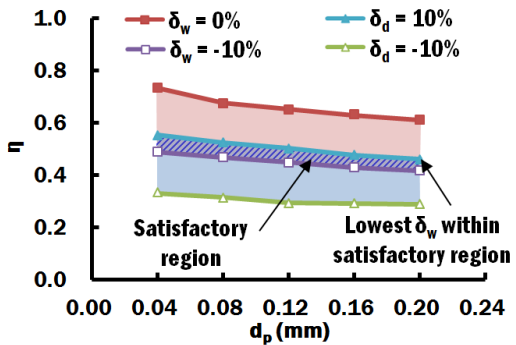
(a) P = 1.5 kW, V = 4.0 mm/s



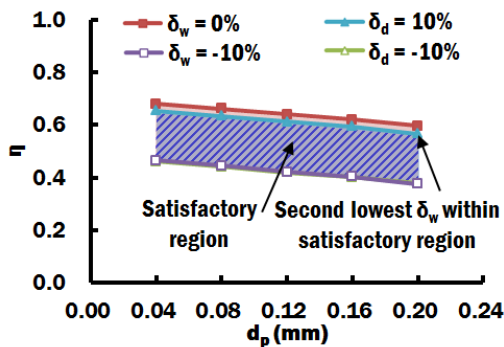
(b) P = 1.5 kW, V = 8.0 mm/s



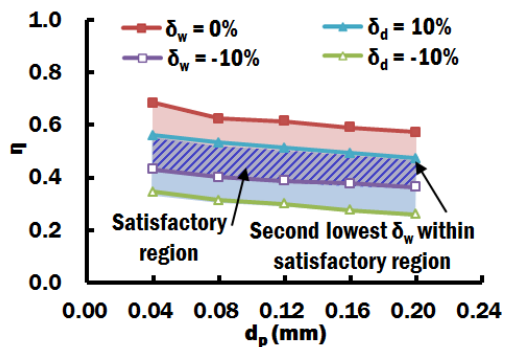
(c) P = 2.0 kW, V = 4.0 mm/s



(d) P = 2.0 kW, V = 8.0 mm/s



(e) P = 2.5 kW, V = 4.0 mm/s



(f) P = 2.5 kW, V = 8.0 mm/s

Fig. 32 Estimated efficiency at limit of acceptable ranges of width errors and depth errors of HAZ for different efficiency of heat flux<sup>99</sup>

A low width error of HAZ is desired in this study because the width of HAZ is easier to predict accurately than the depth of HAZ for a DED process using a cold wire. In Fig. 32, the width error of HAZ is the lowest, and within the satisfactory region, when the point  $\delta_d = 10\%$  is nearer to the point  $\delta_w = 0\%$ .

In this study, only one penetration depth is selected for all the process conditions because a laser beam penetrating the same material possesses the same penetration depth. The penetration depth of heat flux at 0.2 mm gives the best minimal width error of HAZ, and within the satisfactory region in most of the process conditions. Therefore, the penetration depth of heat flux at 0.2 mm is selected.

Subsequently, the efficiencies of heat flux that are used in the FEA at the selected penetration depth of heat flux at 0.2 mm are selected in order to obtain an accurate estimation of error for each process condition. The efficiency of heat flux that has the lowest width error of HAZ and falls within the satisfactory region is selected. The selected penetration depth and efficiency of heat flux with their calculated errors for each process condition is tabulated in Table 14. Using the selected penetration depth and efficiency of laser for different process conditions, the heat flux model is now properly calibrated according to the dimension of HAZ, as shown in Fig. 33.

**Table 14 Calibrated penetration depth and efficiency of laser<sup>99</sup>**

Power of laser (P, kW)	Travel speed of table (V, mm/s)	Penetration depth ( $d_p$ , mm)	Efficiency of laser ( $\eta$ )	Width error of HAZ ( $\delta_w$ , %)	Depth error of HAZ ( $\delta_d$ , %)
1.5	4	0.20	0.70	-1.11	10.00
2.0	4	0.20	0.65	-6.09	7.80
2.5	4	0.20	0.55	-2.15	6.96
1.5	8	0.20	0.60	-3.60	12.20
2.0	8	0.20	0.45	-7.94	8.39
2.5	8	0.20	0.40	-7.92	3.03

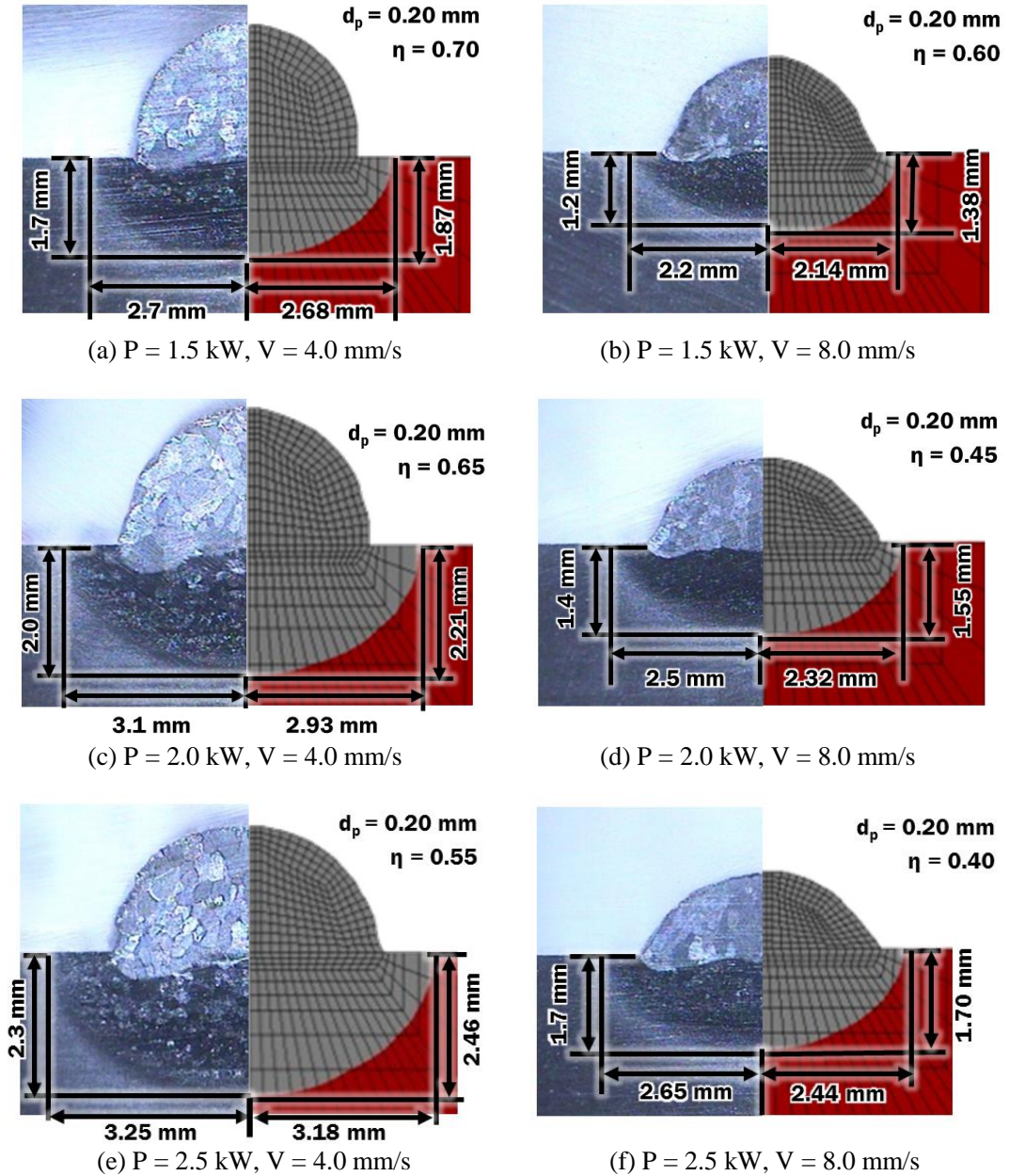


**Fig. 33 Comparison of dimensions of HAZ between experiments and FEAs**

From the selected efficiency of heat flux for different power of laser shown in Table 14, it is noted that the efficiency of laser reduces when the power of laser increases for the same travel

speed of table. The increase of power of laser produces higher peak temperature on the bead and thus a wider deposited bead. This resulted in a larger amount of heat loss and higher material loss via evaporation. Hence, the efficiency of heat flux is lower when the power of laser is increased.

At the same power of laser, it is revealed that the higher travel speed of table has lower efficiency of laser. This can be attributed to the fact that the higher travel speed of table has a shorter laser-metal interaction time for proper conversion of energy from the laser beam to the useful heat absorbed by the material. At a high travel speed, most of the heat energy is used to heat the cold wire and substrate before fusion of material can occur. This heat energy is considered as heat loss and is not accounted for actual heat transfer of the system simulated in the FEAs, which the bead has fused to the substrate. Subsequently, the efficiency of heat flux is reduced when the higher travel speed of table is applied.

These calibrated penetration depth and efficiency of laser are applied in FEAs using SYSWELD for further investigation of thermo-mechanical characteristics of parts during a wire feeding type DED process.

## **IV. SELECTION OF DESIGN PARAMETERS AND DEPOSITION STRATEGIES FOR A WIRE FEEDING TYPE DIRECTED ENERGY DEPOSITION PROCESS**

### **A. Derivation of Proper Gap Between Deposition Beads**

#### **1. Description of the Analysis**

Finite element analyses are used to estimate the heat transfer characteristics and stress-strain characteristics of part during a DED process. From these results of FEAs, important information such as change in microstructures, size of melt pool, hardness, distortion and residual stress can be predicted.<sup>27,60,87,90,95,132</sup>

In AM processes, multiple parts are usually fabricated on a single substrate in order to save experimental setup time. The microstructure changes in a heat affected zone (HAZ) and formation of residual stress at the vicinity of bead may affect an adjacent part deposited on the same substrate. To the knowledge of the author, this has not been studied by other researchers. In this study, the formation of heat affected zone (HAZ) and the stress influenced region (SIR) are estimated according to power of laser, travel speed of table and length of bead during a deposition of single bead using a wire feeding type DED process. An appropriate gap between deposited beads is proposed according to process condition with the goal to minimize undesired thermal effects and residual stress of a deposited bead on an adjacent bead. The work presented in this Section has already been published by the author in 2018.<sup>29</sup>

The FE models of single bead deposition and calibrated heat flux models in Chapter III are applied for the thermo-mechanical analyses in this study.

## 2. Analysis Conditions

Fig. 34 shows a three-dimensional FE model with a single layer straight bead. The shape of the bead has been obtained and regenerated from experiments according to different power of laser and travel speed of table, as described earlier in Chapter II Section B. Different lengths of bead ( $L_B$ ) are applied in this study with a fixed location of start point, as listed in Table 15.

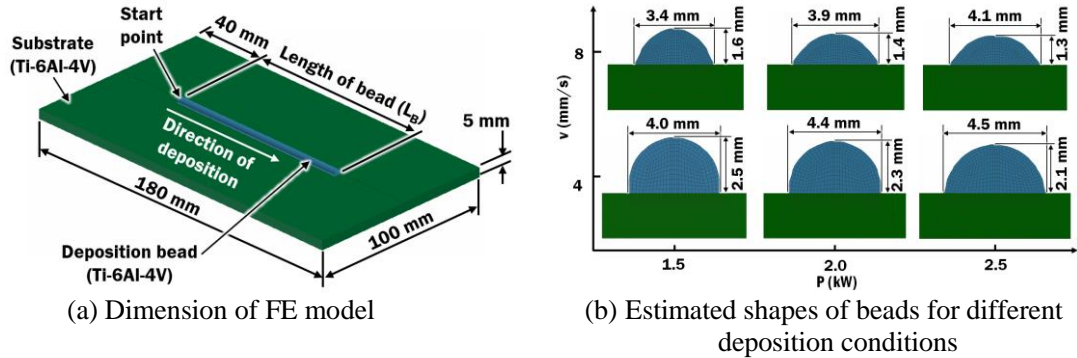


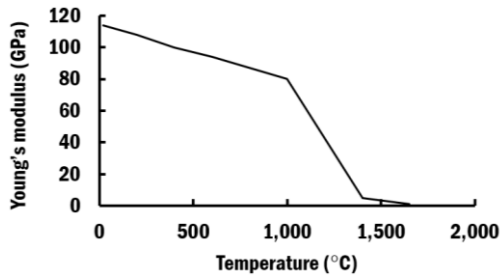
**Fig. 34 FE model to estimate the dimension of HAZ according to different penetration depth and efficiency of heat flux<sup>29</sup>**

**Table 15 Analysis conditions for investigation of proper gap between deposition beads**

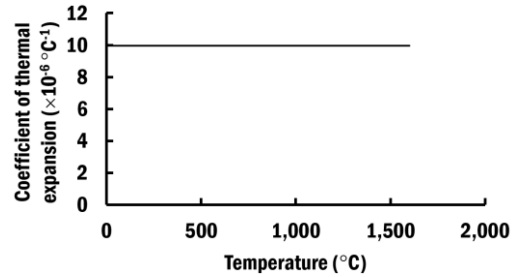
Parameters	Power of laser (P, kW)	Travel speed of table (V, mm/s)	Length of bead ( $L_B$ , mm)
Range	1.5, 2.0, 2.5	4, 8	25, 50, 75, 100

A moving top-hat heat flux model with calibrated penetration depth and efficiency is applied at the top of the bead. Temperature dependent thermal properties of Ti-6Al-4V are applied to the bead and substrate. Temperature dependent Young's modulus (E), yield strength ( $\sigma_y$ ) and plastic strain-stress curve of Ti-6Al-4V are assigned, as shown in Fig. 35.<sup>133,134</sup> A Poisson's ratio ( $\nu$ ) assigned for Ti-6Al-4V is 0.342.<sup>130</sup> The convective cooling by all exposed surfaces of the deposited bead and substrate to the surrounding is considered by using a coefficient of convection ( $h_{conv}$ ) of  $25 \text{ W/m}^2 \cdot \text{K}$ .<sup>125</sup> Emissivity ( $\epsilon$ ) for solid Ti-6Al-4V is assumed at 0.8.<sup>129</sup> A cooling time of the specimen after end of deposition is set as 10 seconds. All nodes at four corners are constrained in translation and rotation. The thermo-mechanical FEAs are carried out using SYSWELD 12.0.

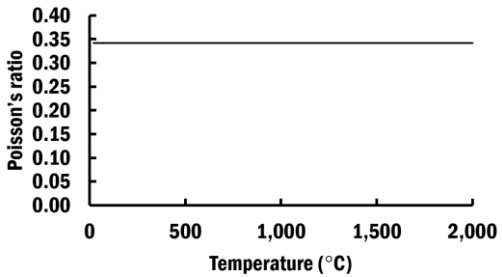




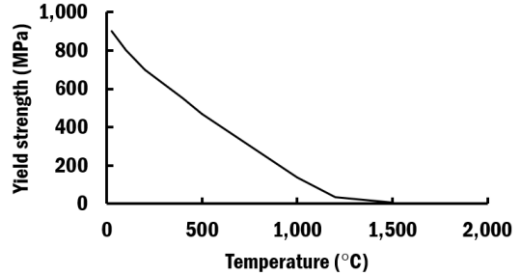
(a) Young's modulus



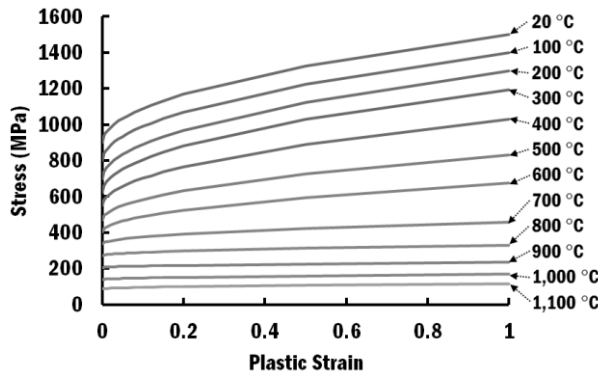
(b) Coefficient of thermal expansion



(c) Poisson's ratio



(d) Yield strength of Ti-6Al-4V



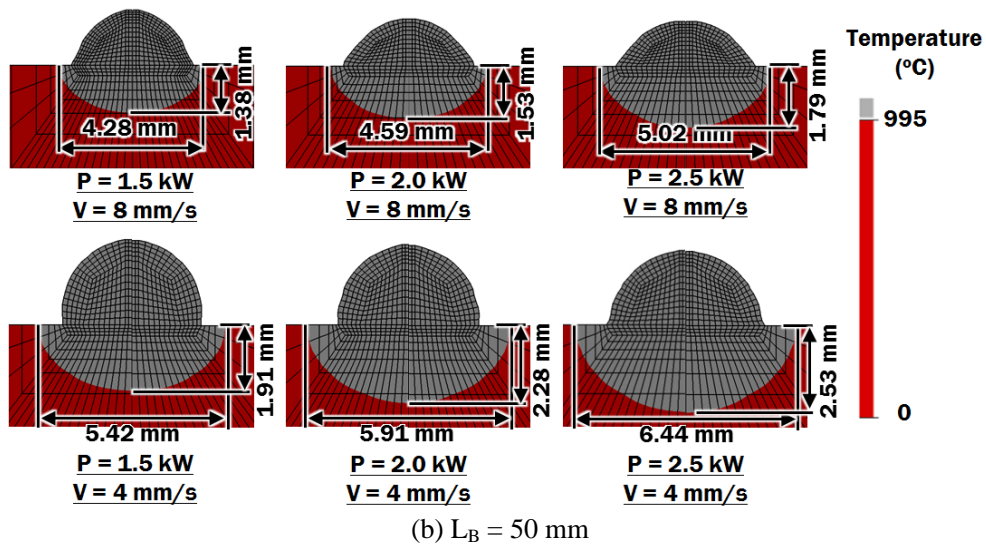
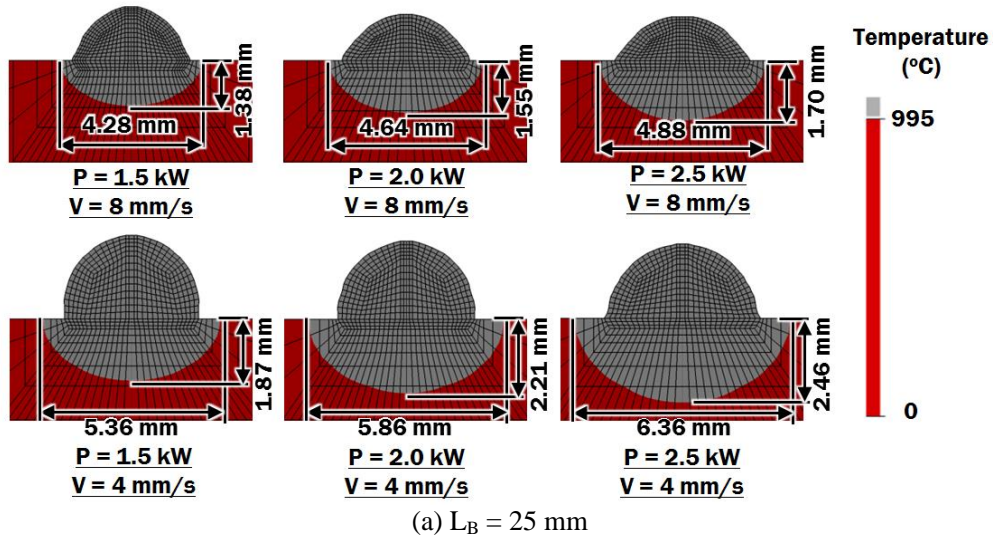
(e) Plastic strain-stress curve of Ti-6Al-4V

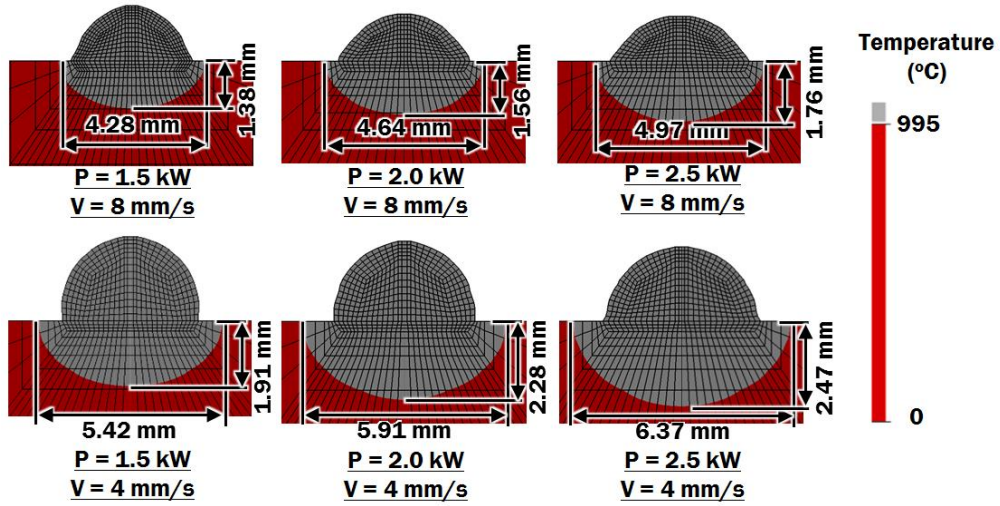
Fig. 35 Mechanical properties of Ti-6Al-4V<sup>133,134</sup>

### 3. Results and Discussion

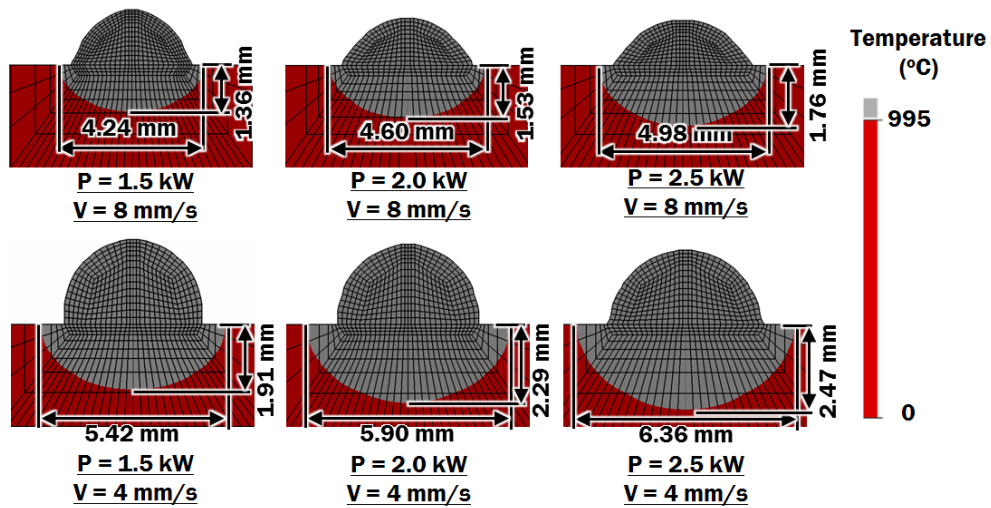
Fig. 36 shows the estimated HAZ for different power of laser, travel speed of table and length of bead. The HAZ is estimated by the region that are heated above the beta transus temperature ( $T_\beta$ ) of 995 °C during the simulation of a deposition process, similar to description of

methodology in Chapter III Section C.<sup>50,102</sup> Fig. 37 shows the influence of the power of laser, the travel speed of table and the length of bead on the formation of HAZ in the vicinity of the deposited bead. From the Fig. 37, it is noted that the dimension of HAZ grows when the power of laser increases. The applied heat flux increases when the power of laser increases. As a result of increased heat flux, the temperature of the bead rises and heat is transferred to a wider region of the specimen. Hence, the increased power of laser forms a wider and deeper HAZ.



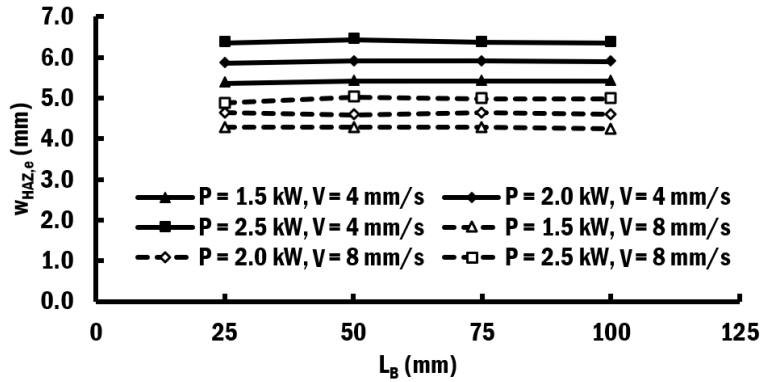


(c)  $L_B = 75$  mm

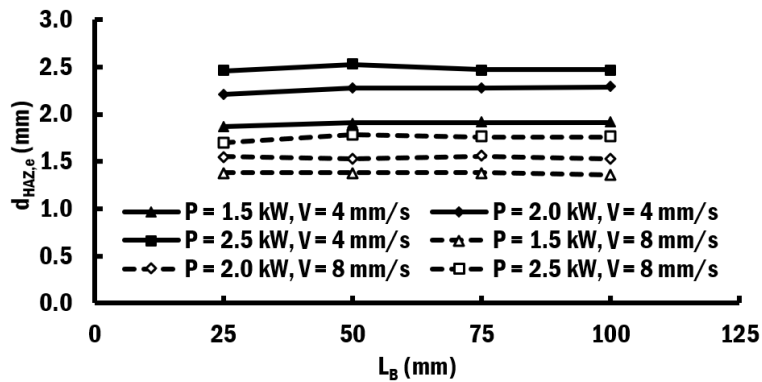


(d)  $L_B = 100$  mm

Fig. 36 Estimated HAZ according to different process parameters<sup>29</sup>



(a) Estimated width of HAZ ( $w_{HAZ,e}$ )



(b) Estimated depth of HAZ ( $d_{HAZ,e}$ )

**Fig. 37 Influence of process parameters and length of bead on the width and depth of HAZ<sup>29</sup>**

However, the dimension of HAZ reduces when the travel speed of table increases. The laser-to-metal interaction time is shortened as the transverse speed of table is increased. Hence, the specific heat energy ( $E_s$ ), defined previously by Eq. (10), transferred to the specimen is reduced as the travel speed of table increases. As a result, the dimension of HAZ reduces as the travel speed of table increases.

From the Fig. 37, it is noted that the width and the depth of HAZ are identical regardless of the length of bead for the same power of laser and travel speed of table. Hence, it is revealed that the length of bead has negligible influence on the formation of HAZ in the quasi-steady state heat transfer region.

In order to quantify the influence of power of laser and travel speed of table on the increment of width and dept of HAZ, four measures are introduced in Eqs (38)-(41)

$$\omega_P = \frac{\Delta w_{HAZ,e}}{\Delta P} \quad (38)$$

$$\omega_V = \frac{\Delta w_{HAZ,e}}{\Delta V} \quad (39)$$

$$\mu_P = \frac{\Delta d_{HAZ,e}}{\Delta P} \quad (40)$$

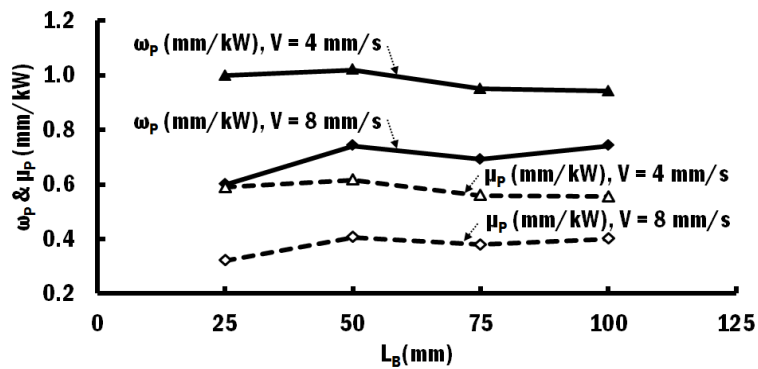
$$\mu_V = \frac{\Delta d_{HAZ,e}}{\Delta V} \quad (41)$$

where  $\omega_P$  is the increment of width of HAZ per unit increment of power of laser,  $\omega_V$  is the increment of width of HAZ per unit increment of travel speed of table,  $\mu_P$  is the increment of depth of HAZ per unit increment of power of laser, and  $\mu_V$  is the increment of depth of HAZ per unit increment of travel speed of table.

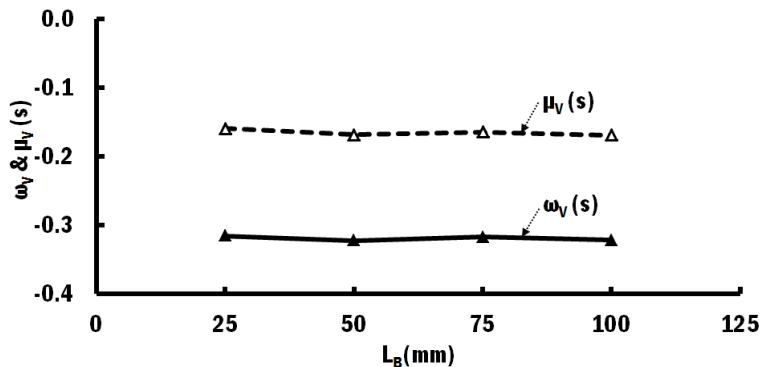
The influence of the power of laser and the travel speed of table on the increment of the width and the depth of HAZ are shown in Fig. 38. As shown in Fig. 38(a), the  $\omega_P$  lies in the ranges of 0.94-1.02 and 0.60-0.74 for the travel speed of table of 4 mm/s and 8 mm/s, respectively. The  $\mu_P$  falls in the ranges of 0.56-0.62 and 0.32-0.41 for the travel speed of table of 4 mm/s and 8 mm/s, respectively. This reveals that the influence of power of laser on the width and depth of HAZ grows when the travel speed of table reduces due to the increase of specific heat energy being transferred to the specimen. The  $\omega_P$  is greater than the  $\mu_P$  by the factor of 1.66-1.70 and 1.82-1.88 for the travel speed of table of 4 mm/s and 8 mm/s, respectively. This indicates that the HAZ is growing faster in the direction of width than in the direction of depth due to the increment of width of bead when the power of laser increases. Besides, greater heat is transferred to the peripheral of the bead because it has larger surface area for heat dissipation.

Fig. 38(b) shows that the  $\omega_v$  falls in the range of -0.32 to -0.31, and the  $\mu_v$  lies in the range of -0.17 to -0.16. From this result, it is revealed the HAZ is shrinking faster in the direction of width than in the direction of depth when the travel speed of table increases. This is attributed to the decrease of width of bead when the travel speed of table increases and a larger surface area for heat dissipation at the peripheral of the bead.

By comparing the magnitude of  $\omega_p$  and  $\omega_v$ , it reveals that the influence of the power of laser on the width of HAZ is 1.9 to 3.2 times larger than the influence of travel speed of table on the width of HAZ. Similarly, it is revealed that the influence of the power of laser on the depth of HAZ is 2.0 to 3.7 times greater than the influence of travel speed of table on the depth of HAZ, by comparing the magnitude of  $\mu_p$  and  $\mu_v$ .



(a) Influence of power of laser and travel speed of table on the increment of width of HAZ



(b) Influence of power of laser and travel speed of table on the increment of depth of HAZ

**Fig. 38 Influence of power of laser and travel speed of table on the increment of width and depth of HAZ<sup>29</sup>**

The stress influenced region (SIR) is defined as the region where the estimated thermal stress is greater than a critical stress of the Ti-6Al-4V. Depending on the type of critical stresses, two SIRs, namely the stress influenced region for yield strength (SIR<sub>y</sub>) and the stress influenced region for fatigue limit (SIR<sub>f</sub>), are estimated. The critical yield stress ( $\sigma_{y,c}$ ) and the critical ultimate stress ( $\sigma_{u,c}$ ) for estimating SIR<sub>y</sub> and SIR<sub>f</sub>, respectively, are defined based on safety factors ( $\lambda_y$  and  $\lambda_f$ ), as given in Eqs. (42)-(43)

$$\sigma_{y,c} = \frac{\sigma_y}{\lambda_y} \quad (42)$$

$$\sigma_{f,c} = \frac{\sigma_u}{\lambda_f} \quad (43)$$

where  $\sigma_y$  is the yield strength,  $\lambda_y$  is the safety factor to estimate critical yield strength,  $\sigma_u$  is the ultimate strength, and  $\lambda_f$  is the safety factor to estimate critical fatigue limit.

In this study, the  $\lambda_y$  is set to be 2.0.<sup>29</sup> The  $\lambda_f$  is set to be 4.0 due to the fatigue limit of Ti-6Al-4V is observed to be greater than 25% of the ultimate tensile strength.<sup>135,136</sup> The SIRs are estimated at the end of the cooling process because the thermal stress after the cooling process is slightly greater than that before the deposition process, as shown in Fig. 39.

From the heat transfer FEA, the maximum temperatures ( $T_{max}$ ) of the deposited beads after cooling process are obtained, as shown in Fig. 40. It is revealed that the highest temperature for each travel speed of table occurs when the power of laser is 2.5 kW and converges when length of bead is greater than 50 mm. Hence, reference temperatures ( $T_{ref}$ ) of 568°C and 401°C are selected for travel speed of table of 4 mm/s and 8 mm/s at power of laser 2.5 kW and length of bead 50 mm, respectively. Using the strength-temperature curves of Ti-6Al-4V in Fig. 41, the critical yield stress and the critical fatigue limit are predicted at the reference temperatures, as given in Table 16.

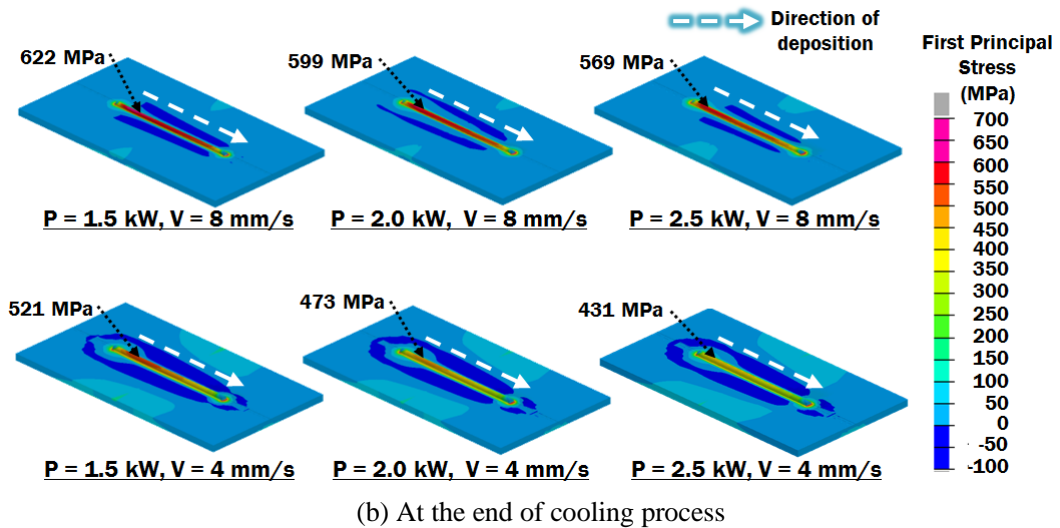
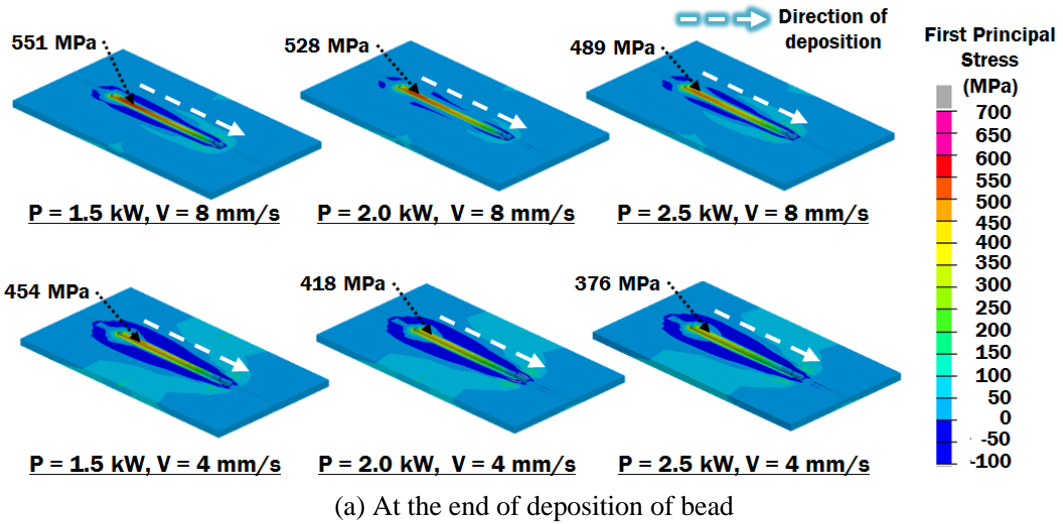


Fig. 39 Comparison of thermal stress distributions at the end of deposition of bead and at the end of cooling process ( $L_B = 100 \text{ mm}$ )<sup>29</sup>



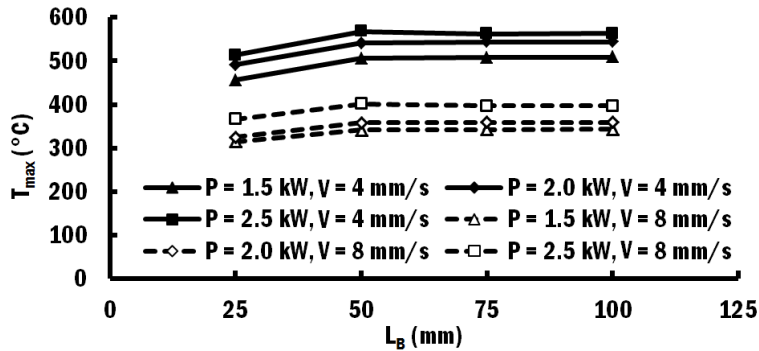


Fig. 40 Maximum temperature of the bead after cooling process<sup>29</sup>

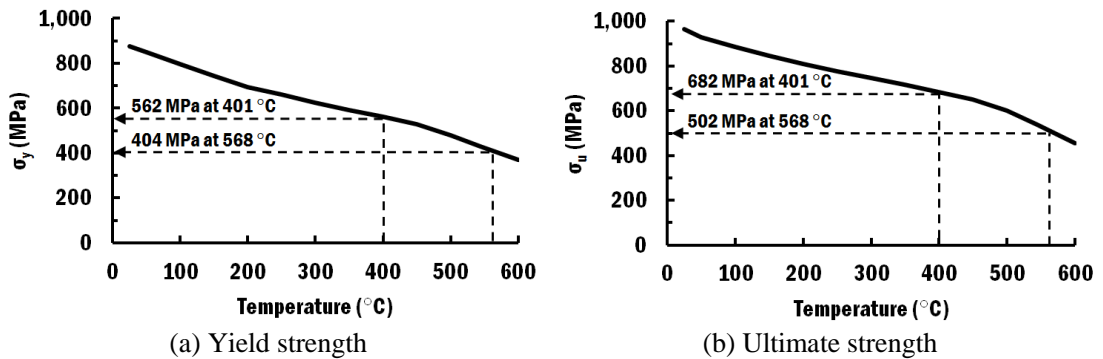


Fig. 41 Temperature dependent yield strength and ultimate strength<sup>134</sup>

Table 16 Estimated critical stresses at reference temperatures<sup>29</sup>

Travel speed of table (V, mm/s)	Reference temperature (T <sub>ref</sub> , °C)	Yield strength (σ <sub>y</sub> , MPa)	Ultimate strength (σ <sub>u</sub> , MPa)	Critical yield stress (σ <sub>v,c</sub> , MPa)	Critical fatigue limit (σ <sub>f,c</sub> , MPa)
4	568	404	502	202	125.5
8	401	562	682	281	170.5

The SIR<sub>y</sub> and SIR<sub>f</sub> are predicted using the estimated critical stresses, as shown in Fig. 42. The regions with gray color are the SIRs, which has its thermal stress greater than the critical stresses. The estimated width of SIR<sub>y</sub> and SIR<sub>f</sub> for different process conditions and length of bead are shown in Fig. 43. The width of SIR<sub>y</sub> and SIR<sub>f</sub> grow when the power of laser increases.

However, the width of  $SIR_y$  and  $SIR_f$  reduces when the travel speed of table increases. This formation characteristic of SIRs is associated with increase of specific heat energy due to the increase in power of laser and the decrease of travel speed of table. The increase of specific heat energy induces higher temperature and thus larger thermal stress in the vicinity of bead. By comparing the width of  $SIR_y$  and  $SIR_f$  in Fig. 43, it is revealed that  $SIR_f$  is larger than  $SIR_y$  for all deposition conditions. Hence, the width of  $SIR_f$  is selected as the width of SIR.

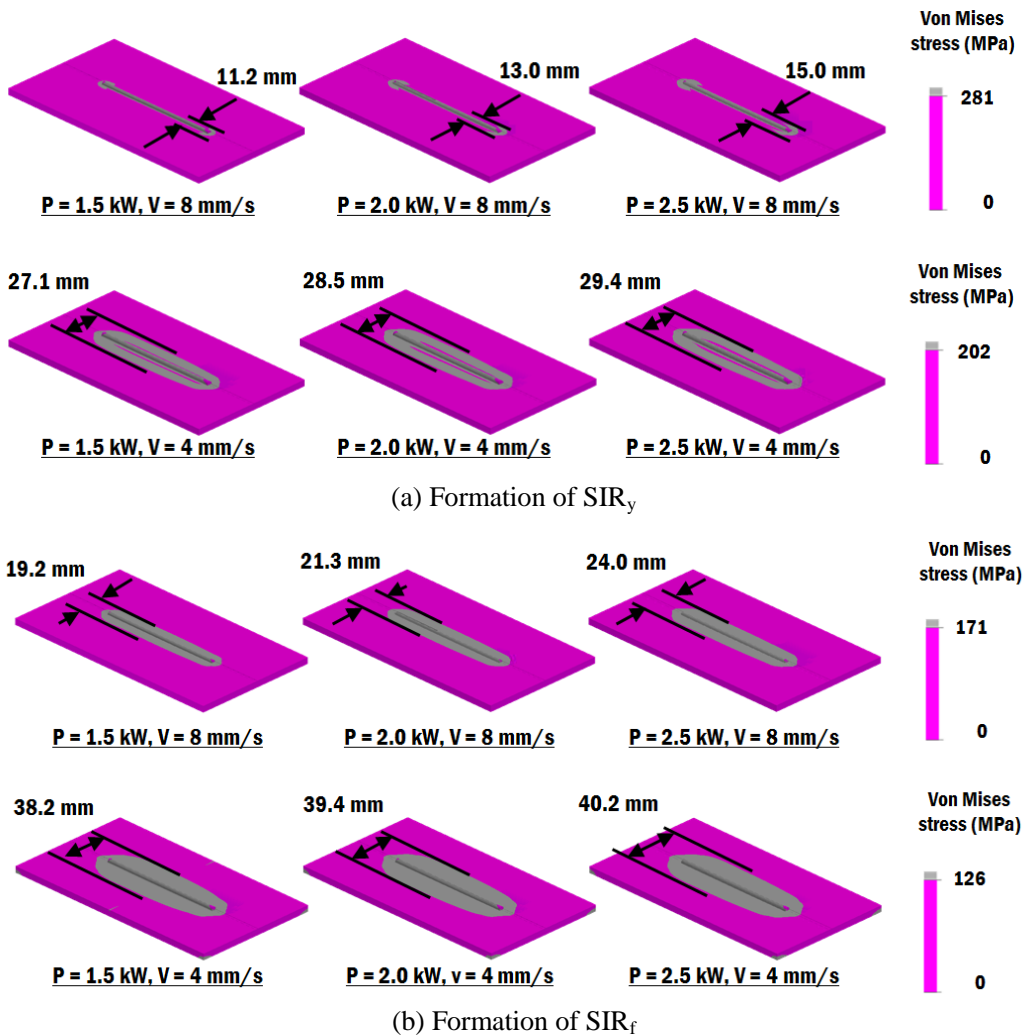


Fig. 42 Formation of  $SIR_y$  and  $SIR_f$  according to power of laser and travel speed of table for  $L_B = 100 \text{ mm}$ <sup>29</sup>

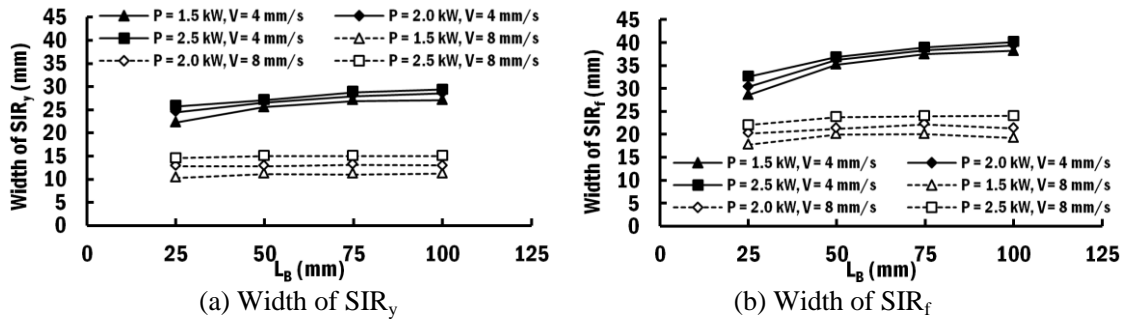


Fig. 43 Width of  $SIR_y$  and  $SIR_f$  according to power of laser, travel speed of table and length of bead<sup>29</sup>

From the Fig. 43(b), it is noted that the width of  $SIR_f$  almost converges for both travel speed of table at 4 mm/s and 8 mm/s when the length of bead is 100 mm. Therefore, the widths of  $SIR_f$  are compared with the width of HAZ when the length of bead is 100 mm, in order to determine the appropriate gap between adjacent beads, as shown in Table 17. The width of  $SIR_f$  is greater than the width of HAZ by a factor of 6.2-7.1 and 4.7-4.8 when the travel speed of table is 4 mm/s and 8 mm/s, respectively. Thus, the width of  $SIR_f$  is used to determine the appropriate gap between adjacent beads for successive deposition. The appropriate gap between adjacent beads for a combination of power of laser and travel speed of table is determined as the shortest distance between adjacent beads such that their  $SIR_f$  regions do not overlap, is shown in Table 17.

Table 17 Appropriate gap between adjacent beads<sup>29</sup>

Power of laser (P, kW)	Travel speed of table (V, mm/s)	Width of $SIR_f$ at $L_B = 100$ mm (mm)	Width of HAZ at $L_B = 100$ mm (mm)	Appropriate gap (mm)
1.5	4	38.2	5.42	38.2
2.0	4	39.4	5.90	39.4
2.5	4	40.2	6.36	40.2
1.5	8	20.0	4.24	20.0
2.0	8	22.1	4.60	22.1
2.5	8	24.0	4.98	24.0

Using the proposed appropriate gap between deposited beads according to power of laser and travel speed of table, the undesired thermal effects and residual stress of a deposited bead are minimized during deposition of adjacent parts on the same substrate.

## **B. Influence of Corner Deposition on Formation of Heat Affected Zone, Stress Influenced Region and Thermal Stress**

### **1. Description of the Analysis**

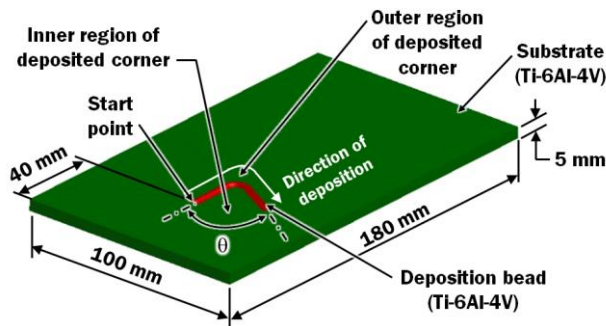
Past investigations of induced residual stress are limited to a straight bead deposition. However, most of the AM parts contain not only straight beads, but angled beads to form a desired shape of structure. The angled bead is defined as the bead deposition where a straight bead change direction at a specific angle to form a corner. In order to investigate the influence of the corner deposition on the formation of HAZ and SIR during a wire feeding type DED process, thermo-mechanical FEAs are carried out according to power of laser and angle of corner deposition ( $\theta$ ) in this study. Travel speed of table at 8 mm/s is applied in this study because it produces a favourable bead profile with proper wetting angle for a wire feeding type DED process, as discussed earlier in Chapter II Section B-3. It is assumed that the bead profile of a single straight bead remains unchanged at the corner deposition in these analyses. The work presented in this Section has already been published by the author in 2018.<sup>88</sup>

The bead section profile of single bead deposition and calibrated heat flux models described in Chapter III are applied for the thermo-mechanical analyses in this study.

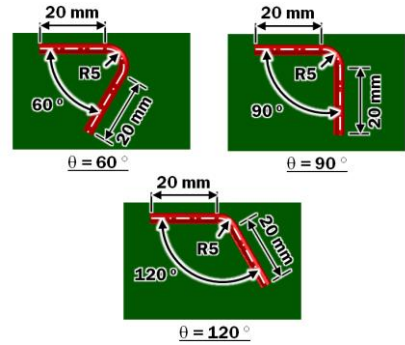
### **2. Analysis Conditions**

Fig. 44 shows a three-dimensional FE model with a corner deposition bead and different angle of corner deposition ( $\theta$ ). The single pass bead starts with a 20 mm straight bead, followed by a corner deposition bead with a radius of 5 mm, and ends with a 20 mm straight bead. The angle of the corner deposition is defined as the angle that encompasses the two straight beads. The 20 mm straight beads are included before and after the corner deposition to eliminate the transient thermal effect at the beginning and the end of a deposition bead. Different shapes of beads are applied

according to power of laser and travel speed of table. The shapes of bead at the straight bead and at the corner deposition are the same. Different angle of corner deposition ( $\theta$ ) are applied in this study with a fixed location for the start point, as listed in Table 18.



(a) Dimension of FE model



(b) Top view of corner deposition bead

**Fig. 44 FE model to investigate the influence of angle of corner deposition on formation of HAZ and SIR<sup>88</sup>**

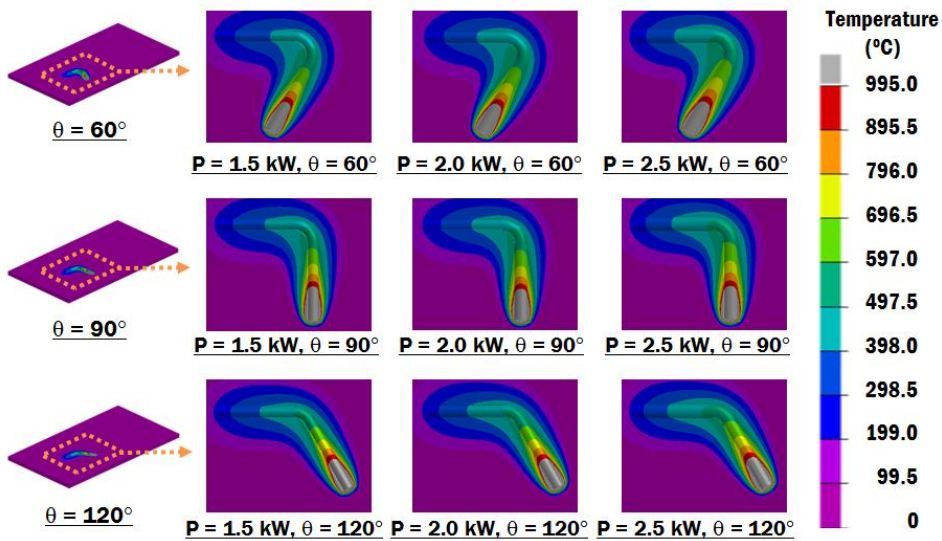
**Table 18 Analysis conditions to investigate the influence of angle of corner deposition on formation of HAZ and SIR**

Parameters	Power of laser (P, kW)	Travel speed of table (V, mm/s)	Radius of corner deposition (mm)	Angle of corner deposition (°)
Range	1.5, 2.0, 2.5	8	5	60, 90, 120

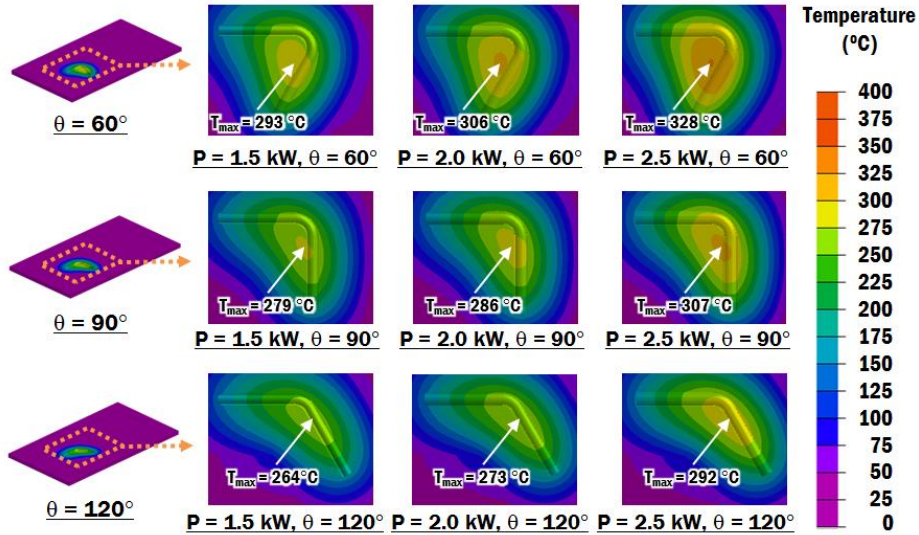
A moving top-hat heat flux model with calibrated penetration depth and efficiency is applied at the top of the bead. Temperature dependent thermal and mechanical properties of Ti-6Al-4V, which have been implemented previously in Chapter IV Section A, are assigned to the bead and substrate. The coefficient of convection and emmissivity are set to be 25 W/m<sup>2</sup>·K and 0.8, respectively.<sup>125,129</sup> A cooling time of the specimen at the end of deposition is set to 10 seconds. All nodes at four corners are constrained in translation and rotation. The thermo-mechanical FEAs are carried out using commercial FE software SYSWELD 12.0.

### 3. Results and Discussion

In order to investigate the influence of angle of corner deposition on the formation of HAZ and SIR, thermal and mechanical FEAs have been carried out. Fig. 45 shows the temperature distribution at the vicinity of the bead at the end of deposition of bead and at the end of the 10 seconds cooling process. From the result of the thermal FEAs, it is revealed that the maximum temperature is located at the inner region of the deposited corner. This phenomenon is clear by observing the temperature histories of the nodes located 5 mm away from the middle of the corner deposition bead, as shown in Fig. 46. This is due to the fact that the smaller angle of corner deposition results in the straight beads within closer proximity with each other. Hence, the heat from the deposition of the straight bead is accumulated within the small region at the inner region of the deposited corner. Consequently, the maximum temperature decreases when the angle of corner deposition increases.



(a) Temperature distribution of the specimen at the end of deposition of bead



(b) Temperature distribution of the specimen at the end of cooling process  
**Fig. 45** Temperature distribution of the specimen at the end of deposition of bead and at the end of cooling process<sup>88</sup>

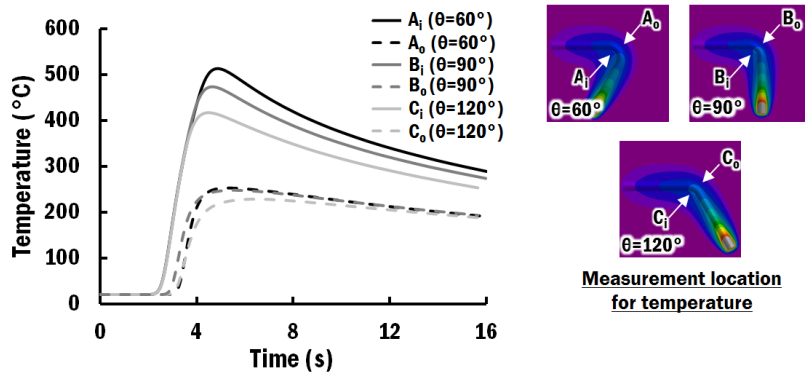


**Fig. 46** Temperature histories at measured locations for different angles of corner deposition ( $P = 1.5$  kW)

From the results of the temperature distribution, the formation of HAZ according to the power of laser and angle of corner deposition is estimated by using the beta transus temperature of Ti-6Al-4V at 995 °C, as shown in Fig. 47.<sup>50,102</sup> It is noted that the inner distance of HAZ ( $L_{i,HAZ}$ ) is larger than the outer distance of HAZ ( $L_{o,HAZ}$ ) at the deposited corner by a factor of 1.09 to 1.17, as



shown in Fig. 48. This is due to the fact that temperature is higher at the inner region of the deposited corner during the corner deposition. The inner distance of HAZ reduces when the angle of corner deposition increases. On the other hand, the outer distance of HAZ increases when the angle of corner deposition increases. The eccentricity of HAZ ( $E_{HAZ}$ ) at corner deposition is estimated by Eq. (44).

$$E_{HAZ} = L_{i,HAZ} - \frac{L_{i,HAZ} + L_{o,HAZ}}{2} = \frac{L_{i,HAZ} - L_{o,HAZ}}{2} \quad (44)$$

It is noted that the eccentricity of HAZ reduces as the angle of corner deposition increases for the same power of laser, as shown in Fig. 48(b). The corner deposition using power of laser 2.0 kW has the highest eccentricity of HAZ at the angle of corner deposition of 60° and 90°, while the corner deposition using power of laser 1.5 kW has the highest eccentricity of HAZ at the angle of corner deposition of 120°. This is due to the change in the shape of bead that has affected the temperature distribution at the vicinity of the bead. Hence, the eccentricity of HAZ is not dependent on the power of laser, but the shape of bead.

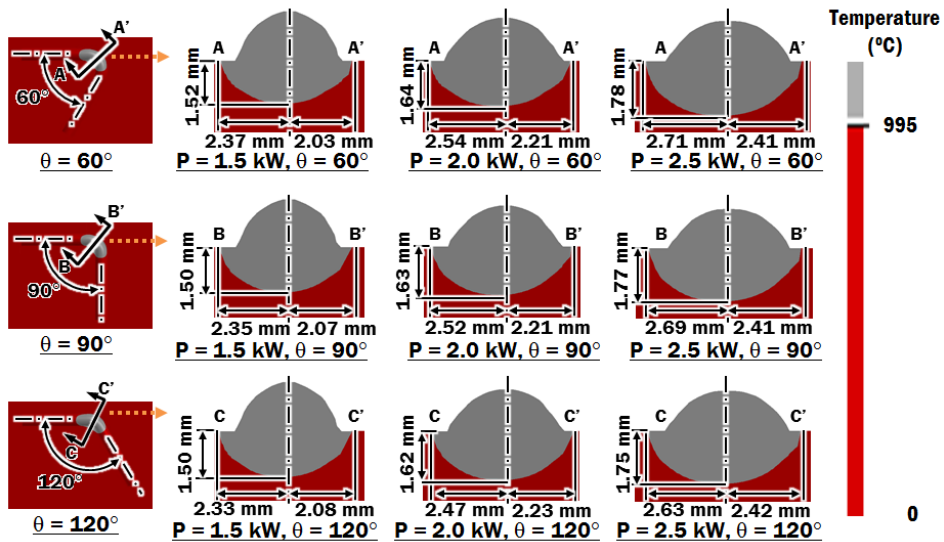


Fig. 47 Estimated HAZ at the middle of corner deposition for different power of laser and traverse speed of table<sup>88</sup>

From the Fig. 48(c), it is revealed that the estimated depth of HAZ grows slightly when the angle of corner deposition becomes smaller. This is because the smaller angle of corner deposition has larger heat accumulated at the inner region of the deposited corner during bead deposition. This raises the temperature at the vicinity of the bead and produces a slightly deeper HAZ when the angle of corner deposition is small.

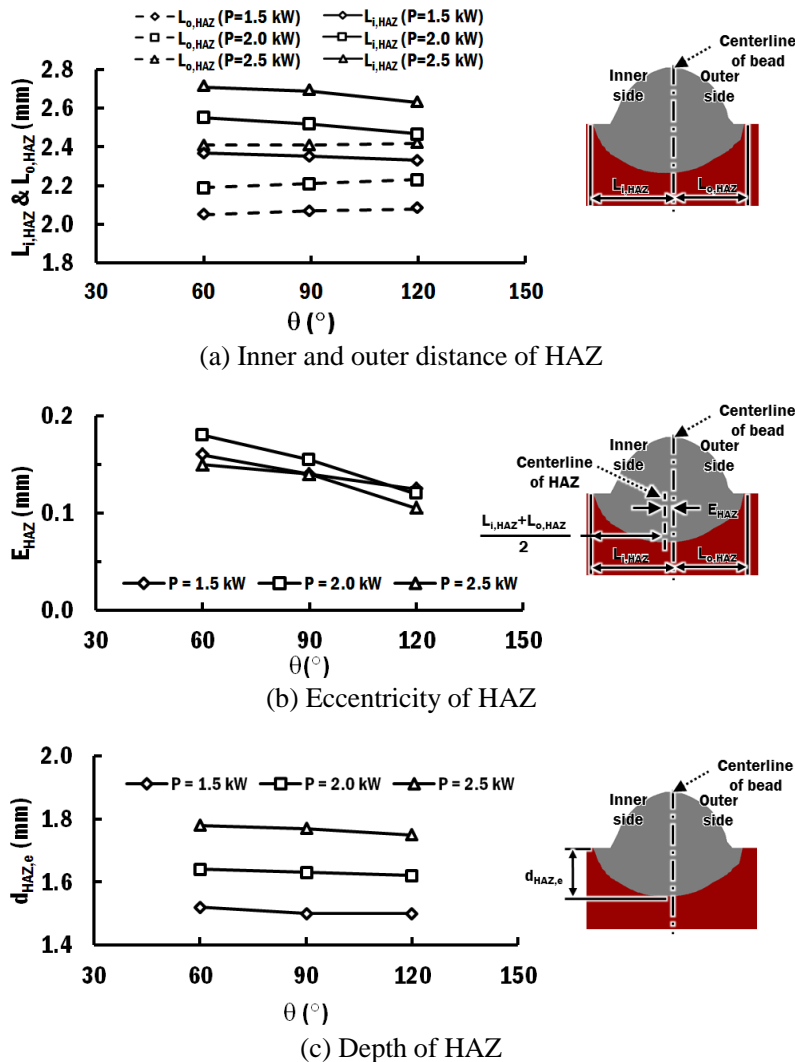


Fig. 48 Estimated dimensions of HAZ at the middle of corner deposition for different power of laser and traverse speed of table<sup>88</sup>

The effect of the angle of corner deposition on the formation of thermal stress on the corner deposition bead after cooling process is investigated using thermo-mechanical FEAs, as shown in Fig. 49. The formation of residual stress is the highest at the inner side of the deposited corner. This is associated with the higher temperature observed at the inner side of the deposited corner. Hence the outer side of the deposited corner, which cool faster, stop to contract earlier than the inner side of the deposited corner. This induces stress at the inner side of the deposited corner.

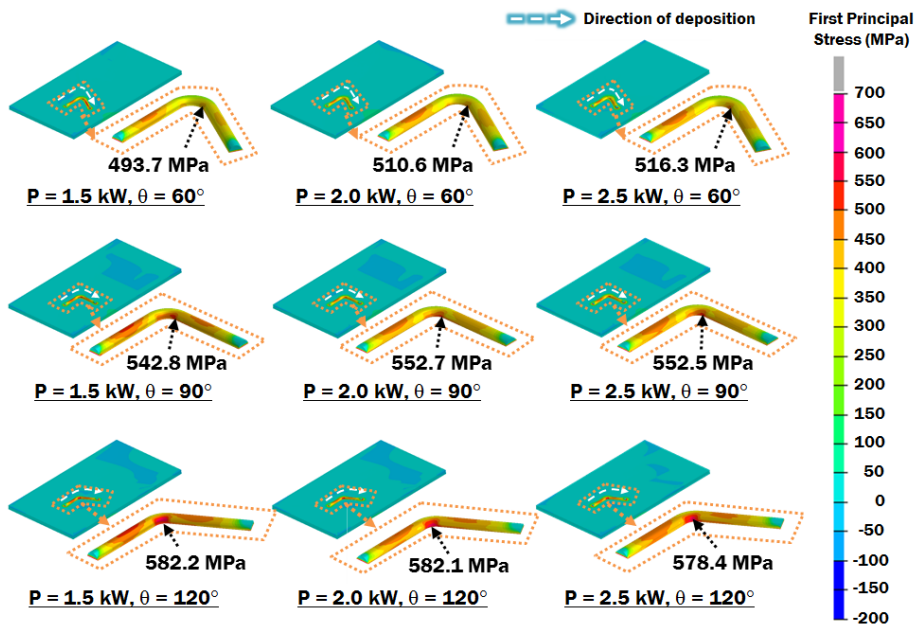
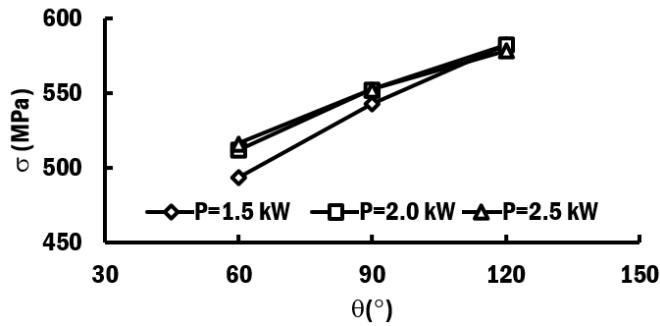


Fig. 49 Residual stress distribution of the deposited bead after cooling process<sup>88</sup>

The residual stress at the deposited corner reduces when the angle of corner deposition reduces for the same power of laser and cross section of bead, as shown in Fig. 50. This is attributed to the fact that the larger angle of corner deposition has higher cooling rate to produce lower temperature as compare with those with smaller angle of corner deposition. Hence, large angle of corner deposition should be avoided during design of parts in order to reduce the residual stress acting on the corner deposition. These informations are useful during the design of a part fabricated by a wire feeding type DED process.



**Fig. 50 Influence of angle of corner deposition and power of laser on residual stress at the deposited corner<sup>88</sup>**

The SIR is estimated based on the critical fatigue limit at 170.5 MPa, as discussed and listed in Table 16 of Section A-3. It is observed that the SIR extends drastically at the inner region of the deposited corner when the angle of corner deposition reduces, as shown in Fig. 51 because the formation of residual stress is the highest at the inner side of the deposited corner. Therefore, the increment of angle of corner deposition can greatly reduce the inner distance of SIR ( $L_{i,SIR}$ ) while slightly increase of outer distance of SIR ( $L_{o,SIR}$ ), as shown in Fig. 52. The inner and outer distances of SIR fall in the range of 3.0-10.7 mm and 6.2-7.7 mm, respectively.



Fig. 51 Formation of SIR according to power of laser and angle of corner deposition<sup>88</sup>

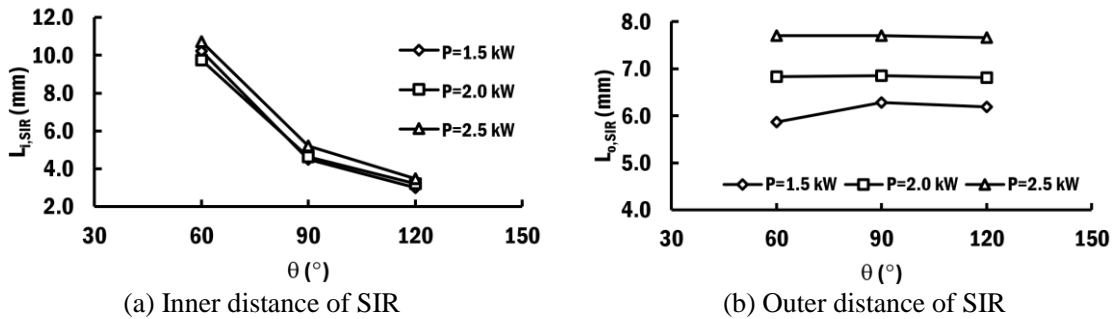


Fig. 52 Inner and outer distances of SIR at the deposited corner<sup>88</sup>

The inner and outer distances of SIR are smaller than the selected width of SIR of 100 mm straight bead, as reported previously in Table 17, by a factor of 1.95-6.90. Therefore, the appropriate gap between adjacent beads for straight beads can be used for corner deposition bead with small radius of 5 mm in order to prevent the critical stress region to overlap.

Although the residual stress is highly dependent on the quality of the deposition such as surface roughness and formation of void in the bead, the knowledge of formation of HAZ, SIR and thermal stress according to the power of laser and angle of corner deposition of a single bead is beneficial for engineers to reduce the residual stress on AM part at the design stage.

## **C. Influence of Deposition Strategy on Thermo-Mechanical Characteristics of a Multi-Layer Deposition**

### **1. Description of the Analysis**

Residual stress induced in a part fabricated by DED process can be reduced by in-situ feedback control of process parameters, deposition strategy, and mechanical control.<sup>64</sup> Typically, the setting of process parameters such as power of laser and travel speed of table is kept consistent throughout a DED process in order to avoid unpredictable change in bead shape. Hence, manipulation of deposition strategy such interpass time and deposition pattern can be used to control the quality of deposited parts. According to the standard guide for DED of metals, an interpass time is defined as the period of time between ending of a specific bead and starting of the subsequent bead.<sup>37</sup> The layer is allowed to cool before the new layer of deposition commences.

In order to investigate the influence of deposition strategy on the formation of residual stresses in a multi-layer deposited part, three influencing factors such as interpass time, deposition direction, and deposition pattern are considered. Short interpass times of 2, 5 and 10 seconds are chosen to minimize the overall process time. The deposition patterns include unidirectional deposition and alternative directional deposition. Sideward and upward deposition directions are considered in this study. The power of laser and travel speed of table are selected as 1.5 kW and 8 mm/s, respectively, because it produces a favourable bead profile with high deposition rate and suitable wetting angle for a wire feeding type DED process. Three layers of beads are simulated during multi-layer deposition. It is assumed that these beads are deposited with symmetrical bead profile and constant width. Argon gas is supplied on top of substrate and beads as the shielding gas during the DED process. The supply of argon is terminated 3 seconds after the end of the deposition. The specimens are cooled by natural convection of air thereafter for 40 minutes after the end of the deposition.

## 2. Analysis Parameters and Boundary Conditions

Fig. 53 shows a three-dimensional FE model with three layers of straight bead to form a multi-layer deposit. The bead section profile for multi-layer deposition is created based on the constant width model, as described in Chapter II Section C. The room temperature is assumed at 20 °C. Calibrated penetration depth and efficiency for top hat heat flux model in Chapter III is applied at the top of the bead. Different interpass times, deposition directions and deposition patterns are applied in this study, as shown in Table 19. All nodes at surface of clamped region are constrained in translation and rotation. Temperature dependent material properties of Ti-6Al-4V are assigned. Heat loss via conduction at clamp region is neglected because the contact area is small and gap conductivity between wood and metal is low.<sup>137</sup> The thermo-mechanical FEAs are carried out using SYSWELD 12.0. Fig. 54 depicts the time frame of multi-layer deposition for different interpass times.

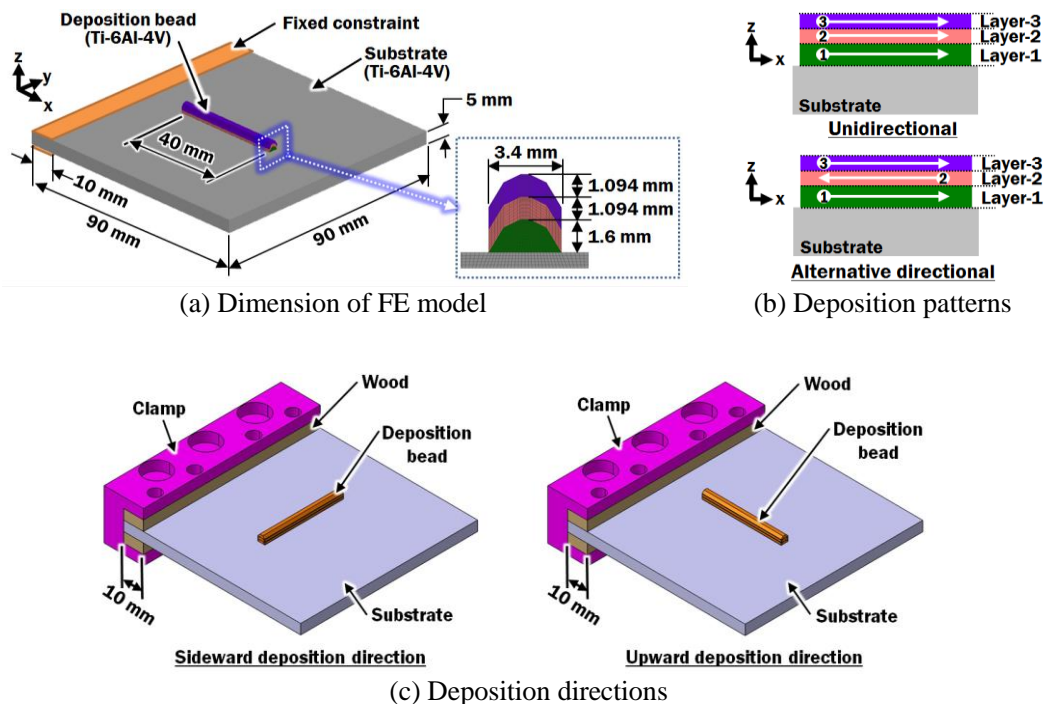


**Fig. 53 FE model to investigate the influence of deposition strategy on thermo-mechanical characteristics of multi-layer deposition**

**Table 19 Analysis conditions to investigate the influence of deposition strategy on thermo-mechanical characteristics of multi-layer deposition**

Parameters	Power of laser (P, kW)	Travel speed of table (V, mm/s)	Interpass time (s)	Deposition direction	Deposition pattern
Range	1.5	8	2, 5, 10	Sideward, Upward	Unidirectional, Alternative directional

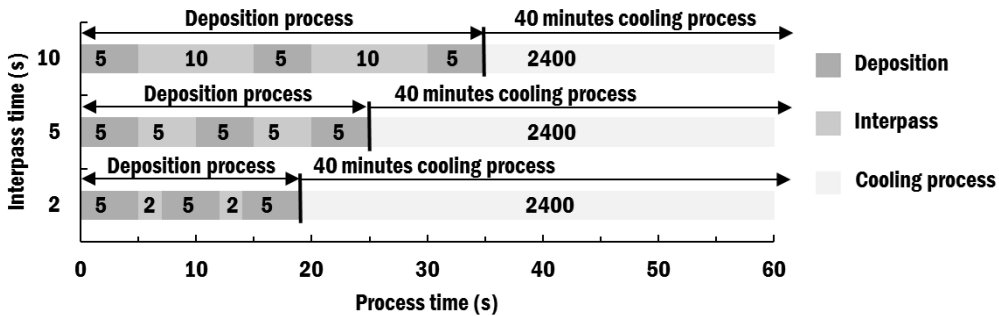


**Fig. 54 Time frame of multi-layer deposition for different interpass times**

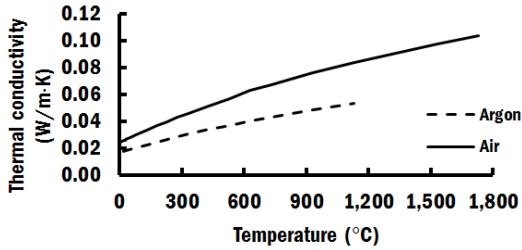
In this study, a long cooling process is involved in order for the part to reach mechanical steady state. The high temperature applied at a localized region of a part during DED process induces a variation of natural convection on a surface due to the buoyancy of air. The natural convection changes during the cooling process. Besides, an inert gas such as argon is applied directly to the heating zone. Hence, coefficient of convection based on the change in condition during the DED process should be considered. Temperature dependent properties for air and argon, as shown in Fig. 55, are implemented to improve the accuracy of the simulation.<sup>138</sup>

The average coefficient of convection is determined by Eq. (45)<sup>126</sup>

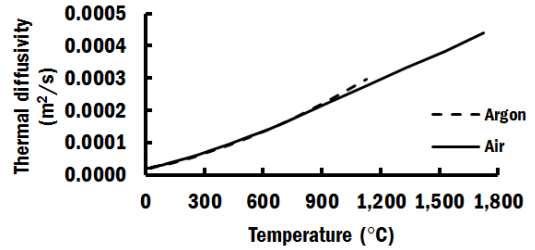
$$h_{\text{conv}} = \frac{Nu_L \cdot k}{L_c} \quad (45)$$

where  $Nu_L$  is the average Nusselt number,  $k$  is the thermal conductivity of air, and  $L_c$  is the characteristic length of the model.

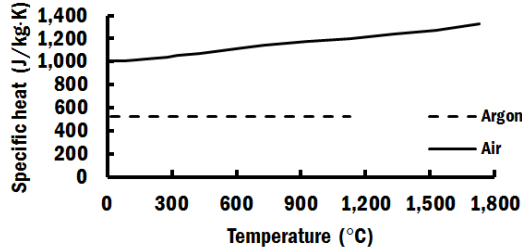




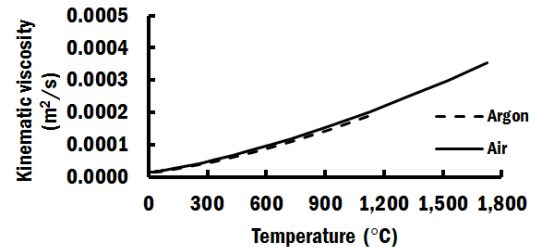
(a) Thermal conductivity of air and argon



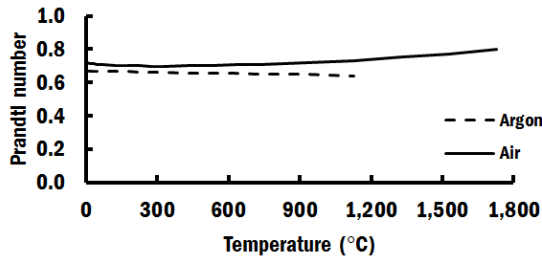
(b) Thermal diffusivity of air and argon



(c) Specific heat of air and argon



(d) Kinematic viscosity of air and argon



(e) Prandtl number of air and argon

**Fig. 55 Gas properties of air and argon<sup>138</sup>**

The average Nusselt numbers for different surface are estimated by using the recommended correlations in Eqs. (46)-(48)<sup>126</sup>

$$Nu_L = 0.54 Ra_L^{1/4} \quad (\text{Condition : } 10^4 \lesssim Ra_L \lesssim 10^7, Pr \gtrsim 0.7) \text{ for upper surface} \quad (46)$$

$$Nu_L = 0.52 Ra_L^{1/5} \quad (\text{Condition : } 10^4 \lesssim Ra_L \lesssim 10^9, Pr \gtrsim 0.7) \text{ for lower surface} \quad (47)$$

$$Nu_L = 0.68 + \left[ \frac{0.670 Ra_L^{1/4}}{(1 + (0.492/Pr)^{9/16})^{4/9}} \right] \quad (\text{Condition : } Ra_L \lesssim 10^9) \text{ for side surface} \quad (48)$$

where  $Ra_L$ , and  $Pr$  are the Rayleigh number and the Prandtl number, respectively.

The Rayleigh number ( $Ra_L$ ) and the air temperature ( $T_f$ ) are estimated by Eqs. (49)-(50)<sup>126</sup>

$$Ra_L = \frac{g(T_s - T_\infty)L_c^3}{\nu_k \cdot \alpha \cdot T_f} \quad (49)$$

$$T_f = \frac{T_s + T_\infty}{2} \quad (50)$$

where  $g$  is the gravitational acceleration constant,  $T_s$  is the surface temperature,  $T_\infty$  is the ambient temperature,  $\nu_k$  is the kinematic viscosity of air, and  $\alpha$  is the thermal diffusivity of air.

By using Eqs. (45)-(50), the average coefficients of convection for different surface temperatures and surfaces of substrate are estimated, as plotted in Fig. 56. It is observed that coefficients of natural convection changes rapidly when temperatures of surfaces increase from room temperature to 500 °C. Besides, coefficients of natural convection are dependent on surfaces of substrate. Hence, the implementation of temperature dependent coefficient of natural convection for different surfaces of substrate is important for long period of cooling time.

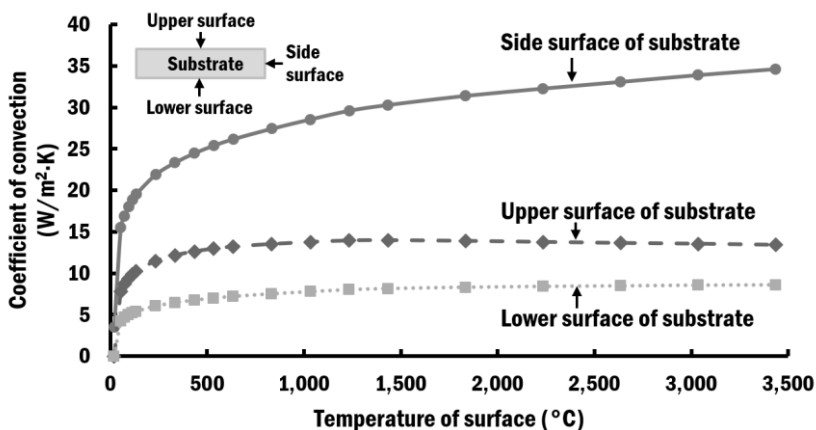


**Fig. 56 Temperature dependent coefficient of natural convection for different surfaces of substrate**

An inert gas such as argon is applied directly to the part during the DED process to shield the process zone from oxidation. In order to determine whether a forced convection should be applied in the FEA, the measure of buoyancy relative to inertial forces must be lesser than 1, as described in Eq. (51)<sup>126</sup>

$$\frac{Gr_L}{Re_L^2} \ll 1 \quad (51)$$

where  $Gr_L$ , and  $Re_L$  are the Grashof number, and the Reynolds number, respectively. Due to the variation of temperature on the surface of substrate during DED process, the measure of buoyancy relative to inertial forces is calculated based on liquidus melting temperature of Ti-6Al-4V in order to ensure that the forced convection is applicable at the melt pool.

These dimensionless parameters of Grashof number and Reynolds number can be estimated by Eqs. (52)-(53)<sup>126</sup>

$$Gr_L \equiv \frac{g\beta(T_s - T_\infty)L_c^3}{\nu_k^2} \quad (52)$$

$$Re_L = \frac{V_f D}{\nu_k} \quad (53)$$

where  $\beta$  and  $V_f$  are the volumetric thermal expansion coefficient of gas, and the velocity of gas, respectively.

Based on the empirical correlation due to an impinging jet from a single round nozzle shown in Fig. 57, average Nusselt number can be estimated by Eqs. (54)-(55)<sup>126</sup>

$$Nu_L = Pr^{0.42} \left[ \frac{2A_r^{0.5}(1-2.2A_r^{0.5})}{1+0.2\left(\frac{H}{D}-6\right)A_r^{0.5}} \right] [2Re^{0.5}(1+0.005Re^{0.55})^{0.5}] \quad (54)$$

$$A_r = \frac{D^2}{4R^2} \quad (55)$$

where  $A_r$  is the relative nozzle area,  $H$  is the distance between nozzle to impingement surface,  $D$  is the diameter of round nozzle, and  $R$  is the effective distance from stagnation point.

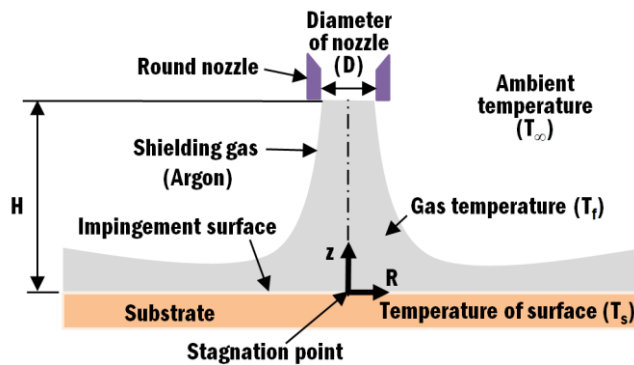


**Fig. 57 Schematic diagram of impinging jet from a single round nozzle<sup>126</sup>**

The calculated measure of buoyancy relative to inertial forces by Eq. (51) shows that the supply of argon has contributed to forced convection. The coefficient of convection due to supply of argon is estimated by applying Eqs. (52)-(55), as listed in Table 20. The coefficient of convection is applied to the upper surface of substrate and deposited beads of the FEA models during the supply of argon gas.

Heat loss via radiation is considered by applying temperature dependent emissivity ( $\epsilon$ ) for solid Ti-6Al-4V, as shown in Fig. 58.<sup>127</sup> The emissivity above 787 °C is extrapolated as a constant value.

**Table 20 Parameters to estimate the coefficient of convection due to supply of argon**

Gas temperature ( $T_g$ , °C)	Measure of buoyancy relative to inertial forces	Flow rate (L/min)	Diameter of nozzle (D, mm)	Velocity of gas ( $V_g$ , m/s)	Distance between nozzle to plate surface (H, m)	Effective distance from stagnation point (R, mm)	Relative nozzle area ( $A_r$ )	Coefficient of convection ( $h_{conv}$ , $W/m^2 \cdot K$ )
20	0.17	20	7	8.66	0.025	45	0.006	46.3

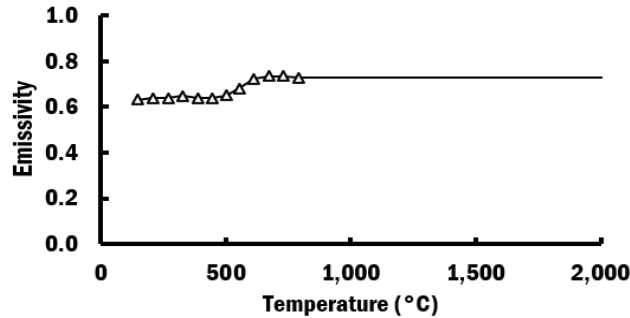


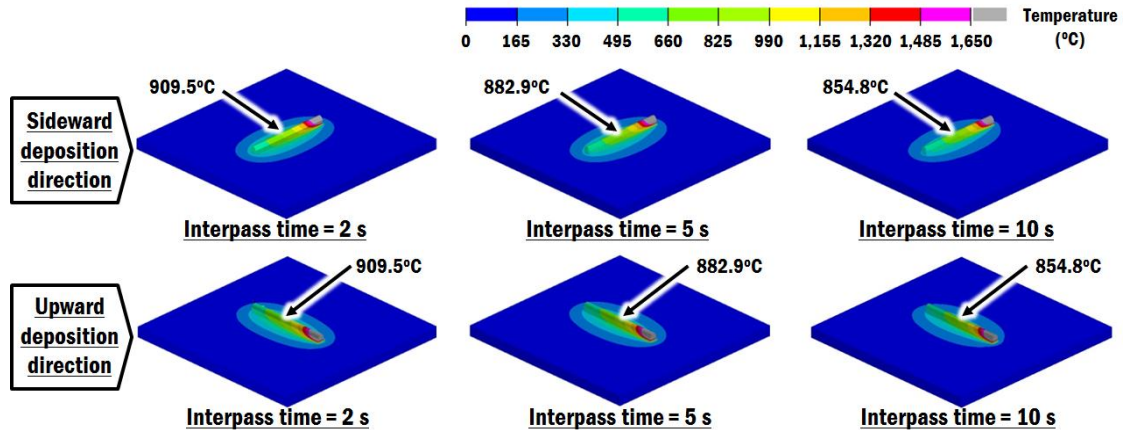
**Fig. 58 Temperature dependent emissivity<sup>127</sup>**

### 3. Results and Discussion

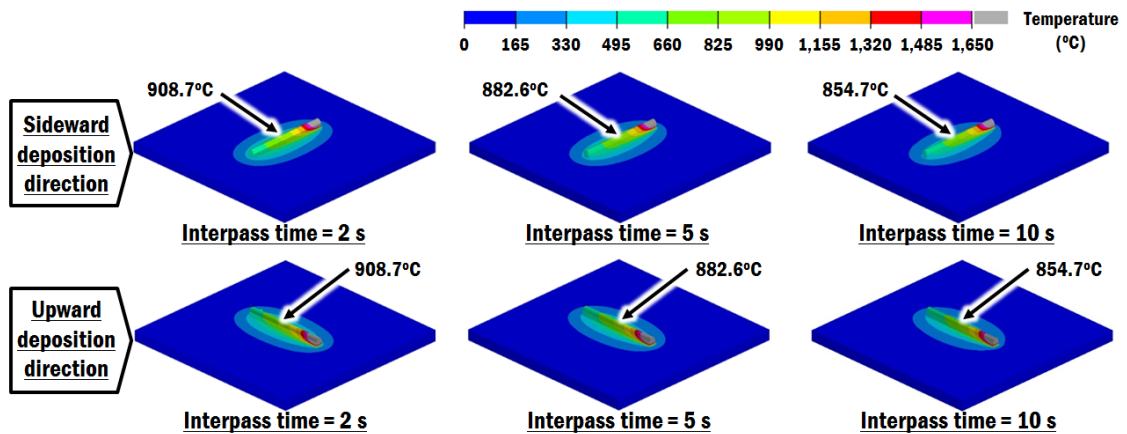
Fig. 59 shows the temperature distributions of the part for different deposition strategies at the end of deposition. The temperatures at the mid-length of layer-3 bead are discussed for different deposition strategies because the mid-length of layer-3 bead is located at the center of the specimen and suitable to represent the overall temperature distributions. The followings observations are obtained from the results of numerical analysis:

- (1) For the same interpass time and deposition pattern, the temperature distributions on the part are same regardless of deposition direction. This is because heat transfer FEAs are performed with same process parameters and boundary conditions.
- (2) Regardless of deposition pattern and deposition direction, the temperature of the mid-length of layer-3 bead at the end of deposition is decreasing when the interpass time is increasing, as shown in Fig. 60. This is due to the fact that longer interpass time allows beads to cool down before the next deposition takes place.

- (3) For the same interpass time and deposition direction, the temperature of the mid-length of layer-3 bead for alternative directional deposition pattern is slightly lower than those in unidirectional deposition pattern. This is attributed to the alternative directional deposition pattern that allows one side of the bead to have longer cooling time than the other before the laser beam irradiates the same location again. This is illustrated by comparing temperature histories for different deposition patterns at interpass time of 2 s and upward deposition direction, as shown in Fig. 61.
- (4) In Fig. 61, it is shown that the temperatures during irradiation of laser beam at same location for layer 1, 2 and 3 (A-1, A-2, and A-3) are almost similar in the case of unidirectional deposition pattern. In the case of alternative directional deposition pattern, the temperature during irradiation of laser beam at same location for layer 1, 2 and 3 (A-1, A-2, and A-3) are different due to the variable cooling time. This contributes to the variable heat transfer characteristics and variable size of melt pool along the deposition of bead using alternative directional deposition pattern.
- (5) High peak temperature above vaporization temperature of Ti-6Al-4V is observed in temperature histories in Fig. 61. This behavior has been reported in FEAs performed by Fu et al. (2014) and Parry et al. (2016) as an isolated singularity inside a melt pool region.<sup>63,139</sup> This is because heat transfer in melt pool due to Marangoni convective flow is not considered in FEAs.<sup>140</sup> The application of computational fluid dynamics (CFD) into heat transfer FEAs is beyond the scope of this thesis.
- (6) From the results of FEAs, the temperatures of the mid-length of layer-3 bead for all cases have converged to the same temperature of 24.7 °C after 40 minutes cooling, regardless of interpass time, deposition direction and deposition pattern. This indicates that the cooling time is sufficient for the specimen to reach mechanical steady state. Hence, the influence of deposition strategy on displacements and residual stresses is discussed based on the mechanical states after cooling process.



(a) Unidirectional



(b) Alternative directional

Fig. 59 Influence of different deposition strategies on temperature distributions of part at the end of deposition

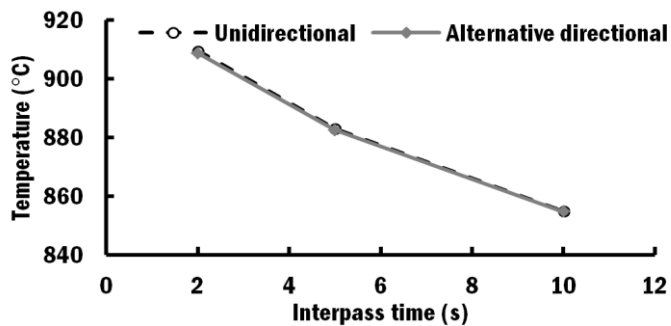
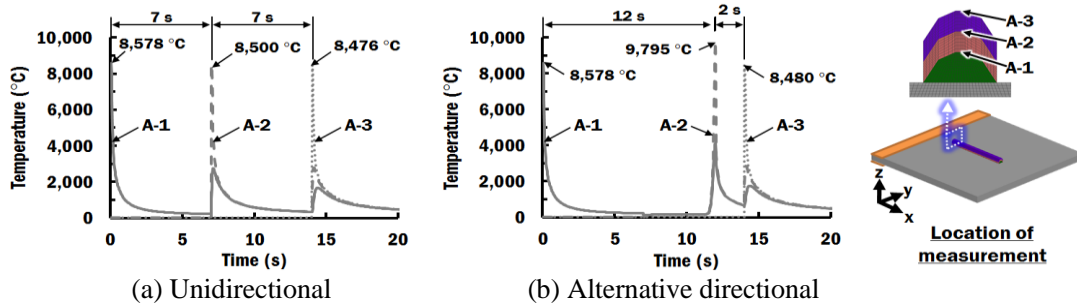


Fig. 60 Influence of interpass time on temperature of the mid-length of layer-3 bead at the end of deposition (upward deposition direction)



**Fig. 61 Comparison of temperature histories for different deposition patterns (interpass time of 2 s and upward deposition direction)**

Microstructure transformation of metallic material is closely related to cooling rate.<sup>141</sup> In order to maintain similar microstructure, consistent cooling rate is desired. Fig. 62 shows the maximum cooling rates of selected nodes occurs after laser beam irradiates at the nodes during the deposition of layer-3 (process time between 14 s to 19 s). The cooling rate ( $C_r$ ) is estimated using rate of change of temperature in Eq. (56)

$$C_r = \frac{dT_t}{dt} = \frac{T_t - T_{(t-1)}}{\Delta t} \quad (56)$$

where  $t$  is the time,  $T_t$  is the temperature at time  $t$ , and  $T_{(t-1)}$  is the temperature at time  $(t-\Delta t)$ . Cooling rate has a negative rate of change of temperature due to temperature drop.

In the case of alternative directional deposition pattern, the maximum cooling rates increase from node L-3 to node N-3. This is attributed to cooling time increases from node L-3 to node N-3 during deposition of beads using an alternative directional deposition pattern. The maximum cooling rates reduces to a similar cooling rate from node L-3 to node N-3 in the case of unidirectional deposition pattern because it has fixed cooling time.

Hence, alternative directional deposition pattern should be avoided due to variable heat transfer characteristics along the bead, particularly when the deposited bead is long. In contrast, the beads produced by unidirectional deposition pattern undergo similar cooling time and cooling rate. This characteristic is desired in order to produce uniform fusion zone and grain size of microstructure along the bead deposition direction.



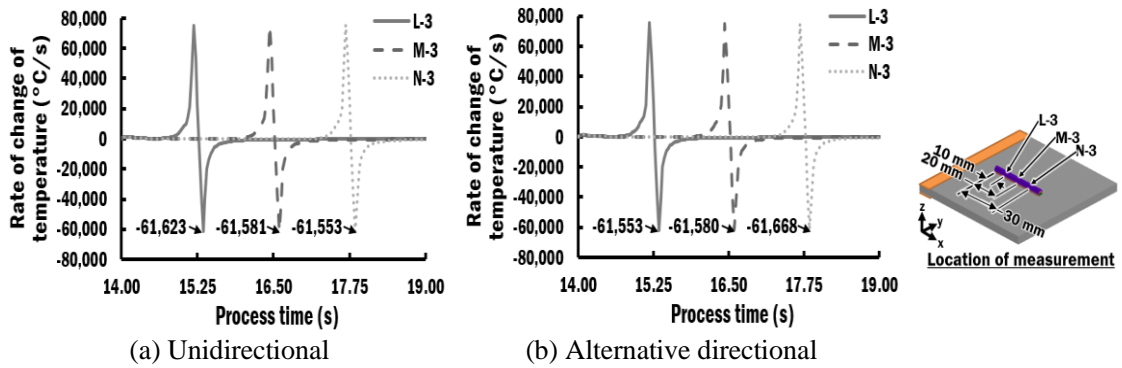


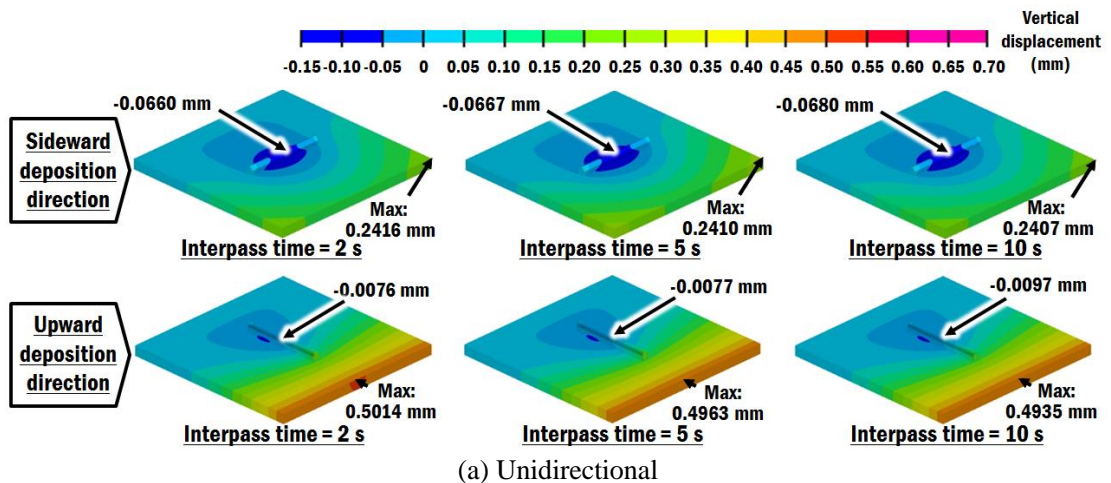
**Fig. 62 Comparison of cooling rates for different deposition patterns (interpass time of 2 s and upward deposition direction)**

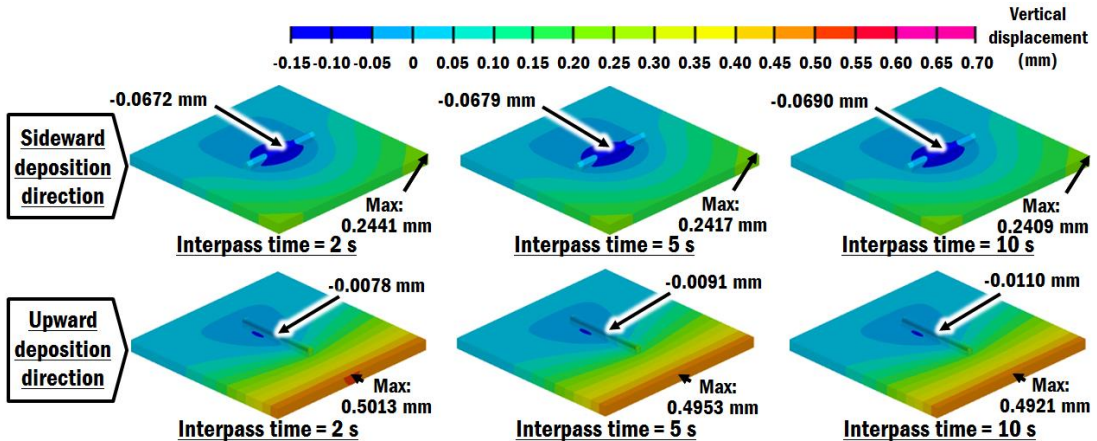
Thermo-mechanical FEAs are carried out to predict the displacements and residual stresses on deposited part. In order to evaluate the deflection of specimen with respect to the horizontal plane surface of substrate, vertical displacement distributions of the part for different deposition strategies after 40 minutes cooling process are evaluated, as shown in Fig. 63. The vertical displacements at the mid-length of layer-3 are discussed for different deposition strategies because the mid-length of layer-3 bead is located at the center of the specimen and suitable to represent the overall displacement of the specimen. The followings observations are obtained from the results of FEAs:

- (1) For the same interpass time and deposition pattern, it is shown that the deposition direction greatly affects the vertical displacement distribution and location of maximum displacement. This is attributed to the different heat transfer characteristics towards the free end of specimen. The heat source is moving toward the free end of the specimen in the upward deposition direction and contributes to high displacement at the free end. In the case of sideward deposition direction, heat is transferred from the deposited bead to the free end of specimen. Therefore, the maximum vertical displacement for upward deposition direction is higher than sideward deposition direction.
- (2) By comparing Fig. 64(a) and Fig. 64(b), it shows that the deposited beads in the sideward deposition direction displace downward at the mid-length of layer-3 bead more

than those of upward deposition direction. This is attributed to the fact that the displacement of deposited beads is restricted when the beads are aligned parallel to the clamp.

- (3) For the same interpass time and deposition direction, the displacement of the mid-length of layer-3 bead for alternative directional deposition pattern is slightly higher (in negative direction) than those in unidirectional deposition pattern. This is because the alternative directional deposition pattern has variable cooling time and contributes to higher temperature gradient along the deposited bead as compare to unidirectional deposition pattern.
- (4) Regardless of deposition pattern and deposition direction, the increment of interpass time slightly increases the displacement of the mid-length of layer-3 bead, as shown in Fig. 64. This is attributed to the fact that longer interpass time allows beads to deflect before the next deposition takes place. This characteristic has been reported by Bandari et al. in their experimental study.<sup>142</sup>





(b) Alternative directional

Fig. 63 Influence of different deposition strategies on vertical displacement distributions of part after cooling process

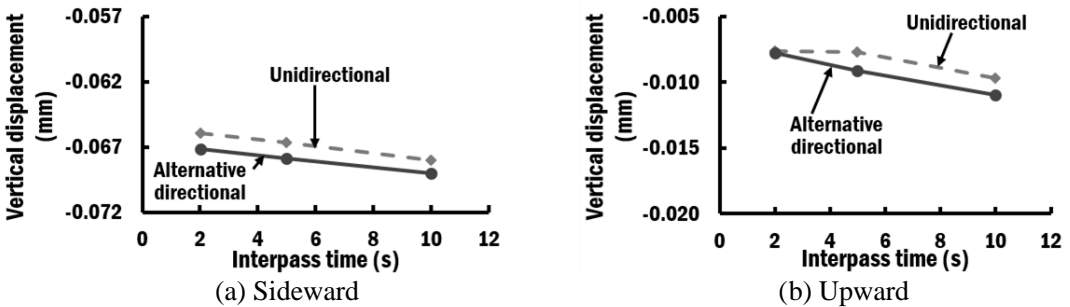


Fig. 64 Influence of different deposition directions on vertical displacement of mid-length of layer-3 bead after cooling process

Fig. 65 shows residual stress distributions of the part for different deposition strategies after 40 minutes cooling process. From the results of numerical analysis, the followings observations are obtained:

- (1) Beads deposited in upward deposition direction have lower residual stress compared to those in sideward deposition direction, as shown in Fig. 66. This is because beads deposited in upward deposition direction have reduced the residual stress by larger displacement.

- (2) The increment of interpass time contributes to small reduction of residual stress of the deposited bead, as shown in Fig. 66. This is attributed to the fact that longer interpass time allows beads to deflect in order to reduce residual stress before the next deposition takes place.
- (3) From Fig. 67, it shows that the residual stresses of beads deposited by unidirectional and alternative directional deposition patterns are almost similar. The residual stresses of beads deposited by alternative directional deposition pattern are slightly lower than those deposited by unidirectional deposition pattern for interpass time of 5 s or greater.

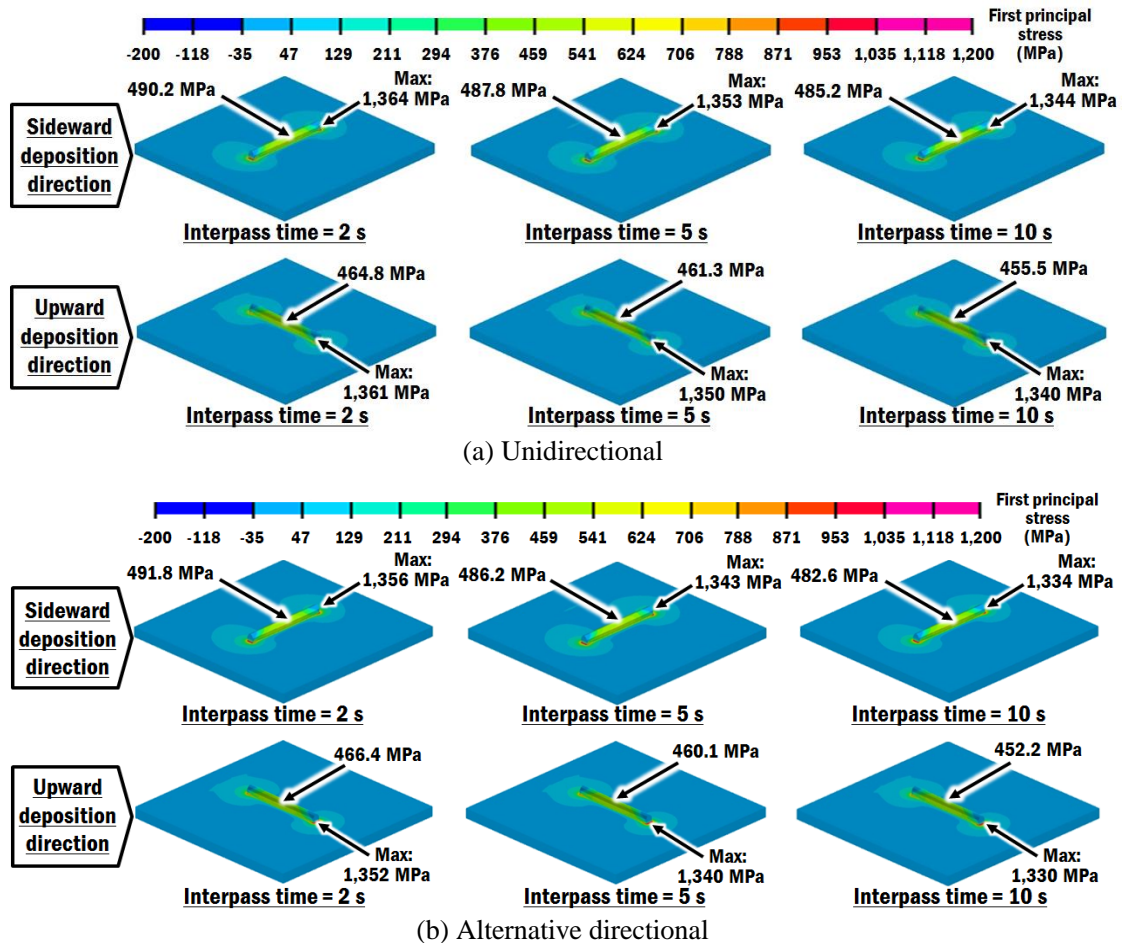
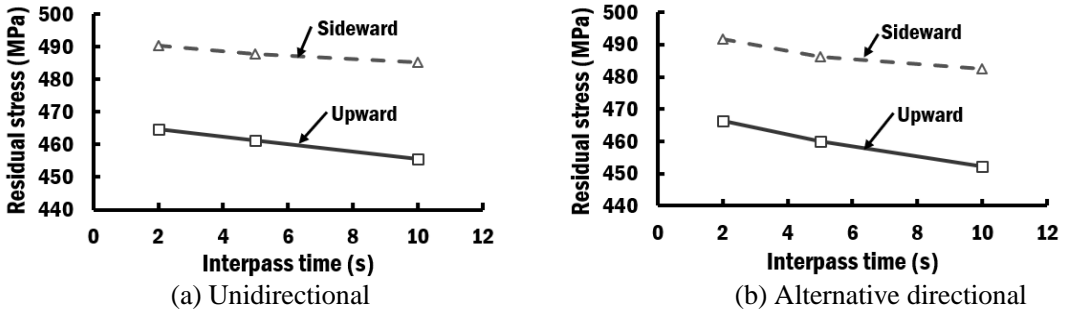
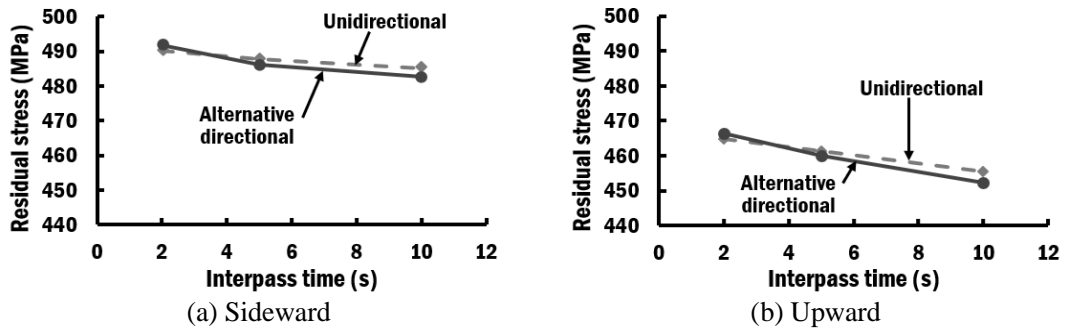


Fig. 65 Influence of different deposition strategies on residual stress distributions of part after cooling process



**Fig. 66 Influence of different deposition patterns on residual stress of mid-length of layer-3 bead after cooling process**



**Fig. 67 Influence of different deposition directions on residual stress of mid-length of layer-3 bead after cooling process**

From these observations, it is revealed that deposition strategy using upward deposition direction and long interpass time of 10 s produces the lowest residual stress in deposited part. However, the long interpass time lengthens the process time and promotes undesirable large temperature drop in beads during cooling between depositions. From this viewpoint, the shorter interpass time of 2 s is recommended. The unidirectional deposition pattern is preferred during a wire feeding type DED process because it offers similar cooling time and cooling rates along the bead deposition direction. These understandings of influence of different interpass times, deposition directions and deposition patterns on formation residual stresses of a multi-layer deposition by a wire feeding type DED process are beneficial in the selection of proper deposition strategy.

## D. Verification of Thermo-Mechanical Analysis for a Multi-Layer Deposition

### 1. Description of the Experiments

In order to validate the results of proposed thermo-mechanical FEAs for a multi-layer deposition using a wire feeding type DED process in Chapter IV Section C, vertical displacements at two locations of the substrate (Pt-1 and Pt-2) are measured experimentally and compared with results of FEAs, as illustrated in Fig. 68. Three layers of 40 mm straight beads were deposited on a 90 mm × 90 mm × 5 mm substrate using unidirectional deposition pattern and interpass time of 2 s. The beads were deposited in sideward and upward deposition directions. The conditions of the experiments are listed in Table 21. The vertical displacements at locations Pt-1 and Pt-2 were measured using strain gauge displacement transducers at 5 minutes, 10 minutes, 25 minutes and 40 minutes of cooling process.

The proposed thermo-mechanical FE models for a multi-layer deposition using a wire feeding type DED process in Chapter IV Section C are applied. The vertical displacements at locations Pt-1 and Pt-2 were compared between the estimated results of thermo-mechanical FEAs and those obtained through experiments.

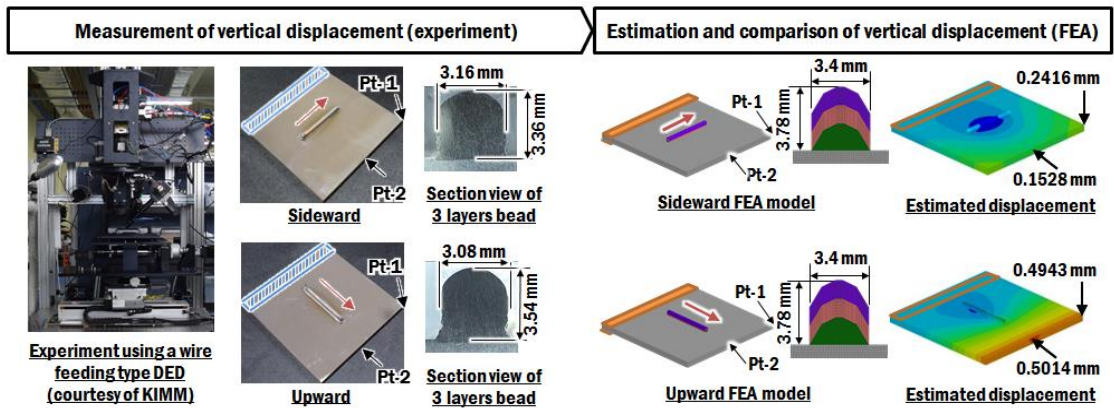


Fig. 68 Procedure to verify the results of thermo-mechanical FEAs

**Table 21 Conditions of experiments to verify the thermo-mechanical FE models**

Parameters	Power of laser (P, kW)	Travel speed of table (V, mm/s)	Interpass time (s)	Deposition direction	Deposition pattern	Period of cooling process (min.)
Range	1.5	8	2	Sideward, Upward	Unidirectional	40

## 2. Results and Discussion

Fig. 69 shows the specimens of the experiments for different deposition directions. In order to ensure that the proposed multi-layer deposition beads estimated using the constant width model are proper, the beads are cut to obtain the cross section view of the three-layer deposition beads, as shown in Fig. 69. Average heights and average widths of multi-layer beads are obtained from the measurement of cross section views of multi-layer beads using a video microscope system (ICS, Sometech Inc.).

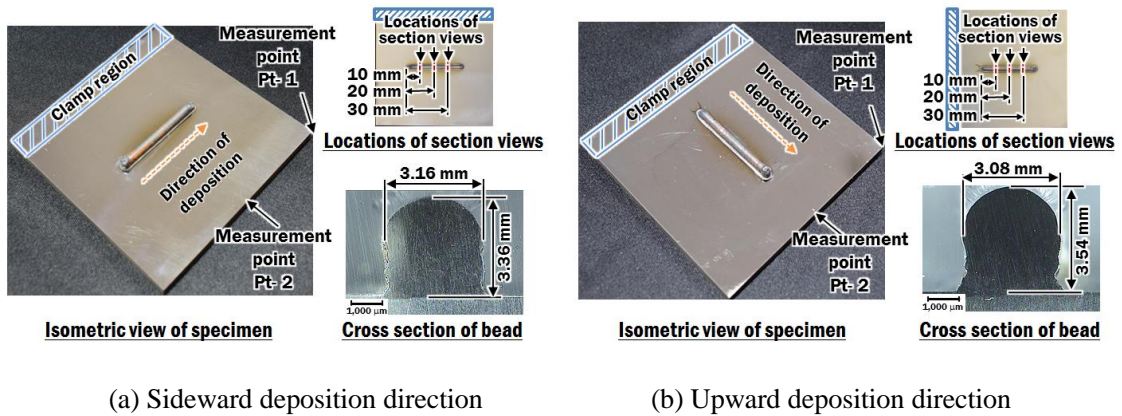


**Fig. 69 Experimental specimen of multi-layer deposition beads for sideward and upward deposition directions**

Table 22 shows that errors between the estimated dimensions of the deposition beads and those measured from experiment. The estimated height and width of multi-layer deposition beads are greater in FE models by 6.8% - 12.5% and 7.6% - 10.4%, respectively. In order to normalize the dimensions of the multi-layer beads for further comparison, the height-to-width ratio ( $R_{h/w}$ ) is

determined using Eq. (57).

$$R_{h/w} = \frac{h_b}{w_b} \tag{57}$$

Errors of height-to-width ratio are +4.7% and -3.5% for sideward and upward deposition directions, respectively. These errors are relatively small and acceptable.

**Table 22 Comparison of dimensions of multi-layer deposition beads between the estimated from constant width model and those from experiments**

Deposition direction	Height of multi-layer beads (h <sub>b</sub> , mm)			Width of multi-layer beads (w <sub>b</sub> , mm)			Height-to-width ratio (R <sub>h/w</sub> )		
	Experiment	FE model	Error	Experiment	FE model	Error	Experiment	FE model	Error
Sideward	3.36	3.78	+12.5 %	3.16	3.4	+7.6 %	1.06	1.11	+4.7 %
Upward	3.54	3.78	+6.8 %	3.08	3.4	+10.4 %	1.12	1.11	-3.5 %

Table 23 shows the results of vertical displacements at measurement points Pt-1 and Pt-2, which were conducted by KIMM. The histories of estimated vertical displacements at points Pt-1 and Pt-2 are obtained from the result of thermo-mechanical FEAs. Fig. 70 illustrates the comparison of vertical displacement at points Pt-1 and Pt-2 between the estimated results from FEAs and those from experiments. Differences (Δd) between the estimated results from FEAs and those from experiments are calculated by Eq. (58)

$$\Delta d = |d_{FEA} - d_{exp}| \tag{58}$$

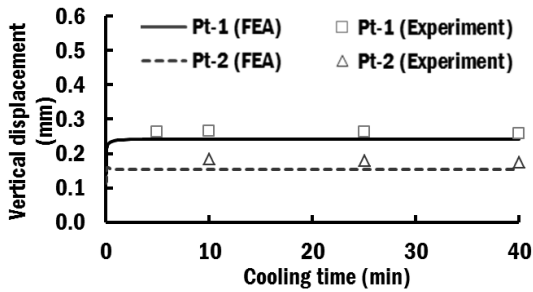
where d<sub>FEA</sub> and d<sub>exp</sub> are the vertical displacement estimated by FEA and the vertical displacement measured in experiment, respectively.

Fig. 71 shows that differences (Δd) between the estimated results from FEAs and those from experiments, for different cooling times are less than 94 μm. These differences are small compared with those in literatures. Hence, the thermo-mechanical model is verified.

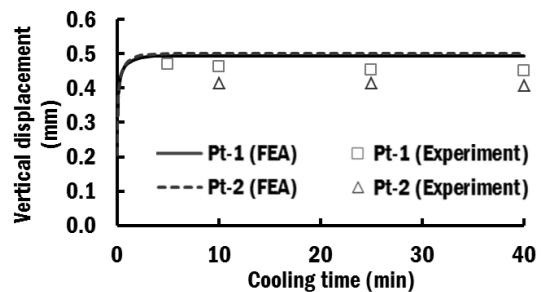


**Table 23** Experimental results of vertical displacement at measurement points according to cooling time (courtesy of KIMM)

Cooling time (min.)	Sideward		Upward	
	Vertical displacement at Pt-1 (mm)	Vertical displacement at Pt-2 (mm)	Vertical displacement at Pt-1 (mm)	Vertical displacement at Pt-2 (mm)
5	0.263	-	0.468	-
10	0.264	0.183	0.461	0.413
25	0.262	0.178	0.452	0.413
40	0.258	0.175	0.451	0.408

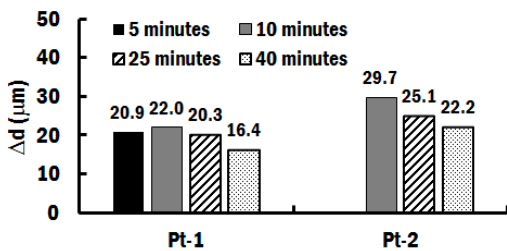


(a) Sideward deposition direction

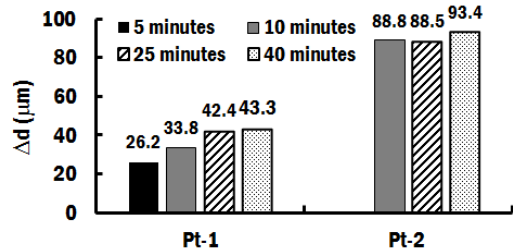


(b) Upward deposition direction

**Fig. 70** Comparison of vertical displacement between estimated results from FEAs and those of experiments



(a) Sideward deposition direction



(b) Upward deposition direction

**Fig. 71** Differences of vertical displacement at measurement points for different cooling times

## E. Investigation of Optimum Interpass Time for a Multi-Layer Deposition

### 1. Description of the Analysis and Methodology

In a multi-layer deposition of thin wall structure, temperature of deposited layer increases as the number of layer increases due to reduced heat dissipation via conduction to substrate.<sup>98,143</sup> As a result of the increased temperature without proper cooling, continuous deposition in a multi-layer deposition results in poor surface finish and the possibility of bead collapse.<sup>98,144</sup> Implementation of interpass time is an important process strategy in multi-layer deposition to passively control the interpass temperature. Interpass temperature is defined as the temperature of the previous deposited layer, immediately before a new layer is deposited.<sup>145</sup> Interpass temperature influences the formation of microstructure, phase concentration and mechanical properties of AM parts. By maintaining a suitable interpass temperature, geometric accuracy and residual stresses within AM parts are improved.<sup>143,145</sup>

It is a challenging task to select a proper interpass time via experiments. Recently, Montevecchi et al. (2018) proposed an algorithm to compute specific interpass time for multi-layer deposition using wire-arc additive manufacturing process based on heat transfer FEA.<sup>146</sup> The algorithm is implemented in MATLAB coding, which continuously runs heat transfer FE simulations in a FEA software, monitor the estimated temperature of specific nodes from heat transfer FEAs, calculate the suitable interpass time, and update the FE models for the subsequent simulations. The implementation of the algorithm is difficult.

A simple and practical methodology is proposed in this study to investigate the optimum interpass time for multi-layer deposition using heat transfer FEAs, as illustrated in Fig. 72. The optimum interpass time is estimated for each layer such that a fixed interpass temperature at the start position of each layer is maintained. The interpass temperature for Ti-6Al-4V is assumed to be 400 °C, based on the recommended interpass temperature for titanium aluminide.<sup>145</sup>

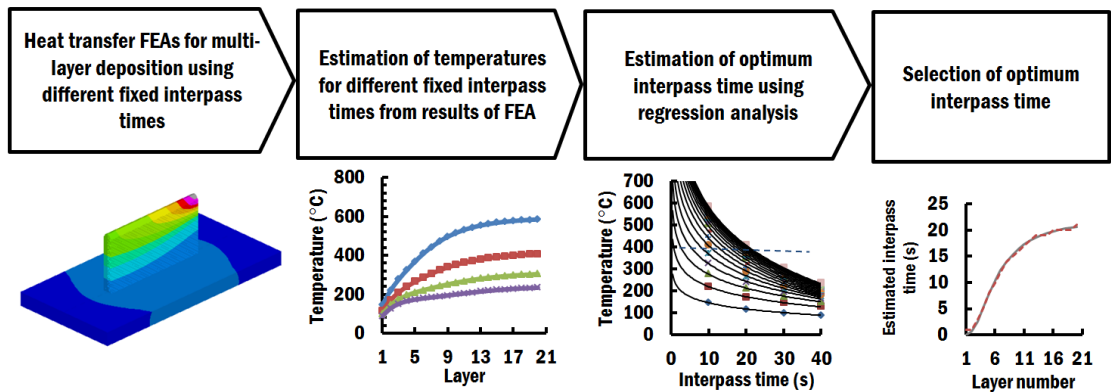


**Fig. 72 Procedure to estimate optimum interpass time for multi-layer deposition**

Four FEAs are performed using four different fixed interpass times. From the results of these FEAs, the temperatures for all layers using different fixed interpass times are obtained. Each layer is represented by an interpass temperature control node. The interpass temperature control node is selected to be the first node on the surface of the bead that the center of laser beam is irradiating, as shown in Fig. 73. From the temperature histories, temperature for each layer after different interpass times is estimated using regression analysis. The optimum interpass time is predicted from regression equation for each layer. For practical implementation during a DED process, optimum interpass time for each layer is rounded to the nearest second. Besides, the optimum interpass time is set to be at least 1 second to provide sufficient time for the worktable to navigate to the desired location before the start of subsequent deposition.

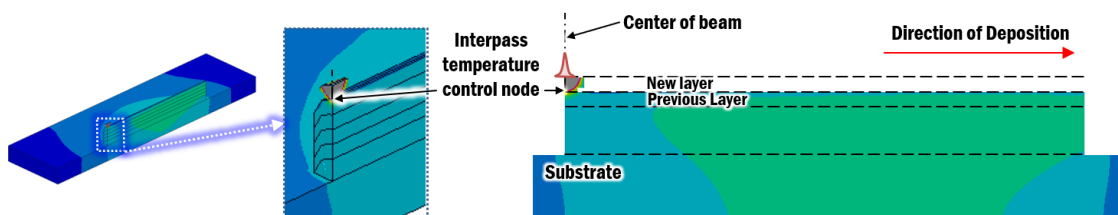


**Fig. 73 Location of interpass temperature control node**

## 2. Analysis Parameters

In order to investigate the optimum interpass time, twenty layers of 40 mm beads are simulated during multi-layer deposition using heat transfer FEAs, as shown in Fig. 74. The dimension of substrate is 80 mm × 40 mm × 5 mm. The power of laser and travel speed of table are selected as 1.5 kW and 8 mm/s, respectively. The bead section profile for multi-layer deposition is created similar to those in Chapter IV Section C. The unidirectional deposition pattern is applied in this study. Argon gas is supplied on top of the substrate and beads as the shielding gas during the DED process. Due to similar setup, the proposed heat transfer boundary conditions for a multi-layer deposition using a wire feeding type DED process in Chapter IV Section C are applied. The coefficient of forced convection is assumed to be constant regardless of the increase in number of layers, in order to maintain the same boundary condition at the melt pool because the distance of shielding gas supply nozzle to the melt pool remains constant during deposition. Temperature dependent material properties of Ti-6Al-4V are applied in these heat transfer FEAs using SYSWELD 12.0.

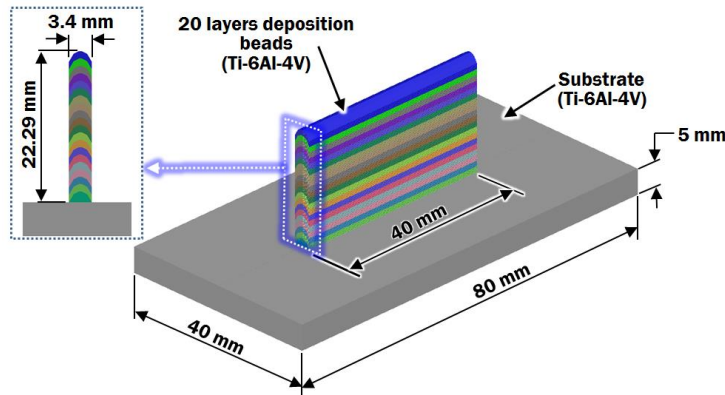


**Fig. 74 Finite element model of 20 layers deposition to investigate optimum interpass time**

Fixed interpass times of 10, 20, 30 and 40 seconds are chosen based on the interpass times range between 0 to 40 s applied in experiments by Denlinger et al. (2015) , as shown in Table 24.<sup>97</sup>

Finally, a FEA using the selected optimum interpass time based on the proposed methodology is carried out in order to evaluate the applicability of the methodology from the viewpoint of interpass temperature and dimension of melt pool.

**Table 24 Conditions of analyses to investigate the optimum interpass time for multi-layer deposition**

Parameters	Power of laser (P, kW)	Travel speed of table (V, mm/s)	Interpass time (s)	Deposition pattern
Range	1.5	8	10, 20, 30, 40, optimum time	Unidirectional

### 3. Results and Discussion

Heat transfer FEAs for 20 layers depositions are carried out using different fixed interpass times. Fig. 75 shows the interpass temperatures estimated from FEAs at the interpass temperature control node of each layer. It shows that the desired interpass temperature of 400 °C can be attained using interpass time of 10 s and 20 s after 6 layers and 16 layers, respectively. Multi-layer deposition using 20 s interpass time results to almost converged interpass temperature at slightly higher than 400 °C. The convergence of interpass temperature is achieved when the deposition occurs far from the substrate, and heat loss occurs mainly at the wall structure.

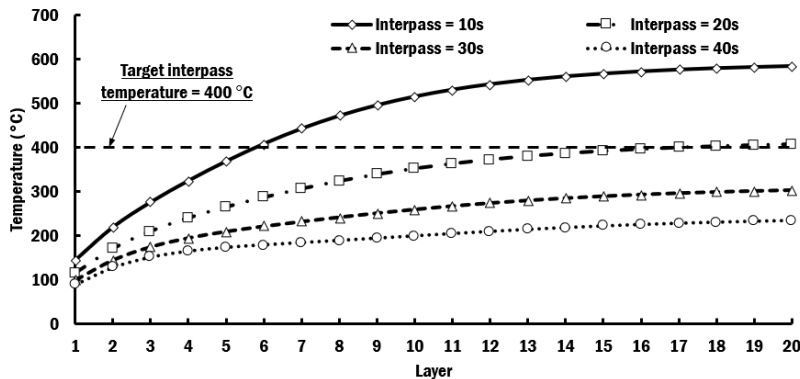


**Fig. 75 Interpass temperatures of multi-layer depositions using different interpass times**

Based on the decaying characteristic of cooling, interpass temperatures ( $T_{ip}$ ) for different layers are estimated by logarithmic regression equations in the form of Eq. (59), as shown in Fig. 76 and Table 25

$$T_{ip} = A + B \log_e (t_{ip}) \quad (59)$$

where A and B are constants of the regression equation, and  $t_{ip}$  is the interpass time.

By solving Eq. (59), the optimum interpass time to maintain a target interpass temperature can be predicted using Eq. (60).

$$t_{ip} = e^{\left(\frac{T_{ip}-A}{B}\right)} \quad (60)$$

Fig. 77 shows optimum interpass times estimated for different layers in order to maintain a target interpass temperature of 400 °C. Selected optimum interpass times after deposition of each layer are rounded to the nearest second with minimum value of 1 second, for practical implementation during a DED process. The curve in Fig. 77 shows a sigmoidal trend, similar to those estimated by Montecvecchi et al. (2018). The same trend indicates that the proposed methodology to estimate optimum interpass time is proper.

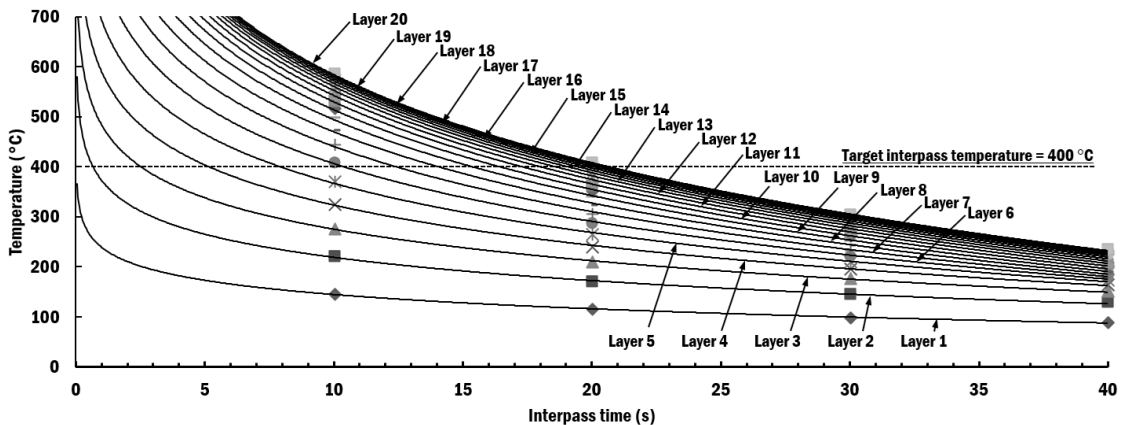
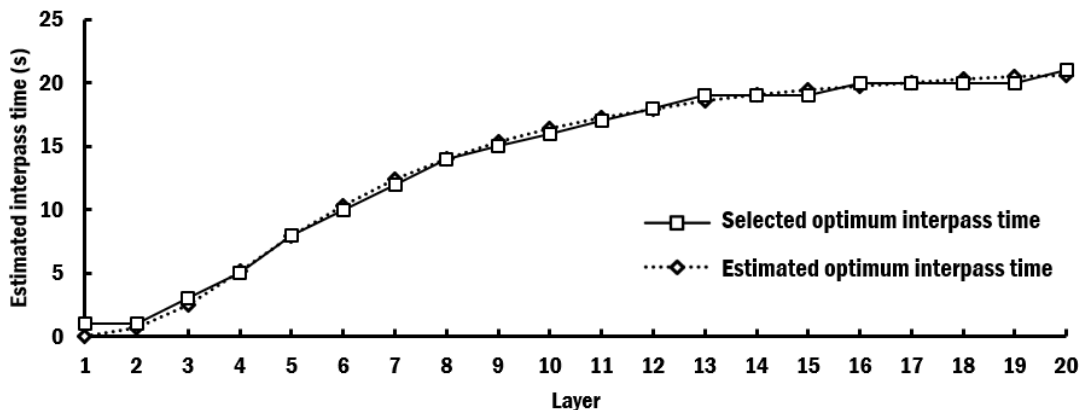


Fig. 76 Estimation of interpass temperatures at each layer for different interpass times

**Table 25 Regression relationship between interpass temperature and interpass time for different layers**

Layer	Regression relationship between interpass temperature ( $T_{ip}$ ) and interpass time ( $t_{ip}$ )	Coefficient of determination ( $R^2$ )
1	$T_{ip} = 239.013 - 41.030 \log_e (t_{ip})$	0.9986
2	$T_{ip} = 372.801 - 66.897 \log_e (t_{ip})$	0.9984
3	$T_{ip} = 483.909 - 90.737 \log_e (t_{ip})$	0.9988
4	$T_{ip} = 590.262 - 115.977 \log_e (t_{ip})$	0.9988
5	$T_{ip} = 693.395 - 141.854 \log_e (t_{ip})$	0.9986
6	$T_{ip} = 788.830 - 166.282 \log_e (t_{ip})$	0.9987
7	$T_{ip} = 872.259 - 187.600 \log_e (t_{ip})$	0.9989
8	$T_{ip} = 941.713 - 205.071 \log_e (t_{ip})$	0.9991
9	$T_{ip} = 997.458 - 218.740 \log_e (t_{ip})$	0.9993
10	$T_{ip} = 1,040.989 - 229.052 \log_e (t_{ip})$	0.9995
11	$T_{ip} = 1,074.282 - 236.604 \log_e (t_{ip})$	0.9996
12	$T_{ip} = 1,099.394 - 242.011 \log_e (t_{ip})$	0.9997
13	$T_{ip} = 1,118.200 - 245.810 \log_e (t_{ip})$	0.9998
14	$T_{ip} = 1,132.220 - 248.440 \log_e (t_{ip})$	0.9998
15	$T_{ip} = 1,142.726 - 250.251 \log_e (t_{ip})$	0.9998
16	$T_{ip} = 1,150.653 - 251.490 \log_e (t_{ip})$	0.9999
17	$T_{ip} = 1,156.691 - 252.342 \log_e (t_{ip})$	0.9999
18	$T_{ip} = 1,161.325 - 252.924 \log_e (t_{ip})$	0.9999
19	$T_{ip} = 1,164.750 - 253.270 \log_e (t_{ip})$	0.9999
20	$T_{ip} = 1,167.590 - 253.545 \log_e (t_{ip})$	0.9999



**Fig. 77 Estimated and selected optimum interpass times for different layers**

A heat transfer FEA is performed using the selected optimum interpass time in order to investigate the interpass temperature and dimension of melt pool. By implementing the optimum interpass time, it is revealed that the target interpass temperature is achieved rapidly and converged within  $\pm 5\%$  range of target interpass time after eight layers of deposition, as shown in Fig. 78. This converging characteristic is faster than those using a fixed interpass time. The highest interpass temperature obtained from FEA using the optimum interpass time is  $442\text{ }^{\circ}\text{C}$  at layer 4.

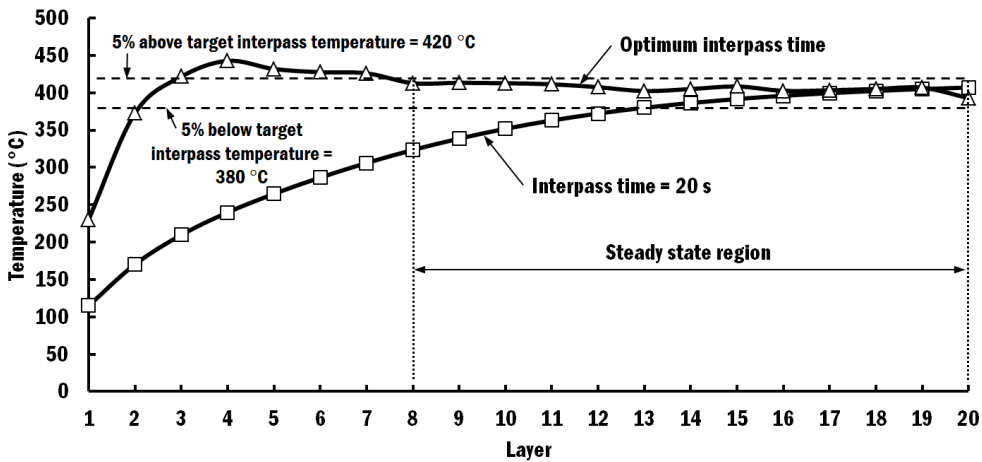


**Fig. 78 Comparison of interpass temperatures between optimum interpass time and fixed interpass time of 20 seconds**

Fig. 79 illustrates the dimensions of melt pool is in steady state region after eight layers of deposition when the interpass temperature is close to the target interpass temperature. The depths and lengths of melt pools at the steady state region vary in the range below  $58\text{ }\mu\text{m}$  and  $166\text{ }\mu\text{m}$ , respectively. These variations are small relative to the dimensions of bead. The steady state dimensions of melt pool and interpass temperatures after eight layers of deposition ensure that the heat transfer characteristic during multi-layer deposition is constant. Hence, the formation of similar microstructure, mechanical properties and cross section of deposited bead after six layers of deposition are consistent. From this viewpoint, the first eight layers have been identified as the



transient layers that should be removed. Therefore, a desired AM part should be fabricated after eight layers of deposition in order to ensure a consistent microstructure and mechanical properties within the part.

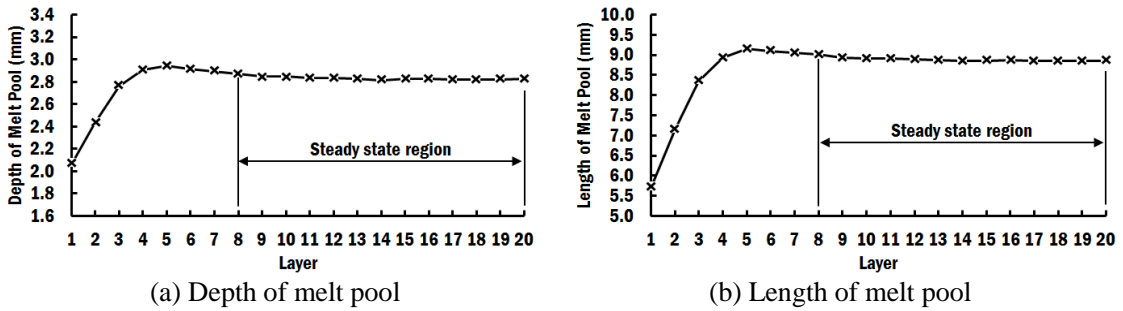


**Fig. 79 Dimensions of melt pool at different layers during deposition process using optimum interpass time**

Fig. 80 shows that the application of optimum interpass time produces promising result in optimizing the total deposition time for 20 layers of beads as compare to those using fixed interpass times. From the aforementioned results and discussion, the proposed methodology to estimate optimum interpass time has been investigated, which can contribute to the improvement of quality and productivity of a wire feeding type DED process.

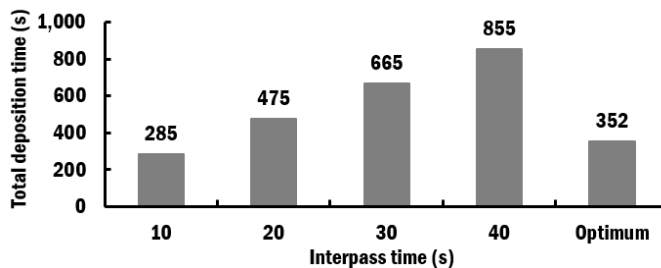


**Fig. 80 Comparison of total deposition time for 20 layers of beads using using different interpass times**

## **F. Investigation of Influence of Power of Laser on Interpass Temperature for a Multi-Layer Deposition**

### **1. Description of the Analysis and Methodology**

In order to shorten the process time during a multi-layer deposition, short interpass time is desired. This study is to investigate the viability of controlling the power of laser to maintain a constant interpass temperature, instead of optimum interpass time.

In this study, short interpass times of 2 seconds and unidirectional deposition pattern are chosen to provide sufficient time for the table to travel to the desired start location of subsequent bead. The travel speed of table is selected as 8 mm/s, respectively. The powers of laser, which can create a bead, are applied such as 1.5 kW, 2.0 kW and 2.5 kW. Twenty layers are simulated during multi-layer deposition. It is assumed that these beads are deposited to form a constant width bead profile. Shielding gas using argon is applied on top of substrate and beads during the DED process.

### **2. Analysis Parameters**

Fig. 81 shows the FEA models of twenty layers deposition are created for different power of laser on a substrate is 80 mm × 40 mm × 5 mm, which are similar to those in Chapter IV Section E to investigate the influence of power of laser on temperature distributions. The unidirectional deposition pattern is applied in this study. Calibrated heat flux is applied according to different power of laser. Due to similar setup, the heat transfer boundary conditions for a multi-layer deposition in Chapter IV Section E are applied. Heat transfer analyses based on analyses conditions shown in Table 26 is carried out using SYSWELD 12.0.

Using the results of FEA, interpass temperatures for different powers of laser are estimated using regression analysis. The applicability of power of laser to maintain a constant interpass temperature and melt pool is evaluated.

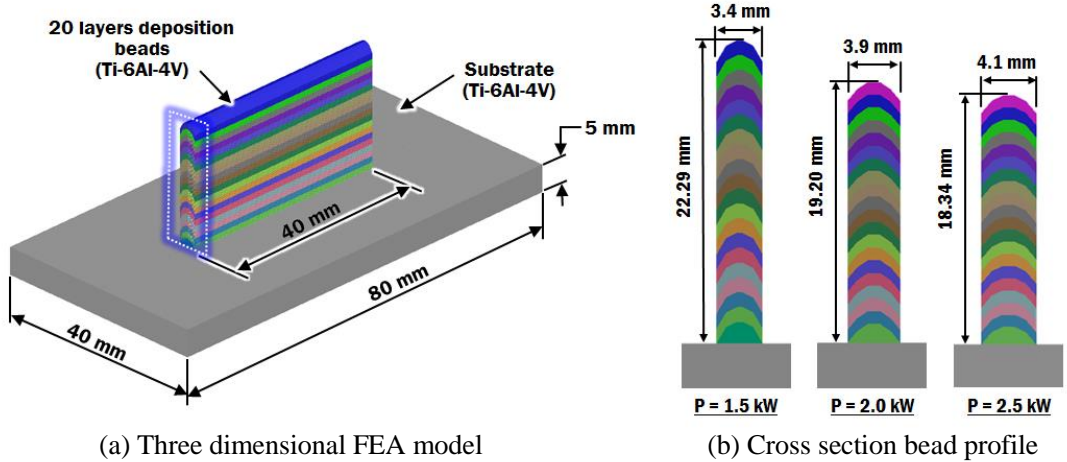


**Fig. 81 Finite element model of 20 layers deposition to investigate influence of power of laser on interpass temperature**

**Table 26 Conditions of analyses to investigate the influence of power of laser on interpass temperature for multi-layer deposition**

Parameters	Power of laser (P, kW)	Travel speed of table (V, mm/s)	Interpass time (s)	Deposition pattern
Range	1.5, 2.0, 2.5	8	2	Unidirectional

### 3. Results and Discussion

Heat transfer FEAs for 20 layers depositions are carried out using different powers of laser with a fixed 2 seconds interpass time. Fig. 82 shows estimated dimensions of melt pools from temperature distributions during deposition of layer 5, 10 and 20 using different powers of laser. It reveals that dimension of melt pool increases as the number of layers increases due to decrease in heat dissipation. The power of laser of 1.5 kW creates the largest size of melt pool due to highest layer thickness and smallest surface area of bead for convection. The size of melt pool is the smallest when the power of laser is 2.0 kW because its efficiency has reduced and its surface area of bead for convection has increased. Even though the power of laser of 2.0 kW has increased, its

reduced efficiency at 45% results to the same total heat input with power of laser of 1.5 kW at efficiency of 60%. At power of laser of 2.5 kW, the size of melt pool increases due to increased total heat input. The observation of size of melt pool matches to the estimated trend of deposition rate for different powers of laser.

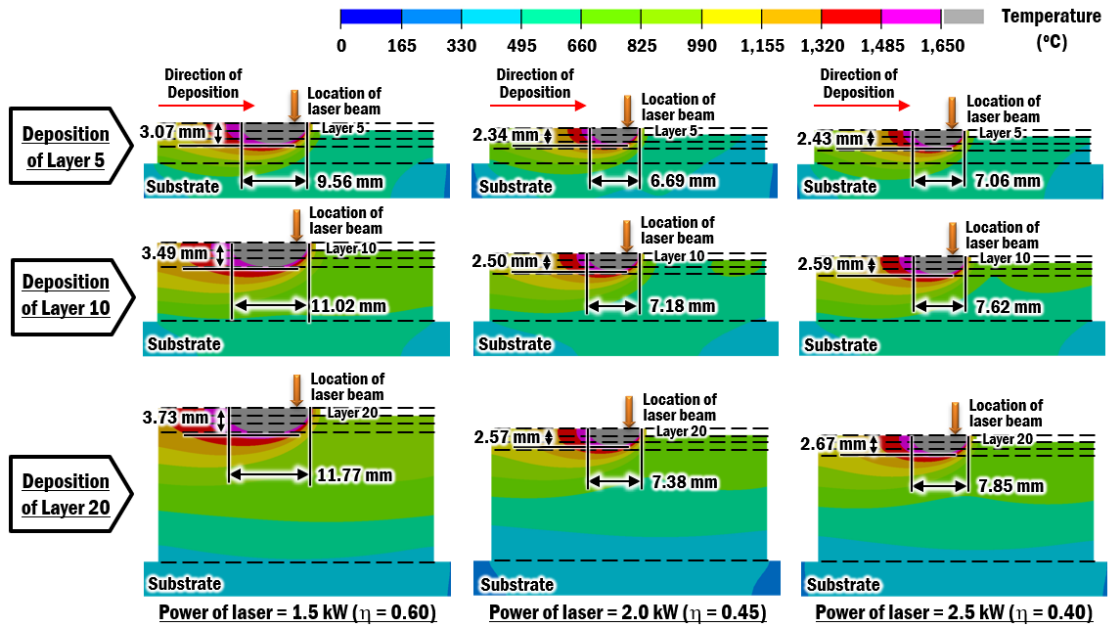


Fig. 82 Estimated melt pool at layer 5, 10 and 20 using different powers of laser

From the results of FEAs, interpass temperatures of each layers are estimated, as shown in Fig. 83. It shows that the interpass temperature approaches a converged value when the number of layers increased for each power of laser. However, none of the power of laser has converged to the desired interpass temperature of 400 °C using interpass time of 2 seconds.

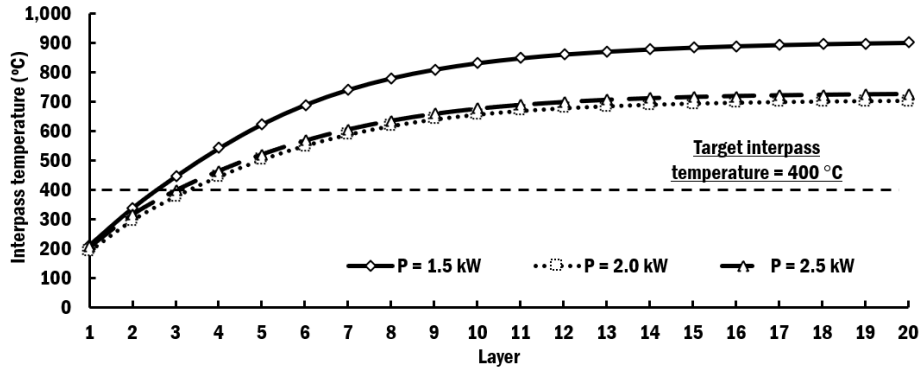


Fig. 83 Interpass temperatures of multi-layer depositions using different powers of laser

From the observation, interpass temperatures ( $T_{ip}$ ) according to power of laser for different layers are best estimated by second order polynomial equations, as shown in Fig. 84. It shows that only polynomial regressions for layer 1 to 3 can be used to predict the power of laser that attain the target interpass temperature of 400 °C. Within the range of power of laser that can create a bead, only polynomial regression for layer 3 can be applied to attain the desired interpass temperature. Hence, control of interpass temperature using power of laser is not viable for this wire feeding type DED system.

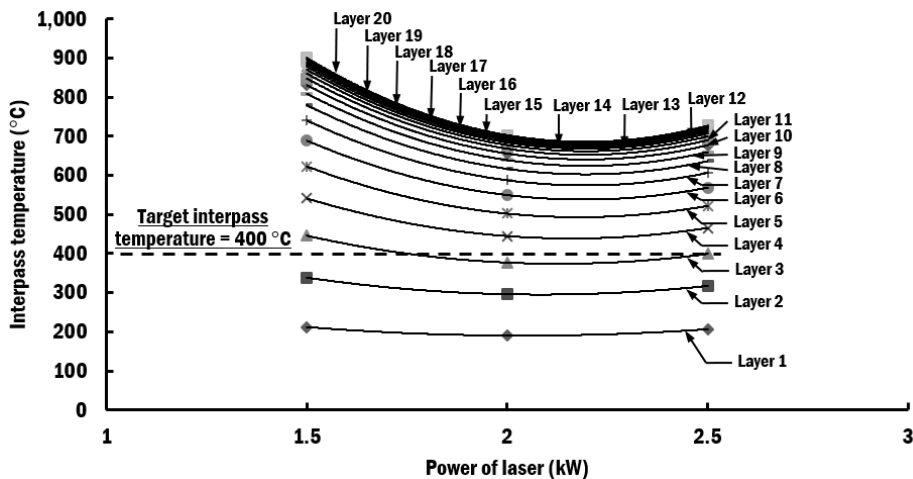


Fig. 84 Estimation of interpass temperatures at each layer for different powers of laser

## **G. Influence of Interpass Time and Deposition Pattern on Thermo-Mechanical Characteristics of a Planar Deposition**

### **1. Description of the Analysis**

Planar deposition is required in DED process in order to obtain a desired width of part. In common practice of DED process, multiple adjacent deposition beads are deposited in succession according to a hatch pattern on a layer.<sup>37</sup> Deposition of beads on the same layer usually occurs with minimal interpass time.

In order to investigate the influence of deposition strategy on the formation of residual stresses in a planar deposited part, two influencing factors such as interpass time and deposition pattern are considered. Short interpass times of 1 second, 2 seconds and 3 seconds are chosen to provide sufficient time for the table to travel to the desired start location of subsequent bead. The deposition patterns include unidirectional deposition and alternative directional deposition. In this study, the power of laser and travel speed of table are selected as 1.5 kW and 8 mm/s, respectively. Six beads are simulated during planar deposition. It is assumed that these beads are deposited at optimum hatch spacing to form a flat top bead profile. Argon gas is supplied on top of substrate and beads as the shielding gas during the DED process. The supply of argon is terminated 3 seconds after the end of the deposition. The specimens are cooled by natural convection of air thereafter, for 40 minutes after the end of the deposition.

### **2. Analysis Parameters and Boundary Conditions**

Fig. 85 shows a three-dimensional FE model with six overlapping beads to form a planar deposit. The bead section profile for planar deposition is created based on the flat top overlapping model, as described earlier in Chapter II Section D. The room temperature is assumed at 20 °C. Calibrated penetration depth and efficiency for top hat heat flux model in Chapter III is applied at

the top of the bead. Different interpass times and deposition patterns are applied in this study, as shown in Table 27. All nodes at surface of clamped region are constrained in translation and rotation. Temperature dependent material properties of Ti-6Al-4V are assigned. The proposed heat transfer boundary conditions such as coefficients of natural and forced convections in Chapter IV Section C are applied due to similar size of substrate and beads. The thermo-mechanical FEAs are carried out using SYSWELD 12.0.

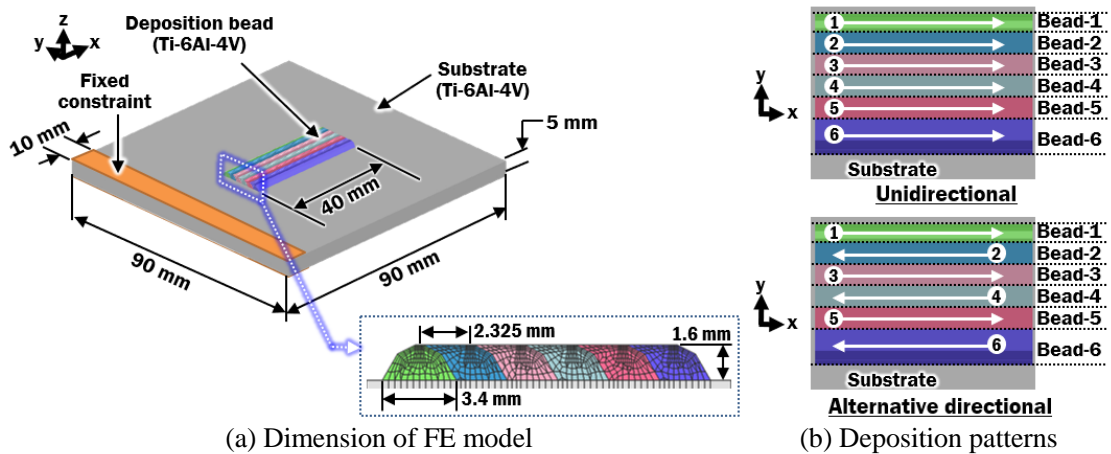


**Fig. 85 FE model to investigate the influence of deposition strategy on thermo-mechanical characteristics of planar deposition**

**Table 27 Analysis conditions to investigate the influence of deposition strategy on thermo-mechanical characteristics of planar deposition**

Parameters	Power of laser (P, kW)	Travel speed of table (V, mm/s)	Interpass time (s)	Deposition pattern
Range	1.5	8	1, 2, 3	Unidirectional, Alternative directional

### 3. Results and Discussion

Finite element analyses are carried out to investigate the heat transfer characteristics on the formation of melt pool during deposition of beads. Fig. 86 illustrates the temperature histories at different measured locations during deposition of three beads for unidirectional and alternative directional deposition patterns. The temperatures during laser irradiation along the same bead are

almost similar, regardless of deposition patterns. This deduces that dimensions of melt pool for the same bead should be similar.

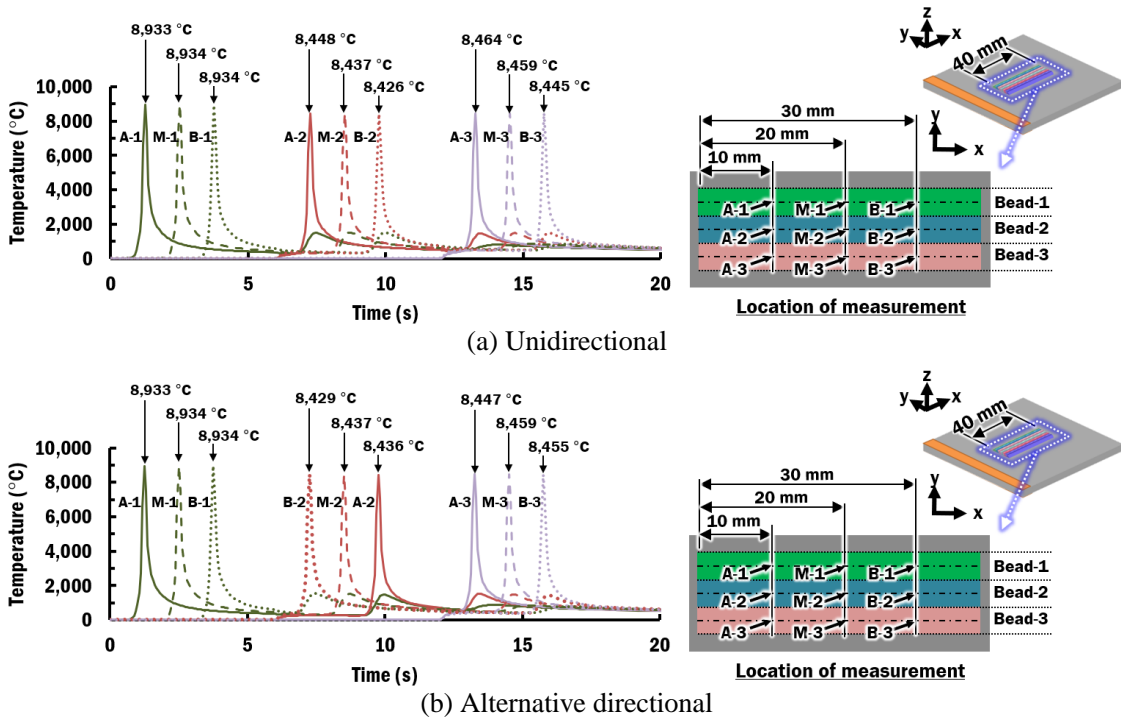


**Fig. 86 Comparison of temperature histories on bead 1, 2 and 3 for different deposition patterns (interpass time of 1 s)**

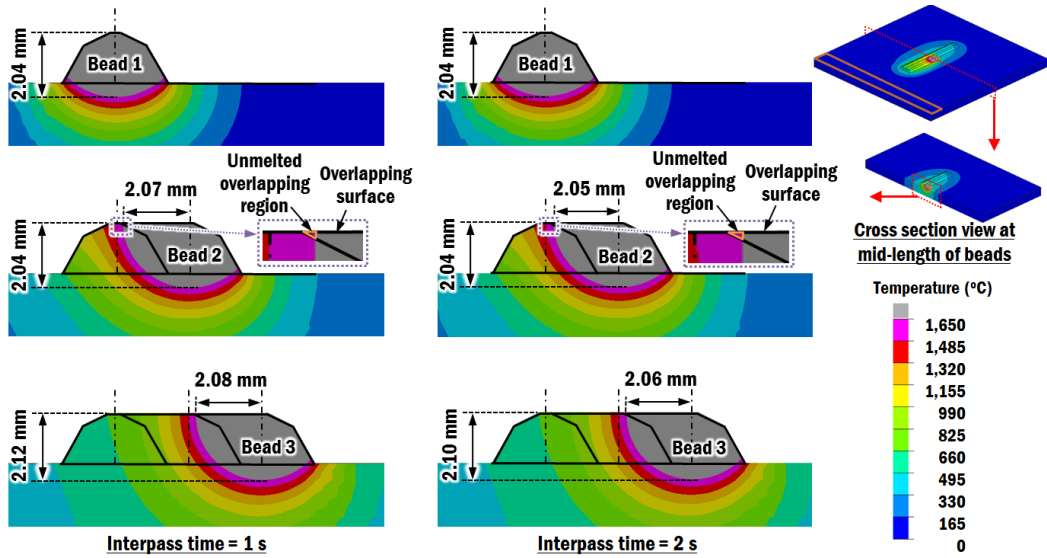
From the results of temperature distribution, the dimensions of melt pool for different beads are estimated during DED planar deposition, as shown in Fig. 87. The melt pool is estimated as the region that has temperature exceeds 1,650 °C, which is the liquidus melting temperature of Ti-6Al-4V.

In the same process condition, it is observed that the depth of melt pool increases slightly from bead 1 to bead 3, due to increase in temperature of substrate. Partial remelting of adjacent bead occurs during deposition of subsequent beads. The increment of depth of melt pools for different beads is less than 0.08 mm, which is relatively small and negligible.

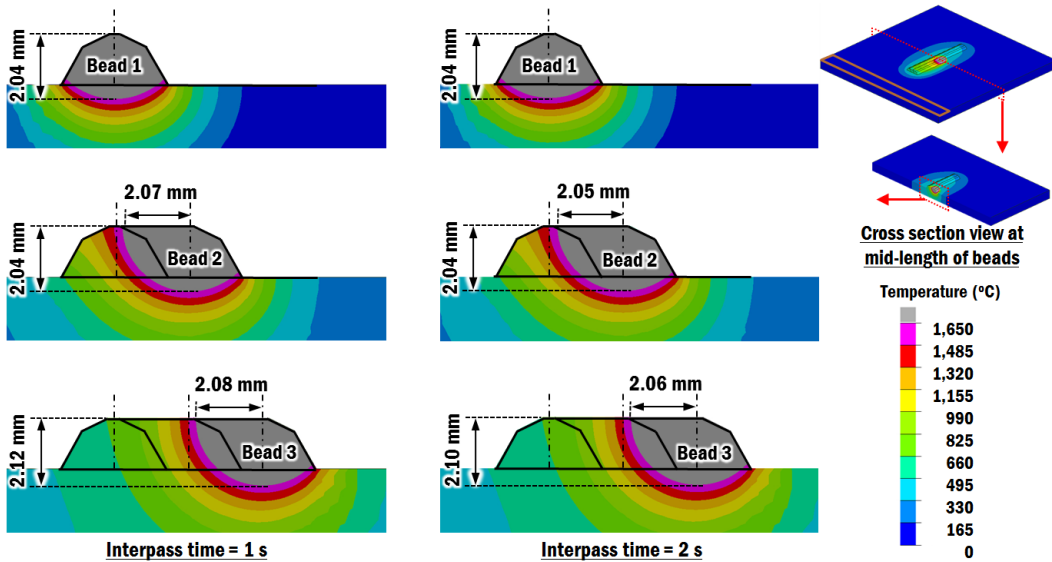
An increment of 0.01 mm in horizontal distance of melt pool measured from the center of



laser beam is observed from deposition of bead 2 to bead 3. The increase of horizontal distance of melt pool is much smaller compared to the increase of depth of melt pool. This indicates that the conductive heat transfer to the substrate is greater than to the adjacent bead due to larger volume for heat dissipation.



(a) Unidirectional deposition pattern



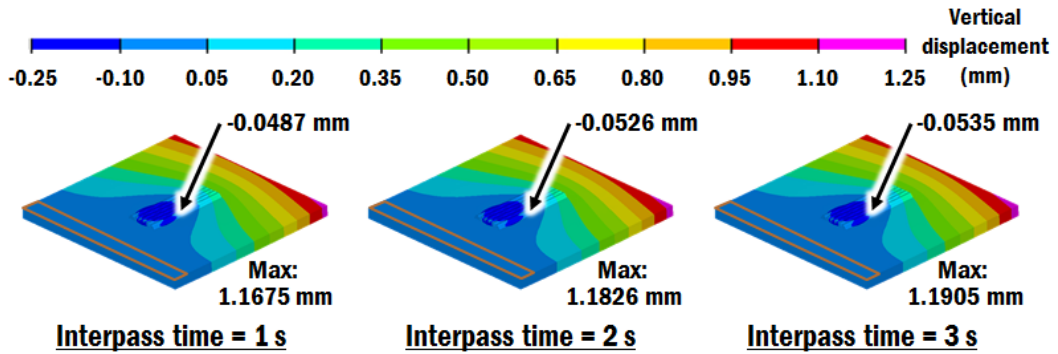
(b) Alternative directional deposition pattern

Fig. 87 Estimated dimensions of melt pool during formation of bead 1, 2 and 3 using different interpass times

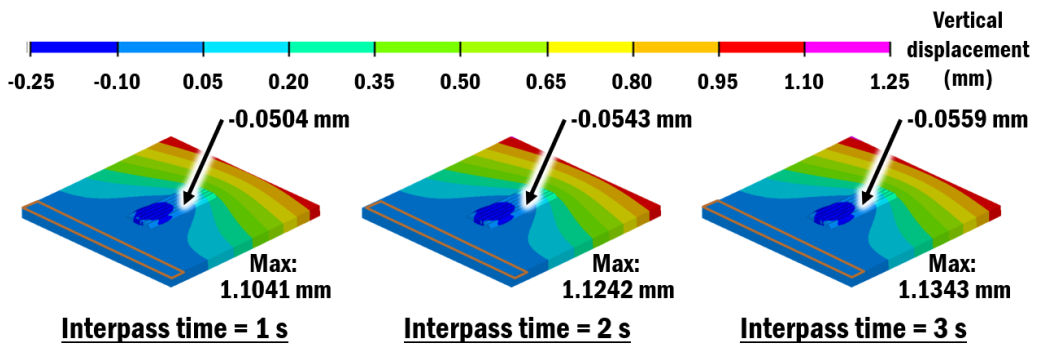
From detail examination of bead 2 in Fig. 87(a), it shows that the horizontal distance of melt pool almost reaches the top surface of bead 1 to form a flat top overlapping surface. Only a tiny unmelted overlapping region is observed. This observation of negligible unmelted overlapping region is crucial to reveal that a flat-top overlapping bead is properly formed by melting across the overlapping surface. Hence, it is deduced that the distance between centers of bead has been properly selected.

For the same deposition pattern, the increment of dimensions of melt pool is slightly reduced when the interpass time is increased due to longer interpass cooling. The dimensions of melt pool for the same interpass time are identical, regardless of deposition pattern. From these observations, it is revealed that the deposition strategy has negligible influence on the formation of melt pool.

Thermo-mechanical FEAs are carried out to estimate the displacements and residual stresses on the planar deposition using different deposition strategies. Vertical displacement distribution of the deposited part for different deposition strategies are evaluated after 40 minutes cooling process, as shown in Fig. 88. It is observed that the maximum vertical displacement occurs at the free end corner of substrate, which lies nearest to the bead 6. The unidirectional deposition pattern causes greater maximum vertical displacement as compared to the alternative directional deposition pattern. This is attributed to the heat source moving consistently towards the free end of substrate and causes the free end to deflect upward in the unidirectional deposition pattern. The maximum vertical displacement of the substrate increases as the interpass time increases. This is because longer interpass time allows more thermal expansion to occur on the substrate.



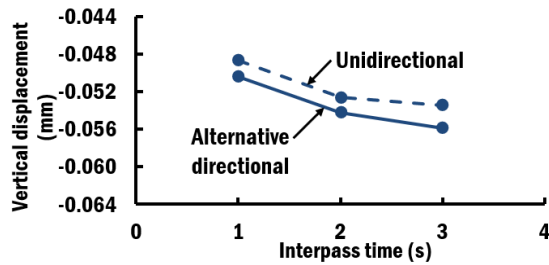
(a) Unidirectional deposition pattern



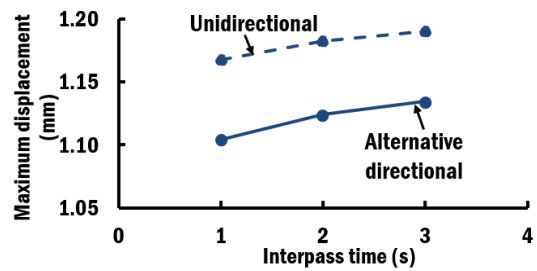
(b) Alternative directional deposition pattern

**Fig. 88 Influence of different deposition strategies on vertical displacement distributions of planar deposited part after cooling process**

In order to further investigate the influence of deposition strategy on vertical displacement of deposited part, estimated vertical displacements at the mid-length of bead 6 are compared and discussed for different deposition strategies in Fig. 89(a). It is revealed that the increase of interpass time slightly increases vertical displacement in the downward direction due to the fact that adjacent beads have longer time to deflect before the next deposition takes place. Hence, slightly larger displacement is accumulated within the bead.



(a) Vertical displacement at mid-length of bead 6



(b) Maximum vertical displacement

**Fig. 89 Influence of different interpass times on vertical displacement after cooling process**

The unidirectional deposition pattern produces slightly lower vertical displacement on the deposited bead as compared to the alternative directional deposition pattern. This characteristic is related to the influence of deposition pattern on the formation of maximum vertical deflection of the substrate because the planar deposition beads are deposited directly on the substrate, as shown in Fig. 89(b). Therefore, alternative directional deposition pattern is preferred for planar deposition to reduce overall distortion of specimen.

Fig. 90 shows residual stress distributions of the part for different deposition strategies after 40 minutes cooling process. It is revealed that induced residual stresses increase from bead 1 to bead 6. The maximum residual stress within the deposited beads lies in the mid-length of bead 6.

In the case of same deposition pattern, the increase of interpass time contributes to small increment of maximum residual stress induced in beads, as shown in Fig. 91. This is attributed to the fact that shorter interpass time produces slight slower cooling rate within the bead. Hence, the induced residual stress is slightly relieved, similar to the effect of preheating.

Planar deposition using alternative deposition pattern induces almost similar maximum residual stress within mid-length of bead 6 as those deposited by unidirectional deposition pattern in case of same interpass time. This is because the alternative directional deposition pattern induces almost identical vertical displacement at the mid-length of deposited bead 6 as compared to the unidirectional deposition pattern. Thus, influence of deposition pattern on the formation of residual stress is negligible.

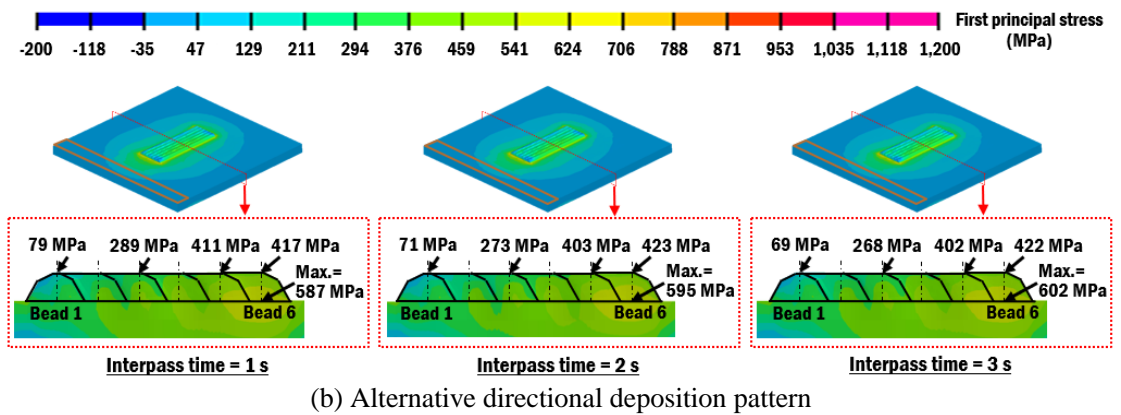
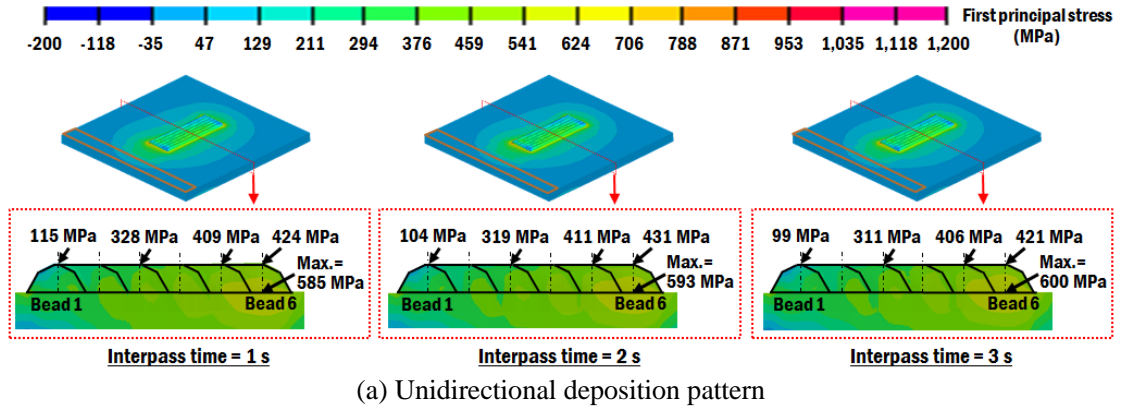


Fig. 90 Influence of different deposition strategies on residual stress distributions of planar deposited part after cooling process

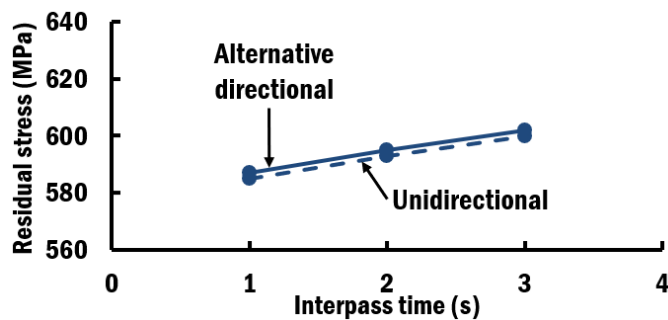
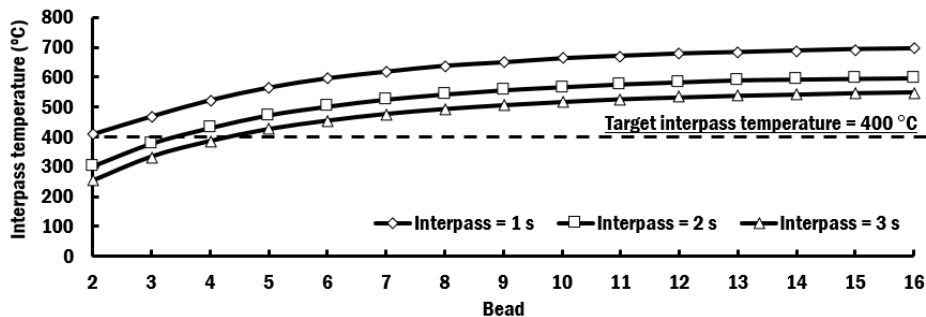


Fig. 91 Influence of different interpass times on maximum residual stress within bead 6 after cooling process

Since the deposition pattern has negligible influence on the formation of residual stresses within deposited bead, alternative directional deposition pattern is recommended for planar deposition from the viewpoint that it induces lesser distortion to the deposited beads and substrate. The short interpass time of 1 s is recommended to produce slightly lower residual stress within deposited beads. However, the selection of proper interpass time to maintain a constant interpass temperature is more critical from the viewpoint of maintaining the similar microstructure and size of melt pool.

Based on the same methodology proposed in Chapter IV Section E, proper interpass time for each bead on planar deposition is estimated using heat transfer analyses of planar deposition of sixteen beads. From the results of heat transfer FEAs, estimated interpass temperatures at the interpass temperature control node of each bead are estimated, as shown in Fig. 92. The convergence of interpass temperature is achieved when the number of bead deposition increases on the substrate. This is because the temperature of substrate has become stable.



**Fig. 92 Interpass temperatures of planar depositions using different interpass times**

Fig. 93 shows the interpass temperatures for different beads estimated by logarithmic regression equations. Using the logarithmic regression equations, proper interpass time of each bead for maintaining a target interpass temperature of 400 °C during planar deposition is predicted and shown in Fig. 94. Selected proper interpass time of each bead is rounded to the nearest second with minimum value of 1 second, for practical implementation during a DED process.

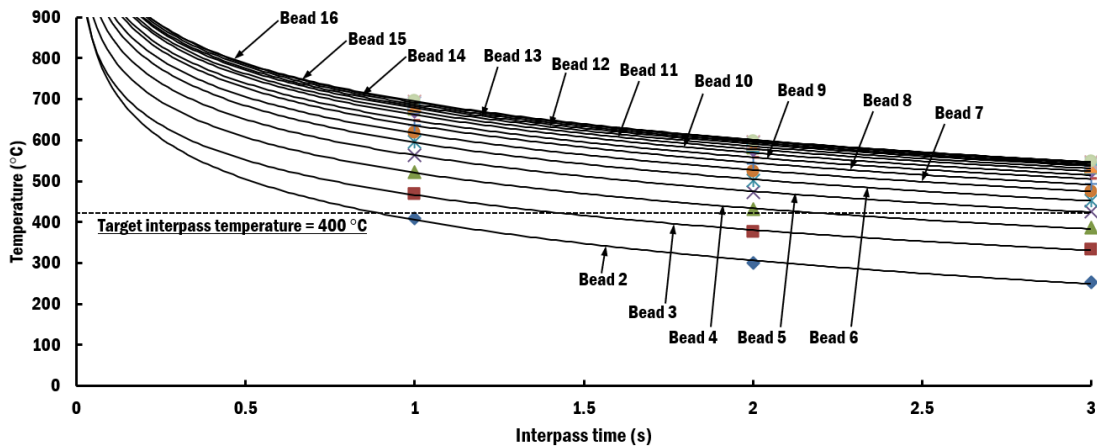


Fig. 93 Estimation of interpass temperatures at each bead for different interpass times

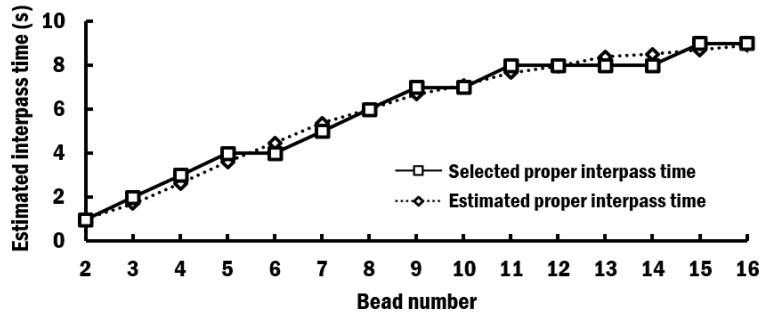


Fig. 94 Estimated and selected proper interpass times for different beads during planar deposition

Fig. 95 illustrates the interpass temperature lies within  $\pm 5\%$  of target interpass temperature at the ninth bead of deposition and onwards. Fig. 96 shows the depth of melt pool is in steady state region at ninth beads of deposition and onwards when the interpass temperature is close to the target interpass temperature. The variation of depths of melt pools at the steady state region is small, which is in the range below  $17 \mu\text{m}$ . The steady state dimensions of melt pool and interpass temperatures ensure that the formation of HAZ and microstructure transformation during planar deposition is constant. From these viewpoints, the selected proper interpass time should be used since the increment of interpass time does not have significant influence on residual stress as compared to the yield strength of Ti-6Al-4V.

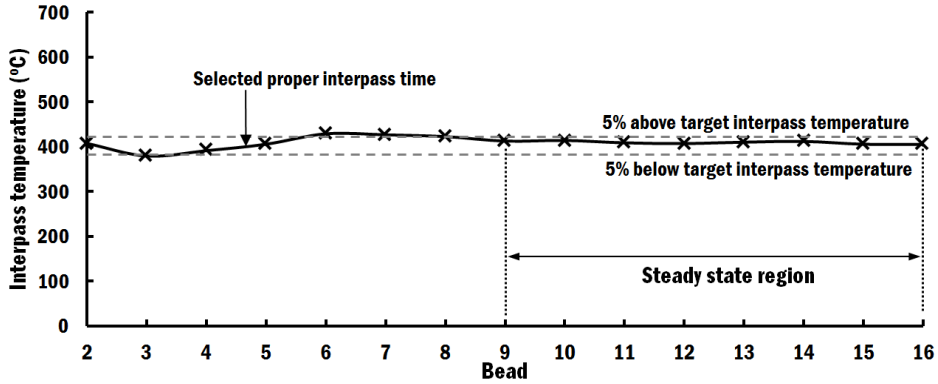


Fig. 95 Interpass temperatures of planar depositions using selected proper interpass time

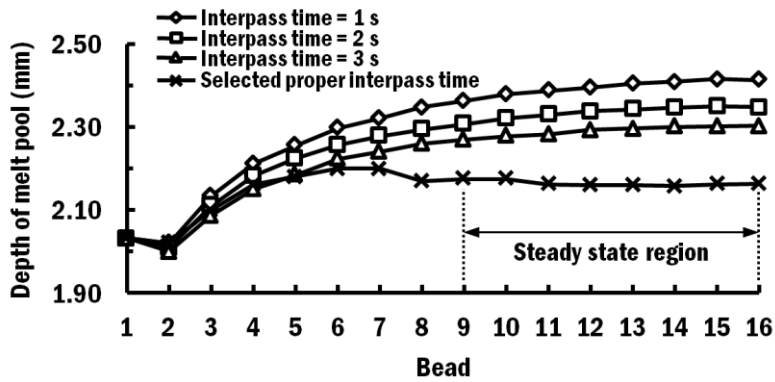


Fig. 96 Depth of melt pool for different beads during deposition process using different interpass times

These understandings of influence of different interpass times and deposition patterns on formation residual stresses of planar deposition by a wire feeding type DED process are important insight for the selection of proper deposition strategy and plan.



## V. ACTIVATION ALGORITHM OF FINITE ELEMENTS

### A. Introductory Remarks

#### 1. Description of Activation Algorithm

In order to simulate the deposition of material on the substrate during a DED process in a FEA model, progressive element activation is applied. The volume of deposited material is assumed to be equal to the volume of elements being activated for numerical consideration in the FE software. The activation of finite elements depends on the usage of either quiet elements or inactive elements.<sup>60,147</sup>

The quiet elements are the finite elements that have been assigned with reduced material properties so that their presence in the FEA model has minimal effect on the analysis. Therefore, quiet elements are included in FEA model at the beginning of simulation. The quiet elements are turned into active finite elements later, by reassigning their material properties to the actual material properties.<sup>60,89,147</sup> A proper selection of reduced material properties is required to avoid ill-condition in the solution matrix.

The inactive elements are the finite elements that have been deactivated in FEA model at the beginning of simulation.<sup>60,90,147</sup> During the solution of analysis, the inactive elements are not included in the system of equations. In order to simulate the material being added, the inactive elements are reactivated progressively during the simulation. Therefore, reactivation of inactive elements requires reconstruction of system of equations during the computation steps. This technique is more accurate than quiet elements method. However, this method is more complicated and may consume more time.<sup>60</sup>

In this study, the activation of inactive elements is chosen to be implemented in a FE software ABAQUS in order to evaluate the accuracy of this method against the commercial software SYSWELD, due to its better performance.

## 2. Related Works

Activation of quiet elements has been implemented by commercial software such as SYSWELD and researchers due to its ease of implementation via subroutines and faster.<sup>74,85,146,147</sup> Small reduction factor of  $1 \times 10^{-6}$  to the material properties of the quiet element has been assigned by Yang et al and Michaleris.<sup>27,147</sup> However, it can result in errors and long computational time depending on the selection of reduction factor of material properties.<sup>89,147</sup> In order to determine the accuracy of quiet element technique, researchers have used the inactive element activation technique as the reference.<sup>147</sup>

Activation of inactive elements has been implemented by several researchers for a DED process such as Chiumenti et al. (2010) and Lundbäck et al. (2011).<sup>60,90</sup> In their study, volume of inactive element, which will be activated during the process, was represented by one finite element cross section that has equal volume as the filler wire at each time-step.<sup>60,90</sup> The activation of inactive elements is according to the position of the center of the heat source. For a heat source model with small radius of beam, a large portion of the heat flux was not absorbed by the yet to be activated element.

Besides, Chiumenti et al. (2010) initialized the elements to be activated with liquidus temperature to prevent high thermal stress during element activation. This setting of temperature was estimated to contribute additional 2.5% to the input power.<sup>60</sup>

Michaleris (2014) applied a complicated element search algorithm to activate inactive elements within the heat application region of 95% of the peak value from the center of heat source.<sup>147</sup> This criteria for element activation is only suitable for the FEA model with finite elements that are much smaller than the heat application region.

Anca et al. (2011) set the inactive element activation according to process time.<sup>89</sup> They also set the initial temperature of the newly activated element to be equal to the metal liquidus temperature.<sup>89</sup> A double elliptical heat source model, which has large heat application region, was

applied in their study.

From these literatures, none of the activation algorithm of inactive elements has been developed for heat source model with small radius of beam such as laser or electron beam. In view of that, an element activation algorithm suitable for heat source model with small radius is required to properly capture the heat flux without burdening the computational load in a FE software. A portion of the work presented here has already been published in the International Journal of Precision Engineering and Manufacturing in 2019.<sup>148</sup>

## B. Proposed Element Activation Algorithm

### 1. Description of Proposed Element Activation Algorithm

This study proposes an activation algorithm of inactive element to be implemented in a general purpose FEA software, ABAQUS. This algorithm is general and can be adapted to be implemented in other general purpose FEA software. In this algorithm, the following assumptions are made to simulate a DED process:

- (1) The substrate and deposited bead are represented by active elements.
- (2) The material yet to be deposited was represented by inactive elements.
- (3) A bead is created with a constant cross section with full layer thickness during material deposition.
- (4) Finite elements are activated before the heat source is applied on the top of the bead at the beginning of each calculation step.
- (5) The displacement of specimen is small such that the location of activated elements on the specimen is predictable based on the location of center of beam.

Fig. 97 shows the activation of inactive elements at the begin of computational steps and the corresponding position of heat source during the steps.

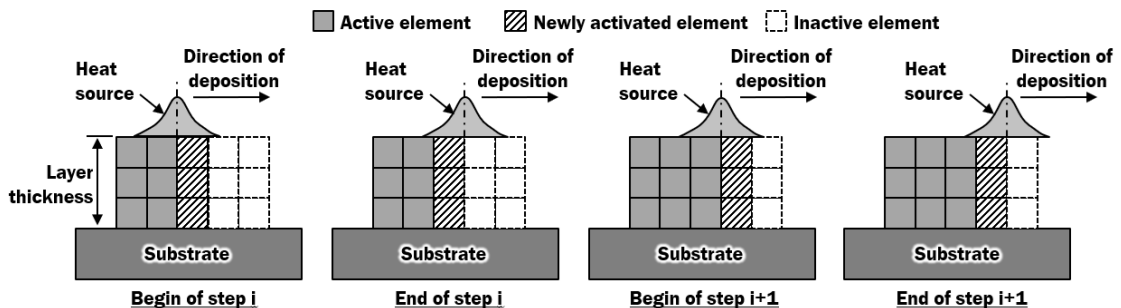


Fig. 97 Schematics of the inactive element activation

A high intensity heat source for additive manufacturing, such as laser and electron beam,

usually has a small radius of beam. In order to capture the heat flux distribution of a heat source model with small radius, the mesh size of finite element ( $x_e$ ) can be designated such that it satisfies the range in Eq. (61)

$$0.5r < x_e \leq r \quad (61)$$

where  $x_e$  and  $r$  are the mesh size of finite element and radius of beam, respectively. The heat source model covers at least three nodes along the direction of deposition when Eq. (61) is satisfied, as shown in Fig. 98. Further reduction of mesh size will increase the computational load, which is not practical for a FEA analysis of a DED process with multiple beads. On the other hand, increasing the mesh size beyond the recommended range can result to loss of heat source profile.

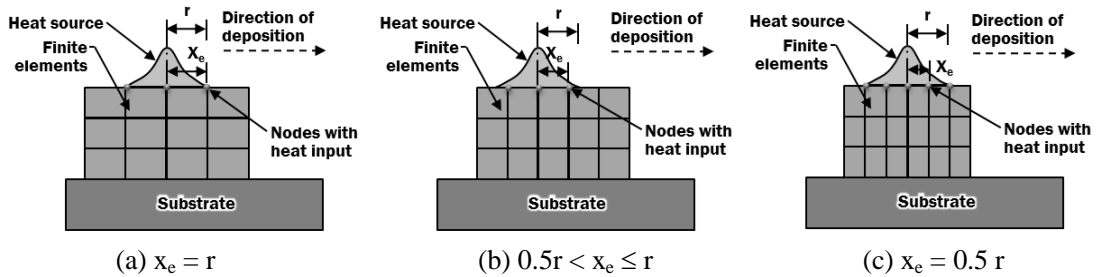


**Fig. 98 Heat flux on top of elements**

The step time ( $t_{\text{step}}$ ) is determined by the mesh size ( $x_e$ ) and travel speed of table ( $V$ ), as described in Eq. (62).

$$t_{\text{step}} = \frac{x_e}{V} \quad (62)$$

The elements to be activated are searched by comparing the coordinate of the nodes with the location of heat source and the list of elements for each layer of bead. The elements to be activated for each step are located within the lower and upper bounds of coordinates in Eqs. (63)-(65)

$$X = \begin{cases} [0, bx_e], & \text{for first step of each layer} \\ [bx_e, (b + 1)x_e], & \text{otherwise} \end{cases} \quad (63)$$

$$Y = [-0.5w_b, 0.5w_b] \quad (64)$$

$$Z = [-h_b, 0] \quad (65)$$

where  $X$  is the  $x$ -coordinate relative to the center of beam,  $Y$  is the  $y$ -coordinate relative to the center of beam,  $Z$  is the  $z$ -coordinate relative to the center of beam,  $b$  is the constant number of front element cross section to be added ahead of beam center,  $w_b$  is the width of deposited bead, and  $h_b$  is the height of deposited bead. Fig. 99 shows the schematic of element cross section being activated with respect to the constant value of  $b$ .

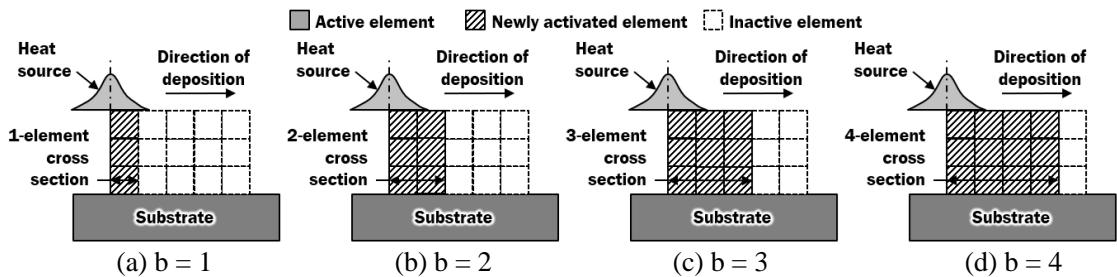


**Fig. 99 Setting of front element cross section activated ahead of center of beam**

Based on the step time and process time, the set of inactive elements to be activated can be selected programmatically via an external program such as Matlab. The set of elements to be activated are inserted into their designated step of a FEA. The predetermined set of elements are activated during step iteration using model change interaction in ABAQUS.

Fig. 100 shows the flowchart of the activation algorithm of inactive finite elements for a heat transfer FEA. In this algorithm, it is clearly revealed that the selection of finite elements is

performed independently using Matlab before they are included into FEA in ABAQUS. This independency has the advantages of saving computational time and memory because each program runs separately and restart files in ABAQUS are not required to be reloaded into memory for every computational step. The sets of inactive finite elements to be activated are grouped into individual input files and included into a main heat transfer FEA file in ABAQUS according to the sequence of steps. The heat transfer FEA is then carried out using ABAQUS to progressively activate the inactive elements until the end of steps. The heat transfer FEA using ABAQUS produces the result of temperature distribution for each node.

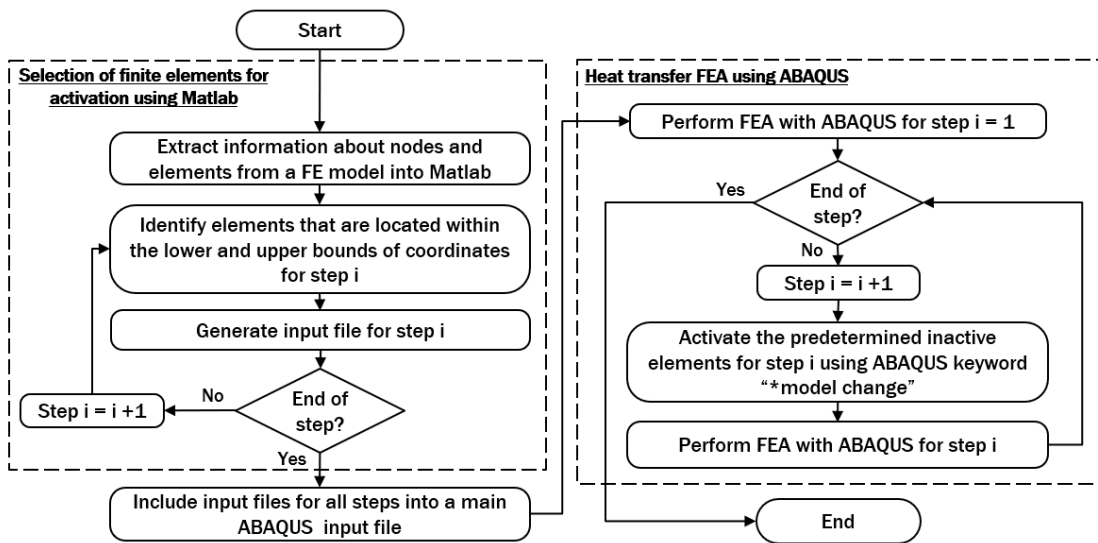


**Fig. 100 Activation algorithm of inactive finite elements for heat transfer FEA using Matlab and ABAQUS**

The activation algorithm of inactive finite elements is extended for a decoupled thermo-mechanical FEA, as illustrated in the flowchart in Fig. 101. Decoupled thermo-mechanical FEA refers to thermo-mechanical FEA that has the heat transfer analysis carried out before the mechanical FEA is performed based on the temperature distribution results of the heat transfer analysis. Hence, the deflection of clamped part during process does not affect the heat transfer

analysis. Decoupled thermo-mechanical FEAs are preferred in most welding and additive manufacturing FEAs because it is less computational expensive and the deflection of clamped part is negligible as compare to the magnitude of travel speed of table during material deposition of an additive manufacturing process. Similar to the activation algorithm of inactive elements for heat transfer FEA, the Matlab code is applied to generate individual input files according to computational step by including the set of inactive elements to be activated. Each individual input file is set to read temperature distribution from result of heat transfer FEA for the corresponding step. These individual input files are included into a main mechanical FEA file in ABAQUS according to the sequence of steps. The mechanical FEA is then carried out using ABAQUS to progressively activate the inactive elements until the end of steps. The mechanical FEA using ABAQUS predicts the displacement and stress distribution on the part based on the input of temperature distribution.

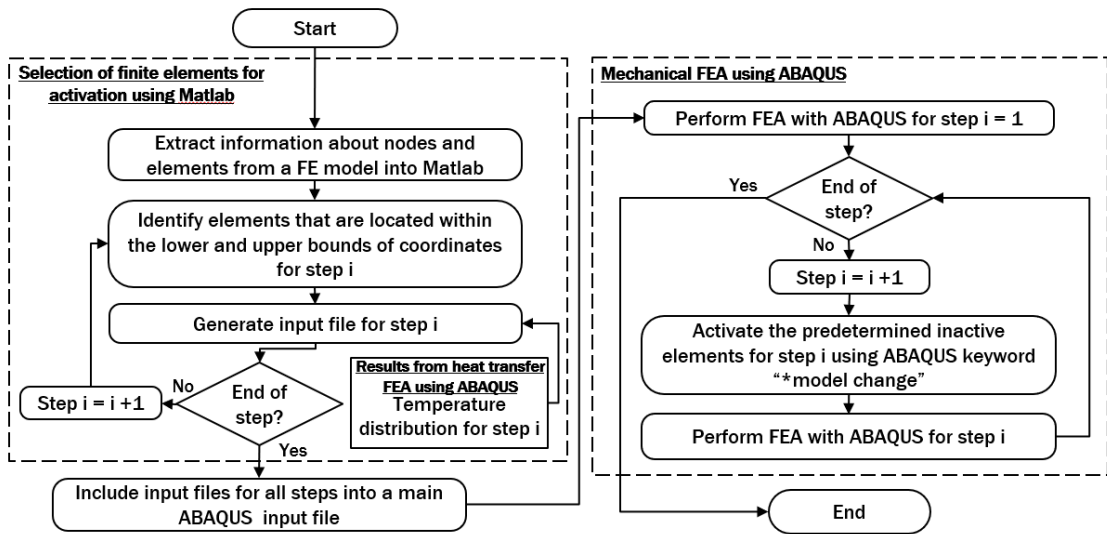


**Fig. 101 Activation algorithm of inactive finite elements for mechanical FEA using Matlab and ABAQUS**



## C. Selection of Front Element Cross Section for Proposed Element Activation Algorithm

### 1. Description of Heat Transfer Analysis and Boundary Conditions

In order to investigate the applicability of the proposed activation algorithm of inactive elements, a simple three-dimensional finite element model is designed as shown in Fig. 102. A heat transfer FEA is performed to simulate three layers DED deposition on a 90 mm × 90 mm × 5 mm substrate. A laser beam with power of 1.5 kW is assumed. The specimen is moving at 8 mm/s in x-direction relative to the position of laser beam during the deposition process. A rectangular cross-sectional bead of 3.4 mm (width) × 1.6 mm (height) is created during the process. An interpass time of 2 s is added in between each deposition layer. Temperature dependent material properties are assigned to the deposited bead and the substrate. All surfaces are subjected to natural convection and radiation, based on values used by Michelaris (2014).<sup>147</sup> The initial temperature of substrate and deposited bead are assumed to be at the ambient temperature. The values for these boundary conditions are shown in Table 28.

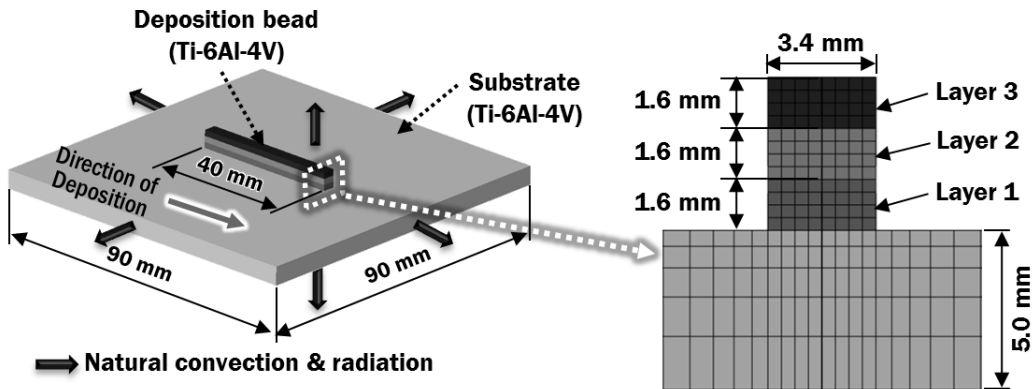


Fig. 102 FEA model to investigate the influence of number of element cross section

**Table 28 Analysis parameters and boundary conditions to investigate the influence of number of element cross section**

Parameters	Number of front element cross section (b)	Ambient temperature (°C)	Coefficient of natural convection ( $h_{conv}$ , $W/m^2 \cdot ^\circ C$ )	Emissivity ( $\epsilon$ )	Material of substrate	Material of deposited bead	Interpass time (s)
Range	1-4	20	10	0.5	Ti-6Al-4V	Ti-6Al-4V	2

## 2. Heat Flux Model

A heat source with Gaussian heat flux distribution is assigned to the top surface of a bead. The heat flux intensity of a surface, which decreases with increasing value of Z-coordinate, is defined by Eq. (66):

$$Q(r, Z) = Q_0 \cdot \left(1 - \frac{Z}{d_p}\right) \cdot e^{\left[-\frac{K(x^2+Y^2)}{r_b^2}\right]} \quad (66)$$

where K is the Gaussian beam propagation factor.

By taking the integral of heat flux equal to the input power of laser, as defined in Eq. (67),

$$P = \int_0^{d_p} \int_0^\infty \int_0^{2\pi} Q(r, Z) \, d\theta_{sys} \cdot r \, dr \cdot dZ \quad (67)$$

the volumetric heat source model is obtained in Eq. (68):

$$Q(X, Y, Z) = \frac{\eta KP}{\pi r_b^2} \cdot \left(\frac{2}{d_p}\right) \cdot \left(1 - \frac{Z}{d_p}\right) \cdot e^{\left[-\frac{K(x^2+Y^2)}{r_b^2}\right]} \quad (68)$$

where Q is the heat flux,  $\eta$  is the efficiency of laser, P is the power of laser, and  $d_p$  is the penetration depth of laser. The conditions of the heat source model are assigned as in Table 29. The  $x_c$  are chosen to be 0.5 mm to satisfy Eq. (61).

**Table 29 Conditions of heat source model and mesh size of finite element**

Parameters	Efficiency of laser beam ( $\eta$ )	Power of laser (P, W)	Radius of laser beam ( $r_b$ , mm)	Penetration depth of laser beam ( $d_p$ , mm)	Mesh size of finite element ( $x_e$ , mm)
Range	0.6	1,500	0.75	0.2	0.5

Using the Lagrangian coordinate system, the coordinates are defined as relative coordinate with respect to the moving frame of heat source by Eqs. (69)-(71):

$$X = x - V_x \cdot t_{\text{layer}} \quad (69)$$

$$Y = y - V_y \cdot t_{\text{layer}} \quad (70)$$

$$Z = z - h_b \quad (71)$$

where  $x$  is the  $x$ -coordinate relative to fixed frame,  $y$  is the  $y$ -coordinate relative to fixed frame,  $z$  is the  $z$ -coordinate relative to fixed frame,  $V_x$  is the travel speed of the table along  $x$ -axis,  $V_y$  is the travel speed of the table along  $y$ -axis,  $t_{\text{layer}}$  is the process time of the corresponding layer, and  $h_b$  is the height of deposited bead. The moving frame of heat source is attached to the center of heat source.

### 3. Results and Discussion

From transient heat transfer analyses for various values of front element cross section (b), the temperature history for three nodes are obtained as shown in Fig. 103. The highest temperature is observed when the center of heat source is located at the measured location of nodes. This

distribution is expected when a Gaussian heat flux is assigned on the surface of bead because the highest heat flux is at the center of beam. The nodal temperatures remain at ambient temperature before the inactive elements are being activated. These nodal temperatures characteristics show that the inactive elements are not affecting the overall heat transfer and are proper in accordance to the phenomena of DED deposition.

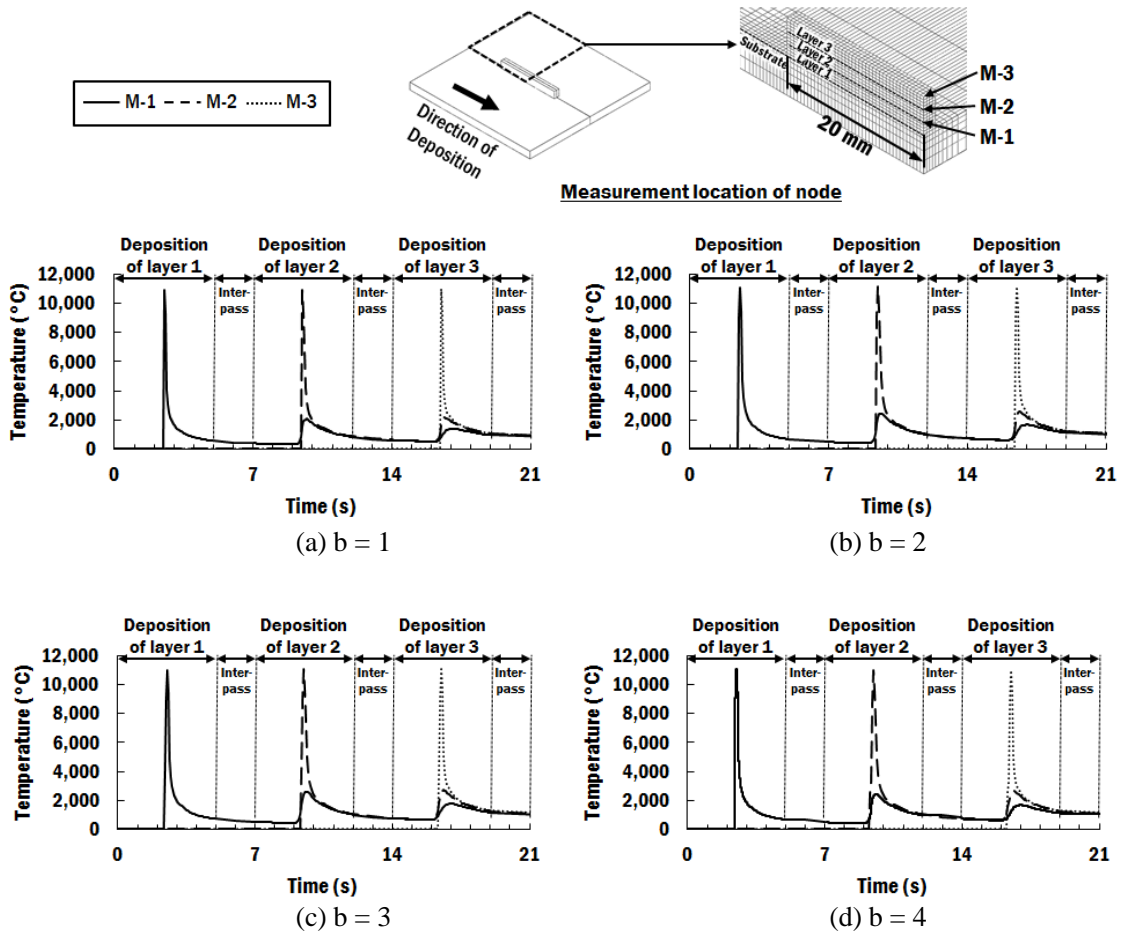


**Fig. 103 Temperature histories at measured nodes for various constants of front element cross section**

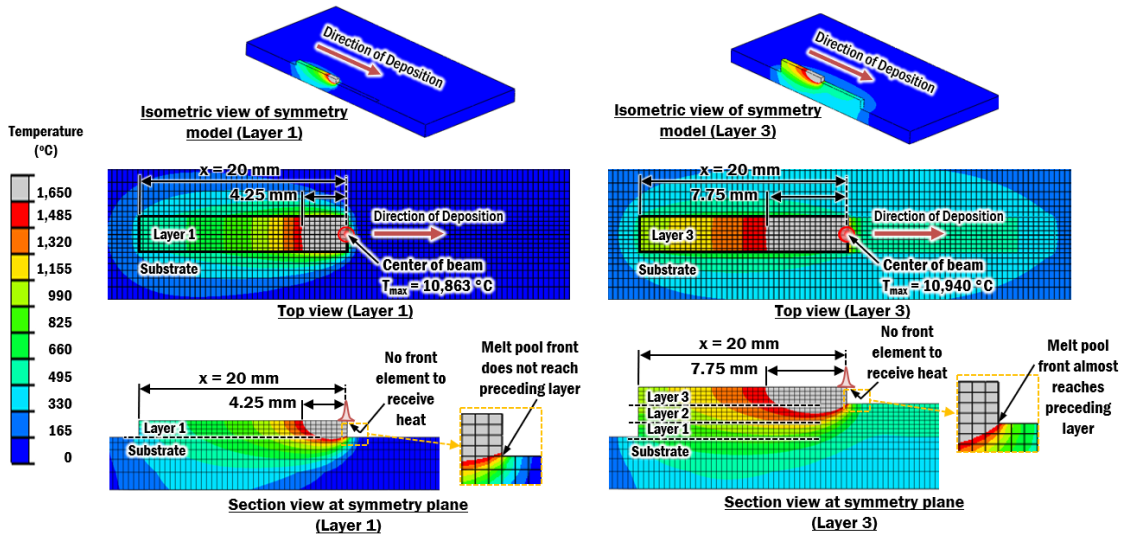
Fig. 104 shows the temperature distributions on the part when the laser beam is irradiating at the middle ( $x = 20$  mm) of first layer and third layer of bead. The second layer of bead is not shown

because its results lie in the first layer and third layer of beads. Therefore, the focus of discussion will be on first layer and third layer of beads, which represent a deposition on a substrate and a deposition on a preceding layer, respectively. The gray color region represents the melt pool, where the temperature exceeds the liquidus melting temperature of Ti-6Al-4V.

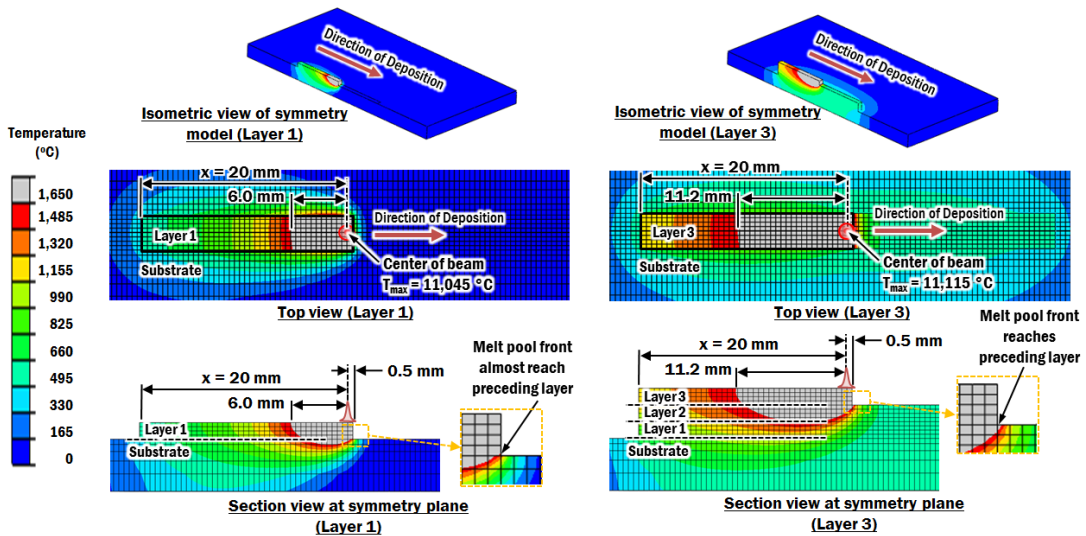
The followings observations are obtained from the results of numerical analysis:

- (1) The highest temperature during irradiation of laser using the proposed activation algorithm with 1-front element cross section ( $b = 1$ ) is the lowest as compare to other cases. This is due to the fact that there is insufficient front element cross section to receive the heat flux at the end of computational step, as shown in Fig. 104(a). Hence, the length of melt pool is significantly shorter compared to the other three cases. This result is not proper and may cause the temperature to fluctuate during analysis. Eventually, the fluctuation in heat flux may cause computational error during iterations.
- (2) The highest temperature during irradiation of laser decreases when the number of front element cross sections increases from  $b = 2$  to  $b = 4$ . This is due to the fact that the additional number of front element cross section provides larger volume of finite elements in the vicinity of the heat source to dissipate heat.
- (3) By increasing the number of element cross sections, the length of melt pool in front of the beam center has increased from 0 mm for case  $b = 1$  to 1.5 mm for case  $b = 4$ . Since the radius of laser beam is 0.75 mm, the length of melt pool in front of the beam center below 1 mm is more realistic.
- (4) From the close-up figures of section views, it is observed that the melt pool formed at the front of deposited bead (known as melt pool front) does not reach the preceding layer for  $b = 1$  and  $b = 4$ . For the case of  $b = 2$ , the melt pool front is nearly reaching to the substrate during deposition of layer 1 and has reached the preceding layer during deposition of layer 3. Meanwhile, the melt pool front does not reach the substrate during deposition of layer 1 but reaches the preceding layer during deposition of layer 3 in the case of  $b = 3$ . The characteristics shown in the case of  $b = 2$  is preferred due to the fact

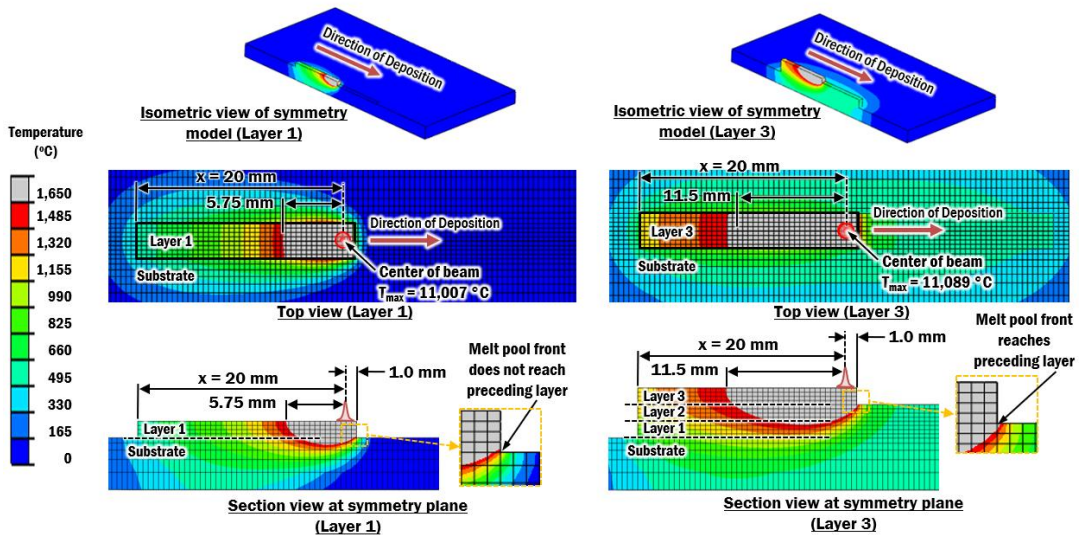
that the melted wire is deposited on a melted preceding layer to form a proper fusion. Therefore, the melt pool front of bead should reach the preceding layer when the new material is added.



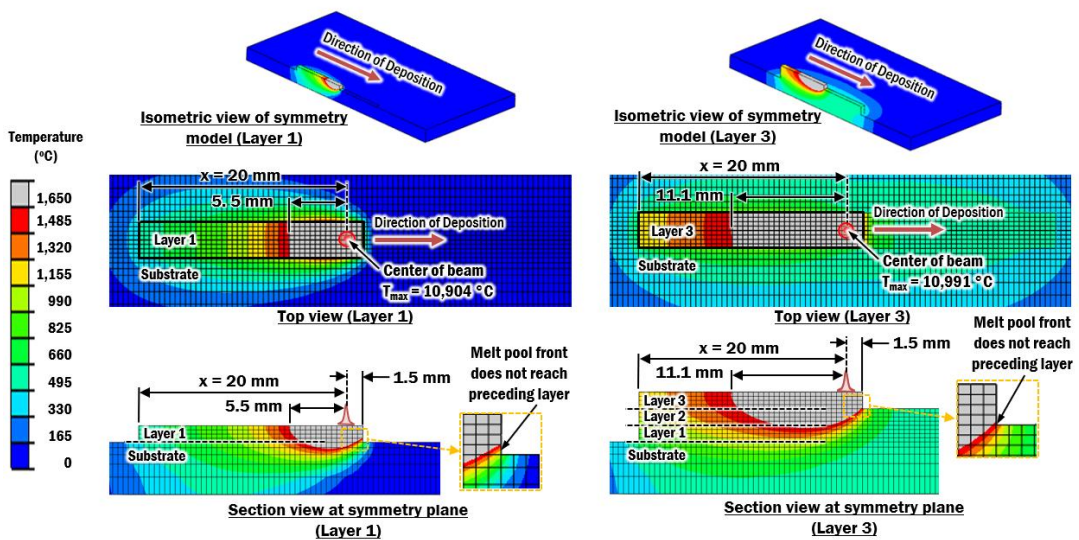
(a) One front element cross section ( $b = 1$ )



(b) Two front element cross section ( $b = 2$ )



(c) Three front element cross section ( $b = 3$ )



(d) Four front element cross section ( $b = 4$ )

**Fig. 104** Temperature distributions and length of melt pool on part during first layer and third layer deposition for various constants of front element cross section

Fig. 105 shows the time taken by a central processing unit (CPU) to complete the simulation of three-layer deposition according to number of element cross sections. The simulation using  $b = 1$  took almost five times longer (471% - 489%) than the other cases due to increase number of iterations per step to reach a converged solution. This can be attributed to the fluctuation in heat flux, as discussed earlier. The fastest analysis among all four cases was completed within 20,250 s using  $b = 3$ . The heat transfer analysis using  $b = 2$  and  $b = 4$  took 2% and 4% longer time to complete, respectively, as compared to simulation using  $b = 3$ . From these results, it is revealed that simulations for all cases except case  $b = 1$  are acceptable in term of computational time.

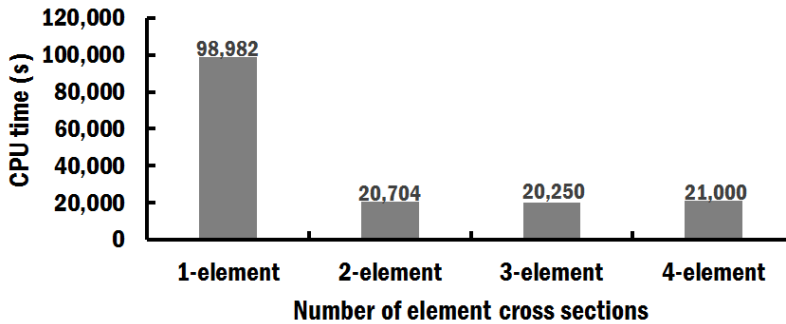


**Fig. 105 Computational time required to complete a three-layer deposition**

Based on the discussions above on the length of melt pool from beam center, characteristics of melt pool front and computational time required, 2-element cross section is recommended.



## D. Heat Transfer Characteristics Using Proposed Element Activation Algorithm

### 1. Description of Analysis and Analysis Conditions

In order to further investigate the applicability of the proposed activation algorithm of inactive elements using the selected two-element cross section, three-dimensional finite element models for multi-layer deposition and planar deposition are created, as shown in Fig. 106. The process conditions such as heat source model, interpass time, and heat transfer boundary conditions similar to previous analysis described in Chapter V Section C-1 are applied in the heat transfer analyses.

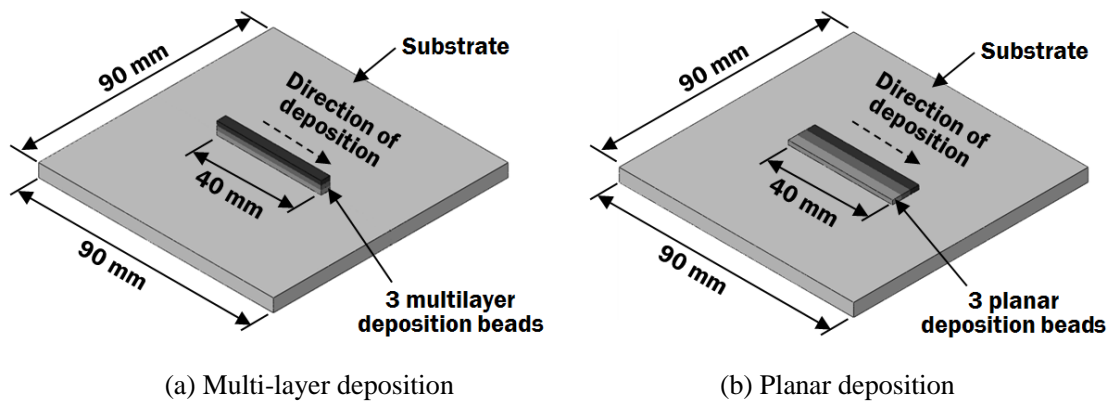


**Fig. 106 FEA model to investigate the heat transfer characteristics using proposed element activation algorithm<sup>148</sup>**

### 2. Results and Discussion

In order to ensure the correctness of the implementation of the proposed element activation algorithm for a heat transfer analysis, the temperature distributions of nodes that the Gaussian heat flux has passed through are observed. Fig. 107 shows the temperature distribution at the vicinity of

heat source for the first three steps of the heat transfer FEA using the proposed element activation algorithm during a multi-layer deposition. The analysis begins with two-element of cross section being included. The temperature at node-1,  $T_1$ , is the highest during the first numerical iteration in step-1. This is because the Gaussian heat flux has the highest heat flux at the center of beam. At the end of step-1, it shows that highest temperature has shifted to node-2 as the center of beam had approached the node-2. The temperature at node-3,  $T_3$ , has risen above melting point of the material. This indicates that the two-element section has been melted under the heat flux. This phenomenon is proper due to the fact that the material must be melted in order to be fused with the substrate.

In order to maintain two-element cross sections ahead of the center of laser, one-element cross section is added at the start of subsequent step-2. The temperature of the newly added node-4,  $T_4$ , has the initial temperature of 20°C. The temperature for the newly deposited elements is interpolated between nodes. This causes a partial region of the newly deposited elements to be melted. This phenomenon is proper because the newly deposited elements should be heated by the adjacent material during the material deposition in a DED process. Therefore, the artificial energy being introduced into the model during inactive element activation, as stipulated by Michaleris<sup>147</sup>, is negligible. A heat transfer FEA is solved numerically based on the temperature distribution at the start of step-2. As the center of beam has moved to align at node-3, the highest temperature at the end of step-2 is shifted to the node-3. Similar to the step-2, the element activation and heat transfer analysis are carried out for step-3. This produces the expected maximum temperature at node-4 at the end of step-3. From the characteristics of nodal temperature, it is confirmed that the proposed element activation algorithm and the heat transfer FEA using a moving heat source has been applied properly.

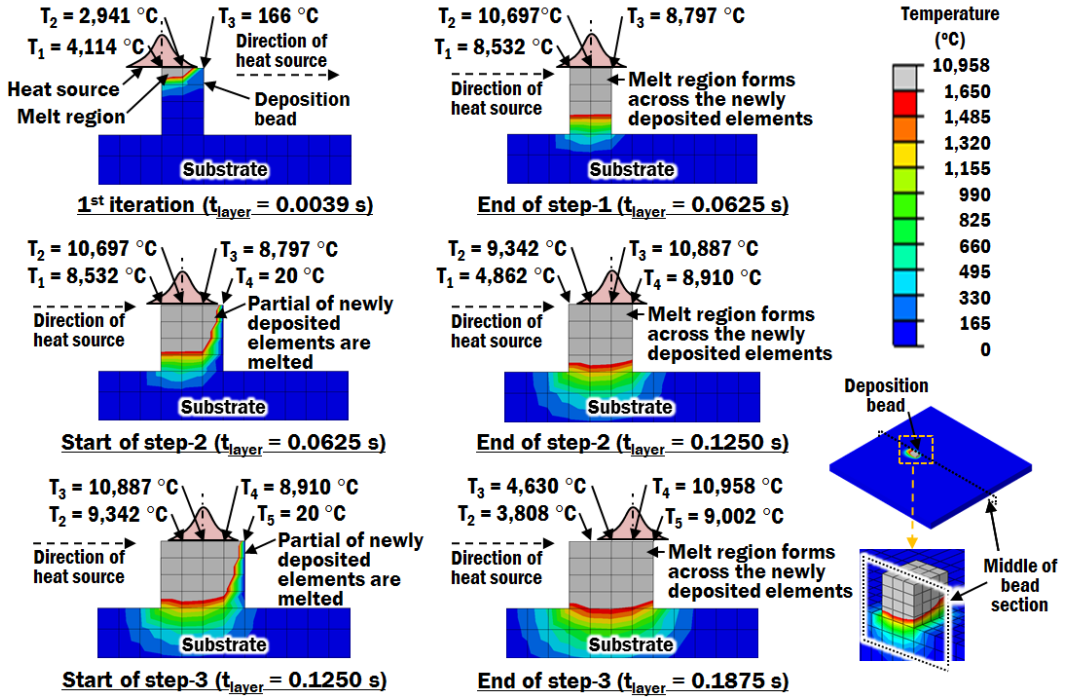


Fig. 107 Temperature distribution at middle of bead section during element activation<sup>148</sup>

Fig. 108 shows temperature distribution of the specimen during deposition of layer 1, 2, and 3, and after 10 s cooling, obtained from a heat transfer FEA carried out using the proposed element activation algorithm. It is observed that the heat from the small radius of beam has been transferred and melt across the width of the activated bead. The temperature is increasing with increasing number of deposition layer in the multi-layer deposition. This is attributed that the upper layer is deposited at the top of a preceding layer, which had not been cooled to the ambient temperature. Furthermore, the heat conduction from the upper layer must flow through the preceding layer. Hence, these heat transfer characteristics are proper, in order to explain a multi-layer deposition process.

The heat transfer FEA has been carried out using the proposed element activation algorithm for planar deposition in order to obtain the temperature distribution of the specimen, as shown in Fig. 109. From the result of the FEA, it shows that the newly deposited bead is fully melted with

slight overlap with adjacent bead during the application of the heat source. In contrast to the multi-layer deposition, the maximum temperatures of the bead during planar deposition are almost similar because the deposition is not directly affected by the preceding deposition of bead. The major heat conduction of new deposition of bead is passed direct to the substrate. From these observations, it shows that heat transfer characteristics of a planar deposition is properly simulated using the proposed element activation algorithm.

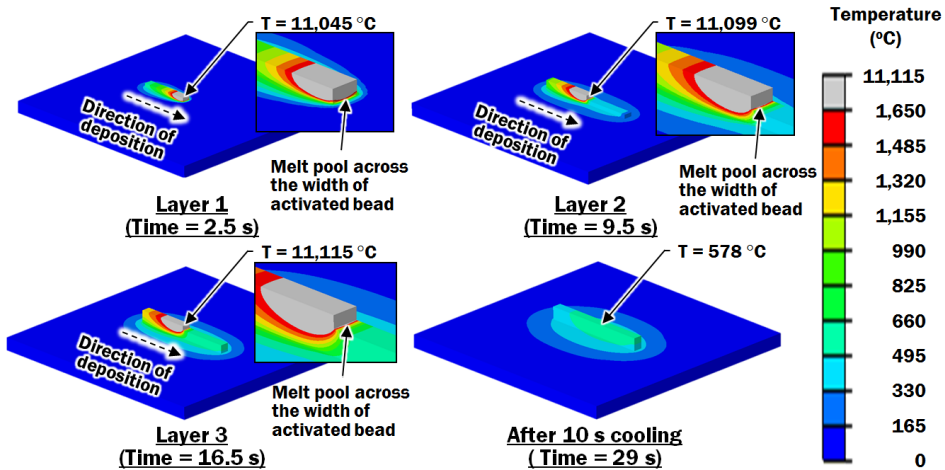


Fig. 108 Temperature distribution during a multi-layer DED deposition

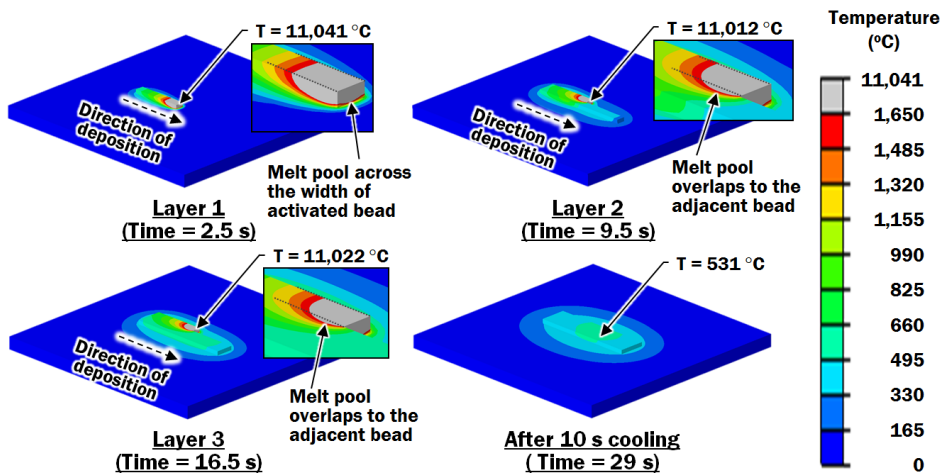


Fig. 109 Temperature distribution during a planar DED deposition<sup>148</sup>

In order to validate the heat transfer result of the proposed activation algorithm on inactive elements, a commercial FEA software SYSWELD is used as the benchmark. The SYSWELD performs heat transfer analysis on quiet elements.

Fig. 110 shows the estimated temperature from the result of heat transfer FEAs for nodes that lie along the top of bead of layer 3 of the symmetry plane when the center of beam is at  $x = 20$  mm. Both analyses results show that the highest temperature is at the node, which the center of beam is aligned with during the transient heat transfer phenomena in DED process due to the application of Gaussian distribution of heat source.

The temperatures for the nodes that are more than 1 mm ahead of the center of laser beam remain at initial temperature of  $20\text{ }^{\circ}\text{C}$  using the proposed algorithm. This accurately simulate the DED process because material is only deposited near the vicinity of the center of beam. In contrast, all the nodes ahead of center of beam have an unrealistic temperature above  $480\text{ }^{\circ}\text{C}$  due to heat from preceding layer that has been transferred to the quiet elements in the SYSWELD. Besides, it is observed that the temperature for the nodes behind the center of laser beam is lower in the SYSWELD than in the proposed algorithm due to the larger amount of heat transferred ahead of the center of laser beam. Therefore, heat loss in SYSWELD is greater as compare with the proposed algorithm due to the application of quiet elements.

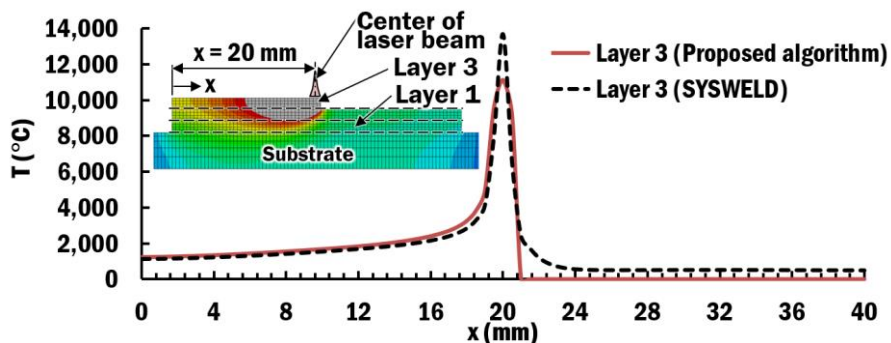
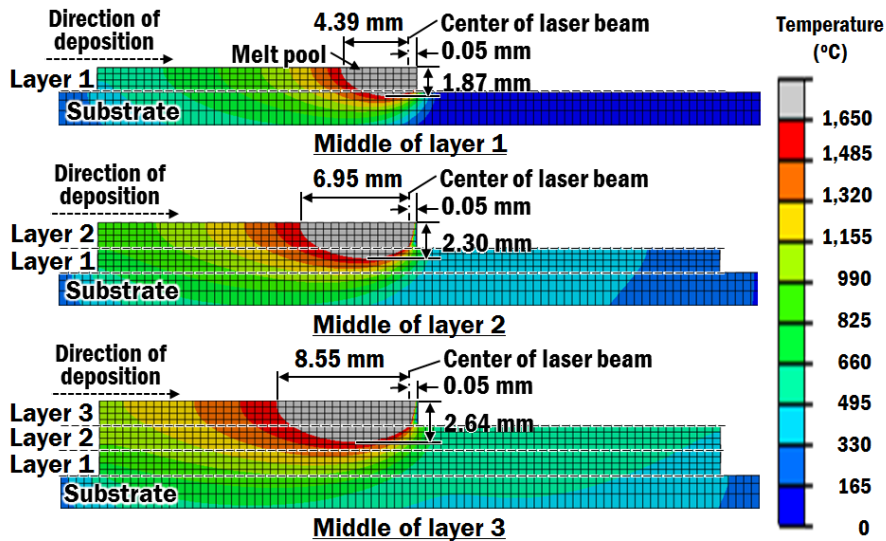


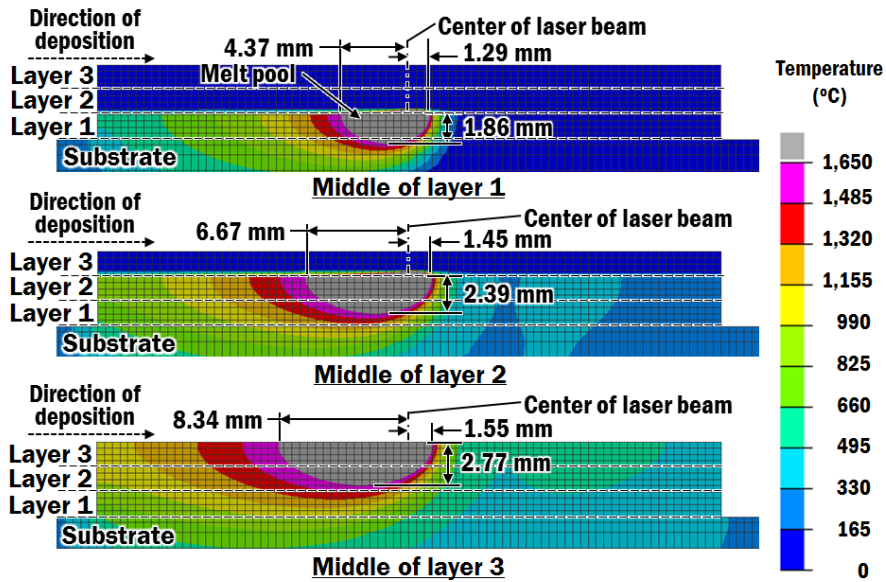
Fig. 110 Nodal temperature along the bead of layer 3 when the center of laser beam is at  $x = 20\text{ mm}$ <sup>148</sup>

In order to match the dimension of melt pool using SYSWELD and proposed algorithm, the efficiency of heat source model is reduced for the proposed algorithm in order to compensate for the lesser heat loss. Fig. 111 shows the predicted dimension of melt pools using the proposed algorithm with reduced efficiency of 0.4 and SYSWELD with efficiency of 0.6. Using the proposed algorithm, the melted region ahead of center of laser beam is kept constant. However, the melted region ahead of center of laser beam in SYSWELD increases when the number of layer increases. Therefore, the constant volume of material deposition in a DED process is not accurately represented in SYSWELD.

In order to compare the dimension of melt pool, the errors in depth of melt pool and length of melt pool behind the center of laser beam are calculated. The calculated errors in depth of melt pool and length of melt pool behind the center of laser beam lie in the ranges of 1.0-4.7% and 1.0-2.5%, respectively. By proper calibration of efficiency of heat source, it is shown that the proposed algorithm can produce similar dimension of melt pool as the SYSWELD.



(a) Estimated melt pool using proposed element activation



(b) Estimated melt pool using SYSWELD

Fig. 111 Comparison of dimension of melt pool for a multi-layer deposition<sup>148</sup>

From the discussions of temperature distributions obtained from the FEAs using the activation algorithm, it is proven that the proposed algorithm is applicable for heat transfer analysis of a DED process. The comparison results of FEAs shows that the proposed algorithm has produced a similar size of melt pool and a more realistic heat transfer characteristics for a DED process compared to SYSWELD. Hence, the heat transfer FEA results using the proposed algorithm can be applied to obtain the thermo-mechanical characteristics of a part deposited by a DED process.

## E. Thermo-Mechanical Analysis Using Proposed Proposed Element Activation Algorithm

### 1. Description of Analysis and Analysis Conditions

Thermo-mechanical analyses using the proposed activation algorithm of inactive elements are applied to investigate the formation of mechanical characteristics of deposited part by a wire feeding type DED process. Validation method described in Chapter IV Section D is applied in order to verify the thermo-mechanical analysis by the proposed activation algorithm of inactive elements. Similar three-dimensional finite element models for multi-layer deposition are created according to those in Chapter IV Section C, as shown in Fig. 112. The process conditions such as heat source model, interpass time, and heat transfer boundary conditions are applied in the heat transfer analyses, as listed in Table 30. Due to different heat transfer characteristics between the proposed algorithm and those in SYSWELD, the efficiency of heat source model is re-calibrated according to the dimension of heat affected zone (HAZ). The vertical displacements at locations Pt-1 and Pt-2 were compared between the estimated results of thermo-mechanical FEAs and those from experiments.

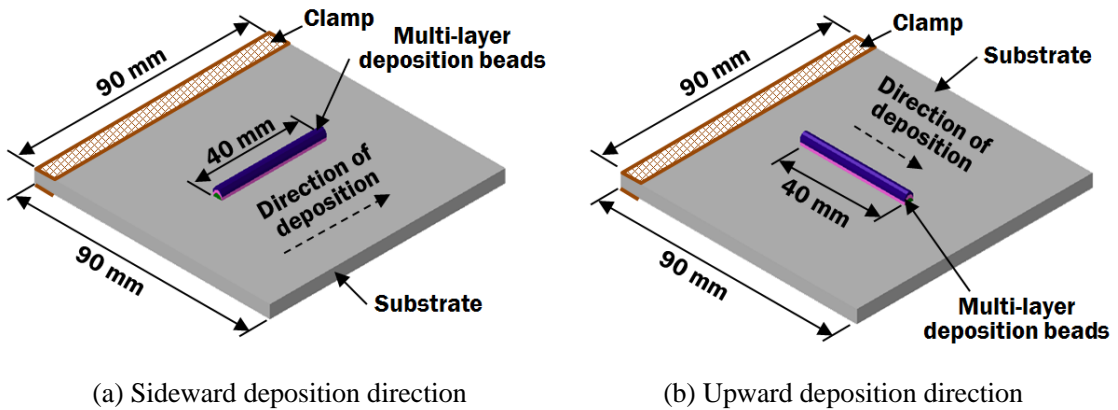


**Fig. 112 FE model to verify thermo-mechanical characteristics of multi-layer deposition**

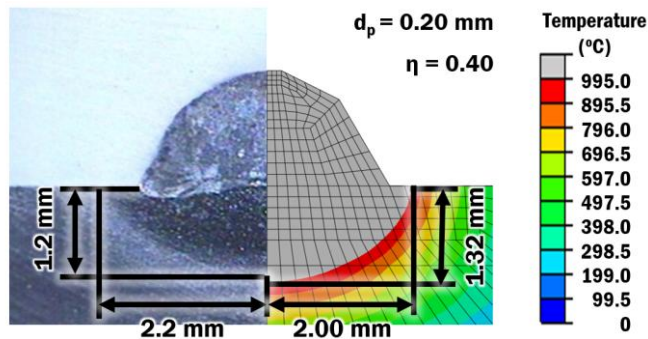


**Table 30 Conditions of analyses to verify the thermo-mechanical FE models**

Parameters	Power of laser (P, kW)	Travel speed of table (V, mm/s)	Interpass time (s)	Deposition direction	Deposition pattern	Period of cooling process (min.)
Range	1.5	8	2	Sideward, Upward	Unidirectional	40

## 2. Results and Discussion

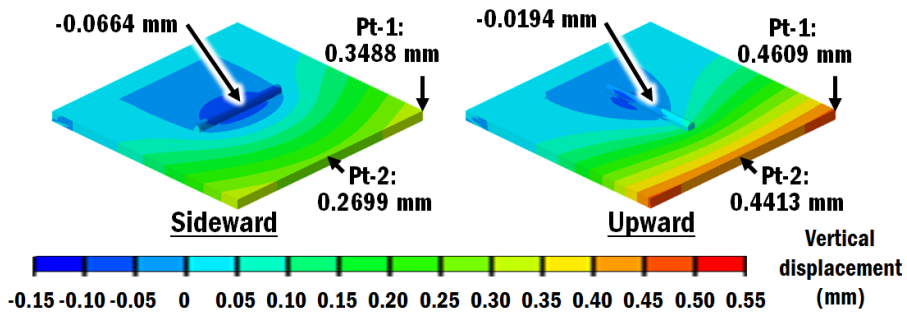
The efficiency of heat source model is re-calibrated according to dimension of heat affected zone, by maintaining the characteristics of the laser beam at penetration depth of 0.2 mm. The efficiency of the heat source model obtained is 0.4, as shown in Fig. 113. The errors of width and depth of HAZ lie within the acceptable range of  $\pm 10\%$ . Hence, the calibrated efficiency of 0.4 is applied in the thermo-mechanical FEAs using the proposed element activation algorithm.



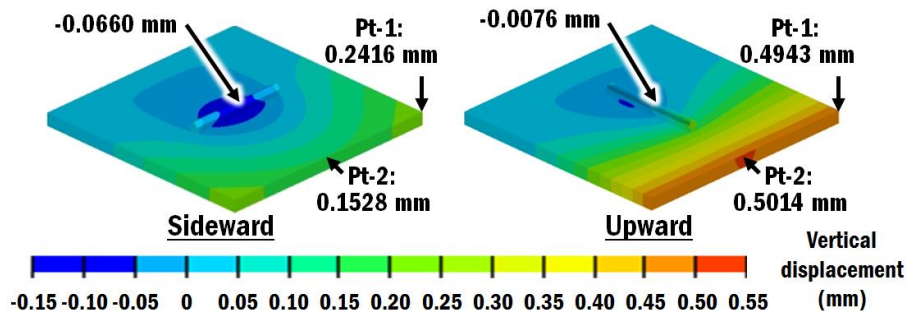
**Fig. 113 Comparison of dimensions of HAZ between estimated result from FEAs and those of experiment**

Fig. 114 shows that thermo-mechanical FEAs using the proposed algorithm successfully predicted the deformation trend of the specimen similar to those from experiments, where Pt-1 is always higher than Pt-2 during cooling process. The predicted vertical displacements from FEAs using the proposed algorithm consistently over-estimated compared to results obtained through

experiments for different deposition directions. In the case of SYSWELD, it under-predicts the vertical displacements for sideward deposition direction and over-predicts the vertical displacements for upward deposition direction. SYSWELD fails to properly estimate the vertical displacements at Pt-1 are higher than those at Pt-2. These results show that the vertical displacement estimated using the proposed algorithm is better than those using SYSWELD. The estimated vertical displacements at the mid-length of layer 3 bead are slightly higher using the proposed algorithm than those of SYSWELD. This is attributed to the application of inactive elements in the proposed algorithm does not interfere with the displacement of those active elements during FEAs.



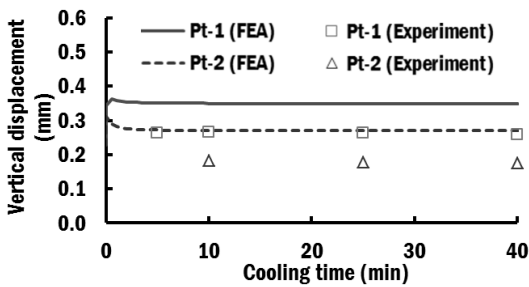
(a) Proposed algorithm



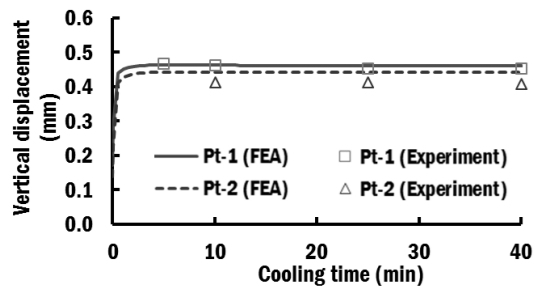
(b) SYSWELD

**Fig. 114 Distributions of vertical displacements estimated using proposed algorithm and SYSWELD**

From the result of thermo-mechanical FEAs, histories of estimated vertical displacements at points Pt-1 and Pt-2 are plotted in Fig. 115 and compared with those from experiments. The predicted vertical displacements from FEAs using the proposed algorithm are consistently over-estimated compared to those obtained through experiments for different deposition directions. Differences ( $\Delta d$ ) between the estimated results from FEAs and those from experiments are less than 95  $\mu\text{m}$ , as shown in Fig. 116. These differences are small compared with those in literatures, and similar to those obtained using SYSWELD. Hence, the thermo-mechanical model is verified.

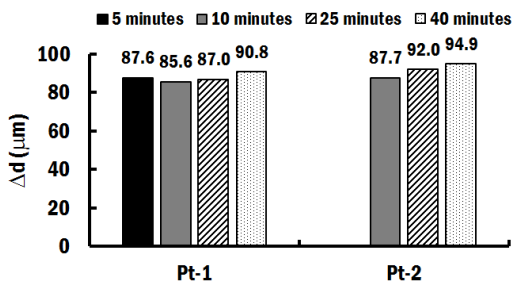


(a) Sideward deposition direction

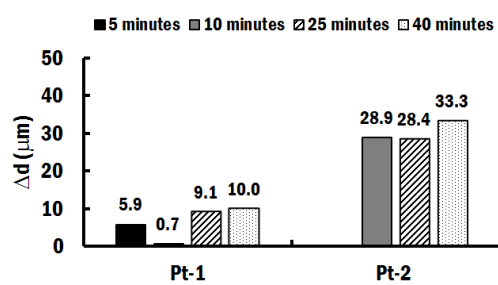


(b) Upward deposition direction

**Fig. 115 Comparison of vertical displacement between estimated results from FEAs using the proposed algorithm and those of experiments**



(a) Sideward deposition direction



(b) Upward deposition direction

**Fig. 116 Differences of vertical displacement at measurement points for different cooling times**

Fig. 117 shows the distributions of residual stresses estimated using proposed algorithm and SYSWELD. It is revealed that residuals stresses at the mid-length of layer-3 are higher in the case of sideward deposition direction than upward deposition direction. These results are similar to those estimated by SYSWELD. However, the proposed algorithm estimated lower residual stresses as compared to those in SYSWELD. This is due to greater vertical displacements estimated on the beads by the proposed algorithm.

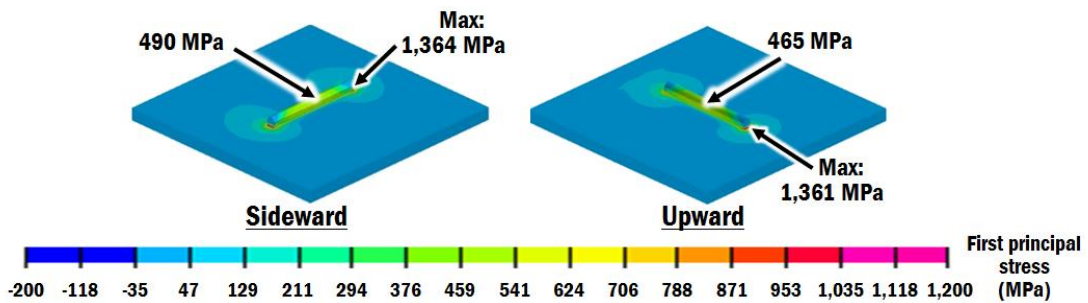
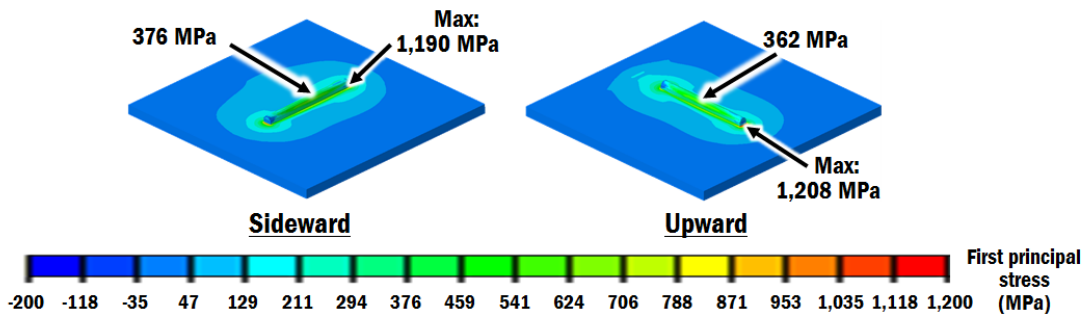


**Fig. 117 Distributions of residual stresses estimated using proposed algorithm and SYSWELD**

From these results, it is concluded that the thermo-mechanical FEAs using the proposed element activation algorithm can estimate the thermo-mechanical characteristics of part deposited using a wire feeding type DED process, comparable to those of SYSWELD. In the case of vertical displacements, the proposed algorithm offers better prediction than those of SYSWELD.

## VI. CONCLUSIONS AND FUTURE WORKS

Recent development in wire feeding type DED process applies high intensity beam such as laser and electron beam as the heat source. These high intensity heat sources have a precise and small beam radius for proper control of melting. However, proper thermo-mechanical analysis has not been developed for a wire feeding type DED process using a high intensity heat source. In this thesis, a novel comprehensive method to develop a thermo-mechanical analysis model for a wire feeding type DED process has been proposed and studied.

The cross section profile of bead depends on the power of laser and travel speed of table. In order to study the effect of power of laser and travel speed of table, proper cross section profile bead must be used in the thermo-mechanical FEAs. A novel methodology to estimate the cross section of deposited bead for different power of laser and travel speed of table via regression analysis has been proposed. The cross section area of the estimated profile and measured profile have shown a good agreement. Subsequently, methodologies to create bead profile for multi-layer and planar depositions have been proposed using a new polygonal-shaped bead profile. A constant width model and a flat top model have been suggested to estimate the cross section profile for multi-layer deposition and planar deposition, respectively. By applying these proposed methodologies, proper bead profile for multi-layer and planar deposition of a wire feeding type DED process according to process parameters have been successfully estimated for further investigation using thermo-mechanical FEAs.

In order to produce an acceptable FEA results, a novel calibration methodology of heat flux model has been proposed. A top-hat distribution heat flux model with consideration of efficiency and penetration depth has been applied to properly emulate the measured profile of laser beam with radius of 0.75 mm in the wire feeding type DED process. Various heat transfer FEAs have been carried out using different efficiency and penetration depth of heat flux model on different shape of deposited beads of FE models to predict the geometry of heat affected zone (HAZ). Penetration

depth and efficiency of heat flux model for each combination of power of laser and travel speed of table has been calibrated by comparing the predicted geometries of HAZ with those of measured geometry of HAZ.

Using the derived bead profiles and calibrated heat flux model, the thermo-mechanical FEAs have been carried out to investigate the influence of process parameters such as power of laser and travel speed of table on the formation of heat affected zone (HAZ), stress influenced region (SIR) and induced thermal stress. A proper gap between deposition beads has been estimated by comparing the width of HAZ and stress influenced region (SIR) in order to avoid the effect of heat and residual stress between two adjacent parts deposited on a single substrate. In addition, the influence of angle of corner deposition on the formation of HAZ, SIR and thermal stress has been investigated and discussed.

In order to minimize the thermal stress on the deposited part, the thermo-mechanical characteristics during planar and multi-layer deposition of a wire feeding type DED process have been investigated according to deposition pattern and interpass time via a FEA software SYSWELD. From the results of thermo-mechanical FEAs, a proper deposition strategy has been identified. The vertical displacements of measured points on a cantilevered specimen have been compared to the predicted vertical displacement from FEAs, in order to validate the thermo-mechanical FEA model. The influences of interpass time and deposition pattern on the formation of thermal stress of a cantilevered specimen have been studied using the validated thermo-mechanical FEA model.

A novel activation algorithm of finite element has been introduced for thermo-mechanical FEAs model of a wire feeding type DED process using a high intensity heat source with small beam radius. A selection criterion of mesh size of finite element and number of front element cross section of bead have been introduced and discussed. The activation algorithm of finite element has been implemented using MATLAB and ABAQUS. Finally, the proposed activation algorithm of finite element has been implemented in ABAQUS in order to obtain the thermo-mechanical characteristics of a multi-layer deposition on a cantilevered specimen. The comparison of vertical

displacements between those estimated from FEA and those measured from experiments has shown a good agreement. From these findings, it has shown that the thermo-mechanical analysis method has been properly investigated.

The development of the thermo-mechanical analysis method for a wire feeding type DED process leads to many potential applications and advancement in process modelling of a DED process in the future. Computational fluid dynamics (CFD) model can be augmented into the heat transfer FEA analysis to enhance the simulation of DED process of a large specimen, which applies a shielding gas according to location of nozzle and evolution of shape of deposited part during deposition. The result of a thermo-mechanical FEA is significantly depends on the geometry of the specimen and inputted material properties. Hence, additional empirical case studies for multi-layer and planar deposition should be carried out in a controlled room temperature condition and inclined surface to improve the estimation model of bead profile. Finally, empirical study to obtain an actual elevated temperature flow stress curves of Ti-6Al-4V used in a DED process should be carried out. Using the actual flow stress curves, a proper material constitutive model can be applied to properly improve the accuracy of the thermo-mechanical analysis in prediction of residual stress.

## REFERENCES

1. Jovane, F., Yoshikawa, H., Alting, L., Boër, C. R., Westkamper, E., Williams, D., Tseng, M., Seliger, G., and Paci, A. M., “The Incoming Global Technological and Industrial Revolution towards Competitive Sustainable Manufacturing,” *CIRP Annals*, Vol. 57, No. 2, pp. 641–659, 2008.
2. Yao, X. and Lin, Y., “Emerging Manufacturing Paradigm Shifts for the Incoming Industrial Revolution,” *The International Journal of Advanced Manufacturing Technology*, Vol. 85, No. 5–8, pp. 1665–1676, 2016.
3. Thompson, M. K. *et al.*, “Design for Additive Manufacturing: Trends, Opportunities, Considerations, and Constraints,” *CIRP Annals*, Vol. 65, No. 2, pp. 737–760, 2016.
4. Li, G., Hou, Y., and Wu, A., “Fourth Industrial Revolution: Technological Drivers, Impacts and Coping Methods,” *Chinese Geographical Science*, Vol. 27, No. 4, pp. 626–637, 2017.
5. Ahn, D.-G., “Direct Metal Additive Manufacturing Processes and Their Sustainable Applications for Green Technology: A Review,” *International Journal of Precision Engineering and Manufacturing-Green Technology*, Vol. 3, pp. 381–395, 2016.
6. ASTM F2792-12a, “Standard Terminology for Additive Manufacturing Technologies,” 2012.
7. ISO/ASTM 52900, “Additive Manufacturing - General Principles - Terminology,” 2015.
8. Herzog, D., Seyda, V., Wycisk, E., and Emmelmann, C., “Additive Manufacturing of Metals,” *Acta Materialia*, Vol. 117, pp. 371–392, 2016.
9. Attaran, M., “The Rise of 3-D Printing: The Advantages of Additive Manufacturing over Traditional Manufacturing,” *Business Horizons*, Vol. 60, No. 5, pp. 677–688, 2017.
10. Gebhardt, A., “Understanding Additive Manufacturing: Rapid Prototyping, Rapid Tooling, Rapid Manufacturing,” Hanser, 2012.
11. Schmidt, M., Merklein, M., Bourell, D., Dimitrov, D., Hausotte, T., Wegener, K., Overmeyer, L., Vollertsen, F., and Levy, G. N., “Laser Based Additive Manufacturing in Industry and Academia,” *CIRP Annals*, Vol. 66, No. 2, pp. 561–583, 2017.



12. Ivanova, O., Williams, C., and Campbell, T., “Additive Manufacturing (AM) and Nanotechnology: Promises and Challenges,” Proc. of the 22th Annual International Solid Freeform Fabrication Symposium, pp. 733–749, 2011.
13. Dizon, J. R. C., Espera, A. H., Chen, Q., and Advincula, R. C., “Mechanical Characterization of 3D-Printed Polymers,” Additive Manufacturing, Vol. 20, pp. 44–67, 2018.
14. Hopkinson, N., Hague, R. J. M., and Dickens, P. M., “Rapid Manufacturing: An Industrial Revolution for the Digital Age,” John Wiley & Sons, 2006.
15. Hofmann, D. C., Roberts, S., Otis, R., Kolodziejaska, J., Dillon, R. P., Suh, J., Shapiro, A. A., Liu, Z.-K., and Borgonia, J.-P., “Developing Gradient Metal Alloys through Radial Deposition Additive Manufacturing,” Scientific Reports, Vol. 4, No. 1, 2015.
16. Wong, K. V. and Hernandez, A., “A Review of Additive Manufacturing,” ISRN Mechanical Engineering, Vol. 2012, pp. 1–10, 2012.
17. U.S. Department of Energy, “Quadrennial Technology Review 2015,” Quadrennial Technology Review 2015, Available at: <https://www.energy.gov/sites/prod/files/2015/11/f27/QTR2015-6A-Additive%20Manufacturing.pdf>.
18. Liu, S. and Shin, Y. C., “Additive Manufacturing of Ti6Al4V Alloy: A Review,” Materials & Design, Vol. 164, pp. 107552, 2019.
19. Columbus, C., “Roundup Of 3D Printing Market Forecasts And Estimates,” Roundup Of 3D Printing Market Forecasts And Estimates, 2015. Available at: <https://www.forbes.com/sites/louiscolombus/2015/03/31/2015-roundup-of-3d-printing-market-forecasts-and-estimates/#5c36f53b1b30>. (Accessed: 22nd July 2018)
20. Frazier, W. E., “Metal Additive Manufacturing: A Review,” Journal of Materials Engineering and Performance, Vol. 23, pp. 1917–1928, 2014.
21. Morgan, H. D., Levatti, H. U., Sienz, J., Gil, A. J., and Bould, D. C., “GE Jet Engine Bracket Challenge: A Case Study in Sustainable Design,” Sustainable Design and Manufacturing 2014 Part, Vol. 1, pp. 95–107, 2014.

22. Gonzalez-Gutierrez, J., Cano, S., Schuschnigg, S., Kukla, C., Sapkota, J., and Holzer, C., “Additive Manufacturing of Metallic and Ceramic Components by the Material Extrusion of Highly-Filled Polymers: A Review and Future Perspectives,” *Materials*, Vol. 11, No. 5, pp. 840, 2018.
23. Tofail, S. A. M., Koumoulos, E. P., Bandyopadhyay, A., Bose, S., O’Donoghue, L., and Charitidis, C., “Additive Manufacturing: Scientific and Technological Challenges, Market Uptake and Opportunities,” *Materials Today*, Vol. 21, pp. 22–37, 2018.
24. Francois, M. M. *et al.*, “Modeling of Additive Manufacturing Processes for Metals: Challenges and Opportunities,” *Current Opinion in Solid State and Materials Science*, Vol. 21, No. 4, pp. 198–206, 2017.
25. DebRoy, T. *et al.*, “Additive Manufacturing of Metallic Components – Process, Structure and Properties,” *Progress in Materials Science*, Vol. 92, pp. 112–224, 2018.
26. Ding, D., Pan, Z., Cuiuri, D., and Li, H., “Wire-Feed Additive Manufacturing of Metal Components: Technologies, Developments and Future Interests,” *The International Journal of Advanced Manufacturing Technology*, Vol. 81, No. 1–4, pp. 465–481, 2015.
27. Yang, Q., Zhang, P., Cheng, L., Min, Z., Chyu, M., and To, A. C., “Finite Element Modeling and Validation of Thermomechanical Behavior of Ti-6Al-4V in Directed Energy Deposition Additive Manufacturing,” *Additive Manufacturing*, Vol. 12, pp. 169–177, 2016.
28. Denlinger, E. R., Heigel, J. C., and Michaleris, P., “Residual Stress and Distortion Modeling of Electron Beam Direct Manufacturing Ti-6Al-4V,” *Proceedings of the Institution of Mechanical Engineers, Part B: Journal of Engineering Manufacture*, Vol. 229, No. 10, pp. 1803–1813, 2015.
29. Chua, B. L., Lee, H. J., Ahn, D.-G., and Kim, J. G., “Influence of Process Parameters on Temperature and Residual Stress Distributions of the Deposited Part by a Ti-6Al-4V Wire Feeding Type Direct Energy Deposition Process,” *Journal of Mechanical Science and Technology*, Vol. 32, No. 11, pp. 5363–5372, 2018.
30. “Laser-Based Additive Manufacturing of Metal Parts: Modeling, Optimization, and Control of Mechanical Properties,” CRC Press, 2018.

31. Zenou, M. and Grainger, L., “Additive Manufacturing of Metallic Materials,” in Additive manufacturing: materials, processes, quantifications and applications, (eds. Zhang, J. & Jung, Y.-G.) pp. 53–104, Elsevier, 1st Ed., , 2018.
32. Chua, Z. Y., Ahn, I. H., and Moon, S. K., “Process Monitoring and Inspection Systems in Metal Additive Manufacturing: Status and Applications,” International Journal of Precision Engineering and Manufacturing-Green Technology, Vol. 4, No. 2, pp. 235–245, 2017.
33. Gibson, I., Rosen, D. W., and Stucker, B., “Additive Manufacturing Technologies: 3D Printing, Rapid Prototyping and Direct Digital Manufacturing,” Springer, 1 Ed., , 2014.
34. Saboori, A., Gallo, D., Biamino, S., Fino, P., and Lombardi, M., “An Overview of Additive Manufacturing of Titanium Components by Directed Energy Deposition: Microstructure and Mechanical Properties,” Applied Sciences, Vol. 7, No. 9, pp. 883, 2017.
35. Kim, D.-I., Lee, H.-J., Ahn, D.-G., Kim, J.-S., and Kang, E. G., “Preliminary Study on Improvement of Surface Characteristics of Stellite21 Deposited Layer by Powder Feeding Type of Direct Energy Deposition Process Using Plasma Electron Beam,” Journal of the Korean Society for Precision Engineering, Vol. 33, No. 11, pp. 951–959, 2016.
36. Wolff, S., Lee, T., Faierson, E., Ehmann, K., and Cao, J., “Anisotropic Properties of Directed Energy Deposition (DED)-Processed Ti-6Al-4V,” Journal of Manufacturing Processes, Vol. 24, pp. 397–405, 2016.
37. ASTM F3187-16, “Standard Guide for Directed Energy Deposition of Metals,” 2016.
38. Brandl, E., Baufeld, B., Leyens, C., and Gault, R., “Additive Manufactured Ti-6Al-4V Using Welding Wire: Comparison of Laser and Arc Beam Deposition and Evaluation with Respect to Aerospace Material Specifications,” Physics Procedia, Vol. 5, pp. 595–606, 2010.
39. Pinkerton, A. J., “[INVITED] Lasers in Additive Manufacturing,” Optics & Laser Technology, Vol. 78, pp. 25–32, 2016.
40. Pinkerton, A. J. and Li, L., “Modelling the Geometry of a Moving Laser Melt Pool and Deposition Track via Energy and Mass Balances,” Journal of Physics D: Applied Physics, Vol. 37, No. 14, pp. 1885–1895, 2004.
41. Peyre, P., Dal, M., Pouzet, S., and Castelnau, O., “Simplified Numerical Model for the Laser Metal Deposition Additive Manufacturing Process,” Journal of Laser Applications, Vol. 29, No. 2, pp. 022304, 2017.

42. Clayton, R. M., “Electron Beam Coupling Efficiency in EBF3,” 2012 Midwest Section Conference of the American Society for Engineering Education, pp. 1–3, 2012.
43. Reed, R. C., Stone, H. J., Dye, D., Roberts, S. M., and McKenzie, S. G., “Process Modelling of the Electron Beam Welding of Aeroengine Components,” *Superalloys 2000* (Ninth International Symposium), pp. 665–674, 2000. doi:10.7449/2000/Superalloys\_2000\_665\_674
44. Ding, J., Colegrove, P., Mehnen, J., Ganguly, S., Sequeira Almeida, P. M., Wang, F., and Williams, S., “Thermo-Mechanical Analysis of Wire and Arc Additive Layer Manufacturing Process on Large Multi-Layer Parts,” *Computational Materials Science*, Vol. 50, pp. 3315–3322, 2011.
45. Tadamalle, A. P., Reddy, Y. P., Ramjee, E., and Reddy, V., “Evaluation of Nd: YAG Laser Welding Efficiencies for 304L Stainless Steel,” *Procedia Materials Science*, Vol. 6, pp. 1731–1739, 2014.
46. Geng, H., Li, J., Xiong, J., Lin, X., and Zhang, F., “Optimization of Wire Feed for GTAW Based Additive Manufacturing,” *Journal of Materials Processing Technology*, Vol. 243, pp. 40–47, 2017.
47. Mok, S. H., Bi, G., Folkes, J., and Pashby, I., “Deposition of Ti–6Al–4V Using a High Power Diode Laser and Wire, Part I: Investigation on the Process Characteristics,” *Surface and Coatings Technology*, Vol. 202, pp. 3933–3939, 2008.
48. Kim, J.-D. and Peng, Y., “Plunging Method for Nd:YAG Laser Cladding with Wire Feeding,” *Optics and Lasers in Engineering*, Vol. 33, pp. 299–309, 2000.
49. Brandl, E., Palm, F., Michailov, V., Viehweger, B., and Leyens, C., “Mechanical Properties of Additive Manufactured Titanium (Ti–6Al–4V) Blocks Deposited by a Solid-State Laser and Wire,” *Materials & Design*, Vol. 32, pp. 4665–4675, 2011.
50. Brandl, E., Michailov, V., Viehweger, B., and Leyens, C., “Deposition of Ti–6Al–4V Using Laser and Wire, Part I: Microstructural Properties of Single Beads,” *Surface and Coatings Technology*, Vol. 206, pp. 1120–1129, 2011.
51. Taberero, I., Paskual, A., Álvarez, P., and Suárez, A., “Study on Arc Welding Processes for High Deposition Rate Additive Manufacturing,” *Procedia CIRP*, Vol. 68, pp. 358–362, 2018.

52. Williams, S. W., Martina, F., Addison, A. C., Ding, J., Pardal, G., and Colegrove, P., “Wire + Arc Additive Manufacturing,” *Materials Science and Technology*, Vol. 32, No. 7, pp. 641–647, 2016.
53. Fuentek, “NASA’s EBF3: The Future of Art-to-Part Manufacturing,” *NASA’s EBF3: The Future of Art-to-Part Manufacturing*, Available at: <https://dougfoster.me/wp-content/uploads/2018/03/ebf3-fuentek-blog.pdf>.
54. Knezović, N. and Topić, A., “Wire and Arc Additive Manufacturing (WAAM) – A New Advance in Manufacturing,” in *New Technologies, Development and Application*, (ed. Karabegović, I.) Vol. 42, pp. 65–71, Springer International Publishing, 2019.
55. Griffith, M. L., Keicher, D. M., Atwood, C. L., Romero, J. A., Smugersky, J. E., Harwell, L. D., and Greene, D. L., “Free Form Fabrication of Metallic Components Using Laser Engineered Net Shaping (LENS<sup>TM</sup>),” *Proc. of the 7th Annual International Solid Freeform Fabrication Symposium*, pp. 125–132, 1996.
56. Hrabe, N., Gnäupel-Herold, T., and Quinn, T., “Fatigue Properties of a Titanium Alloy (Ti–6Al–4V) Fabricated via Electron Beam Melting (EBM): Effects of Internal Defects and Residual Stress,” *International Journal of Fatigue*, Vol. 94, pp. 202–210, 2017.
57. Szost, B. A., Terzi, S., Martina, F., Boisselier, D., Prytuliak, A., Pirling, T., Hofmann, M., and Jarvis, D. J., “A Comparative Study of Additive Manufacturing Techniques: Residual Stress and Microstructural Analysis of CLAD and WAAM Printed Ti–6Al–4V Components,” *Materials & Design*, Vol. 89, pp. 559–567, 2016.
58. Xu, F., Dhokia, V., and Newman, S. T., “Process Control for Wire-Arc Additive Manufacturing,” Available at: <https://www.nottingham.ac.uk/research/groups/advanced-manufacturing-technology-research-group/documents/manufacturing-metrology-team/qcam-17/bath1.pdf>. (Accessed: 23rd January 2019)
59. Biegler, M., Graf, B., and Rethmeier, M., “Assessing the Predictive Capability of Numerical Additive Manufacturing Simulations via In-Situ Distortion Measurements on a LMD Component during Build-Up,” *Procedia CIRP*, Vol. 74, pp. 158–162, 2018.

60. Chiumenti, M., Cervera, M., Salmi, A., Agelet de Saracibar, C., Dialami, N., and Matsui, K., “Finite Element Modeling of Multi-Pass Welding and Shaped Metal Deposition Processes,” *Computer Methods in Applied Mechanics and Engineering*, Vol. 199, No. 37–40, pp. 2343–2359, 2010.
61. Mukherjee, T., Zhang, W., and DebRoy, T., “An Improved Prediction of Residual Stresses and Distortion in Additive Manufacturing,” *Computational Materials Science*, Vol. 126, pp. 360–372, 2017.
62. Zhang, J., Wang, X., Paddea, S., and Zhang, X., “Fatigue Crack Propagation Behaviour in Wire+arc Additive Manufactured Ti-6Al-4V: Effects of Microstructure and Residual Stress,” *Materials & Design*, Vol. 90, pp. 551–561, 2016.
63. Parry, L., Ashcroft, I. A., and Wildman, R. D., “Understanding the Effect of Laser Scan Strategy on Residual Stress in Selective Laser Melting through Thermo-Mechanical Simulation,” *Additive Manufacturing*, Vol. 12, pp. 1–15, 2016.
64. Li, C., Liu, Z. Y., Fang, X. Y., and Guo, Y. B., “Residual Stress in Metal Additive Manufacturing,” *Procedia CIRP*, Vol. 71, pp. 348–353, 2018.
65. Song, Y.-A., Park, S., Choi, D., and Jee, H., “3D Welding and Milling: Part I—a Direct Approach for Freeform Fabrication of Metallic Prototypes,” *International Journal of Machine Tools and Manufacture*, Vol. 45, No. 9, pp. 1057–1062, 2005.
66. Song, Y.-A., Park, S., and Chae, S.-W., “3D Welding and Milling: Part II—Optimization of the 3D Welding Process Using an Experimental Design Approach,” *International Journal of Machine Tools and Manufacture*, Vol. 45, No. 9, pp. 1063–1069, 2005.
67. Korea Institute for Advancement of Technology, “(심층분석보고서2)선재아크 용접기법을 이용한 차세대 금속 3D 프린팅 기술현황 및 전망,” 2018. Available at: [https://www.gtonline.or.kr/kor/data/issue/dataView.do?cPage=1&sch\\_national\\_cd=&sch\\_report\\_gbn\\_cd=&sch\\_tech\\_1st\\_gbn\\_cd=&sch\\_tech\\_2nd\\_gbn\\_cd=&searchField=&keyword=&data\\_sid=232913](https://www.gtonline.or.kr/kor/data/issue/dataView.do?cPage=1&sch_national_cd=&sch_report_gbn_cd=&sch_tech_1st_gbn_cd=&sch_tech_2nd_gbn_cd=&searchField=&keyword=&data_sid=232913). (Accessed: 11th June 2019)
68. Byun, J.-G., Yi, H., and Cho, S.-M., “The Effect of Interpass Peening on Mechanical Properties in Additive Manufacturing of Ti-6Al-4V,” *Journal of Welding and Joining*, Vol. 35, No. 2, pp. 6–12, 2017.

69. No, W. R., “[WELDING KOREA 2018 영상] 베스트에프에이, 경제적인 용접 자동화 시스템 장비들 선배,” 2018. Available at: [http://kr.aving.net/news/view.php?articleId=1427725&Branch\\_ID=kr&rssid=naver&mn\\_name=news](http://kr.aving.net/news/view.php?articleId=1427725&Branch_ID=kr&rssid=naver&mn_name=news). (Accessed: 11th June 2019)
70. Kim, J. and Lee, C.-W., “Laser Assisted Additive Manufacturing by Rotating Metal Wire Feeder,” *KSPE*, Vol. 35, No. 9, pp. 847–852, 2018.
71. Sridhar, N., “Additive Manufacturing Efforts in DNVGL,” 2017.
72. Gockel, J., Beuth, J., and Taminger, K., “Integrated Control of Solidification Microstructure and Melt Pool Dimensions in Electron Beam Wire Feed Additive Manufacturing of Ti-6Al-4V,” *Additive Manufacturing*, Vol. 1–4, pp. 119–126, 2014.
73. Baufeld, B., Biest, O. V. der, and Gault, R., “Additive Manufacturing of Ti-6Al-4V Components by Shaped Metal Deposition: Microstructure and Mechanical Properties,” *Materials & Design*, Vol. 31, pp. S106–S111, 2010.
74. Wang, L., Felicelli, S., Gooroochurn, Y., Wang, P. T., and Horstemeyer, M. F., “Optimization of the LENS® Process for Steady Molten Pool Size,” *Materials Science and Engineering: A*, Vol. 474, No. 1–2, pp. 148–156, 2008.
75. Wang, L. and Felicelli, S., “Analysis of Thermal Phenomena in LENS™ Deposition,” *Materials Science and Engineering: A*, Vol. 435–436, pp. 625–631, 2006.
76. Peyre, P., Aubry, P., Fabbro, R., Neveu, R., and Longuet, A., “Analytical and Numerical Modelling of the Direct Metal Deposition Laser Process,” *Journal of Physics D: Applied Physics*, Vol. 41, No. 2, pp. 025403, 2008.
77. Amine, T., Newkirk, J. W., and Liou, F., “An Investigation of the Effect of Direct Metal Deposition Parameters on the Characteristics of the Deposited Layers,” *Case Studies in Thermal Engineering*, Vol. 3, pp. 21–34, 2014.
78. Ghosh, S. and Choi, J., “Modeling and Experimental Verification of Transient/Residual Stresses and Microstructure Formation in Multi-Layer Laser Aided DMD Process,” *Journal of Heat Transfer*, Vol. 128, No. 7, pp. 662, 2006.
79. Lindgren, L.-E., Lundbäck, A., Fisk, M., Pederson, R., and Andersson, J., “Simulation of Additive Manufacturing Using Coupled Constitutive and Microstructure Models,” *Additive Manufacturing*, Vol. 12, pp. 144–158, 2016.

80. Megahed, M., Mindt, H.-W., N'Dri, N., Duan, H., and Desmaison, O., "Metal Additive-Manufacturing Process and Residual Stress Modeling," *Integrating Materials and Manufacturing Innovation*, Vol. 5, No. 1, 2016.
81. Nickel, A. H., Barnett, D. M., and Prinz, F. B., "Thermal Stresses and Deposition Patterns in Layered Manufacturing," *Materials Science and Engineering: A*, Vol. 317, No. 1–2, pp. 59–64, 2001.
82. Nickel, A., Barnett, D., Link, G., and Prinz, F., "Residual Stresses in Layered Manufacturing," *Proc. of the 10th Annual International Solid Freeform Fabrication Symposium*, pp. 239–246, 1999.
83. Vasinonta, A., Beuth, J., and Griffith, M., "Process Maps for Controlling Residual Stress and Melt Pool Size in Laser-Based SFF Processes," *Proc. of the 11th Annual International Solid Freeform Fabrication Symposium*, pp. 200–208, 2000.
84. Tsirkas, S. A., Papanikos, P., and Kermanidis, T., "Numerical Simulation of the Laser Welding Process in Butt-Joint Specimens," *Journal of Materials Processing Technology*, Vol. 134, No. 1, pp. 59–69, 2003.
85. Mughal, M. P., Mufti, R. A., and Fawad, H., "The Mechanical Effects of Deposition Patterns in Welding-Based Layered Manufacturing," *Proceedings of the Institution of Mechanical Engineers, Part B: Journal of Engineering Manufacture*, Vol. 221, No. 10, pp. 1499–1509, 2007.
86. Deus, A. M. and Mazumder, J., "Three-Dimensional Finite Element Models for the Calculation of Temperature and Residual Stress Fields in Laser Cladding," *Proc. of the 25th International Congress on Applications of Laser and Electro-Optics*, 2006.
87. Bate, S. K., Charles, R., and Warren, A., "Finite Element Analysis of a Single Bead-on-Plate Specimen Using SYSWELD," *International Journal of Pressure Vessels and Piping*, Vol. 86, No. 1, pp. 73–78, 2009.
88. Chua, B. L., Lee, H. J., Ahn, D.-G., and Kim, J. G., "Influence of Angle of Corner Deposition on Temperature and Residual Stress Distributions in the Vicinity of the Deposited Region by a Ti-6Al-4V Wire-Feeding Type of Direct Energy Deposition Process," *Journal of the Korean Society for Precision Engineering*, Vol. 35, No. 9, pp. 853–859, 2018.



89. Anca, A., Fachinotti, V. D., Escobar-Palafox, G., and Cardona, A., “Computational Modelling of Shaped Metal Deposition,” *International Journal for Numerical Methods in Engineering*, Vol. 85, No. 1, pp. 84–106, 2011.
90. Lundbäck, A. and Lindgren, L.-E., “Modelling of Metal Deposition,” *Finite Elements in Analysis and Design*, Vol. 47, No. 10, pp. 1169–1177, 2011.
91. Ding, J., Colegrove, P., Mehnen, J., Williams, S., Wang, F., and Almeida, P. S., “A Computationally Efficient Finite Element Model of Wire and Arc Additive Manufacture,” *The International Journal of Advanced Manufacturing Technology*, Vol. 70, No. 1–4, pp. 227–236, 2014.
92. Zhang, C. (Sam), Li, L., and Deceuster, A., “Thermomechanical Analysis of Multi-Bead Pulsed Laser Powder Deposition of a Nickel-Based Superalloy,” *Journal of Materials Processing Technology*, Vol. 211, No. 9, pp. 1478–1487, 2011.
93. Liu, H., Sparks, T. E., Liou, F. W., and Dietrich, D. M., “Numerical Analysis of Thermal Stress and Deformation in Multi-Layer Laser Metal Deposition Processes,” *Proc. of the 24th Annual International Solid Freeform Fabrication Symposium*, pp. 577–591, 2013.
94. Farahmand, P. and Kovacevic, R., “An Experimental–Numerical Investigation of Heat Distribution and Stress Field in Single- and Multi-Track Laser Cladding by a High-Power Direct Diode Laser,” *Optics & Laser Technology*, Vol. 63, pp. 154–168, 2014.
95. Crespo, A. and Vilar, R., “Finite Element Analysis of the Rapid Manufacturing of Ti–6Al–4V Parts by Laser Powder Deposition,” *Scripta Materialia*, Vol. 63, No. 1, pp. 140–143, 2010.
96. Denlinger, E. R. and Michaleris, P., “Effect of Stress Relaxation on Distortion in Additive Manufacturing Process Modeling,” *Additive Manufacturing*, Vol. 12, pp. 51–59, 2016.
97. Denlinger, E. R., Heigel, J. C., Michaleris, P., and Palmer, T. A., “Effect of Inter-Layer Dwell Time on Distortion and Residual Stress in Additive Manufacturing of Titanium and Nickel Alloys,” *Journal of Materials Processing Technology*, Vol. 215, pp. 123–131, 2015.
98. Lee, Y. S., Bandari, Y., Simunovic, S., Richardson, B., and Kirka, M. M., “Correlations of Interlayer Time with Distortion of Large Ti-6Al-4V Components in Laser Metal Deposition with Wire,” *Proc. of the 29th Annual International Solid Freeform Fabrication Symposium*, pp. 606–622, 2018.

99. Chua, B. L., Lee, H. J., Ahn, D. G., and Kim, J. G., “Investigation of Penetration Depth and Efficiency of Applied Heat Flux in a Directed Energy Deposition Process with Feeding of Ti-6Al-4V Wires,” *Journal of the Korean Society for Precision Engineering*, Vol. 35, No. 2, pp. 211–217, 2018.
100. Rodrigues, T. A., Duarte, V., Miranda, R. M., Santos, T. G., and Oliveira, J. P., “Current Status and Perspectives on Wire and Arc Additive Manufacturing (WAAM),” *Materials*, Vol. 12, No. 7, pp. 1121, 2019.
101. Kolomiets, A., Popov Jr, V. V., Strokin, E., Muller, G., and Kovalevsky, A., “Benefits of Titanium Additive Manufacturing for Industrial Design Development. Trends, Limitations and Applications,” *Global Journal of Researches in Engineering: J General Engineering*, Vol. 18, No. 2, pp. 1–8, 2018.
102. Donachie, M. J., “Titanium: A Technical Guide,” ASM International, 2nd Ed., , 2000.
103. Niinomi, M., “Mechanical Properties of Biomedical Titanium Alloys,” *Materials Science and Engineering: A*, Vol. 243, No. 1–2, pp. 231–236, 1998.
104. Wu, B., Pan, Z., Ding, D., Cuiuri, D., Li, H., Xu, J., and Norrish, J., “A Review of the Wire Arc Additive Manufacturing of Metals: Properties, Defects and Quality Improvement,” *Journal of Manufacturing Processes*, Vol. 35, pp. 127–139, 2018.
105. Martina, F., “Titanium Pressure Vessel for Space Exploration Built Successfully Using the Wire + Arc Additive Manufacturing Process,” 2019. Available at: <https://www.cranfield.ac.uk/press/news-2019/titanium-pressure-vessel-for-space-exploration-built-successfully-using-the-waam-process>. (Accessed: 13th June 2019)
106. Sciaky, “Sciaky Works with the Leading Additive Manufacturing R&D Organizations to Push the Boundaries of Metal 3D Printing,” Available at: <http://www.sciaky.com/additive-manufacturing/additive-manufacturing-r-d>. (Accessed: 13th June 2019)
107. Titomic, “Consumer Goods,” Available at: <https://www.titomic.com/consumer-goods.html>. (Accessed: 13th June 2019)
108. Weisstein, E. W., “Least Squares Fitting--Polynomial,” Available at: <http://mathworld.wolfram.com/LeastSquaresFittingPolynomial.html>. (Accessed: 20th March 2019)

109. Madić, M., Brabie, G., and Radovanović, M., “An Artificial Neural Network Approach for Analysis and Minimization of HAZ in CO<sub>2</sub> Laser Cutting of Stainless Steel,” *U.P.B. Sci. Bull., Series D*, Vol. 75, No. 2, pp. 85–96, 2013.
110. Kumar, A., Paul, C. P., Padiyar, A. S., Bhargava, P., Mundra, G., and Kukreja, L. M., “Numerical Simulation of Laser Rapid Manufacturing of Multi-Layer Thin Wall Using an Improved Mass Addition Approach,” *Numerical Heat Transfer, Part A: Applications*, Vol. 65, No. 9, pp. 885–910, 2014.
111. Pinkerton, A. J., “Advances in the Modeling of Laser Direct Metal Deposition,” *Journal of Laser Applications*, Vol. 27, No. S1, pp. S15001, 2015.
112. Suryakumar, S., Karunakaran, K. P., Bernard, A., Chandrasekhar, U., Raghavender, N., and Sharma, D., “Weld Bead Modeling and Process Optimization in Hybrid Layered Manufacturing,” *Computer-Aided Design*, Vol. 43, No. 4, pp. 331–344, 2011.
113. Cao, Y., Zhu, S., Liang, X., and Wang, W., “Overlapping Model of Beads and Curve Fitting of Bead Section for Rapid Manufacturing by Robotic MAG Welding Process,” *Robotics and Computer-Integrated Manufacturing*, Vol. 27, No. 3, pp. 641–645, 2011.
114. Xiong, J., Zhang, G., Gao, H., and Wu, L., “Modeling of Bead Section Profile and Overlapping Beads with Experimental Validation for Robotic GMAW-Based Rapid Manufacturing,” *Robotics and Computer-Integrated Manufacturing*, Vol. 29, No. 2, pp. 417–423, 2013.
115. Ding, D., Pan, Z., Cuiuri, D., and Li, H., “A Multi-Bead Overlapping Model for Robotic Wire and Arc Additive Manufacturing (WAAM),” *Robotics and Computer-Integrated Manufacturing*, Vol. 31, pp. 101–110, 2015.
116. Li, Y., Sun, Y., Han, Q., Zhang, G., and Horváth, I., “Enhanced Beads Overlapping Model for Wire and Arc Additive Manufacturing of Multi-Layer Multi-Bead Metallic Parts,” *Journal of Materials Processing Technology*, Vol. 252, pp. 838–848, 2018.
117. Hong, M.-H., Min, B., and Kwon, T.-Y., “The Influence of Process Parameters on the Surface Roughness of a 3D-Printed Co–Cr Dental Alloy Produced via Selective Laser Melting,” *Applied Sciences*, Vol. 6, No. 12, pp. 401, 2016.

118. Mughal, M. P., Fawad, H., and Mufti, R., “Finite Element Prediction of Thermal Stresses and Deformations in Layered Manufacturing of Metallic Parts,” *Acta Mechanica*, Vol. 183, No. 1–2, pp. 61–79, 2006.
119. Yang, S.-J. *et al.*, “Determination of the Optical and the Thermal Properties of an Absorbing Medium by Using Infrared Thermometry,” *Journal of the Korean Physical Society*, Vol. 69, No. 12, pp. 1744–1749, 2016.
120. Marchandise, E., Mouraux, A., Plaghki, L., and Henrotte, F., “Finite Element Analysis of Thermal Laser Skin Stimulation for a Finer Characterization of the Nociceptive System,” *Journal of Neuroscience Methods*, Vol. 223, pp. 1–10, 2014.
121. Hecht, E., “Optics,” Pearson Education, Global Ed., , 2017.
122. Polyanskiy, M. N., “Optical Constants of Ti (Titanium),” Refractive index database, Available at: <https://refractiveindex.info/?shelf=main&book=Ti&page=Johnson>. (Accessed: 27th March 2019)
123. Roberts, I. A., Wang, C. J., Esterlein, R., Stanford, M., and Mynors, D. J., “A Three-Dimensional Finite Element Analysis of the Temperature Field during Laser Melting of Metal Powders in Additive Layer Manufacturing,” *International Journal of Machine Tools and Manufacture*, Vol. 49, No. 12–13, pp. 916–923, 2009.
124. Frenk, A., Vandyoussefi, M., Wagnière, J.-D., Kurz, W., and Zryd, A., “Analysis of the Laser-Cladding Process for Stellite on Steel,” *Metallurgical and Materials Transactions B*, Vol. 28, No. 3, pp. 501–508, 1997.
125. Azizpour, M., Ghoreishi, M., and Khorram, A., “Numerical Simulation of Laser Beam Welding of Ti6Al4V Sheet,” *Journal of Computational and Applied Research in Mechanical Engineering*, Vol. 4, No. 2, pp. 145–154, 2015.
126. Incropera, F. P., DeWitt, D. P., Bergman, T. L., and Lavine, A., “Incropera’s Principles of Heat and Mass Transfer.,” John Wiley & Sons, Global Ed., , 2017.
127. Romano, J., Ladani, L., and Sadowski, M., “Thermal Modeling of Laser Based Additive Manufacturing Processes within Common Materials,” *Procedia Manufacturing*, Vol. 1, pp. 238–250, 2015.

128. Boivineau, M., Cagran, C., Doytier, D., Eyraud, V., Nadal, M.-H., Wilthan, B., and Pottlacher, G., "Thermophysical Properties of Solid and Liquid Ti-6Al-4V (TA6V) Alloy," *International Journal of Thermophysics*, Vol. 27, No. 2, pp. 507–529, 2006.
129. Arce, A. N., "Thermal Modeling and Simulation of Electron Beam Melting for Rapid Prototyping on Ti6Al4V Alloys," Ph.D. Thesis, North Carolina State University, 2012.
130. Wang, X., Gong, X., and Chou, K., "Scanning Speed Effect on Mechanical Properties of Ti-6Al-4V Alloy Processed by Electron Beam Additive Manufacturing," *Procedia Manufacturing*, Vol. 1, pp. 287–295, 2015.
131. Nazemi, N. and Urbanic, J., "A Finite Element Analysis for Thermal Analysis of Laser Cladding of Mild Steel with P420 Steel Powder," *Proceedings of the ASME 2016 International Mechanical Engineering Congress and Exposition*, pp. 1–10, 2016.
132. Bontha, S., Klingbeil, N. W., Kobryn, P. A., and Fraser, H. L., "Thermal Process Maps for Predicting Solidification Microstructure in Laser Fabrication of Thin-Wall Structures," *Journal of Materials Processing Technology*, Vol. 178, No. 1–3, pp. 135–142, 2006.
133. ESI Group, "SYSWELD Visual-Weld 12.0," 2016.
134. Carpenter Technology Corporation, "Titanium Alloy Ti 6Al-4V Datasheet," Available at: <http://cartech.ides.com/datasheet.aspx?i=101&E=269&FMT=PRINT>. (Accessed: 7th January 2018)
135. Hosseini, S., "Fatigue of Ti-6Al-4V," in *Biomedical Engineering – Technical Applications in Medicine*, pp. 75–92, InTech, 2012.
136. Gerov, M. V., Vladislavskaya, E. Yu., Terent'ev, V. F., Prosvirnin, D. V., Kolmakov, A. G., and Antonova, O. S., "Fatigue Strength of a Ti-6Al-4V Alloy Produced by Selective Laser Melting," *Russian Metallurgy (Metally)*, Vol. 2016, No. 10, pp. 935–941, 2016.
137. Gouge, M. F., Michaleris, P., and Palmer, T. A., "Fixturing Effects in the Thermal Modeling of Laser Cladding," *J. Manuf. Sci. Eng.*, Vol. 139, No. 1, pp. 011001, 2016.
138. Çengel, Y. A., "Heat Transfer: A Practical Approach," WBC McGraw-Hill, 1998.
139. Fu, C. H. and Guo, Y. B., "3-Dimensional Finite Element Modeling of Selective Laser Melting Ti-6Al-4V Alloy," *Proc. of the 25th Annual International Solid Freeform Fabrication Symposium*, pp. 1129–1144, 2014.

140. Ali, H., Ghadbeigi, H., and Mumtaz, K., “Residual Stress Development in Selective Laser-Melted Ti6Al4V: A Parametric Thermal Modelling Approach,” *The International Journal of Advanced Manufacturing Technology*, Vol. 97, No. 5–8, pp. 2621–2633, 2018.
141. Galarraga, H., Warren, R. J., Lados, D. A., Dehoff, R. R., Kirka, M. M., and Nandwana, P., “Effects of Heat Treatments on Microstructure and Properties of Ti-6Al-4V ELI Alloy Fabricated by Electron Beam Melting (EBM),” *Materials Science and Engineering: A*, Vol. 685, pp. 417–428, 2017.
142. Bandari, Y., Lee, Y. S., Nandwana, P., Richardson, B., Adediran, A. I., and Love, L. J., “Effect of Inter-Layer Cooling Time on Distortion and Mechanical Properties in Metal Additive Manufacturing,” *Proc. of the 29th Annual International Solid Freeform Fabrication Symposium*, pp. 425–437, 2018.
143. Cunningham, C. R., Flynn, J. M., Shokrani, A., Dhokia, V., and Newman, S. T., “Invited Review Article: Strategies and Processes for High Quality Wire Arc Additive Manufacturing,” *Additive Manufacturing*, Vol. 22, pp. 672–686, 2018.
144. Lu, X., Zhou, Y. F., Xing, X. L., Shao, L. Y., Yang, Q. X., and Gao, S. Y., “Open-Source Wire and Arc Additive Manufacturing System: Formability, Microstructures, and Mechanical Properties,” *Int J Adv Manuf Technol*, Vol. 93, No. 5–8, pp. 2145–2154, 2017.
145. Ma, Y., Cuiuri, D., Shen, C., Li, H., and Pan, Z., “Effect of Interpass Temperature on In-Situ Alloying and Additive Manufacturing of Titanium Aluminides Using Gas Tungsten Arc Welding,” *Additive Manufacturing*, Vol. 8, pp. 71–77, 2015.
146. Montevicchi, F., Venturini, G., Grossi, N., Scippa, A., and Campatelli, G., “Idle Time Selection for Wire-Arc Additive Manufacturing: A Finite Element-Based Technique,” *Additive Manufacturing*, Vol. 21, pp. 479–486, 2018.
147. Michaleris, P., “Modeling Metal Deposition in Heat Transfer Analyses of Additive Manufacturing Processes,” *Finite Elements in Analysis and Design*, Vol. 86, pp. 51–60, 2014.
148. Chua, B. L., Lee, H. J., Ahn, D. G., and Wang, Y., “A Study on Activation Algorithm of Finite Elements for Three-Dimensional Transient Heat Transfer Analysis of Directed Energy Deposition Process,” *International Journal of Precision Engineering and Manufacturing*, Vol. 20, No. 5, pp. 863–869, 2019.

## ACKNOWLEDGEMENTS

The decision to leave my family and venture into a country where I could not speak their language was one of the biggest and hardest decisions I have ever made. I am feeling grateful to be able to pursue into the long-tail additive manufacturing area and complete this Doctoral research project. The success of this project is the outcome of accumulated contributions from numerous great individuals and organisations, either directly or indirectly.

First and foremost, I would like to express my sincere gratitude and appreciations to my research advisor, Professor Ahn Dong-Gyu for his continual guidance, enthusiasm and support that he has provided me throughout the years. I could not be more fortunate to have such extraordinary person who guides me through this work.

Second, I would like to express my thankfulness to the examination committee, which consists of Professor Han Gil-Young, Professor Park Jong-Rak, Professor Oh Dong-Wook and Dr. Son Yong, for their valuable time and constructive comments to sharpen this thesis.

I would like to thank the former and current members of the CAD/CAM/CAE Laboratory for their direct support and assistances, particularly to Dr. Lee Ho-Jin, Jang Yong-Hun, Kim Dong-In, Lee Kwang-Kyu, Kim Hyun-Sik and Kim Ho. My stay in Korea may not be as smooth as it would be due to my language barrier.

Acknowledgements are also due to Chosun University for providing me the scholarship that covers 83% of my tuition fee, and Dr. Kim Jae-Gu of Korea Institute of Machinery and Materials for leading the project grant that supports most of my researches and publications. Besides, I should acknowledge Professor Wang Yeqing of Mississippi State University, who assisted in getting me started with the Abaqus-Matlab integration using his element deletion code. Not forgotten, my acknowledgement to Universiti Malaysia Sabah (UMS) for the support to undergo this study leave in order to pursue the research in the area that I had wished.

Besides, I would like to express my heartfelt appreciation to my friends, Dr. Renee who

diligently combed through the draft, fine-tuned the write-up and saved me from numerous mistakes throughout the writing of this thesis. I could not thank you enough for this.

I would like to express my heartfelt gratitude to my great buddies, particularly to Ahmad Ijaz, Lam Thuy Giang, and Lilian C. Mutalemwa, whom brighten up my stay in Chosun University. Not forgotten are the groups of close friends who stay in touch with me from Malaysia. Your presences and helps do mean a lot to me to get through some hard time in Korea.

My very special thank goes to my dearest family. My wife, Chang Shui Han for her unconditional love, trust, understanding, patience and emotional supports throughout the good and bad times for the last 20 years; My children, who grew up and adapted well without my presence for the last 3 years; My brother and sister, who always there to support me; My parents, who I have failed to care enough. My thanks to you are boundless.

CHUA BIH LII

July 1, 2019



## CURRICULUM VITAE

### Academic Qualifications:

- I. B.Eng (Hons) Mechanical Engineering, Universiti Malaysia Sabah, Malaysia, 2004.
- II. M.Eng Mechanical Engineering (Robotics and Industrial Automation), Universiti Malaysia Sabah, Malaysia, 2008.

### Professional Membership:

- I. Professional Engineer (Mechanical-PE17189), Board of Engineers, Malaysia.
- II. Associate ASEAN Engineering Technologist (AAET-173), ASEAN Engineering Register.

### Journal Publications (September 2016 – April 2019):

- 1) Bih-Lii Chua, Yong-Hun Jang, and Dong-Gyu Ahn, *Influence of corrugation angle and load position on the flexural characteristics of lightweight plastic sandwich panel with corrugated cores*, Journal of the Korean Society and Precision Engineering, Vol. 34, No. 7, pp. 493-500, 2017.  
(ISSN 1225-9071 (Print) / 2287-8769 (Online) - SCOPUS, KCI)
- 2) Bih-Lii Chua, Ho-Jin Lee, Dong-Gyu Ahn, and Jae-Gu Kim, *Investigation of penetration depth and efficiency of applied heat flux in a directed energy deposition process with feeding of Ti-6Al-4V wires*, Journal of the Korean Society and Precision Engineering, Vol. 35, No. 2, pp. 211-217, 2018.  
(ISSN 1225-9071 (Print) / 2287-8769 (Online) - SCOPUS, KCI)
- 3) Bih-Lii Chua, Ho-Jin Lee, and Dong-Gyu Ahn, *Estimation of effective thermal conductivity of Ti-6Al-4V powders for a powder bed fusion process using finite element analysis*, International Journal of Precision Engineering and Manufacturing, Vol. 19, No. 2, pp. 257-264, 2018.  
(ISSN 2234-7593 (Print) / 2005-4602 (Online) – SCI-e, SCOPUS)
- 4) Bih Lii Chua, Ho Jin Lee, Dong-Gyu Ahn, and Jae Gu Kim, *Influence of angle of corner deposition on temperature and residual stress distributions in the vicinity of the deposited region by a Ti-6Al-4V wire-feeding type of directed energy deposition process*, Journal of the Korean Society and Precision Engineering, Vol. 35, No. 9, pp. 853-859, 2018.  
(ISSN 1225-9071 (Print) / 2287-8769 (Online) - SCOPUS, KCI)
- 5) Bih Lii Chua, Ho Jin Lee, Dong-Gyu Ahn, and Jae Gu Kim, *Influence of process parameters on temperature and residual stress distributions of the deposited part by a Ti-6Al-4V wire feeding type directed energy deposition process*, Journal of Mechanical Science and Technology, Vol. 32, No. 11, pp. 5363-5372, 2018.  
(ISSN 1738-494X (Print) / 1976-3824 (Online) - SCI-e, SCOPUS)

- 6) Bih-Lii Chua, Ho-Jin Lee, Dong-Gyu Ahn, and Yeqing Wang, *A study on activation algorithm of finite elements for three-dimensional transient heat transfer analysis of directed energy deposition process*, International Journal of Precision Engineering and Manufacturing, Vol. 20, No. 5, pp. 863-869, 2019.  
(ISSN 2234-7593 (Print) / 2005-4602 (Online) – SCI-e, SCOPUS)

**Conference Publication (September 2016 – April 2019):**

- 1) B. L. Chua, Y. H. Jung, and D. G. Ahn, *Influence of the geometry of corrugated inner structures on flexural characteristics of plastic sandwich panel*, 7th International Conference on Manufacturing, Machine Design and Tribology (ICMDT 2017), Jeju, 19-22 April 2017. (Oral)
- 2) B. L. Chua, H. J. Lee, and D. G. Ahn, *A study on the variation of effective thermal conductivity according to contact area of the sintered Stellite 21 powder in a vacuum environment*, Korean Society of Precision Engineers Autumn Conference 2017, Jeju, 17-19 May 2017. (Poster)
- 3) H. J. Lee, B. L. Chua, and D. G. Ahn, *Development of the principal heat transfer analysis model for plasma electron beam melting process*, Korean Society of Precision Engineers Autumn Conference 2017, Jeju, 17-19 May 2017. (Oral)
- 4) B. L. Chua, H. J. Lee, D. G. Ahn, and J. G. Kim, *A study on the estimation of efficiency and penetration depth of laser beam in a wire feeding type DED process*, Korean Society of Mechanical Engineers Autumn Conference 2017, Jeju, 1-3 November 2017. (Poster)
- 5) H. J. Lee, B. L. Chua, and D. G. Ahn, *Investigation into characteristics of the deposition bead in a selective electron beam melting process using a plasma electron beam*, International Mechanical Engineering Congress & Exposition (IMECE 2017), Florida, 3-9 November 2017. (Poster)
- 6) B. L. Chua, H. J. Lee, and D. G. Ahn, *Preliminary heat transfer analysis of melting process for a powder bed fusion system using an electron beam*, 7th International Conference of Asian Society for Precision Engineering and Nanotechnology (ASPEN 2017), Seoul, 14-17 November 2017. (Poster)
- 7) D. G. Ahn, H. J. Lee, B. L. Chua, E. G. Kang, and J. S. Kim, *Investigation into the fabrication characteristics of melting bead in electron beam melting process using a plasma electron beam*, 7th International Conference of Asian Society for Precision Engineering and Nanotechnology (ASPEN 2017), Seoul, 14-17 November 2017. (Oral)
- 8) B. L. Chua, H. J. Lee, D. G. Ahn and J. G. Kim, *A study on the thermal stress analysis for a single-layer straight path deposition in a wire feeding type DED process*, Korean Society of Precision Engineers Autumn Conference 2017, Gyeonggi, 13-15 December 2017. (Poster)
- 9) H. J. Lee, B. L. Chua, and D. G. Ahn, *Investigation into the fabrication characteristics of melting bead for additive manufacturing process using plasma electron beam*, Korean Society of Precision Engineers Autumn Conference 2017, Gyeonggi, 13-15 December 2017. (Oral)

- 10) H. J. Lee, B. L. Chua, D. G. Ahn, and W. S. Woo, *Investigation into the sintering characteristics of Stellite21 powders according to heating temperature using fiber laser system*, Korean Society of Thermophysical Properties Symposium 2018, Gwangju, 5-6 April 2018. (Poster)
- 11) B. L. Chua, H. J. Lee, D. G. Ahn, and J. G. Kim, *A study on the thermal stress analysis for a single-layer planar deposition using a wire feeding type DED process*, Korean Society of Precision Engineers Spring Conference 2018, Jeju, 9-11 May 2018. (Oral)
- 12) H. J. Lee, B. L. Chua, E. G. Kang, and D. G. Ahn, *Development of analysis model for electron beam melting process using plasma electron beam*, Korean Society of Precision Engineers Spring Conference 2018, Jeju, 9-11 May 2018. (Oral)
- 13) H. J. Lee, B. L. Chua, K. K. Lee, and D. G. Ahn, *Investigation into morphology of melting bead of deposition process using plasma electron beam*, Korean Society of Precision Engineers Spring Conference 2018, Jeju, 9-11 May 2018. (Poster)
- 14) B. L. Chua, H. J. Lee, D. G. Ahn, and J. G. Kim, *A preliminary study on the thermal stress analysis of multi-layer deposition for a wire feeding type DED process*, Korean Society of Mechanical Engineers Spring Conference 2018, Seoul, 1-2 June 2018. (Oral)
- 15) D. G. Ahn, B. L. Chua, H. J. Lee, and J. G. Kim, *Thermo-mechanical analysis of corner deposition of a Ti-6Al-4V Wire feeding type DED process*, International Symposium on Precision Engineering and Sustainable Manufacturing (PRESM2018), Sapporo, 3-7 July 2018. (Oral)
- 16) D. G. Ahn, H. J. Lee, and B. L. Chua, *Development of re-melting analysis model for the metal additive manufacturing process using plasma electron beam*, Korean Society for Technology of Plasticity Fall Conference, Jeju, 11-12 October 2018. (Poster)
- 17) B. L. Chua, H. J. Lee, D. G. Ahn, and J. G. Kim, *A study on thermo-mechanical analysis of multi-layer deposition for a wire feeding type DED process*, Korean Society of Precision Engineers Autumn Conference 2018, Gunsan, 25-26 October 2018. (Oral)
- 18) H. J. Lee, B. L. Chua, E. G. Kang, and D. G. Ahn, *Development of powder bed fusion process using plasma electron beam*, Korean Society of Precision Engineers Autumn Conference 2018, Gunsan, 25-26 October 2018. (Oral)
- 19) H. J. Lee, B. L. Chua, and D. G. Ahn, *Development of analysis model for powder bed fusion process using plasma electron beam*, Korean Society of Precision Engineers Autumn Conference 2018, Gunsan, 25-26 October 2018. (Poster)
- 20) B. L. Chua, D. G. Ahn, H. J. Lee, and J. G. Kim, *Influence of convection on thermal-displacement distribution of multi-layer deposition for a wire feeding type directed energy deposition process*, International Conference on Mechanical Engineering, Energy and Advanced Materials 2018 (ICMEEAM2018), Kota Kinabalu, 29-30 November 2018. (Oral)
- 21) B. L. Chua, H. J. Lee, and D. G. Ahn, *A study on heat transfer analysis using element activation technique for a directed energy deposition process*, Annual Conference of the Korean Society of Mechanical Engineers 2018, Gangwon, 12-14 December 2018. (Oral)

- 22) D. G. Ahn, H. J. Lee, and B. L. Chua, *Study on the powder spreading phenomenon of electron beam based powder bed fusion process using heat transfer analysis*, Annual Conference of the Korean Society of Mechanical Engineers 2018, Gangwon, 12-14 December 2018. (Poster)
- 23) B. L. Chua, D. G. Ahn, and J. G. Kim, *A study into thermo-mechanical characteristics for a multi-layer deposition using a wire feeding type DED process*, International Conference on Manufacturing, Machine Design and Tribology 2019 (ICMDT2018), Kagoshima, 24-27 April 2019. (Oral)